Structural studies of the aggregation of selected beta-amyloid peptides in the presence of human albumin and human cystatin C

Badania strukturalne agregacji wybranych peptydów beta-amyloidowych w obecności ludzkiej albuminy i ludzkiej cystatyny C

Mgr Adriana Żyła

Doctoral dissertation conducted at the Department of Biomedical Physics under the supervision of prof. dr hab. Maciej Kozak

Supporting supervisor: dr Łukasz Popenda

Poznań, 2022

Abstract

The development of neurodegenerative disorders, such as Alzheimer's, or Parkinson's disease, correlates with the extended lifetime of the human population of the 21st century. These diseases represent a serious challenge for medicine, science, and even society. To this day, no effective drugs able to cure and reverse neurodegenerative disorders have been discovered. It is, therefore, of significant importance to study their mechanisms at the molecular level, which can contribute to effective drug design or the development of new therapeutic strategies that could slow down or even stop neurodegeneration. The discovery of proteins and peptides involved in the development of these diseases was a milestone in understanding Alzheimer's disease (AD) at the molecular level. Determination of the three-dimensional structures of these macromolecules led to a better understanding of the basics of protein aggregation and the formation of their neurotoxic oligomers or amyloid deposits. However, mechanisms of amyloid-beta peptides aggregation in the human brain and the role of associated proteins involved in this process still require further classification.

The studies presented in this work allowed to describe the structural parameters of Aβ peptides interacting with two proteins - the human cystatin C (HCC) and human serum albumin (HSA). Both proteins have been reported as macromolecules involved in the inhibition of the Aβ aggregation process. Moreover, HCC was found to be a co-deposit in senile plaques in AD individuals. The three Aβ peptides variant (1-16, 3-28, and 1-42) were selected for studies presented in this PhD thesis because of their specific properties and their role in the development of AD. Potential interaction between these two HSA and HCC proteins was also explored. To characterize the mechanism of the interactions between Aβ, HSA and HCC, a set of biophysical methods was chosen. Among them, mass spectroscopy, small angle scattering of X-ray and neutrons, and atomic force microscopy were used to characterize sample topology and to track the disaggregation process.

The most important outcome of this research implicates that HCC can disaggregate Aβ 3-28 fibers, while fibers formed by Aβ 1-42 remain resistant. The proposed model of interactions and the properties of those macromolecular complexes is important for better understanding of the pathological role of Aβ same as the protective role of HCC and HSA proteins against Aβ aggregation. These studies shed light not only on the mechanism of Aβ aggregation inhibition

and also the disaggregation of Aβ fibrils, but also provide new ideas for the development of improved therapies.

Streszczenie

Rozwój zaburzeń neurodegeneracyjnych (m. in. choroby Alzheimera, Parkinsona) koreluje z wydłużaniem się życia w populacji ludzkiej XXI wieku. Choroby te stanowią poważne wyzwanie dla medycyny, nauki, a nawet społeczeństwa. Wciąż nie ma skutecznych leków, które byłyby w stanie leczyć i odwracać skutecznie skutki chorób neurodegeneracyjnych. Dlatego bardzo ważne jest badanie mechanizmów choroby na poziomie molekularnym, co może przyczynić się do skutecznego projektowania leków lub opracowywania nowych strategii terapeutycznych, które mogą spowolnić, a nawet zatrzymać procesy neurodegeneracyjne w chorobie Alzheimera. Odkrycie cząsteczek (białek i peptydów) zaangażowanych w rozwój tych chorób było kamieniem milowym w zrozumieniu choroby Alzheimera na poziomie molekularnym. Jednak mechanizmy agregacji peptydów beta-amyloidowych w mózgu człowieka i rola białek towarzyszących biorących udział w tym procesie wymagają jeszcze dalszej klasyfikacji. Określenie trójwymiarowych struktur tych makrocząsteczek umożliwiło zrozumienie niektórych podstaw agregacji białek i powstawania ich neurotoksycznych oligomerów lub złogów amyloidowych.

Przedstawione w niniejszej pracy badania opisują parametry strukturalne peptydów Aβ oddziałujących z dwoma białkami – ludzką cystatyną C i ludzką albuminą surowicy. Oba białka opisano jako makrocząsteczki zaangażowane w hamowanie procesu agregacji Aβ. Co więcej, HCC znaleziono jako depozyt w blaszkach starczych u osób z AD. Do badania wybrano trzy warianty peptydów Aβ jako reprezentujące specyficzne właściwości beta-amyloidu (1-16, 3-28 i 1-42). Zbadano również potencjalną interakcję między tymi dwoma białkami HSA i HCC. Do scharakteryzowania mechanizmu oddziaływań między Aβ HSA i HCC wybrano zestaw metod biofizycznych. Do scharakteryzowania topologii próbki i śledzenia procesu desegregacji wykorzystano m.in. spektroskopię masową, małokątowe rozpraszanie promieni rentgenowskich i neutronów czy spektroskopię sił atomowych.

Najważniejszy wynik przeprowadzonych badań wskazuje, że HCC może dezagregować włókna Aβ 3-28, jednak włókna utworzone przez Aβ 1-42 były odporne. Zaproponowany model oddziaływań i właściwości oddziaływań w tych wielkocząsteczkowych kompleksach był istotny dla lepszego zrozumienia patologicznej roli Aβ oraz ochronnego działania białek HCC i HSA przed agregacją Aβ. Badania te mogą rzucić światło nie tylko na mechanizm hamowania

agregacji peptydów Aβ i dezagregacji fibryli Aβ, ale także mogą przynieść nowe rozwiązania w zakresie zwalczania tych czynników chorobowych.

Acknowledgments

Thank You

To my thesis supervisor Maciej Kozak, for his guidance and encouraging me to work independently. As a supervisor, he was very motivating which inspired me to give my best efforts.

To Anne Martel for her mentorship, and long discussions about science during my year internship at ILL.

To Aneta Szymańska, Przemysław Jurczak, Ewa Banachowicz, Kosma Szutkowski, Igor Zhukov, Augustyn Moliński, Paulina Czaplewska, Aline Le, Christine Ebel. Łukasz Popenda, and Zuzanna Pietralik-Molińska, for support and scientific collaboration.

To my parents Elżbieta and Wiesław who always supported me.

To Dorota Niedziałek who always supports me and continues to inspire me in my journey as a scientist and human.

To Marcin Magnus and Katarzyna Merdas, for precious help and support.

To Julien Volle for his great support and patience.

Funding

This work was supported by the following sources:

NCN National Science Center (NCN) – grant 2017/27/B/ST4/00485, Mechanisms of binding and transport in plasma of amyloid beta oligomers by human serum albumin (HSA) in presence of selected ligands to Professor Maciej Kozak (principal investigator), Adriana Żyła as subcontractor

Polish National Center for Research and Development / European funds, Environmental interdisciplinary PhD studies program in nanotechnology, POWR.03.02.00-00-I032/16 - scholarship

ILL Long term visitor supportive grant - awarded by the director of the Institute of Laue-Langevin.

Table of Contents

Abbreviations

AD - Alzheimer's disease

Aβ - beta amyloid peptide

AcD - acidic linker between E1 and E2 in APP

AFM – atomic force microscopy

AICD - intracellular domain of APP

AMP - ampicillin

APP - amyloid precursor protein

AUC - analytical ultracentrifugation

BS - binding site

C - cysteine

CD - circular dichroism

X^2 - X squared test (also chi-square or $\chi 2$ test)

CSF - cerebrospinal fluid

CNS - central nervous system

CuBD - copper binding domain of APP

D - aspartic acid

DI-III - domain 1- domain III

OD_{600} - optical density measured at wavelength λ=600

E - glutamic acid

E. coli - Escherichia coli

F - phenylalanine

G - glycine

GFLD - N-terminal growth factor-like domain of APP

H - histidine

HCC - Human Cystatin C

HCCAA - hereditary Cystatin C amyloid angiopathy

HFIP - 1,1,1,3,3,3-Hexafluoro-2-propanol, (CF3)2CHOH

HSA - Human Serum albumin

HSQC - heteronuclear single quantum coherence

I - isoleucine

IEX - ion exchange chromatography

JMR - juxtamembrane region of APP

K - lysine

KAN - kanamycin antibiotic

L - leucine

LB - lysogeny broth medium

MD - molecular dynamics

MMSE - mini-mental state examination

MS – mass spectrometry

NFTs - neurofibrillary tangles

NMR - nuclear magnetic resonance

NOE - nuclear Overhauser effect spectroscopy

PDB - protein data bank

PrP - prion protein

RMSD - root mean square deviation

SANS - small angle neutron scattering

SAS - small angle scattering

SAXS - small angle X-ray scattering

SDS PAGE - sodium dodecyl sulfate–polyacrylamide gel electrophoresis

SEC - size exclusion chromatography

ss - secondary structure

TB - terrific broth medium

TEM - transmission electron microscopy

TM - transmembrane domain

Tris - buffer, trometamol, 2-amino-2-(hydroxymethyl)-1,3-propanediol,

V - valine

V57G - Val57Gly, HCC mutation – valine in position 57 exchanged to glycine

Y – tyrosine

1. Aim of the thesis

Amyloid beta (Aβ) peptides were discovered almost 40 years ago in people suffering from dementia, and since then researchers have been trying to determine in details the processes underlying the neurodegeneration of Alzheimer's disease (AD). Currently, there are only a few treatments available that can only treat a part of the symptoms of the disease, but so far, no effective treatment for reversing and curing AD dementia has been established. The advancements in medicine and technology extended the life expectancy, which in turn increased the frequency of diagnosing. The disease has become a growing problem since medical and technological advances have allowed the extension of the average human life. Further research focusing on understanding disease pathology, accompanied by the development of new therapeutics, appears to be critical for society.

The conducted study aimed at characterizing the role of human cystatin C (HCC) and human serum albumin (HSA) and their molecular interactions with selected beta-amyloid peptides which are a fingerprint of AD disease. Both proteins were reported to inhibit the aggregation process of Aβ peptides. Those proteins are present in significant concentrations in body fluids and are also abundant in the central nervous system (CNS). Moreover, HCC was also found to be a part of co-deposits in senile plaques in AD individuals. The chosen molecular system was investigated by a set of biophysical techniques to describe the structural parameters and dynamics of Aβ peptides in presence of HCC and HSA to uncover a potential model of interactions. This doctoral dissertation aspires to improve the understanding of the complexation mechanisms of Aβ peptides assembly in the presence of HSA and HCC, which ideally may bring new explanations and ideas on how to stop or delay this pathogenic process.

Considering the fact that HCC and HSA are present in high concentrations in cerebrospinal fluid (CSF) and may inhibit oligomerization of Aβ peptides, we hypothesized that above-mentioned proteins can have a protective role, which has not yet been unambiguously described. The main aims of this study were:

A1) Determination of the structural parameters of potential complexes between Aβ peptides and HSA and HCC;
A2) Determination of the structural parameters of potential complex between HSA and HCC;
B) Description of the interactions between HCC and HSA and selected Aβ peptides;

C) Determination the zone in the protein structure which is engaged in these interactions.

These research aims serve as a starting point for the performed studies, which can shed more light on the Aβ aggregation process, with the emphasis on investigating the mechanisms preventing this pathological event. Additionally, the investigation will focus on interactions between HSA and HCC and toxic oligomers and fibrils, exhibiting potential protecting role in preventing dementia caused by senile plaques.

For the purpose of this research and to provide a description of the molecular system, the following specific tasks were designed:

A) Expression of HCC protein for the studies of protein-protein, protein-peptides interactions;
B) Designing high yield protocol for expression of deuterium-labeled HCC protein for SANS studies of the interaction between HCC and Aβ fibrils
C) Synthesis and purification of Aβ peptides for peptide-protein interaction
D) Investigation of HSA-HCC complex by AUC, SAXS, NMR
E) Investigation of HSA and chosen Aβ peptides complex by MS, SAXS, SANS
F) Studies of the possible influence of HCC (deuterated) on Aβ fibrils
G) Characterization of Aβ peptides fibrils by AFM and its interactions with HCC
H) Proposing a possible model of interactions and theoretical full atom models for studies of complexes

2. Introduction

2.1. Neurodegenerative Disorders

According to the World Health Organization (WHO), dementia as a chronic disease is represented by a wide range of symptoms resulting from progressive damage to the neuronal cells and their connections in the central nervous system, in particular, in the brain[1]. In consequence, dementia disrupts many functions of the organism such as mobility, coordination, muscle strength, learning and cognition resulting in memory impairment, anxiety, and mood disorder. With the wide range of symptoms, dementia prevents independent functioning in society and very often completely excludes sick individuals[2].

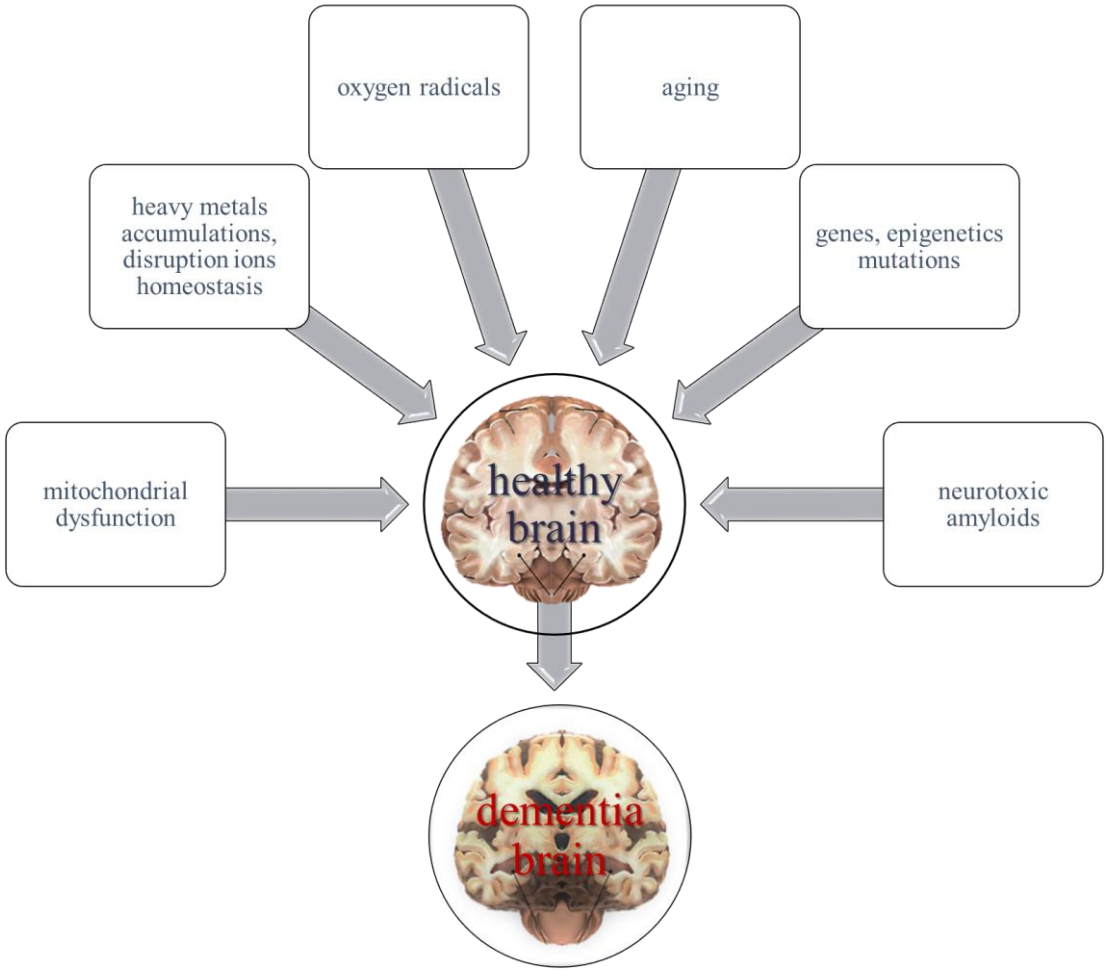

Figure 1. Schematic graph showing factors increasing neurodegeneration process in the human brain

One of the major risks of developing a neurodegenerative disease is linked to the natural aging process. Occurrence of neurodegenerative diseases increases with age[1]. Current technological and medical progress has significantly prolonged the average lifespan of the population. Due to an older society, diseases of old age, including dementia and neurodegenerative diseases, have become one of the main challenges of today's medicine and they are called “civilization diseases”. Besides the correlation with age, there are many other factors such as genetic trends, and the environmental factors, that may contribute to the development of these neurodegenerative conditions (Figure 1)[3]. Some statistical data indicated that lower intellectual activity was associated with an increased risk for developing dementia[4]. Many studies implicate that DNA damage[5] results from the accumulation of heavy metals[6], oxidative stress[7], and provides the underlying causative link between aging and neurodegenerative disease. The most common neurodegenerative disease in Europe is Alzheimer’s Disease (AD)[8]. AD is diagnosed by the presence of insoluble aggregates protein. Nevertheless, there are many already known neurodegenerative diseases caused by similar processes of aggregation of pathogenic forms of polypeptides (Table 1). Same as in AD, risk factors for these diseases include irregularities in the brain and CNS, such as genetic mutation, misfolded proteins, or metabolism anomalies.

Table 1. Neurodegenerative disorders caused by aggregates of pathogenic polypeptides (adapted from: Yadav, 2015[7])

NEURODEGENERATIVE DISORDERS	AGGREGATED PROTEIN	LESION AND ACCUMULATED SITES
Alzheimer's disease	amyloid-β peptide	Amyloid plaques extracellularly
	Tau	NFT in intracytoplasmic neurons
	α-Synuclein	Lewy bodies variants in intracytoplasmic neurons
Parkinson's disease	α-Synuclein	Lewy bodies in intracytoplasmic neurons
Huntington's disease	Huntington (polyglutamine repeats)	Neuronal inclusions in nuclei of neurons
Amyotrophic lateral sclerosis	SOD1	Hyaline inclusions in intracytoplasmic neurons
Dementia with Lewy bodies	α-Synuclein	Lewy bodies in intracytoplasmic Neurons
Multiple system atrophy	α-Synuclein	Glial cytoplasmic inclusions in cytoplasm of oligodendrocytes
Supranuclear palsy	tau	Tau inclusions in intracytoplasmic neurons, astrocytes, oligodendrogliocytes
Spinocerebellar ataxia	Ataxin (polyglutamine repeats)	Neuronal inclusions in nuclei of neurons
Prion diseases	protease-resistant prion proteins	Prion plaques extracellularly
Pick's disease	tau	Pick bodies in intracytoplasmic neurons

2.1.1. Social impact, prevalence of neurodegenerative diseases

The current worldwide estimation of people suffering from dementia is around 50 million, furthermore this number will significantly increase up to 115 million by 2050[1]. Due to development of technology, medicine and improved diagnosis of patients, each next prognosis of AD cases is always more dramatic than the previous. AD alone is responsible for 50% of all dementia cases and 5 million new AD cases are reported each year. Aging is the most influential known risk factor for dementia, and it is estimated that 25% to 45% of people over the age of 85 will suffer from neurodegeneration.

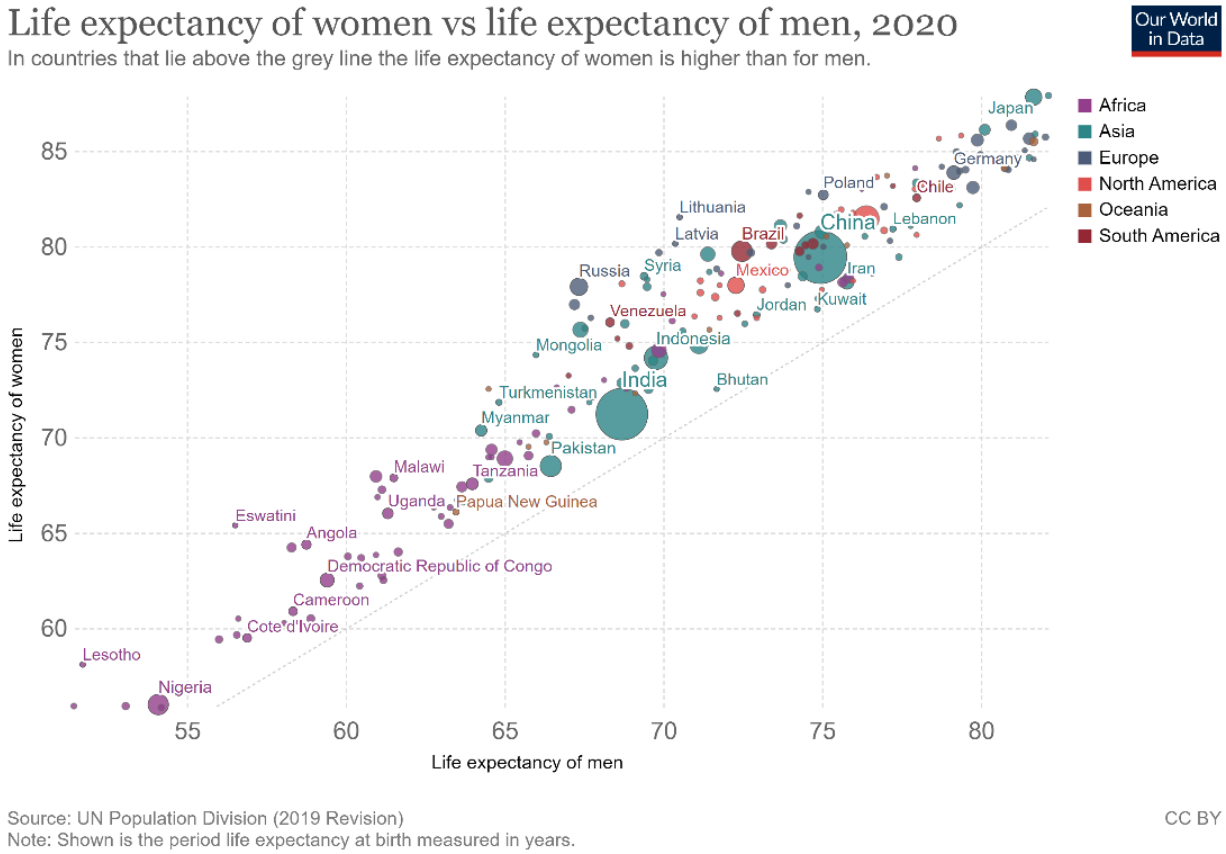

Figure 2. Average life expectancy of women and men in different part of the word (Adapted from https: www.ourworldindata.org)

It is important to mention that dementia presents a gender predisposition. Almost 66% of AD cases are females (Figure 3). The main reason to explain this phenomenon is that the life expectancy of women is superior to men[9] (Figure 2) and aging is the greatest risk factor for AD.

Moreover, recent studies suggest a connection with gender is linked with the loss of sex hormones like estrogen[10].

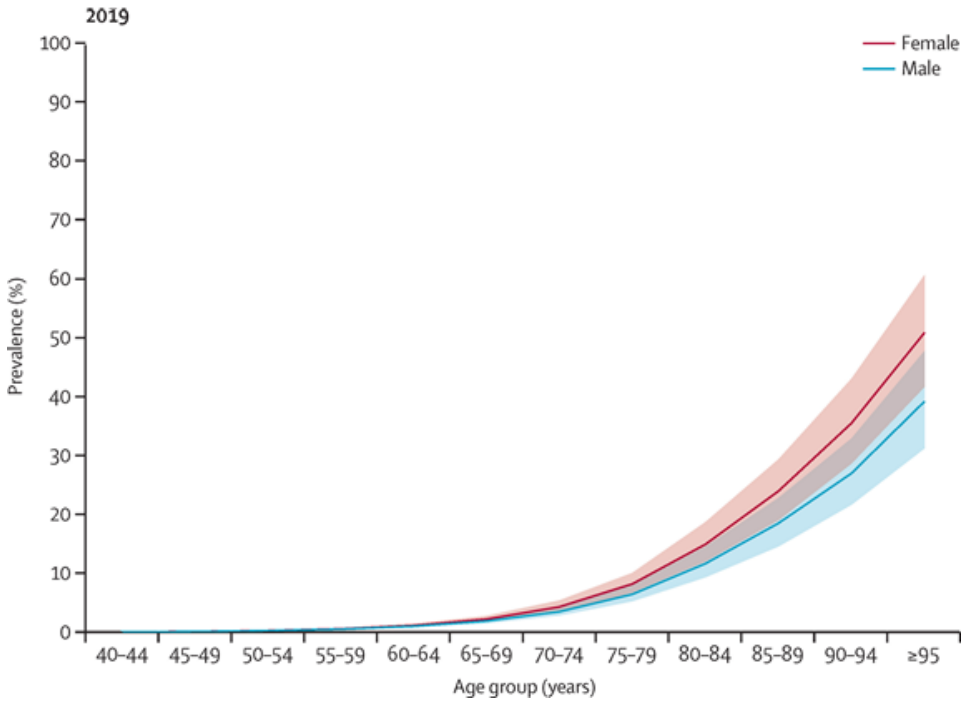

Figure 3. Global prevalence of dementia (with 95% uncertainty intervals) by age group and sex in 2019 (Adapted from: GBD 2019 Dementia Forecasting Collaborators, 2022 [1])

2.1.2. Alzheimer's disease

Alzheimer's disease (AD) is the most common degenerative brain disease (so-called Alzheimer's-type dementia)[11]. On a cellular level, AD is characterized by the major loss of neurons and synapses in the brain[12]. In particular, it includes the degeneration of the temporal lobe and parietal lobe and also parts of the frontal cortex and cingulate gyrus regions (cerebral cortex and hippocampus). Besides the degradation of the brain, there are two other biological fingerprints characteristics of AD. A typical pathogenic hallmark is the presence of extracellular senile plaques (composed of amyloids beta peptides (Aβ))[13] and intracellular neurofibrillary tangles (τ protein aggregates)[14] (Figure 4). These pathological products of oligomeric Aβ and misfolded τ protein present in the central nervous system (CNS) of AD individuals have neurotoxic properties and are suspected of playing a role in the progression of the disease.

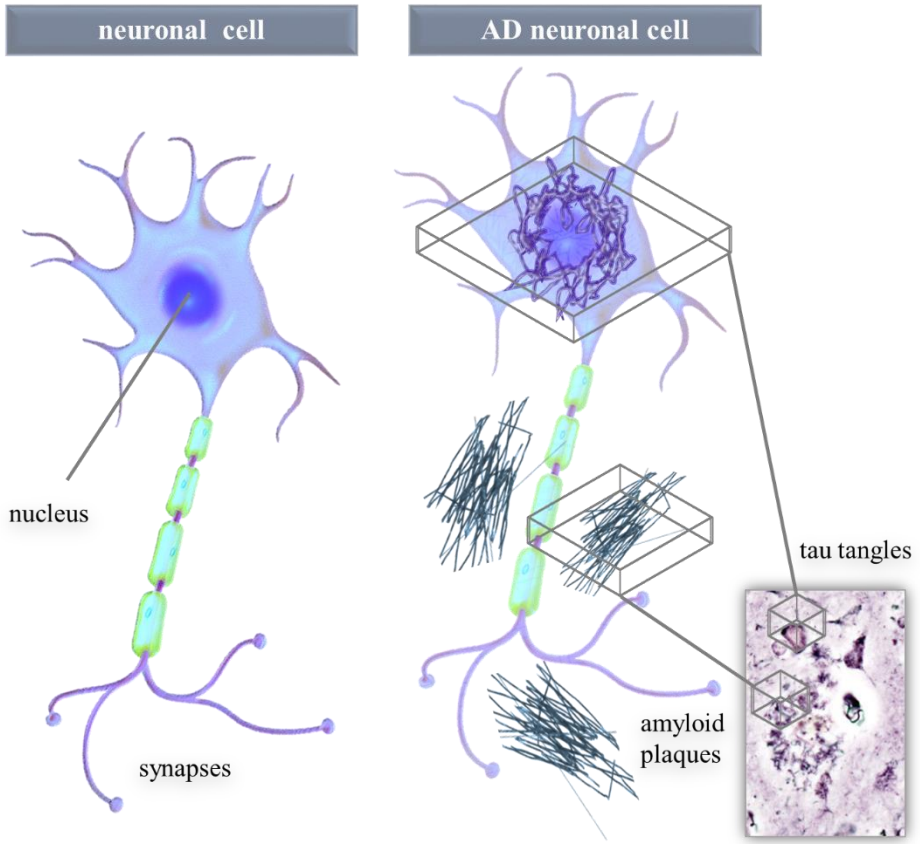

Figure 4. Schematic comparison of healthy and pathological neuronal cells. In the pathological condition, the misfolded τ protein creates neurofibrillary tangles within the neuronal cell. The Aβ peptides secreted to extracellular space form insoluble senile plaques[15].

The direct cause of AD remains unknown, however, during years of investigation scientists proposed some theories explaining the origin and the predisposition to suffer from AD:

The cholinergic hypothesis

The oldest hypothesis of AD occurrence is the cholinergic hypothesis[16]. It claims that AD is caused by decreased level of synthesis of acetylcholine which is an important neurotransmitter produced in acetylcholine neurons. The dysfunction of cholinergic neurons contributes to the cognitive decline observed in the elderly and in AD. In acetylcholine loss-based AD therapy muscarinic, nicotinic-cholinergic ligands and acetylcholinesterase inhibitors were tested. Studies in AD patients involving the use of

acetylcholinesterase inhibitors (donepezil, rivastigmine, etc.) have shown efficacy in addressing the symptoms of AD but have also been burdened with side effects.

The amyloid peptides

After 1991, scientists put forward the amyloid hypothesis (Aβ plaques were discovered in 1984)[17,18]. It is speculated that Aβ exerts its main effects early in the disease progression by triggering a cascade of processes involved in neurodegeneration. Aβ deposits, which create senile plaques found in AD patients, is disrupting neuronal homeostasis and play a significant a role in the pathogenesis of this disease[19]. The Aβ peptides are created alongside the degradation path of amyloid precursor protein (APP)[20], and accumulate in the form of amyloid deposits in the brain, whose presence has important consequences its proper functioning. This hypothesis is supported by the fact that APP gene is located on chromosome 21 and the role of this chromosome has been reported in Down's syndrome (DS, chromosome 21 trisomy)[21]. People suffering from DS in the age of 40 and above have an elevated risk of developing AD. Many mutations in the APP genes may be correlated with the increased appearance of Aβ 1-42 peptides in CNS. Therapeutic strategies targeting APP include ligand inhibitors for β, γ secretases[22], which are enzymes cleaving APP in the amyloidogenic pathway. Recently, it was proposed that the immunotherapy approach, in which antibodies are targeting Aβ plagues in order to desegregate those complexes. This approach represents a major step in the development of new therapies[23].

The τ protein

The τ (tau) hypothesis assumes that the misfolded conformation of the protein τ initiates a nucleation reaction and starts disease events[14]. The τ protein forms insoluble fibers that accumulate as neurofibrillary tangles (NFTs). The hyperphosphorylated polypeptide chains of the τ protein, begin to aggregate and as result, they create neurofibrillary tangles inside the neuronal cells causing apoptosis. The cause of the hyperphosphorylation of the τ protein, which leading to its aggregation, is unambiguously due to an anomaly in cell signaling, which is the consequence of a disturbance in the activity of various protein kinases and phosphatases[14]. This

phenomenon is alike the prion peptides infection. In AD therapy where the τ protein is targeted a few strategies were designed[14]. One approach is focusing on the inhibition of the abnormal τ hyper-phosphorylation process by controlling the activity of some protein kinases (e.g. CaMK II and MAPK family). Other ones are focusing on the degradation of τ's NFTs or triggering the autophagy by the ubiquitin-proteasome. Same as in the case of Aβ, the τ targeted immunotherapy is also being studied.

Apolipoprotein

One of the well-studied genetic risk factors for AD is the expression of the isomeric forms of apolipoprotein (APOE)[24]. The role of APOE is the transport of cholesterol, which is involved in the repair processes of the brain, lipid transfer, and the build-up of lipid raft cell membranes. Genetic abnormalities in the expression of APOE isomers have been correlated with the pathological state in AD patients[24]. Caring only one of the potential abnormal genes of APOE form increases the risk of AD. APOE alleles are polymorphic with three different forms of APOE: APOE2, APOE3, and APOE4. APOE4 carriers have a higher risk of developing AD[25]. This APOE4 variant is expressed in over 50 percent of AD patients. On the contrary the variant APOE2 shows protective properties against AD[25].

Triggering receptor expressed on myeloid cells 2

TREM2 is a triggering receptor expressed on macrophage cells of the bone marrow and cortex and belongs to the species of immune receptors[26]. Its role is to induce phagocytosis in the bone marrow, in particular in microglia and macrophages. TREM2 is a transmembrane receptor and is associated with AD immune response and inflammatory pathways. TREM2 variants (gene variant, rs75932628 (encoding R47H))[27] related to AD disrupt the function of the TREM2 protein and the maintenance of microglial cells. The statistical analysis of samples derived from the brain of AD patients revealed that the presence of the TREM2 variant was positively correlated with AD and independently of APOE ε4 allele presence[27].

Alzheimer's disease Continuum.

AD continuum can be described as a constant disease progression, initially from unnoticed metabolic and biological changes in the brain to severe brain damage that ultimately results in physical and psychological disabilities. Currently, it is known that dementia is generally preceded by mild cognitive impairment (MCI)[28]. The early diagnosis of AD is a difficult challenge and is currently based on the Mini-Mental State Examination (MMSE) and medical imaging such as magnetic resonance imaging (MRI) or computed tomography scan (CT). AD continuum (Figure 5) has several phases: 1) preclinical AD, 2) mild cognitive impairment (MCI). The dementia phase of AD is further divided into stages that reflect the severity of the symptoms leading to a severe burden in daily life activities: 1) mild, 2) moderate, 3) severe. Until now, there is no available therapy to reverse the progressive degeneration of neurons and thus, AD is considered to be incurable.

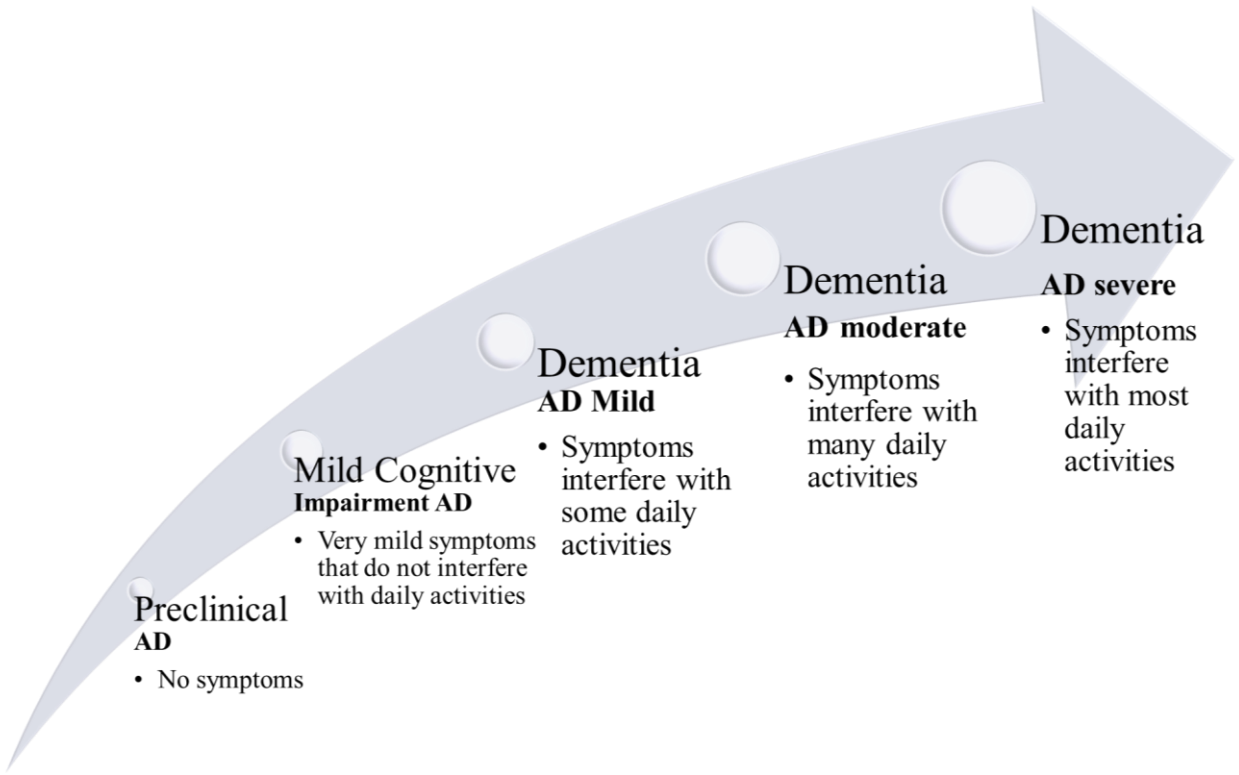

Figure 5. Alzheimer's disease continuum[28].

2.1.3. Therapeutic approaches

The treatment allowing an effective prevention and reversion of AD are still unknown. All the therapies developed until now are only treating symptoms but they do not stop or reversing the pathological development (Table 2). It is worth mentioning that epidemiological studies have reported a relationship between the probability of developing dementia and comorbidities factors such as diabetes, cardiovascular disease, sports practice[29], cigarettes usage, diet, and even education and level[4] intellectual activity. Interestingly, studies on long-term use of non-steroidal anti-inflammatory drugs (NSAIDs) revealed a decrease in the risk of developing AD[30]. Nevertheless, currently there is no medical treatment for AD which cures the disease but, there are available drugs that can temporarily reduce the symptoms slow down or stop the progress of the disease. The U.S. Food and Drug Administration (FDA) has approved several drugs which are commonly prescribed to AD patients. The list of drugs approved by FDA in AD treatment is presented at Table 2[31].

Table 2. FDA approved AD treatments compounds with examples of available products.

DRUG, PRODUCT (MANUFACTURE)	APPROVED	TREATMENT
DONEPEZIL HYDROCHLORIDE: *Aricept* (Pfizer, Eisai)	**1996**	Routine use to treat AD ➢ Cholinesterase inhibitors (ChEIs)
RIVASTAGMINE: EXELON (Novartis)	**1997**	To slow down the progression of moderate to severe AD ➢ Inhibitor: cholinesterase, utyrylcholinesterase
GALANTAMINE: *Razadyne* (Jansen)	**2000**	To slow down the progression of moderate to severe AD ➢ Cholinesterase inhibitors (ChEIs) ➢ Positive allosteric modulator acetylcholine receptors (nAChRs, mAChRs)
MEMENTINE: *Akatino* (Forest Laboratories, Merz Pharma)	**2003**	Routine use to treat AD ➢ NMDAr antagonist
TACRINE: *Cognex* (Pfizer, Shionogi Pharma)	**1993 - 2013**	Discontinued in the U.S., but generic versions may be available. ➢ Inhibitor: cholinesterase
NAMZARIC combination of memantine and donepezil: *Axura, Ebixa, Biomentin* (Merz Pharmaceuticals, Lundbeck, Biofarm)	**2002**	To slow down the progression of moderate to severe AD ➢ Cholinesterase inhibitors (ChEIs) ➢ NMDAr antagonist
ADUCANUMAB: *Aduhelm* (Biogen Inc)	**2021**	An Aβ-peptide directed monoclonal antibodies. ➢ Able to remove amyloid aggregates

2.2. The Aβ peptides

Aβ is a peptide built from up to 49 amino acids residues with a molecular weight over ~4.5 kDa[32]. The sequence of Aβ has been first examined in 1984, from the samples derived from meningeal blood vessels of AD and trisomy 21 patients. It is characterized by specific hydrophobic properties, which cause conformational transition into β-sheet secondary structure (ss) and promote their self-assembly. Aβ peptides can aggregate into different forms of oligomers and fibrils or create senile plaques in brains of AD patients. Such protein deposits, present in the intercellular space, disturb homeostasis and lead to the death of neurons by inducing apoptosis[33]. Aβ peptides are produced naturally by degrading APP[34] in one of the enzymatic cleavage pathways. Aβ monomers released during the sequential proteolytic sequential cleavage of β- and γ-secretase can aggregate into various oligomeric forms[20]. The soluble oligomers can spread further within a CNS and aggregate into amyloid seed inducing a rapid reaction of self-assembly.

For many years of investigation, the Aβ peptides were studied using diverse methods to track the conformational changes of various species of Aβ peptides. The structure of monomeric Aβ 1-28 shorter fragments was proposed with the NMR method[35]. NMR studies of this fragment were facilitated by using shorter C-terminal sequence exhibiting lower aggregation tendency. The structural studies of the longer variants like Aβ 1-40 (PDB: 6SZF)[36] shed more light on the conformation of misfolded monomer where the native monomer is primary without secondary structure. According to monomeric Aβ peptide structure, the C-terminus (15-36) may form the β-hairpin secondary structure motif with a turn at 25-27, where the N-terminal part including residues 1-14 is most likely unstructured[32]. The discovered properties of exemplary Aβ species are shown in Figure 6. Various external factors such as an increase of temperature, pH, oxygen radicals, solvation, or ions presence can induce a conformational shift towards the β-sheet secondary structure and initiate self-assembly reaction.

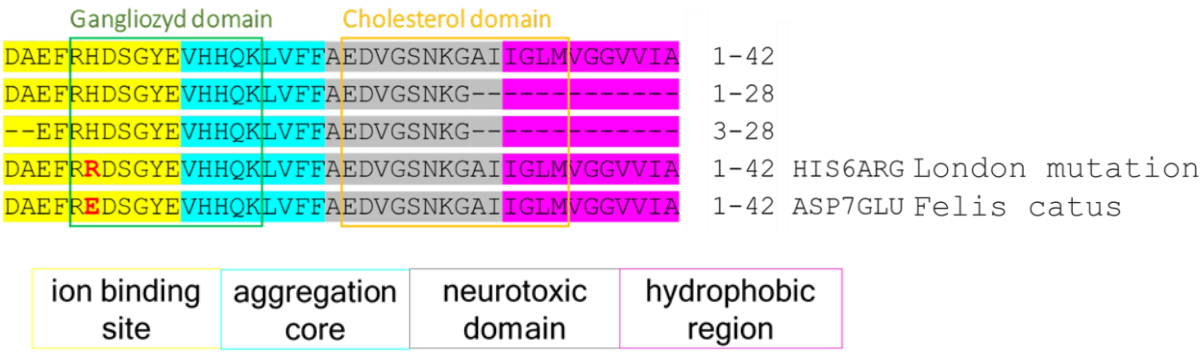

Figure 6. Multiple sequence alignment of different Aβ peptide with marked functional domains[37].

After the conformation shift, the misfolded Aβ peptide forms a β strand-turn-β strand (β-turn-β) structure, where the two β-sheets spanning residues 10-22 and 30-42 are separated by a turn (Figure 7). The N-terminal fragment of the peptide was found to be unstructured similarly in the monomer case[38]. Consequently, the small oligomers can assemble into higher molecular mass complexes, creating protofibrils, fibrils, and finally senile plaques[13] at the cellular level. However, many studies reporting that the most toxic species appear to be soluble low-mass oligomers[39], which can be freely distributed within the body fluids. The structural transitions with graphical visualization of already published Aβ peptides assemblies are shown in Figure 7.

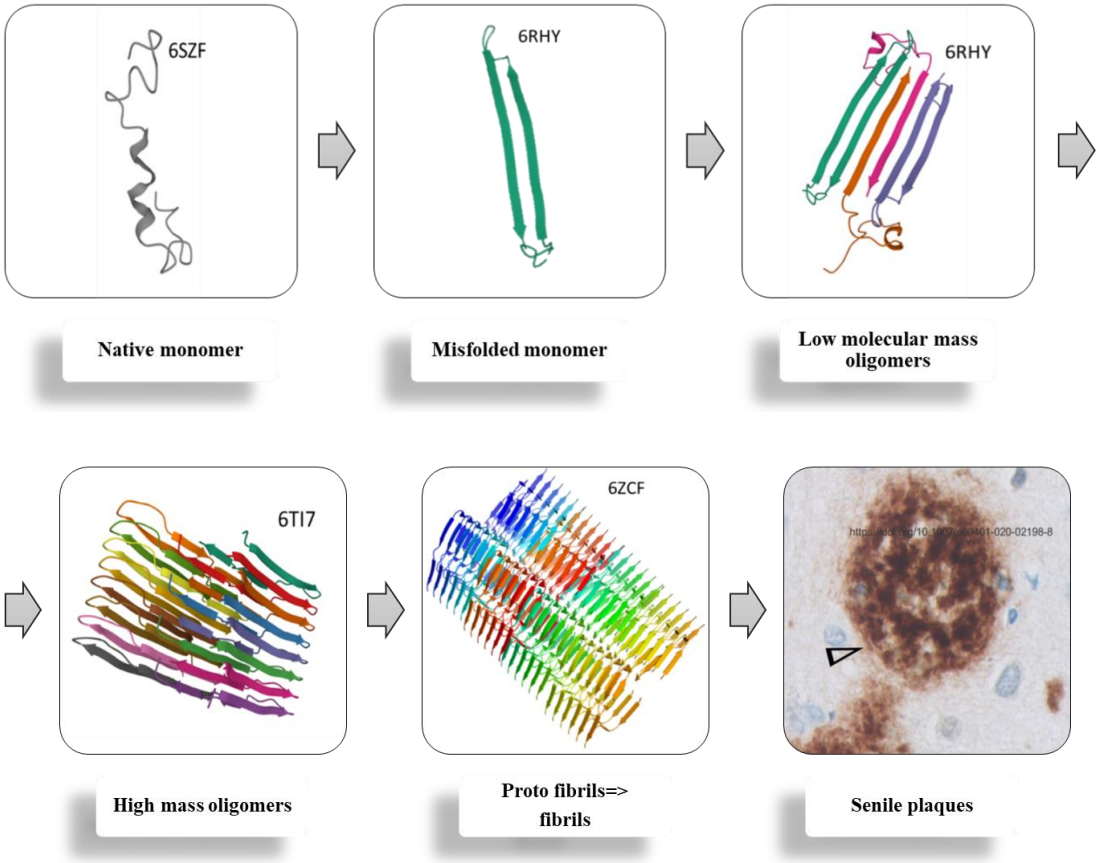

Figure 7. Schematic representation of structural transitions and assembly of Aβ peptides into various structural forms. The PDB database codes of used structures are presented in each subfigure.

2.2.1. The role of transmembrane APP in formation of Aβ peptides

The APP is a 120 kDa transmembrane protein that is expressed mainly in the synapses of neurons and its isoforms are reported in other tissues such as the hepatocytes in the liver[20]. One of the main functions of this protein is to serve as a surface receptor for nerve cells and regulate several metabolic processes like synaptic formation and neuronal plasticity. The APP is also involved in the immune antimicrobial response[40] and transport of iron ions[41]. Another key role of APP is in synaptic formation and reparation. There is a correlation between decreasing level of APP in alternated dendritic length and complexity, and spine density [42]. This data are supported by the high expression of APP during neuronal cells differentiation as well after neural injury[43]. APP sequence and structure is evolutionarily highly conserved among the

mammalian species[44]. The APP protein is expressed in a few isoforms and its gene is located on chromosome 21 in humans. N-terminal fragment of the APP protein, which is the most conserved part of the protein, forms the receptor part on the outer side of the cell membrane, while the C-terminal fragment is located on the cytoplasmic side of the cell membrane[45].

For APP, several distinct, largely independently folding structural domains have been identified (Figure 8):

- E1-domain:
  - N-terminal growth factor-like domain (GFLD)
  - copper binding domain (CuBD)
- Acidic linker between E1 and E2 (AcD)
- E2 domain or CAPPD
- juxtamembrane region (JMR)
- transmembrane domain (TM)
- intracellular domain (AICD)

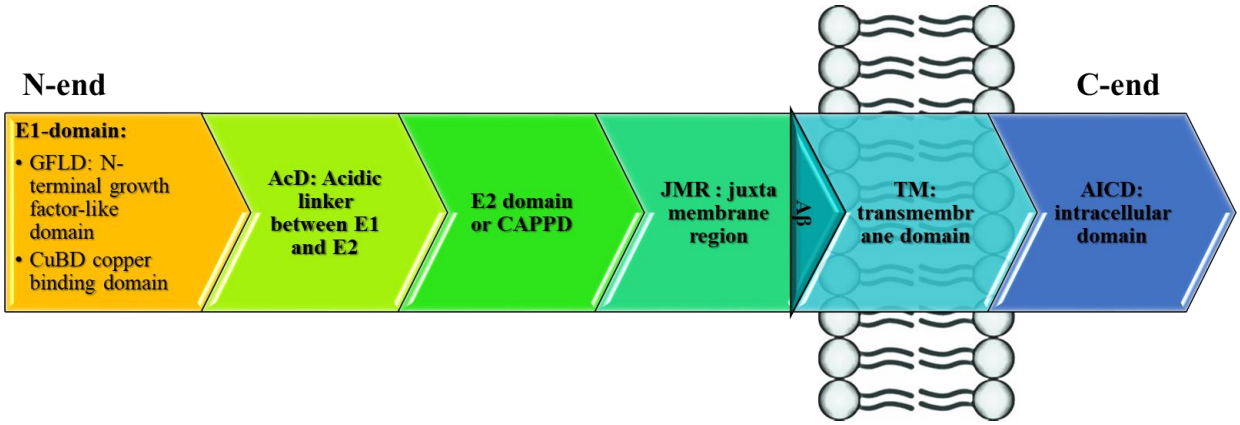

Figure 8. Schematic representation of APP structural domains, positioned with respect to a neuronal cell membrane.

It has been shown that the amyloidogenic degradation pathway of APP may be related to interactions within the lipid rafts present the cell membrane[46]. These interactions initiate conformational changes in APP, exposing it to enzyme β-secretase[47]. In the degradation pathway of APP, the enzymatic cleavage is primarily performed by a non-amyloidogenic α-secretase and γ- secretase. The activity of the β-secretase is modulated by the presence of lipid

rafts in lipids bilayer[47]. Due to the accumulation of Aβ in the extracellular space of the CNS in AD, it was hypothesized that the APP level would elevate level as well. Nonetheless, neuronal cells found in close proximity to amyloid deposits show a lower expression of APP[48]. This data indicates that the APP is simultaneously degraded via the amyloidogenic pathway. It was hypothesized that a loss of neuronal APP may be connected to dementia.

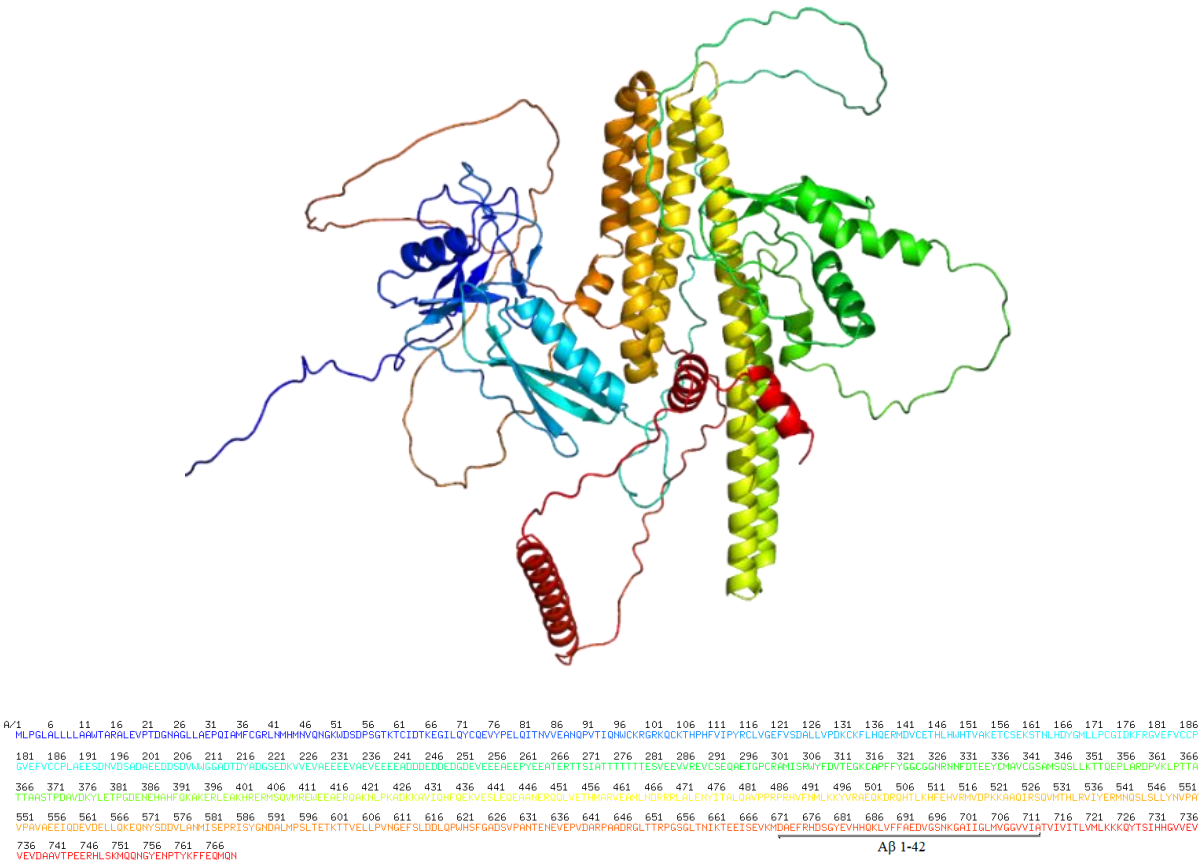

Figure 9. APP model predicted by Alpafold2 (deposited in Uniprot: P05067). The model results from the homology modeling approach, based on structural data for 3KTM - E1 domain, 1ZJD - Kunitz protease inhibitor (KPI domain), 3UMK - E2 domain, 2LLM transmembrane domain (TMD), 3DXC - intracellular domain. The hypothetical structure of APP was previously proposed by Dawkins and Small[45].

The complete structure of APP protein molecule has not been solved yet even though structures of a few domains were solved by X-ray crystallography and NMR. The newest approach to 3D structure protein prediction is based on machine learning strategies like AlphaFold[49]. The APP structure was proposed and deposited in the UniProt database[50]. This structure is presented in Figure 9.

The APP in iron export

APP may show ferroxidase activity in the E2 domain but this activity was not well confirmed[41]. The proposed model of APP iron transport suggests that APP contains an iron response binding protein stem-loop motive stabilizing the iron export of ferroportin (a transmembrane protein that transports iron ions) and APP may impact expression level of ferroportin in cell membranes. Moreover, the studies of APP and ions interactions exposed that the zinc[41] ions, which accumulate in the brain of AD patients, may compete with iron ions and inhibit APP-iron interactions. As the result thus disrupting the iron ions export. Nevertheless, more studies are required to confirm the above-mentioned supposition.

Hormonal regulation

APP and all its associated enzymes such as secretases are already expressed upon differentiation of embryonic stem cells into neural precursor cells (NPCs). At the beginning of the development of the human embryo[51] the hCG hormone modulates the increased expression of APP. It has been reported that the progesterone promotes the non-amyloidogenic APP decomposition pathway, which is indirectly involved in the differentiation of NPCs, and hence affects the proliferation and differentiation of post-mitotic neurons[51]. The studies focused on the consequences of Aβ peptide elevation due to aging and exposed the correlation between occurrence the Aβ and the decrease or loss of sex hormones like progesterone (menopause or andropause)[10]. In addition, those hormonal changes exhibit an impact on the cell cycle of post-mitotic neurons.

2.2.2. Aβ aggregates as results of APP degradation pathway

Several degradation pathways of APP by enzymatic cleavage have been identified[45]. During degradation, the APP can be cleaved by secretases in non-amyloidogenic, amyloidogenic, or η-secretase pathway. In the classic pathway of APP decomposition, fragments of the polypeptide are formed (sAPPα, P3 and AICD), which are utilized in the cell with no negative effect on the functioning of the nervous system. Two enzymes, α-secretase and γ-secretase, are involved in the cutting process of APP in this pathway.

In the non-amyloidogenic pathway, the α-secretase (Figure 10) cleaves the APP, and sAPPα polypeptide is released into extracellular space, while the CTF-α fragment is still bound to the membrane. In the next step, this fragment is cleaved by γ-secretase, and then the P3 peptide and the AICD part (inside the cells) are formed and degrade further. In the so-called amyloidogenic pathway, the APP is cleaved first by β-secretase and form the sAPPβ polypeptide and CTF-β fragments (anchored in the membrane) and, as in the non-amyloidogenic pathway, CTF-β is further processed by γ-secretase. As a final product of the degradation of APP, the Aβ (aggregating) and AICD polypeptide fragments are formed. The AICD fragment can be translocated to the nucleus and regulate gene expression.

The last known degradation pathway of APP decomposition, includes the action of η-secretase. In this process, the APP is cleaved first by η-secretase, leading to the formation of sAPP-η and CTF-η. These fragments are enzymatically cleaved by β-secretase or α-secretase, then the Aη-β or Aη-α and AICD polypeptide fragments are formed[20,43]. It was reported that during APP degradation many forms of Aβ peptide are found (Figure 10). Moreover, external factors such as glycosylation of APP protein, and the presence of ions or reactive oxygen species (ROS) can impact on final products of APP degradation (Figure 10C)[52].

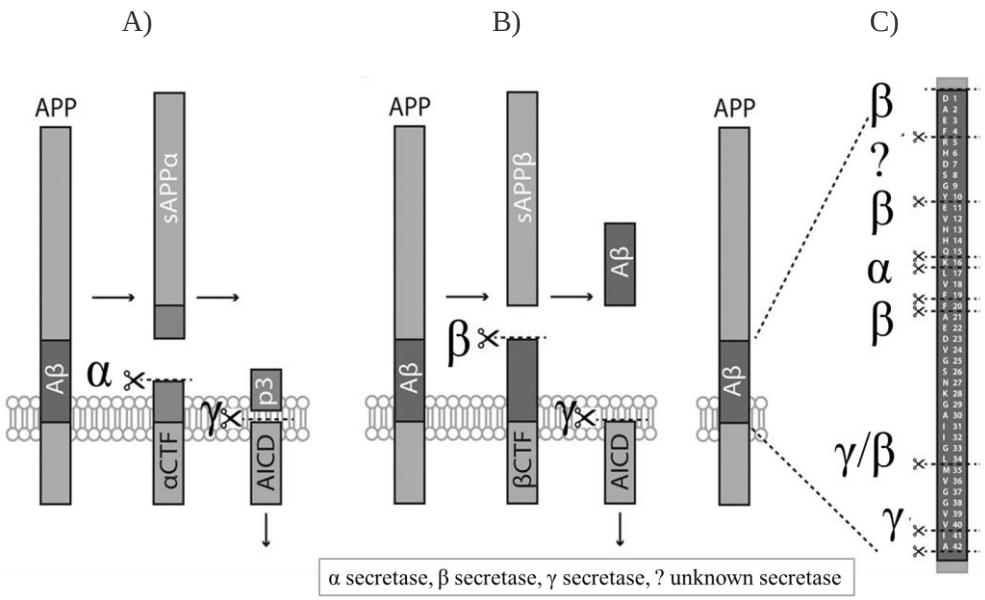

Figure 10. Processing of APP. APP can undergo non-amyloidogenic, amyloidogenic or η-secretase processing. ***A)*** *α-Secretase cleavage of APP* ***B)*** *β-Secretase cleavage of APP* ***(C)*** *alternative cleavage sites for α- and β-secretase. Unknown enzyme market as "?" cleaves at 5th residue of Aβ (Adapted from: Bergstorom et al., 2016* [34]*)*

2.2.3. Neurotoxicity – Aβ species, and mechanism

Aβ peptides are found in large amounts and forms in the brain of AD patients[21]. For this reason, it has been suggested that Aβ peptide could play a role in the pathophysiological mechanisms associated with this type of dementia. It is well-described that Aβ form senile plaques in the brain of AD patients. The presence of neuropathological changes such as senile plaques[13] and neurofibrillary tangles[14] is considered as a pathological landmark of the AD neuronal tissue. Consequently, progressing dementia is causing a loss of nerve tissue in the cortex and an atrophy of the hippocampus. The presence of Aβ peptides also affects many other metabolic processes. The presence of Aβ fibrils in the CSF may induce hyper phosphorylation of the τ protein[53] leading to its structural changes and misfolding conformation. Furthermore, there is a hypothesis that neuronal dystrophy can be induced by the presence of the Aβ peptide fibrils[54]. Neuronal dystrophy is connected with synaptic loss in the neuronal cells in the AD patients brain (which was only confirmed by studies on cell cultures)[12]. The loss of synapses is another unique hallmark of AD. In vivo studies in transgenic organism models show neurite dystrophy and distortion within proximity of Aβ localization[55].

The Aβ peptides undergo a large conformational transformation and assemble to form large molecular mass deposits while during the initial stage, Aβ peptides are in soluble forms: trimer, pentamer, or higher molecular weight oligomers composed of 15-20 monomers, etc. (Figure 11)[32]. Studies of CSF collected from AD patients and medium of human brain cell cultures revealed a presence of low soluble oligomers. That suggested that these soluble Aβ oligomers produced in the cortex, may propagate in the CSF and exhibit neurotoxic properties[39].

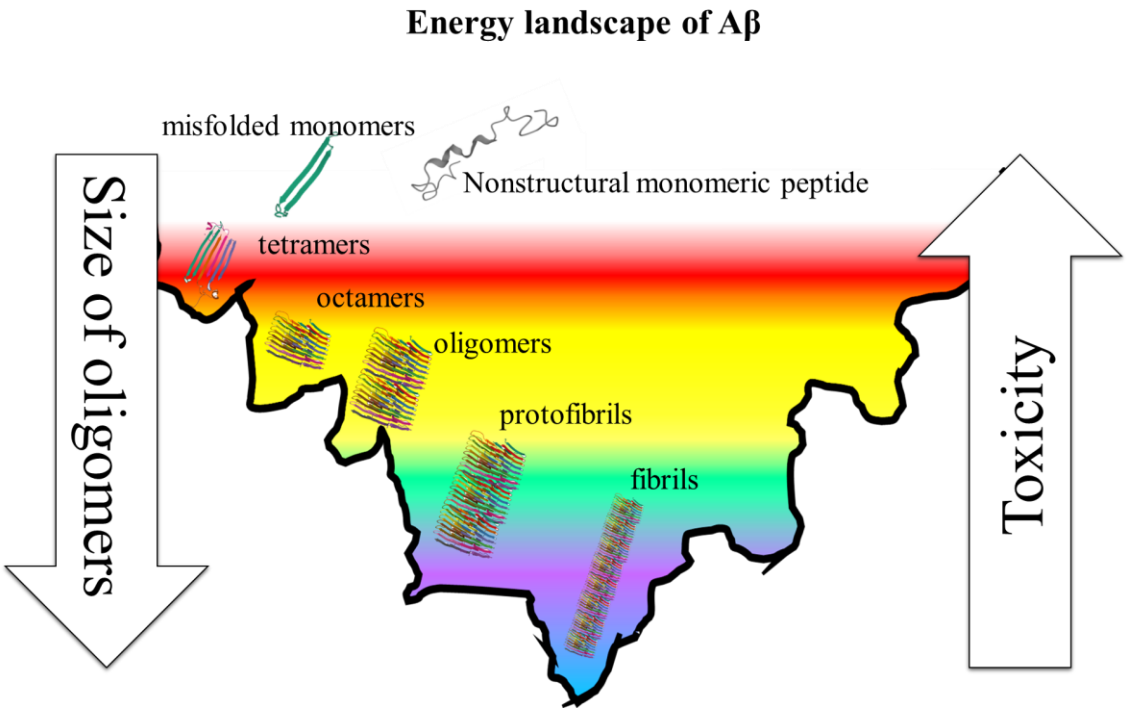

Figure 11. The relationship between the size of Aβ assemblies and their toxic effects visualized on the energy landscape of conformational changes.

The study of rodents exposed to the presence of soluble Aβ oligomers in CNS reported cognitive dysfunction[39] and the presence and levels of soluble Aβ oligomers in the brain strongly correlating (more than presence of fibrillary Aβ forms) with the severity of cognitive impairment and neuronal dysfunction. The similar pathological pattern is found in other neurodegenerative diseases associated with protein aggregates (Table 1) like spongiform encephalopathies (prion protein), Parkinson's disease (α-synuclein) and Huntington's disease (polyglutamine). Various Aβ conformations, including soluble and insoluble fibrils forms of Aβ peptides, may contribute to the pathology of AD through various mechanisms such as cross-interaction with other biomolecules and causing inflammation state. The presence of Aβ oligomers may disrupt the structure of cell membrane[56] which leads to forming channels for ions. This disturbance of cell homeostasis activates inflammation processes and leads to apoptosis[33].

2.2.4. Cross-interactions between Aβ peptides and other biomolecules

A possible toxic effect on synapses induced by Aβ oligomers can be caused by cross-interaction with several postsynaptic receptors and triggering different signaling pathways. So far, a few synaptic receptors triggered by Aβ oligomers have been reported: neuroligin-1, cellular prion protein, p75 receptor of neurotrophin, α7-nicotinic acetylcholine receptor, N-methyl-D-aspartate receptor, metabotropic glutamate receptors[57].

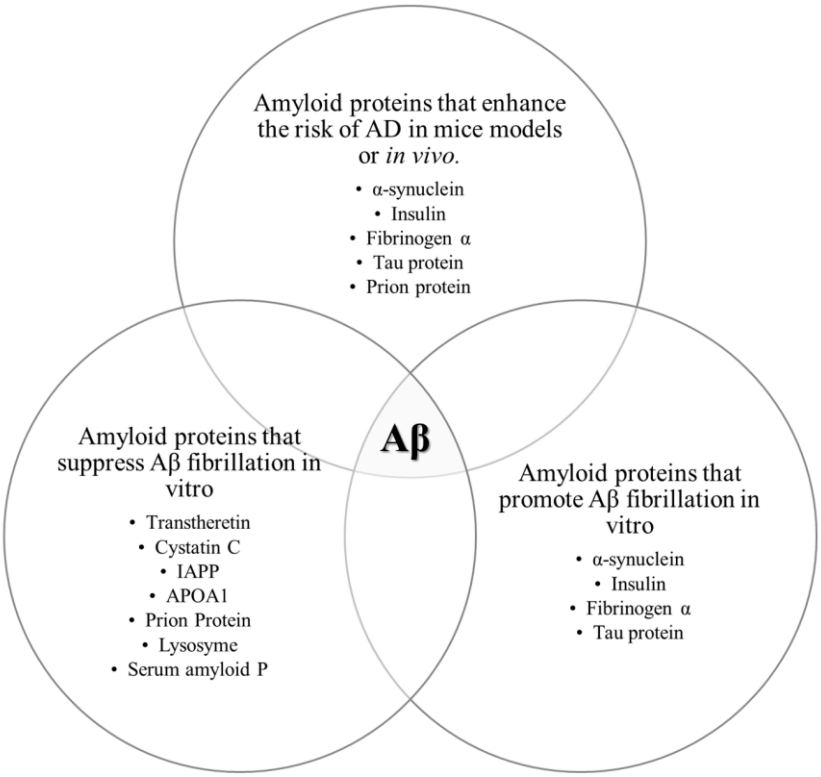

Figure 12. Known cross-interactions between Aβ peptides and its oligomers with other amyloidogenic proteins.

In addition, the aliphatic properties of Aβ peptides awzllow those peptides to interact with many plasma proteins such as human serum albumin (HSA), human Cystatin C (HCC), a2-macroglobulin (a2M), a1-antichymotrypsin, transthyretin, apoferritin, apolipoproteins and lipoproteins. The confirmed cross-interactions of Aβ with other macromolecules and proteins are depicted in Figure 12[57].

The presence of the previously mentioned biomolecules (and their isomers) can increase the risk of AD dementia or trigger the Aβ aggregation process (misfolded τ protein). On the other hand, proteins like HCC or HSA can delay or inhibit this process. HSA and HCC proteins are suspected of protective actions in the neuronal cells on the way of aggregation inhibition due to binding to Aβ[58].

2.2.4.1. Human Cystatin C

HCC is a small globular protein (120 amino acid, molecular weight 13.3 kDa), present in all human body fluids and it is also located and expressed in the brain. HCC occurs in high concentration in the CSF in comparison to other proteins. The concentration of HCC in CSF is a few times higher than in plasma (around 6 mg/mL)[59]. HCC protein participates in diverse processes in the human body, but its dominant role is to act as an inhibitor of cysteine proteases (mostly from cathepsin family). However, HCC can be rapidly degraded by serine proteinases[59]. Studies focusing on the other functions of HCC showed that it may take a part in neural stem-cell growth and it is involved in many pathological processes, including oxidative stress, neurodegeneration, and inflammation[59]. Moreover, HCC level and its dimeric form may have a meaningful impact on different diseases. Starting from kidney disease[60] through cancer to neurodegenerative disorders[61], especially dementia. HCC is also an "amyloid-like"[62] protein which means that in certain conditions it may undergo the conformational transition[63] (called domain swapping) and self-oligomerization into a bigger assembly[64]. In domain-swapped dimeric structure, the two monomers exchange N-terminal fragments of β-strand-turn-β-strand. These conformational changes are conditioned by the flexibility of valine 57, which is placed in the bend between two antiparallel β-strands. The stable monomer was obtained by exchanging valine 57 for glycine[65] (Figure 13, PDB: 6RPV). In the N-terminal fragment, the four cysteine residues form two disulfide bridges, C73-C83 and C97-C117, which stabilize the C-terminal domain. Disruption of these bonds by radiolysis can cause misfolding and, consequently, conformation transition into dimeric form. Thanks to the flexible conformation, HCC molecule undergo oligomerization and can be found in a few molecular states like dimer, oligomer, or even fibril[66]. Monomer and dimer structures solved experimentally (monomer - NMR, dimer - X-ray diffraction) are shown in Figure 13.

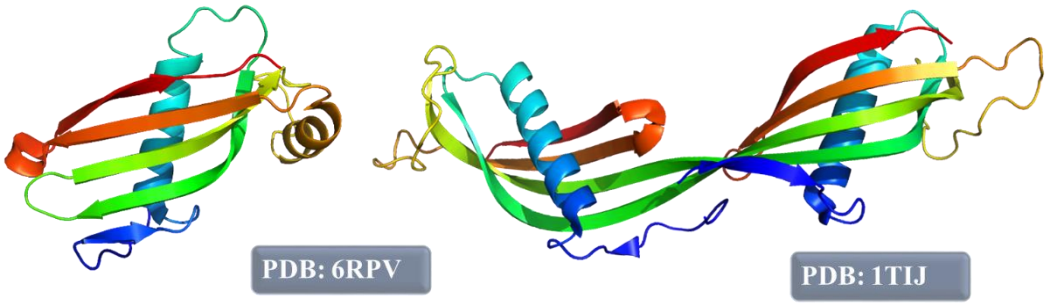

Figure 13. Structures of HCC solved by X-ray crystallography. On the left: monomer, on the right: dimer (with exchanged secondary structure domains – domain swapping).

HCC is a monomeric molecule in its native functional state. However, the increasing amounts of dimeric HCC or other forms may be the hallmark of a pathological state[61]. The presence of the dimeric form of HCC is strictly connected with kidney failure[67]. The mutation of HCC (L68Q) may lead directly to the amyloidogenic disease which is called hereditary Cystatin C amyloid angiopathy (HCCAA)[68]. Scientists reported an increased HCC level for patients with CNS disorders such as encephalitis, meningitis, acute Guillain-Barre syndrome, chronic inflammatory demyelinating polyneuropathy[61].

HCC and Alzheimer's disease and co-deposition with Amyloid β

It was already reported that HCC plays an important protective role in CNS and may be involved in preventing neurodegeneration at the intramolecular interaction level. The is a dependency on the polymorphism of the gene coding HCC and the fact that miscoding increases the risk of developing AD[69]. HCC is co-localized with Aβ senile plaques in the brain of AD patients[60]. Furthermore, its presence in senile plaques was also observed in non-demented elderly individuals. HCC is one of the factors of mTOR autophagy pathways[70] and can enhance autophagy activation in neurons with disrupted homeostasis like oxidative stress etc.. The data from immunochemistry experiments indicated that Aβ 1-42 is accumulated in a specific population of pyramidal neurons[61], which are also exhibiting high HCC expression. This data suggests a direct connection and possible interaction between these two macromolecules. Many *in vivo* and *in vitro* studies reported that HCC may inhibit Aβ aggregation and fibril formation[71]. Nevertheless, the molecular mechanism of these interactions is not known. Studies showed that in genetically modified mice, the induced overexpression of HCC can prevent the degradation

of neurons by a decline in the activity of cathepsin (B, D)[72]. In addition, the samples extracted from the transgenic mice overexpressing HCC showed the association of HCC and Aβ oligomers and reduction of the amyloid plaques formation[73]. HCC may be involved in the protection of neuronal cells from neurodegeneration and apoptosis induced by Aβ oligomers. All the above scientific studies support the thesis that HCC has a meaningful protective role in CSF and may be involved in biological processes against AD development.

2.2.4.2. Human Serum Albumin

Human serum albumin belongs to the albumin family, which consists proteins found in fluids (e.g., blood plasma and milk) and other tissues, and in plant seeds. They are characterized by globular fold and high solubility in water (hydrophilic), experience heat denaturation, and are easy to crystallize. In their sequence, HSA contains a lot of aspartic and glutamic acid (up to 25%), leucine, and isoleucine (about 16%).

HSA[74] protein is built by 585 amino acids and has a molecular weight of 66.5 kDa. As all albumins HSA is a very resistant protein that is soluble in aqueous solvents at an extremely high concentration (50 mg/mL). The gene encoding HSA is located on chromosome 4, and HSA is expressed in the liver[75]. HSA is a protein that constitutes most of the blood plasma but also it is found in the raw material of tears[76] and is responsible for maintaining the homeostasis and the colloidal osmotic pressure in body fluids[77]. HSA is known to be a molecule that transports many substances in the blood (hormones, biomolecules, ions etc.), and, is considered as a good drug carrier[78].

HSA sequence contains a lot of negatively charged amino acids and many cysteines, which form 17 disulfide bridges and hold the tertiary structure of the protein[79]. The secondary structure consists mainly of helical motifs that form 3 domains, each of them is divided into two subdomains (A, B). Each domain contains 10 helices. HSA appears in body fluids in mostly monomeric form, but it can combine into dimers and trimers[80]. Currently, the PDB database contains over 100 HSA experimentally solved structures also in presence of various biomolecules such as ibuprofen, bilirubin, or fatty acids (details in appendix, Figure 14). The complexes of HSA with chemical compounds are characterized by high stability for a wide range of environmental conditions. In addition, HSA may extend the half-life of drugs due to

its antioxidant properties[78]. As mentioned before, a wide variety of substances binds to HSA such as hormones and drugs having a hydrophobic region. HSA possesses two active sites which are able to bind small molecules like drugs[81] and four iodothyronine and fatty acids binding sites. In addition, HSA is a zinc transporter in blood[82], and it is able to bind about 80 % of all zinc ions in the plasma. In nanomedicine, HSA is very often used as the carrier in the immobilization of nanoparticles and drug transport[83]. In some applications, the drugs are covalently linked to polypeptides, which are attached to HSA on the C and N-terminus[84]. The graphical representation of the X-ray crystal structure of HSA was shown in Figure 14.

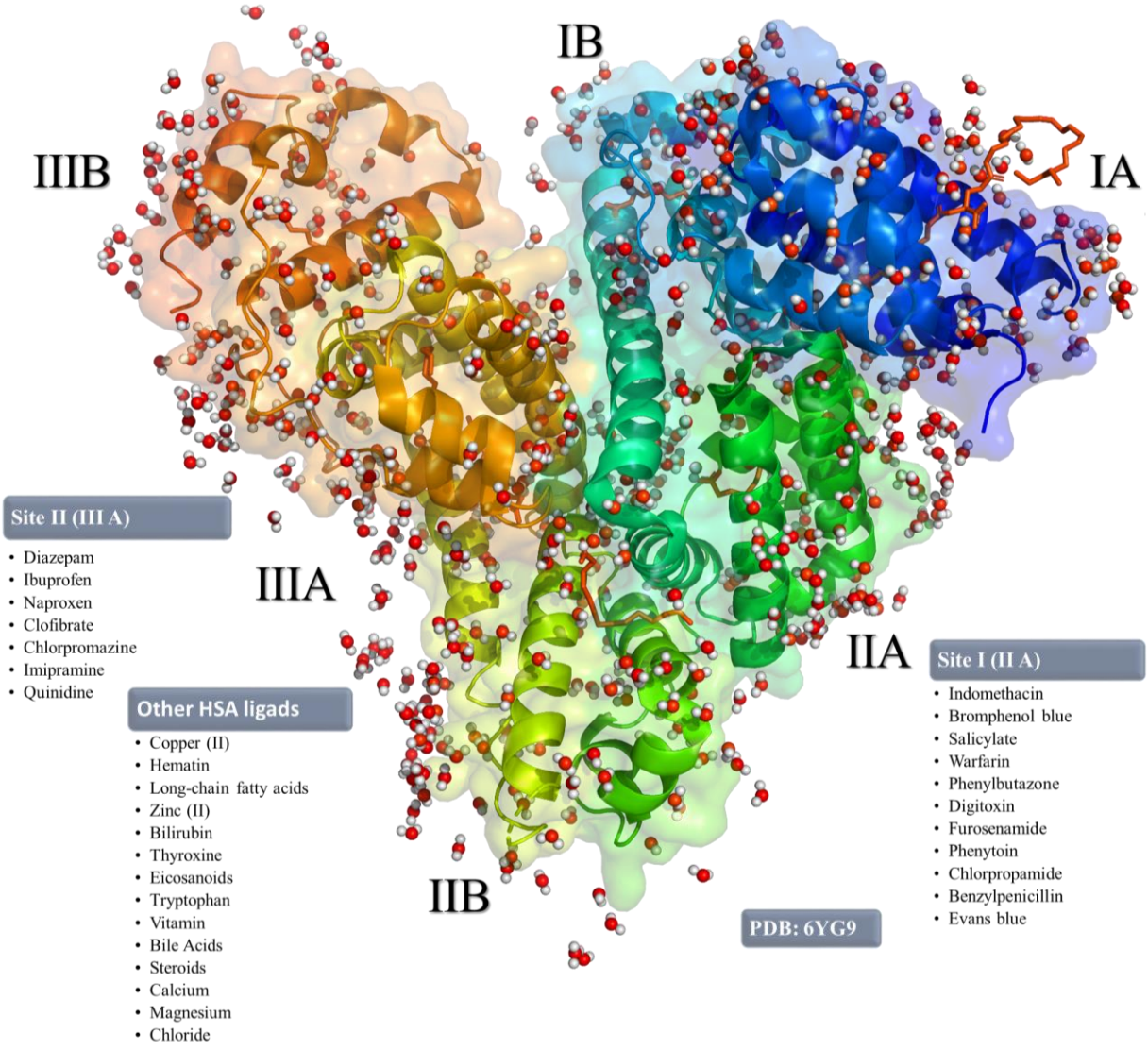

Figure 14. The graphical visualization of the crystal structure of HSA (PDB: 6YG9[85]) with marked structural domains and reference to known ligands. Figure created with Pymol.

Summarizing, HSA is present in all body fluids (including CSF), has many diverse roles and takes a part in many biological processes. HSA can transport a wide range of substances and small molecules and exhibit high stability, which is particularly important and interesting for designing pharmaceutical therapies. Current medicine already proposed many potential applications of HSA as a therapeutic target. However, the uniqueness of HSA properties still opens new possibilities.

HSA and Aβ peptides interactions

It was reported that HSA has a remarkably high concentration in blood (640 μM) and the studies of dementia patients' plasma showed that HSA protein binds 90% of Aβ in the blood[86]. This fact suggests that high concentration of HSA prevents the formation of amyloid deposits in the peripheral tissue. However, it is known that such a large macromolecule as HSA cannot freely cross the blood-brain barrier (BBB). The concentration of HSA in CSF is drastically decreased ranging from 1 to 5 μM[86]. This may explain why Aβ plaques are only observed in the extracellular space of the CNS tissue. Nonetheless, HSA is still one the most abundant protein in CSF and it is suggested that, like HCC protein, it may have a protective function against the neurotoxic Aβ aggregates[87]. Some data suggest that HSA delays the aggregation of Aβ in CSF, potentially by direct binding to Aβ monomers or oligomers. The experimental data suggest that HSA binds with Aβ peptide in 1:1 molar ratio[87]. Although, there is still some debate as to whether HSA binds to monomers or oligomers of Aβ peptide. Many studies reported that HSA can bind with monomers as well as Aβ oligomers, but there is no direct evidence of a specific binding site. According to the experiments of Milojevic et al.[88], the binding of HSA was observed with oligomers but not with Aβ monomers. Moreover, the work of Litus et al.[89] suggested that introducing other ligands like cholesterol, palmitic acid and warfarin can shift the HSA-Aβ equilibrium towards their complex formation via a directed increase of HSA affinity to Aβ. The Flemish mutation in HSA sequence (A21G) as well increases its binding affinity with Aβ[90].

2.2.4.3. Interactions of Aβ peptides with small molecules

Many studies suggest a connection between oxidative stress and changes in neural transition metal ion homeostasis as a cause of AD[91]. Copper, zinc, and iron ions are involved in the oxidation leading to apoptosis and neuronal damage. Free transition metal ions promote the production of ROS[7] and their toxicity contributes to proteins and DNA damage, inflammation, tissue damage, and subsequent induced cellular apoptosis. *In vivo* studies of senile plaques reported the presence of copper ions[91], while other studies reported that zinc, copper, and iron ions interact with monomers and oligomeric Aβ[92]. In the work on the interaction of copper ions during the aggregation process, authors showed that in presence of copper, Aβ only undergoes oligomerization but not fibrillation[93]. Those ions may induce shifts in the free energy landscapes of Aβ leading to faster conformation changes. The coordination bond of copper occurs in the region of Aβ peptide 1-16 residues, where the copper binds via the side chains of histidine[94].

Cholesterol[95] and estradiol[10] (sex hormone, derivative of cholesterol) can also have significant contribution to the development of AD. It is well known that apolipoprotein E (apoE)[24] transporting and metabolizing cholesterol, is involved in the building of amyloid deposits. An experimental study also proved the interaction between Aβ peptides with melatonin and cholesterol in the anionic lipid membrane[96]. Moreover, genetic studies have shown that the frequency of the apoE-4[25] allele is significantly increased in AD patients compared with healthy individuals.

2.2.4.1. HSA and HCC: Molecular guardians of CNS

HSA, like HCC, has been reported to have the same protective properties against aggregation of Aβ peptides. However, there are no published studies describing these interactions in detail, although both HSA and HCC coexist in blood plasma and CSF. Nevertheless, it should be taken into consideration that other amyloidogenic proteins e.g., serum amyloid A (a small globular protein) have been reported to interact with serum albumin and this protein shares structural similarities with HCC. The NMR studies presented by P. Jurczak[97], describe the molecular interaction of HCC with HSA homolog, bovine serum albumin.

2.3. Structural studies of Aβ peptides

The various forms of Aβ peptides have been studied using a different biophysical method (see Figure 15).

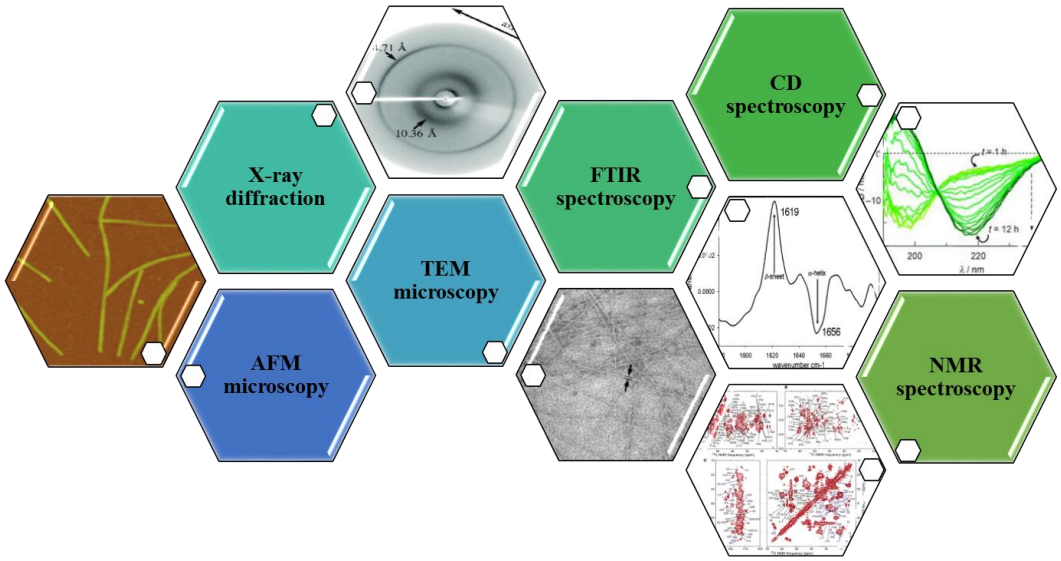

Figure 15.Combination of different biophysical methods used to study Aβ peptides.

These biophysical methods for the study of biomolecules allow the determination of the relative population of secondary structures, information on the complete tertiary and quaternary structure, or the conformational changes at the atomic level. The techniques listed in Figure 15 reveal the general structural characteristics of the molecules. Obtaining structures with the atomic resolution of Aβ fibrils, and in particular of Aβ oligomers, is an extremely challenging task. The main difficulties include complicated sample preparation and rapid self-induced assemble reactions resulting in a major challenge to perform experiments. Conventional high-resolution structural methods, such as X-ray crystallography or NMR in solution, provide only a limited understanding of the structures, and the interaction of Aβ molecules. Characterization of the oligomers in the solution is hindered by the wide variety of oligomer structures and their transitional nature, which is the result of various structured forms with a wide range of atomic masses from 4 kDa to > 40 kDa[98]. On the other hand, the Aβ aggregated in the form of fibrils show a high ordering structure at the molecular level, but some polymorphism exists also in the fibril formation[36].

2.4. Structural polymorphism of Aβ

Fibrils of Aβ peptide are arranged with the intermolecular β-sheet conformation which is unique among protein folds[54]. This characteristic β-sheet steric zipper motif is a fingerprint of all "amyloid-like" proteins. The central part of the fibrils is created by an intermolecular β-sheet structure with hydrogen bonds that connect β-strands elements into a β-sheet structure with parallel alignment to the fibril axis[36]. The side chains of amino acids are arranged perpendicularly to the fibril axis and in addition, a rotational alignment yields a helical or screw symmetry (Figure 16). The studies on fibril formation in different external conditions revealed that the environment has a significant impact on promoting certain fibril morphologies forming through the polypeptide chain. By manipulating factors like solvation, pH, temperature, and addition of other compounds, it is possible to induce specific morphology formation[99]. Some experimental data suggest that within the same variant of Aβ peptide many other types of fibril morphology may coexist[100]. For example, the addition of metal ions support formation of stable small oligomeric forms instead of the fibrils[96].

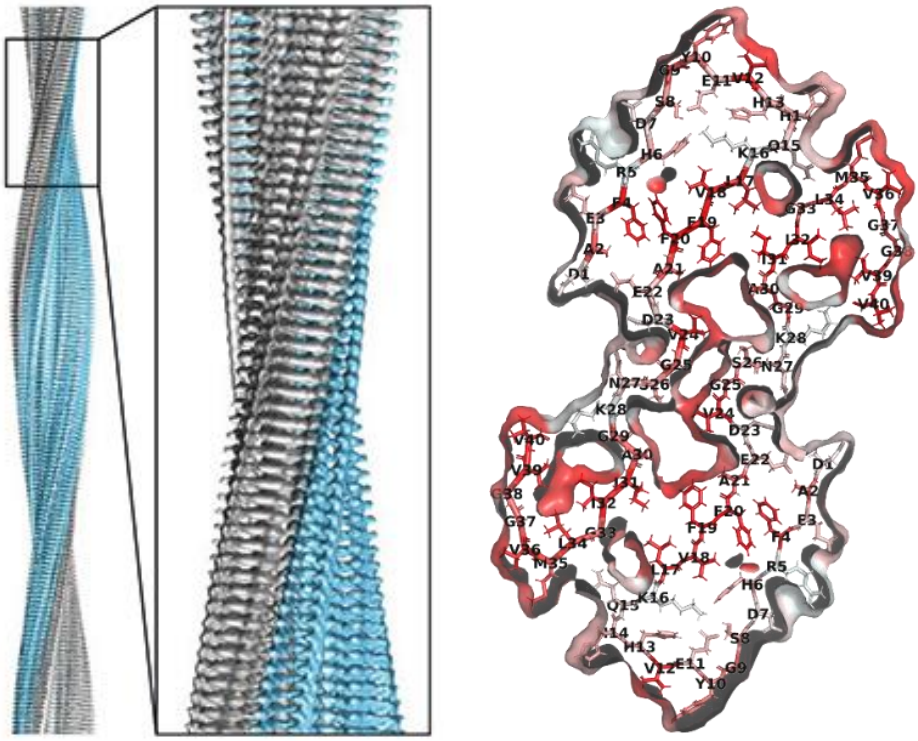

Figure 16. The model of the fibril and cryo-EM fibril model[36]. One the right: the cross-section view of fibril generated with Pymol and colored by hydrophobicity[101].

Data derived from cryo-EM imaging studies on the Aβ peptides extracted from the AD brains indicate the structural polymorphism of fibrils[36]. The dominant morphology is characterized by the narrow width of 74 Å and a crossover distance of 415 Å. The secondary structure forms the β-sheets in parallel with respect to the orientation of the hydrogen-bonded β-strands with a right-handed turn. It has been suggested that in *in vitro* studies the sample also contained fibrils with left-hand twisted β-sheets. In brain derived samples of fibrils, two other conformations have been observed. One with 123 ± 10 Å width and a cross-over distance of 1290 ± 100 Å and the second with a width of 179 ± 10Å and a cross-over distance of 1428 ± 100 Å. Those fibrils exhibit polar properties[36].

3. Selected methods used to study the structure of macromolecules

Advanced research of biological systems very often requires an explanation of the studied phenomenon at the atomic level using the spatial structure and molecular dynamics of biomolecules. The development of technology and new computational methods have expanded significantly in the last decades. The experimental tools used in the classic molecular biophysics are specialized now to study complex biological systems. On the other hand, the application of computational methods is very often combined with providing input data (restraints) derived from experimental data. The combination of experimental and computational methods allows to obtain faster, more reliable results.

Molecular biophysics deals with widely understood biological processes and systems on the border of biochemistry and molecular biology. Biophysics attempts to explain the interactions between different cellular systems, including the interactions between nucleic acids, proteins, and other biomolecules using advanced methods of experimental physics.

These techniques include:

- Imaging: fluorescence microscopy, electron microscopy (TEM, cryo-EM);
- Atomic structure determination: X-ray crystallography, nuclear magnetic resonance spectroscopy (NMR);
- Characterization of sample topology: atomic force microscopy (AFM);
- Dynamic and structure of macromolecules in solution: small angle scattering (SAS) using X-ray and neutrons (SAXS / SANS);
- Characteristics of the secondary structure - circular dichroism (CD), Raman spectroscopy or Fourier infrared spectroscopy (FTIR);
- Biomolecular dynamics (NMR).

To the experimental methods listed above, there are a number of computational methods that describe biological systems through statistical mechanics, thermodynamics, and chemical kinetics (bioinformatics, molecular dynamics (MD) simulations). With the interdisciplinary approach and the use of experimental and computational techniques, it is possible to observe, model of studied macromolecular system, and even manipulate the atomic structure, dynamics and type of interactions.

Chosen methods to study Aβ and interaction with HSA and HCC proteins

In this work only the most significant experimental results are presented to give a reliable view of the studied molecular system of Aβ peptides, HSA and HCC proteins. The most time-consuming and crucial step was developing suitable protocols for sample production and preparation.

Sample preparation was performed in several steps. The protocol of Aβ peptides synthesis and purification using the high-performance liquid chromatography (HPLC) technique was developed. The monomeric peptide was obtained following the protocol[102] where the purified peptides were dissolved in hexafluoroisopropanol (HFIP).

HCC protein was produced by overexpression in *E. coli*. In addition, the protocol for a deuterium labeled HCC (overexpression in a D_2O medium) was developed by optimizing all new conditions of overexpression and purifications.

Several biophysical methods were used to characterize Aβ and their interaction with HCC and HSA proteins: native mass spectrometry (native MS), SAXS or SANS, NMR relaxation, and analytical centrifugation (AUC).

TEM and AFM microscopes were used for the imaging of the sample topology and track the Aβ peptide aggregation.

Experimental methods were supported by structural bioinformatics methods to predict 3D models (MD, molecular docking).

3.1. Small angle scattering

The small angle scattering technique (SAS)[103] investigates the interaction of radiation with heterogeneity in matter. Such an interaction can cause the radiation to scatter in all directions from its direction of incidence (plane and monochromatic electromagnetic wave). A study of this phenomenon can provide information about structures larger than the incident beam wavelength. In the SAS technique, the angle of the scattered radiation is between 0.1-10 ° (Figure 17). SAS technique can provide information about the size, shape, and orientation of nano- or microstructures in a sample. Thanks to this technique, it is possible to study shape of macromolecules at low-resolution (up to 8-10 Å) in a solution. The SAS allows to annotate the internal structure of disordered systems and obtain a direct structural characteristic of the sample with a random distribution of density heterogeneity ranging from nanometers to micrometers. The SAS experiments can use several types of radiation: X-ray (SAXS) or neutrons (SANS). Those two different types of experiments are complementary, however there are some differences in the provided information. (e.g., neutrons are scattered by atomic nuclei whereas X-ray photons are scattered by electrons).

SAS experimental methods permit the study of complex molecular structures, describe their structure and population at different size scales, and describe complex hierarchical structures. Methods such as small-angle neutron scattering (SANS) and small-angle X-ray scattering (SAXS) have wide applications to characterize complex biological systems and biomolecules. The use of SAXS and SANS scattering is diverse, ranging from the study of nanomaterials to the determination of low-resolution structures of single macromolecules and other higher hierarchy complexes. Thanks to this method, it is possible to determine the flexibility as well as dynamic and structural changes over time depending on the different environments of the sample[104].

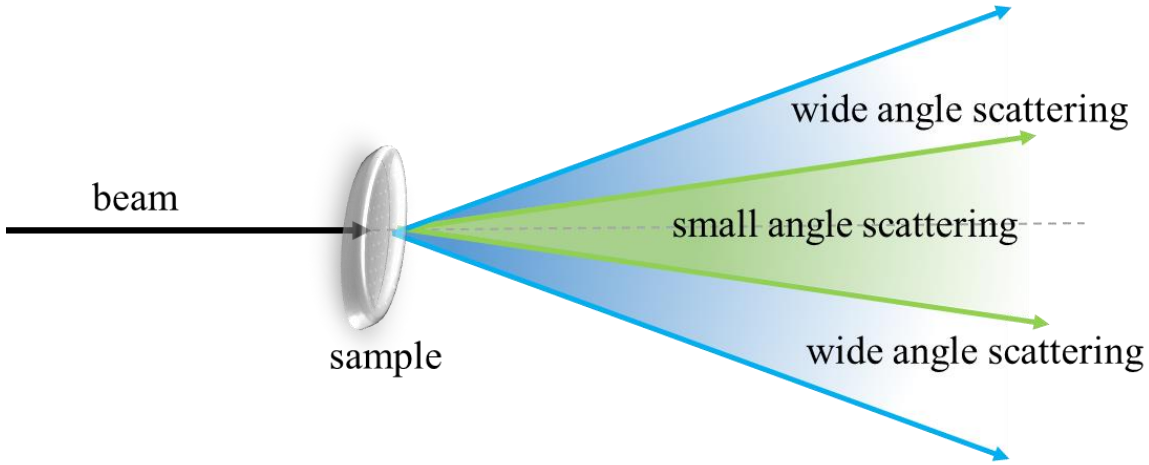

Figure 17. The scattered X-ray or neutrons can be measured at different angles. The SAS is recorded in 0.1-10 º.

The SAS experiment on macromolecular systems uses the definition of the scattering vector q (or sometimes defined as s). SAS scattering pattern is determined as a dependency of a scattered intensity in function of the magnitude of the scattering vector q ($q=4\pi sin\theta/\lambda$) under a certain angle. λ represents the wavelength of the incident beam (X-ray radiation or neutrons) and θ corresponds to the values of the angle between the direction of the incident beam and the observed direction of the scattered radiation.

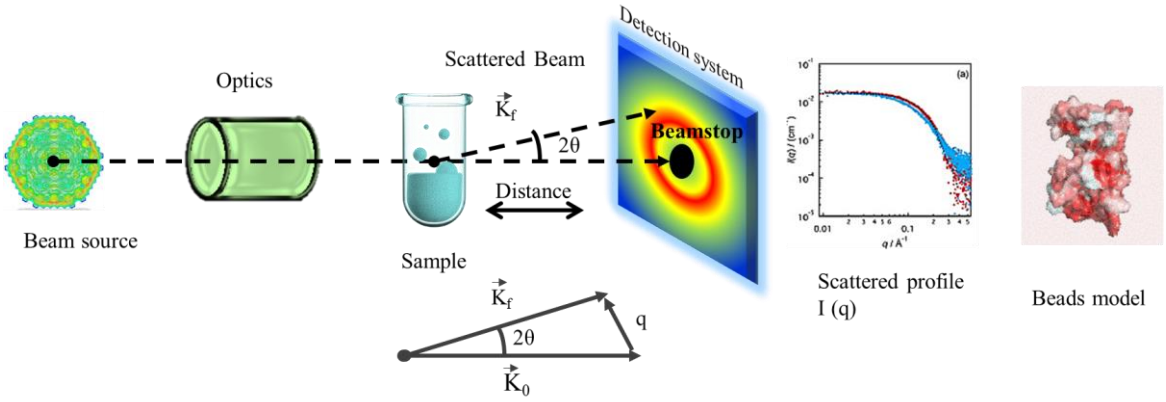

Figure 18. Schematic representation of a small-angle scattering experiment. The scattered beams are collected on a 2D detector.

The direction and properties of the incident beam is described by the vector $\overrightarrow{\boldsymbol{k_0}}$. For the scattered beam vector, the parameter $\overrightarrow{\boldsymbol{k_f}}$ is introduced. The wave vector transfer, also called scattering vector describes the difference between the incident vector wave and the vector of the scattered wave (Equation 2, Figure 18).

$$\vec{\boldsymbol{q}} = \overrightarrow{\boldsymbol{k_f}} - \overrightarrow{\boldsymbol{k_0}} \qquad (2)$$

The scattering intensity and angle of the scattered beam depends upon the size of the particles, similarly as the principle of dynamic light scattering. The bigger particle is the intensity of the scattered beam is higher and it is shifted towards smaller angles.

3.1.1. X-ray and neutron scattering

X-ray scattering on electrons and elastic scattering of neutrons

X-rays are widely used to investigate the structural matter properties of solids, liquids, or gels by methods like X-ray diffraction (XRD) or small angle X-ray scattering (SAXS). X-ray photons affecting the sample interact with electrons and provide information about the fluctuations of electronic densities in the matter. In the case of the data obtained by the SAXS experiment, a SAS pattern can be fitted with the theoretical intensities calculated from different model shapes when the size distribution is known. The ideal experimental condition to measure particles in solution is the monodisperse sample and the optimal data collection strategy is to measure them at different concentrations. If the concentration is too low the intensity of the signal may contain too much noise at wide angles. Conversely, high concentrations induce intramolecular interactions which impact the shape parameters of measured particles at small angles, in so called the Guinier region.

SAXS

The wavelength of radiation that is used in a typical SAXS experiment is in the range 0.1-0.2 nm. In 1939, Guinier published an article describing a simple approximate mathematical relationship between the rate of decrease in SAS signal intensity at the smallest angles and the size of the scattering particle[105]. He described that the SAS phenomenon close to the prime beam carries information about the shape and size of the scattering particle and also information about fluctuations in the internal structure of matter. The collected signal on the scattered incident beam in the registered scattering profile comes from all the components of the sample including buffer and surroundings. Those additional contributions are removed by post processing data with a background subtraction procedure. Then, the data are represented as the SAXS profile of the scattering intensity from the macromolecules as a function of the scattering angle. Based on the principle of the SAS phenomenon, sample scattering profile of intensity in function of angle is strictly connected with the size distribution and structure of the studied macromolecule. The high-flux X-ray beam, necessary for bio-SAXS studies, is provided by synchrotron sources.

SANS

The SAS principle like in the case of SAXS can also be applied also to SANS. However, the source of the beam are neutrons. Neutrons can be produced in a few ways. For example, in the nuclear reactors the neutrons are produced by the fission of uranium 235. Each fission event releases 2-3 neutrons. The innovative approach of spallation neutron source using a high-energy accelerated proton which collides with nucleus (usually liquid mercury) and eject neutron in spallation process.

Neutrons can go through long distances in the material without scattering or absorption, and can penetrate strongly to a depth of 0.1-0.01 m. Neutrons are elastically scattered by interactions with the nuclei or with the magnetic moment of unpaired electrons. Because neutrons interact with the nuclei (protons, neutrons) they can also be scattered by also hydrogen H^+. The advantages of SANS over SAXS are the lack of radiation damage and sensitivity to light elements, which allow for labeling by isotopes (e.g. deuterium), and the strong scattering by magnetic moments. In SANS, the intensity depends more on the composition (structure) of the nucleus than on its mass.

3.1.2. Scattering data analysis - Inverse Fourier transform I (s) and the intramolecular distance distribution function

It is known that X-rays are scattered by electrons. For a monodisperse sample, where the electron density is homogeneous in the solution, the number of electrons per unit volume is the same everywhere[106]. If X-rays are passed through the sample at a certain angle, each electron is a secondary (diffractive) wave source that can be described by a complex number of $aexp(i\varphi)$ that reaches the detector. The detected amplitude of the scattered beam is the same, while the wave phase depends on the position of the electron in the spaces (x, y, z). The recorded amplitude is the sum of all the amplitudes of the coalescing electrons in the sample (Equation 3).

$$A = aexp\,(i\varphi_1) + aexp\,(i\varphi_2) + aexp\,(i\varphi_3) + a \ldots \qquad (3)$$

The scattered intensity is represented by the squared modulus of the Fourier transform of a material's electron density which state that equal volumes of material contain equal numbers of electrons, and where ρ is the electron density of the particle.

$$I(q) = |\iiint_{Particle} exp(iqy)\,\rho\,dx\,dy\,dz\,|^2 \qquad (4)$$

The angular dependence of the scattering intensity $I(q)$ of a single macromolecule over the entire range of q (may be represented also as s) is called the shape factor $P(q)$:

$$I(q) = \rho^2 V^2 P(q) \qquad (5)$$

Where, the particle volume is V and $P(q) = 1$ for small q. The form factors can be calculated by diverse types of macromolecule spheres and ellipsoids like globular proteins or liposomes, cylinders like in case of fibrils etc.

3.1.3. Guinier's equation, the radius of gyration, cross-section, shape factor

Guinier's law[106,107] provides a universal and model-independent estimation of particle sizes obtained from SAS data. Guinier approximation allowing to estimate the overall size of the particles, where the R_G is so-called radius of gyration and R_G^2 is described as the average squared distance between any point of the particle in its center of mass. The *I(0)* is the intensity at zero scattering angle *(q=0)*:

$$I(q) \approx I(0) \exp\left(-\frac{q^2 R_G^2}{3}\right) \qquad (6)$$

Because of the exponential in the Guinier approximation, R_G and *I(0)* can be determined by a linear fit (at low *q*) to a plot ln[*I(q)*] against q^2 (Figure 19). Then, the slope value correlates directly with $-\frac{R_G^2}{3}$. For folded proteins, the Guinier approximation of R_G is reliable up to limit $qR_G \lesssim 1.3$[108].

$$P(q) \cong \exp\left[-\frac{(qR_G)^2}{3}\right] \qquad (7)$$

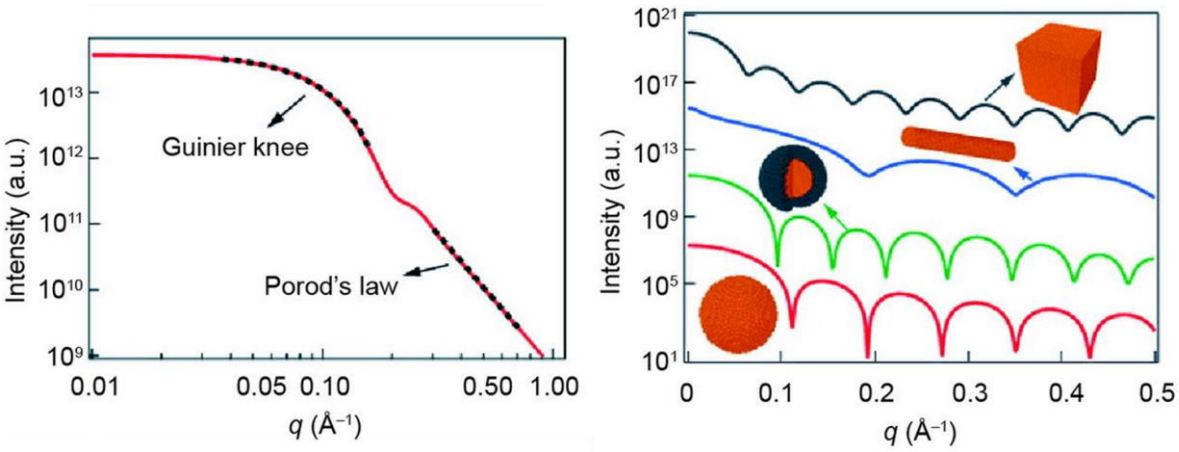

Figure 19. An example of a Guinier fitting in SAXS curve and illustration of different scattering curves characterizing certain form factors. (Adapted from: Zhang et al., 2020[109])

The q-range over which the intensity is off the phase map is made smaller than the particle size. For any given angle of scattering, it is possible to compute the phase map (x, y, z) which is characteristic of the instrument and related with power laws:

$$I(q) \propto q^{-\alpha} \quad (8)$$

Where α is called the scattering exponent. The integer value of α describes the scattering results of a d-dimensional object (1-4D, a four-dimensional space is a mathematical extension of the 3D Euclidean space). If α is not an integer, the scattering is from the fractal structure (Hausdorff dimension D). The slope of α on a double logarithmic plot allows for determining the overall structural properties of the studied sample (Figure 20). For finite q, the multiplying factor depends on the shape and size of the aggregates. The particle size distributions of monodisperse systems consist of particles described by voids with contrast $\Delta\rho$, R_G and surface area S of the particle, can be obtained by Guinier (Equation 8) and Porod law:

$$I(q) \approx 2\pi(\Delta\rho)^2 q^{-4}\mathrm{S} \quad (9)$$

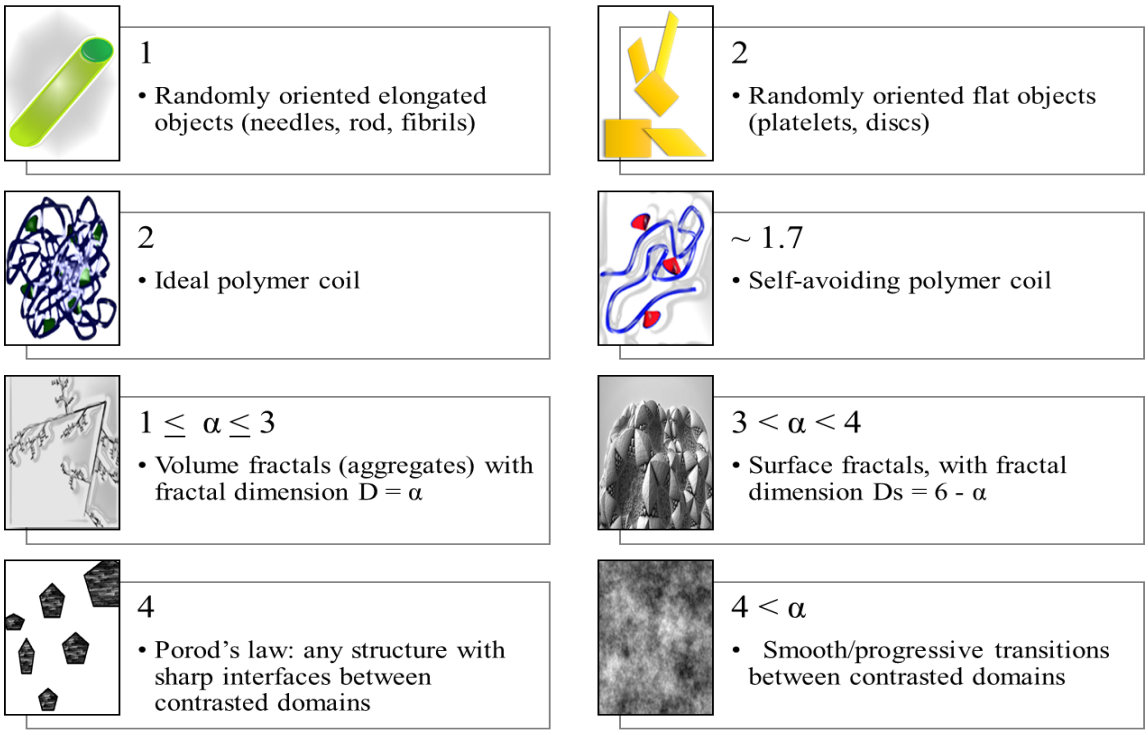

Figure 20. The different values of scattering exponent α and its structural representation[103].

3.1.4. Contrast match in neutron scattering

Contrast variation method in SANS experiment is a powerful method to investigate the biomolecular complexes and analyze the particle shape and inner structure. In general, the bio-SANS method uses a variation of the scattering length density of the sample induced by deuterium labeling in D_2O buffer solution[110].

Neutrons interacting with matter can pass through the atomic nucleus with a probability determined by the distance of the nuclear interaction, be absorbed, or be scattered (coherent or inconsistent). The interference effects on scattering can be calculated using the coherent neutron scattering length, which is based on the principle that any point on a wave front (e.g., an atom in a crystal) can be treated as a source of a new wave – partial wave (in an isotropic medium - a partial wave is spherical). The scattering length is dependent on the strong nuclear force and contribution due to the magnetic dipole coupling with the magnetic electrons and is different for isotopes of the same element.

The contrast variation method allows to detecting differences between the coherent scattering lengths of hydrogen and deuterium, which is not possible by the SAXS method, because X-ray radiation is scattered on electrons. It means that, the X-ray wave is blind to the hydrogen environment.

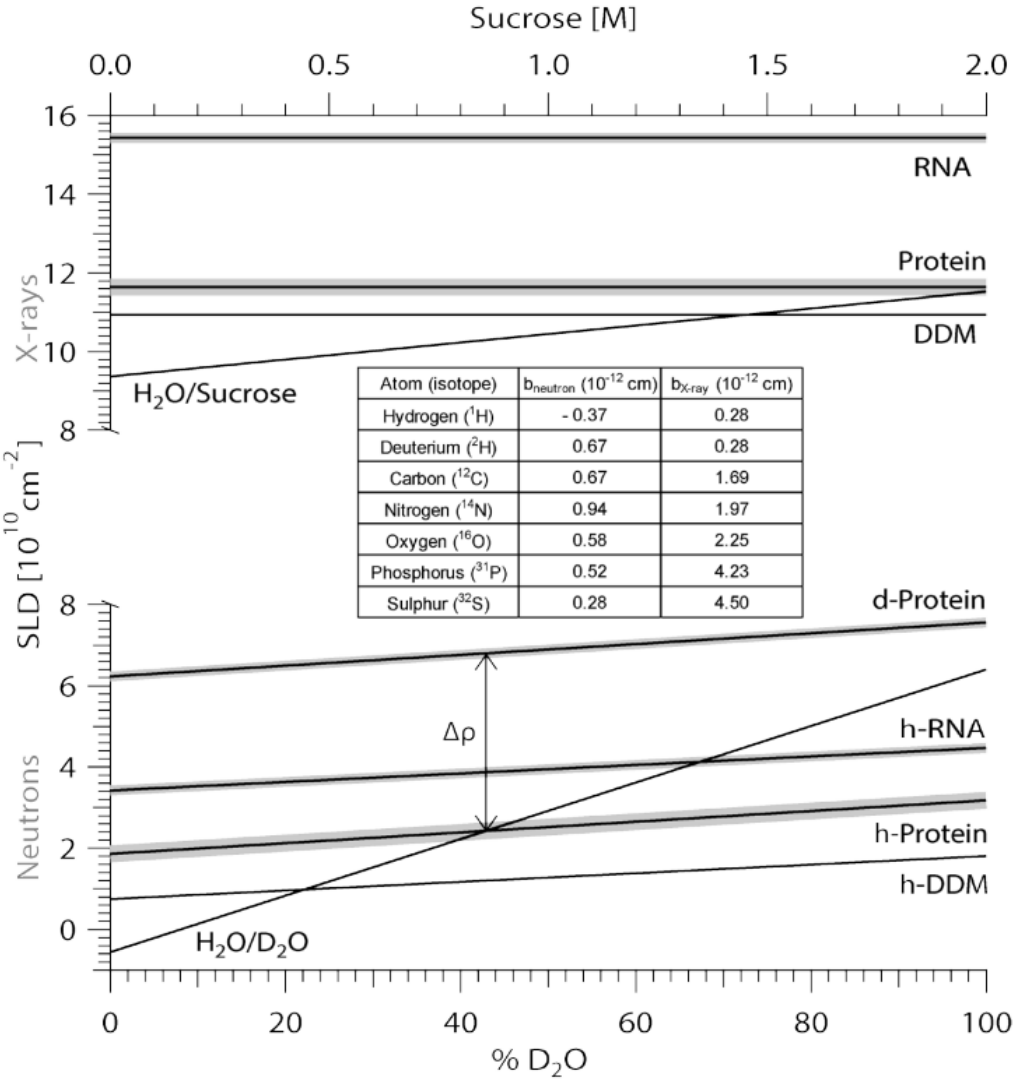

Atom (isotope)	$b_{neutron}$ (10^{-12} cm)	$b_{X\text{-}ray}$ (10^{-12} cm)
Hydrogen (^{1}H)	- 0.37	0.28
Deuterium (^{2}H)	0.67	0.28
Carbon (^{12}C)	0.67	1.69
Nitrogen (^{14}N)	0.94	1.97
Oxygen (^{16}O)	0.58	2.25
Phosphorus (^{31}P)	0.52	4.23
Sulphur (^{32}S)	0.28	4.50

Figure 21. Scattering length densities (SLD) of neutrons and X-ray estimated for several biomolecules. (Adapted from: Mahieu et al., 2020[111])

By manipulating an exchange of hydrogen-deuterium of solvent, it is possible to adjust scattering contrasts of components of the investigated system. Moreover, different biomolecules have different scattering contrasts. The nucleic acids and proteins (Figure 21) are characterized by different scattering densities. The complexes of those two can be studied without a deuterium labeling procedure. The average contrasting point of all proteins is around

42% D_2O and for DNA/RNA match points are around 65% D_2O. The analysis of data for biomolecular complexes allows for observing each component of the complex separately due to scattering intensities at different scattering contrasts - different D_2O % of the buffer (Figure 22).

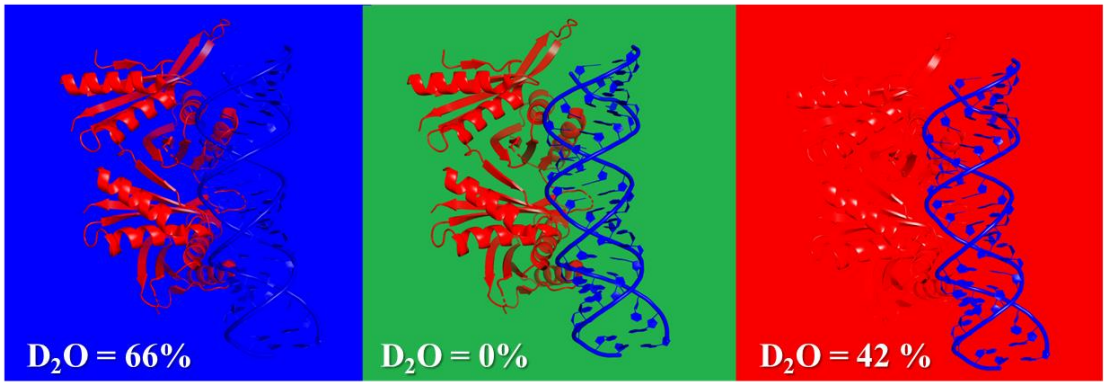

Figure 22. Simplified representation of protein (red) and RNA (blue) complex in contrast match conditions (PBD: 3WBM).

3.1.5. *Ab initio* methods used in SAS data for modeling of low-resolution structures of proteins and nucleic acids

The previous chapters have covered the theoretical basis of small-angle X-ray and neutron scattering. Knowing the form factor and the experimental scattering data, it is possible to calculate the low resolution 3D model that will correlate with an experimental curve. The software used for calculation of the low-resolution models applies dummy beads for structure representation. Each molecule in a system can be described as a system of N spheres (dummy atoms). The greater the number of dummy atoms, the more accurately we will be able to calculate a model correlating to the scattering curve. The predicted dummy atom low-resolution model represents the structure of the macromolecule. Those algorithms can predict a dummy-beads model and can be described by theoretical scattering profile (using Debye formula) which corresponds to the experimental scattering curve. The algorithm search for the model characterized by the best correlation between the theoretical curve and experimental scattering data.

The development of new methods and software for scattering data analysis has made significant progress in data processing, and improved the resolution and reliability of models provided by SAS. The available ATSAS[112] package offers several tools for processing SAS data and analyzing scattering data. Besides processing the data, the ATSAS package includes software for prediction of three-dimensional models obtained from SAS data. These *ab initio* methods allow for visualization of the shape of molecules studied by SAS and the characterization of their structural properties.

The authors of the ATSAS package developed a sequence of algorithms implemented in several programs such as DAMMIN[113], DAMIF[114], GASBOR[115], or MONSA[113] to calculate possible structural models from scattering data. The DAMMIN algorithm implements the search space (a sphere with radius r, which is half the maximum particle size D_{max}) and is filled with densely packed spherical beads. Each dummy atom can represent the part of the studied molecule (index=1) or the solvent space (index=0). The space search algorithm adjusts the beads to correlate with the scattering curve. However, not always one unique shape can be determined for one SAS profile. Nevertheless, the ATSAS package contains the AMBIMETER[104] algorithm that enables the assessment of the uniqueness of the model to acquired SAXS data. The predicted 3D atomic models solved using bioinformatics methods, can be scored against scattering profile data using e.g., CRYSON[116].

Figure 23. Schematic picture of DAMMIN algorithm placing the beads of molecule (black) and solvent (white).

3.2. Isotopic labeling biomolecules for structural studies

Structural studies such as SANS or NMR, require the replacement of certain atoms by their isotopes[117]. For the study of biomolecules, hydrogen, nitrogen, and carbon atoms are most often replaced with their isotopes. This procedure is known as isotopic labeling. Biological molecules such as proteins can be synthesized primarily by GMO organisms such as specialized *E. coli* bacteria. The exchange of the naturally present atoms with their isotopes, e.g., hydrogen (H) exchanged with deuterium (D), strongly influences biological systems and can disrupt their proper functioning. The higher eukaryotes, such as plants and mammals, can hardly survive deuterium levels >30%. The molecule containing for e.g., -NH group (like in polypeptide chain) placed in a solution containing deuterium, exchange hydrogen on deuterium -ND group until full equilibrium (Figure 24).

In order to increase the deuteration level (^{2}H, deuterium (D)), labeling by nitrogen ^{15}N or carbon isotopes ^{13}C, it is necessary to introduce the isotopes into the main chain of polypeptide as well. Such a process can only be performed at the level of intracellular synthesis of the protein[117], and the GMO organism needs to be placed in a medium containing nutrient with desired above isotopes.

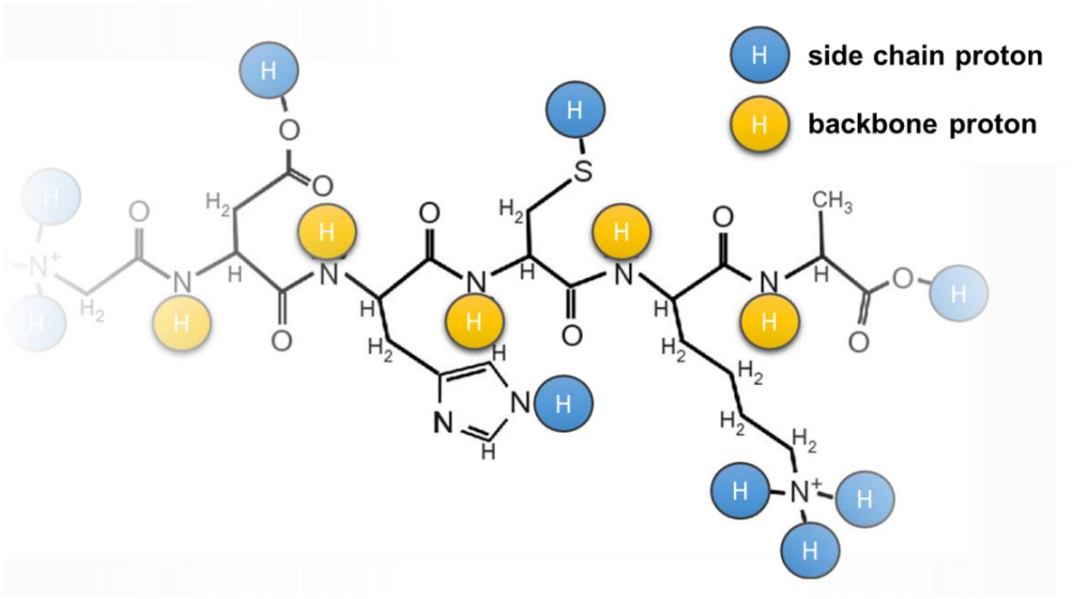

Figure 24. Schematic structure of protein backbone with marked exchangeable protons in D_2O solution.

The overexpression in deuterium conditions is challenging but *E. coli* bacteria in optimal conditions can grow in fully deuterated media. In most cases, *E. coli* cells grow in typical (like LB media) deuterium-based medium, but with a much lower optical density at 600 nm wavelength λ (OD_{600}). To optimize the production in an isotropic medium, the so-called minimum media needs to possess a strictly defined composition. It is critical to properly calibrate growth factors such as temperature, mixing, etc. The same rules apply during the induction of protein overexpression[118]. Protein production under deuterium conditions is much more complicated than in hydrogenated aqueous media. The proteins in D_2O have a high tendency to aggregate due to increasing hydrophobic interaction[119].

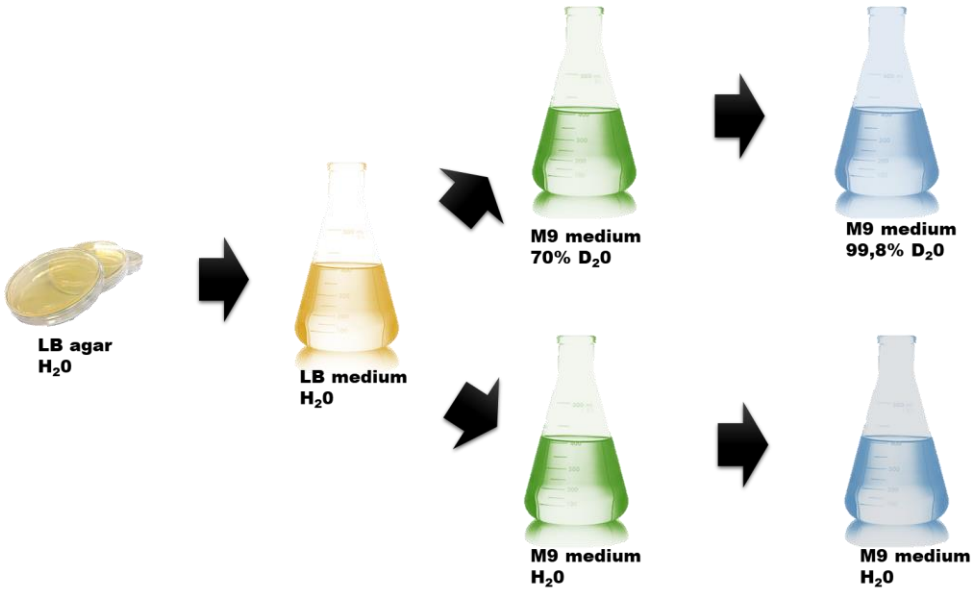

Figure 25. Schematic representation of the adaptation process of E. coli cells to the deuterated media. Each arrow represents the bacteria transfer to a fresh medium[120].

The level of deuteration of the expressed protein can be validated by mass spectrometry. Labeling with deuterium is a common procedure in the study of biomolecular complexes by SANS or NMR (in case of big proteins). Not only to study proteins but also protein - lipid bilayer interactions (e.g., nanodiscs and membrane proteins).

3.3. Computational modeling of biomolecules

The experimental studies of complex biological macromolecules remain still a challenge. In addition to experimental techniques, computational modeling methods can also be used to characterize the atomic structures and dynamics of biomolecules. There are many bioinformatics methods and algorithms developed to deal with solving the structure and studying the dynamic of overly complicated molecular systems. With current techniques, knowing only the sequence of the protein is sufficient to predict its atomic 3D structure of proteins with high accuracy[121] (Figure 26). These bioinformatics methods designed for structure prediction of biomolecules are usually based on the so-called homology modeling, when the structure (or a fragment of the structure) of the available homolog (e.g. a protein with the same function) is known, or by the *ab initio* method, when the structure is calculated based on quantum mechanics, like in Monte Carlo simulation.

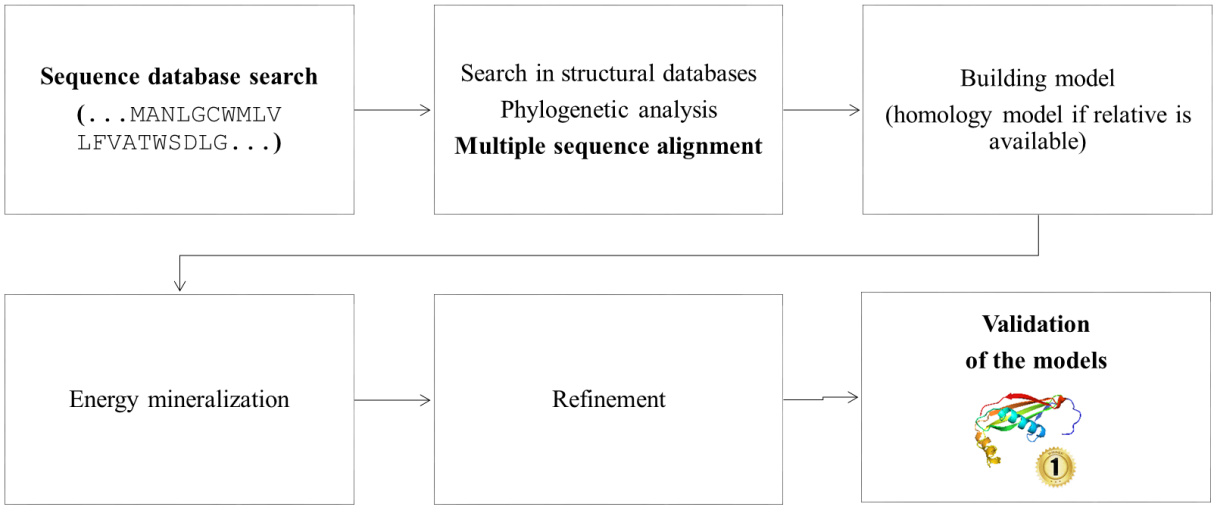

Figure 26. Diagram of bioinformatics modeling procedure of protein 3D structure starting with information about the primary sequence.

Currently, a very hot topic is the development of so-called machine learning algorithms to predict the structures of biomolecules. The algorithm of AlphaFold[49] - an artificial intelligence program developed by DeepMind of Alphabet/Google started a revolution the in developing solutions for modeling the structure of biomolecules and designing drugs. Generally, the

method is based on collecting the set of data of already known structures, and searching for specific patterns or motifs that will be correlated within a given sequence. In addition to other computational methods, many programs also provide input derived from experimental data (from NMR, FRET, SAXS, or SANS) which significantly improve the accuracy of the structural modeling. The computational approach for solving the protein structure, apart from being easier to apply, is also much cheaper than the experimental studies.

3.3.1. Molecular dynamics simulations

The method to study a macromolecular structure and dynamics of the system in various conditions can be performed by molecular dynamics (MD)[122] simulations. MD is a computational method using a computer simulation that describes and analyzes the physical properties and movements of atoms in molecules, the so-called dynamic "evolution" of the system. MD is widely used in many interdisciplinary fields such as computational chemistry, material science and molecular biophysics. One of the basic principles of MD states that the motion and trajectories of atoms or molecules are described by means of a numerical solution of Newton's equations of motion describing the system of interacting particles (Equation 10, 11, Figure 27, 28).

Newton's 2nd law of motion:

$$\overrightarrow{\mathbf{F_i}} = \mathrm{m_i} \frac{\mathrm{d}^2\overrightarrow{\mathbf{r_i}}}{\mathrm{dt}^2} \qquad (10)$$

Numerical integration:

$$\overrightarrow{\boldsymbol{F_i}} = \overrightarrow{\boldsymbol{\nabla_{ri}}} V(\overrightarrow{\mathbf{r_1}}, \ldots, \overrightarrow{\mathbf{r_N}}) \qquad (11)$$

Where, the acceleration is the second derivative of the position with in relation to time; *F* – force, *V* – speed, *t* – time, *m* – mass of the particle.

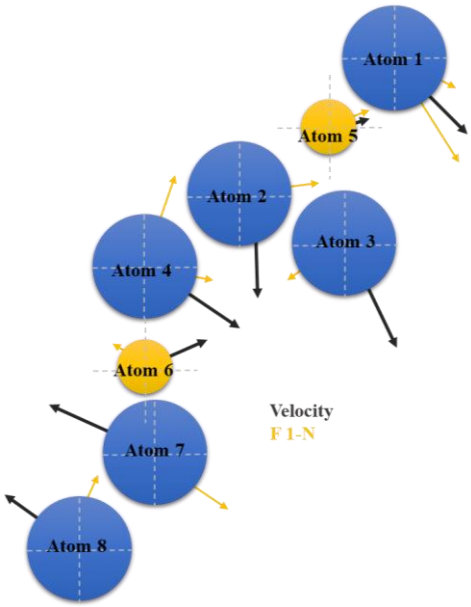

Figure 27. Simplified schematic description of atoms movements according to Newton laws descriptions.

In order to solve these mathematical formulas, the intermolecular forces and their potential energies are matched by what is known as interatomic potentials or force fields of molecular mechanics. Very often, as in the case of biological macromolecules for example, systems consist of an enormous number of atoms and the computational cost is high, and the analytical cost is unattainable. Therefore, specially designed algorithms are used to address this issue.

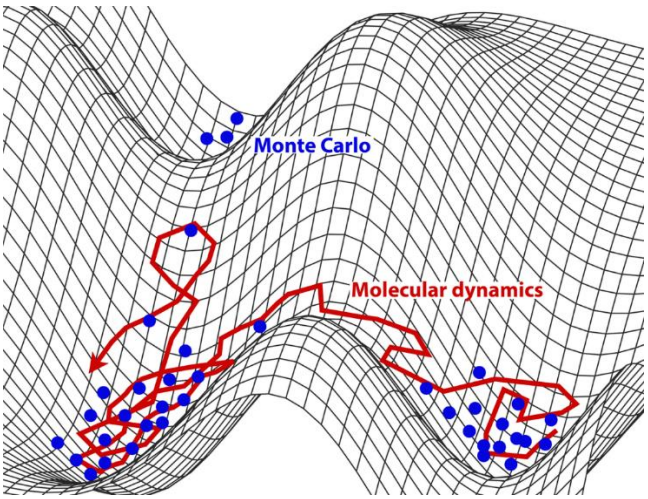

Figure 28. Schematic representation of the sampling of the system's potential energy surface with molecular dynamics (in red) compared to Monte Carlo methods (in blue). (Adapted from: Wikipedia, license: Creative Commons, Attribution 4.0 International)

The main problem of long MD simulations is that they are poorly conditioned mathematically. Numerical approximations are cumulating, thus increasing the error ratio. Nevertheless, there are some solutions, such as intelligently designing algorithms and parameters, which may slightly compensate for the errors.

3.3.2. Macromolecular docking

Thanks to the bioinformatics method of molecular docking[123–125] it is possible to study complicated complexes of biomolecules. Depending on the parameters (e.g., type of the ligand and the target), the 3D structure of the complex is determined. Molecular docking is an extremely relevant method in the modern field of drug design. The molecular docking method can bring information about the area of interaction (binding site) and the type of interaction. Two strategies can be used to dock two molecules (two proteins) to each other. Docking with a rigid body approach, where the angles, lengths, and torsion angles of the components do not change during the docking procedure. If the structural parameters are adjusted during docking, then it is called flexible docking. The problem with flexible docking is that the calculations deliver many possible conformations of the studied molecules, which are also difficult to assess. Elastic docking methods are much more computationally expensive.

3.3.3. Coarse-grain methods for modeling of large biomolecules

Computer simulations such as MD or multi-atom biological systems are extremely computationally expensive. To address this problem, scientists developed the so-called coarse-grained modeling[126]. Coarse-grain simulation method was invented in the 1970s by M Lavitt and A Warshel[127] (Nobel Prize winners). Coarse-grained models simplify full-atomic biological systems and thus limit the number of parameter combinations for computational simulations. It is commonly used to mediate large protein particles or nucleic acids.

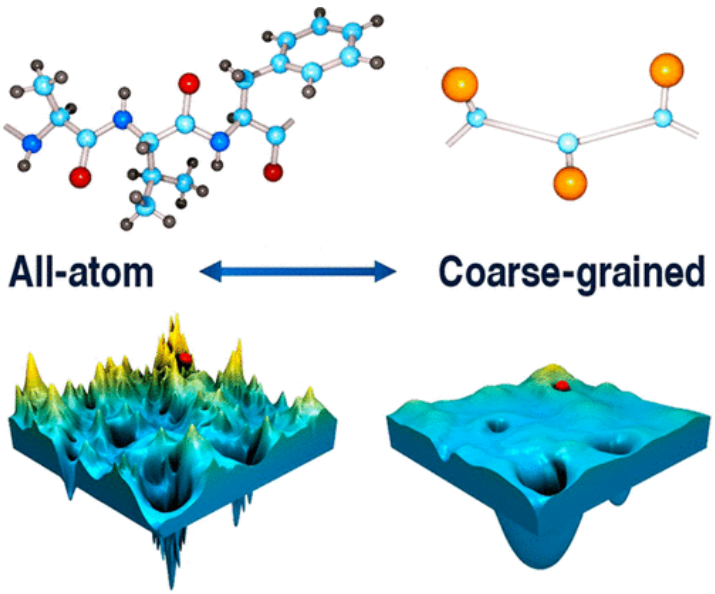

Figure 29. Graphical representation of coarse grain methods including a difference in energy landscape. (Adapted from: Kmiecik et al., 2016[128])

In this method, atoms are grouped according to their properties and puckering into the representation of so-called "pseudo-atoms" (Figure 29). For example, an amino acid residue can be represented by a single pseudo-atom describing the physicochemical parameters of all atoms forming that amino acid group. The reduction of "atoms" directly affects the degrees of freedom, which consequently reduces the cost and time of simulations. Coarse-grain approach in statistical mechanics solves the entropy problem and refers to the second law of thermodynamics. The coarse-grained simulations and protein-structure prediction, without ancillary information from structural databases, can be done with the physics-based UNRES model and dedicated force field[129]. In addition, the coarse-grain method for protein structure prediction was developed as a part of popular Rosetta software[130].

3.4. Atomic force microscopy, characterization of a sample topology

Atomic force microscopy is a type of scanning probe microscope that scans the surface of a sample with a resolution, even at almost atomic level[131]. The AFM is derived from the scanning tunneling microscope (STM) and was first constructed in 1986 by Binnig, Quate and Gerber (Nobel Prize winners)[132]. The AFM method allows to scan any type of sample (also to study samples that have conductive properties). The topological image reveals information about the structure of the sample i.e., the height profile of their surface. In addition to the parameters describing the sample topology, it is possible to obtain information about the mechanical parameters of studied surface such as adhesion and flexibility.

AFM performance is comparable to the confocal microscopes. The sample area is scanned point by point or pixel by pixel and the probe moves in a given area, i.e., XY axis same as the height Z axis (Figure 30). Measurement of the height in the sample results from the movement of the probe over the sample while maintaining the set parameters. Depending on the parameters of the probe, a different resolution can be obtained. Ideally, a single atom is found at the edge of the probe tip.

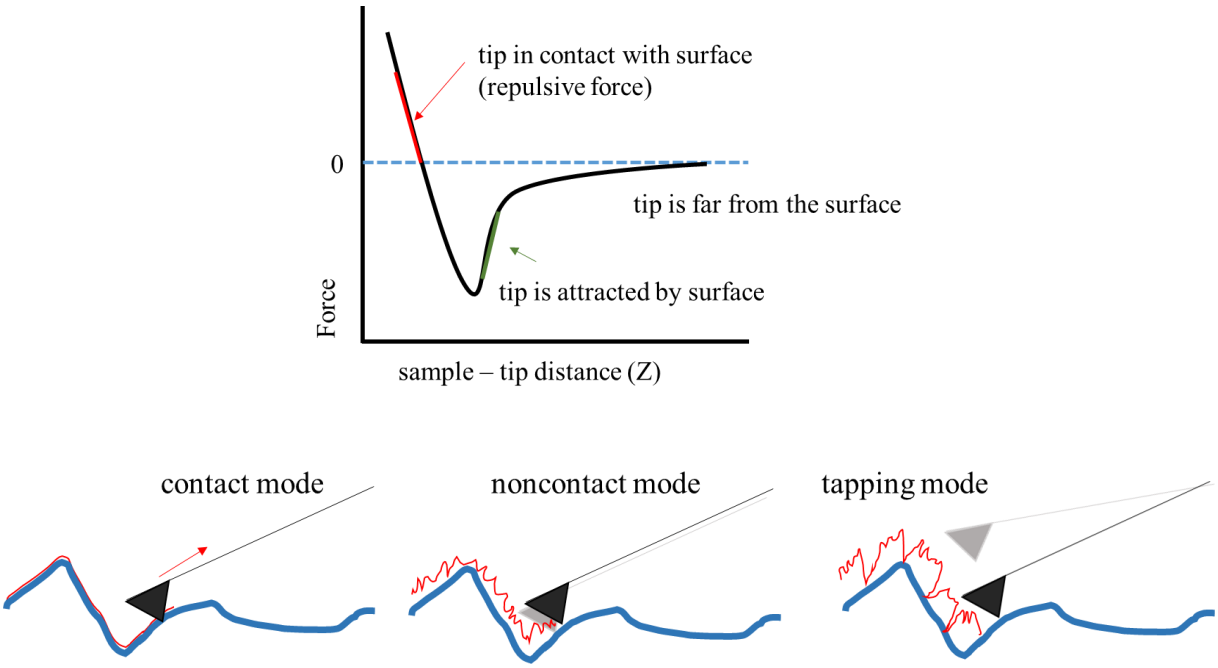

Figure 30. Schematic diagram of principle of AFM imaging and AFM working modes[133].

There are several different modes of measuring sample topology with AFM (Figure 30):

Contact Mode:

In AFM contact mode the forces of attraction (e.g., Columb) or repulsion (van der Waals) between the probe and the sample surface are determined. This phenomenon is known as close-range interaction. In this mode, the tip depresses the surface of the sample with a force ranging from 10^{-11} to 10^{-7} Newtons. The space between the tip and the sample is small and they repel each other. The measured parameter is the bending force of the ring to which the tip is attached.

Non-contact mode:

In non-contact mode, there is a distance of 1-10 nm between the tip and the sample surface. The tip and sample interact with each other by electrostatic, magnetic or attractive van der Waals forces. Contrary to the contact mode, the differences in the magnitude of the vibration frequency of the lever are measured. Each time before measuring the sample, a calibration of the lever vibration is required to be as close as possible to its resonance constant (which may depend, for example, on the ambient temperature). The measurements are possible on diverse types of samples, including soft surfaces.

Tapping mode:

In this mode, the probe (tip) is not scanning the sample surface but instead, the probe with the tip vibrates near its resonant frequency, causing the tip to vibrate in Z height. The probe comes into close contact with the sample surface only periodically. This AFM mode reduces the probability of damaging the sample during measurements.

3.5. Transmission electron microscopy

Transmission electron microscopy (TEM)[132] is widely used for imaging of biological systems such as the ultrastructure of tissues, cells, and macromolecules (e.g., viruses, ribosomes, DNA). Recently the sub-method cryogenic electron microscopy (cryoEM) was awarded a Nobel Prize[134] to Dubochet, Frank, and Henderson, for "*developing cryo-electron microscopy for the high-resolution structure determination of biomolecules in solution*". The resolution limit in microscopy is defined by the wavelength of the incident beam that interacts with the sample. According to this principle, two objects located closer to each other than half a wavelength will no longer be distinguishable as single points. Since the high energy electron beam wavelength is much smaller than the wavelength of visible light, the TEM resolution is much higher. The related methods such as electron tomography, used for 3D imaging, or the energy dispersive X-ray spectroscopy (EDS) method, are used to determine the chemical composition from the discrete spectra of atoms.

The basic element of an electron microscope is a column containing a source of electrons. The pre-shaped (optics) electron beam in the area between a cathode and an anode is accelerated to obtain energy:

$$E = eU \qquad (12)$$

E - Energy, e - charge of electron, U - voltage between the cathode and the anode

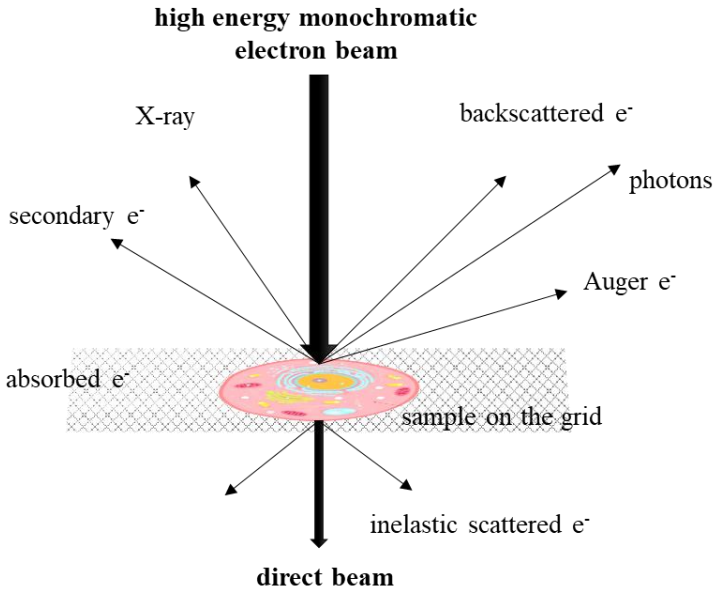

Figure 31. Schematic visualization of electron beam diffraction and the sample imaging by TEM.

Electrons interacting with the sample collide with its atoms. In this colliding process the electron loses the kinetic energy and it can be completely absorbed, reflected from the sample, emit radiation or pass through without any interactions (Figure 31). Absorbed kinetic energy is transformed primarily into heat. When the sample is thin, a large part of the electrons penetrates through. The volume in which 95% of the electrons are dispersed is named the zone of interactions.

3.6. Analytical Ultracentrifugation Experiments

Analytical ultracentrifugation (AUC)[135] is used to determine the structural parameters of macromolecules. AUC analyzes interactions between biomolecules[136], e.g., binding constant of non-covalent complexes. Moreover, AUC technique made possible the evaluation of the shape and size of macromolecules and their conformational changes. In addition, it allow us to define the quality of the sample. Information that can be obtained from an AUC experiment includes the overall shape of the macromolecules and the size distributions. Thanks to this method, it is

also possible to obtain the information on the number and stoichiometry of the subunits in non-covalent complexes and the binding constants.

In the AUC experiment, the macromolecules suspended (dissolved) in the solution are subjected to centrifugal force and the sedimentation profile of the sample is monitored by an optical detection system (in real time). The optical detectors allowing to monitor the absorption of light (e.g. ultraviolet absorbance, interference) and an optical refractive index. The sensor is made of an array of photosensitive diodes allowing the optical system to monitor the change in sample concentration as a function of the axis of the rotation profile over time resulting from the applied centrifugal field. The most popular AUC experiments are sedimentation velocity and sedimentation equilibrium experiments.

Sedimentation velocity experiment

In this experiment the concentration gradient (sedimentation) of macromolecules in a solution is measured in the presence of centrifugal force[137]. Optical parameters such as the absorption and shift of the interference fringes as a function of time are measured, including the distance to the rotation axis. Based on this information, it is possible to determine macromolecule parameters such as mass or shape. For every substance (particles) dissolved in the solution, the sedimentation is primarily related to the so-called sedimentation coefficient S (Equation 13). This factor is related to the particle velocity v in response to the acting centrifugal field $\omega^2 r$, where ω represents the angular velocity in rad/s:

$$S = \frac{v}{\omega^2 r} \qquad (13)$$

The system of molecules moving in solution in the presence of centrifugal force can be described by the diffusion coefficient D. In a mixture with one type of molecules dissolved in solution, the Lamm's equation determining (Equation 14) the change at concentration c as a function of time t and regarding to the distance from the axis of rotation r:

$$\frac{\partial c}{\partial t} = D\left[\left(\frac{\partial^2 c}{\partial r^2}\right) + \frac{1}{r}\left(\frac{\partial c}{\partial r}\right)\right] - s\omega^2\left[r\left(\frac{\partial c}{\partial r}\right) + 2c\right] \qquad (14)$$

The size (hydrodynamic radius R_H or Stokes radius R_S) of a molecule, molecular weight ($M=mN_{Av}$) and its partial specific volume V, influence the movement of the molecules in the solution. This is described by the sedimentation coefficient S. The sedimentation coefficient is also affected by the medium in which the particles are dissolved, i.e., the solvent density $\rho°$ and the viscosity of the solvent $\eta°$. This relationship is described by Svedberg's Equation:

$$S = \frac{M(1-v\,\rho°)}{N_{Av}6\pi\,\eta°\,Rs} \qquad (15)$$

Where friction f in Stokes relation is described as:

$$f = 6\pi\,\eta°\,Rs \qquad (16)$$

Equilibrium sedimentation experiment

Equilibrium sedimentation experiment[137] is based on the equilibrium sedimentation (ES) parameter. This parameter describes the concentrations of macromolecules in the medium in the presence of centrifugal force, under equilibrium conditions (Figure 32). The optic system analyzes the absorption of molecules in the solution buffer. With this method, the molecular weight of macromolecules can be determined. The method is also used to determine the association-dissociation equilibrium constant of complexes.

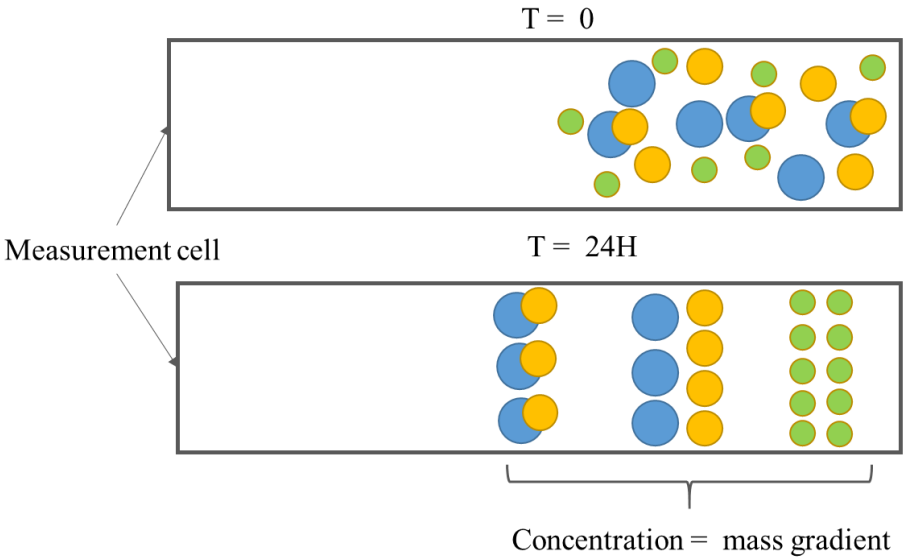

Figure 32. Schematic representation of sedimentation equilibrium experiment.

Thanks to the equilibrium condition being maintained during measurements, the Lamm's equation is simplified to a formula presented below (Equation 17), where concentration c is dependent on the radial distance *c(r)*. The experiments are usually performed in a set of different sample concentrations. The different profiles of sedimentation equilibrium can be obtained for different protein concentration.

$$c(r) = \Sigma\, c_{0i}\, exp\left[\frac{\omega^2 M_{bi}}{2RT}\right](r^2 - r_0^2) + \delta \quad (17)$$

R - gas constant. *T* - temperature (K)

In this formula a c_{0i} is corresponding to the concentration of one type of the molecule at radial distance. The signal from the buffer solution constant is added as a noise δ. M_{bi} is the so-called buoyant molar mass corresponding to the following equation (Equation 18):

$$M_{bi} = M_i(1 - v\, i\, \rho°) \quad (18)$$

3.7. Mass spectrometry

Mass spectrometry (MS) is a spectrometric analytical method which is used for detection of the molecular (or atomic) mass of tested substances[138]. There are many techniques implemented to MS, depending on the intended application and each requiring a different type of instrument. MS is used to identify chemical compounds, their mixtures and determine their elemental composition. Moreover, MS can generate data about isotopic composition. This method has a wide range of applications in chemistry and biology, where it can be used for example to define the sequence of nucleic acids in DNA or amino acids in proteins[139]. With the native MS method, macromolecular complexes can be also characterized.

The MS method was developed by J.J. Thomson, who built in 1911 the first mass spectrometer[138]. MS uses the ionization phenomenon of molecules or atoms and analyzes the number of ions as a function of their mass-to-charge ratio (m/z). A time-of-flight analyzer implemented in MS (TOFMS) describes the ion's mass-to-charge ratio to a "time of flight" (move) of molecule during measurement. TOFMS analyzes the dependency on the mass and charge of molecules and their movement in the magnetic field (Equation 20, 21, Figure 33). As a result of the experiment, the mass spectrum profile of the investigated substance is obtained. Native MS[140] is used mainly for research and determination of masses and stoichiometry of complexes of biological particles such as polypeptides and proteins. This method allows a study of the intact quaternary structures of protein complexes. Besides, it is characterized by high sensitivity and the wide molecular mass range.

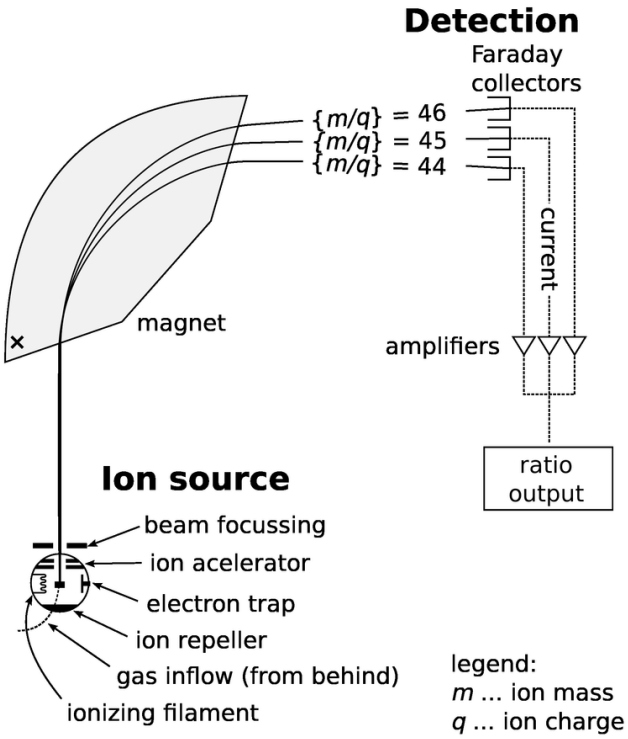

Figure 33. Schematic picture of mass spectrometer. (Adapted from: Mesuere et al., 2016[50])

In each mass spectrometer, there is an ion source or ionizer (Figure 33). It is a device responsible for the ionization of molecules. Depending on the ionization method, it can simply charge the molecule (native MS) or cause e.g., denaturation and separation. After the ionization process, the charged particles are separated by an analyzer. During the last step, the detector counts ions. The mass analyzer is separating the ions according to the physical principle of Lorentz force (Equation 19) and Newton's II (the non-relativistic case, Equation 20) laws. The mass-to-charge ratio is the result of the dynamics of the charged particles in electric/magnetic fields in the vacuum condition.

$$F = Q(E + vB) \qquad (19)$$

$$F = ma \qquad (20)$$

Where *m* is the mass of the ionic charge *Q* which is influenced by the force *F* and moving with acceleration *a* in the electric field *E*. The $v \times B$ represents the cross vector of the ion velocity and the magnetic field. Those two equations are equivalent:

$$\frac{ma}{Q} = E + vB \quad (21)$$

The above equation determines the particle's motion in space and time with *m/Q* taking into account the initial directions. This equation 22 is usually given by the dependence on the elementary charge *e*:

$$z = \frac{Q}{e} \qquad (22)$$

So it describes the relationship of the mass number of the ion to the charge number.

3.8. Nuclear magnetic resonance spectroscopy

Nuclear magnetic resonance (NMR) spectroscopy, is a valuable technique used for studies of macromolecules and their interactions in solution and solid states[141]. This technique can provide numerous information about site-specific dynamics of the macromolecule in an aqueous buffer. Detailed data from the NMR experiment can be used to identify the exact atoms taking part in protein-ligand / protein-protein interactions.

The study of proteins with NMR is using the approach of multidimensional NMR experiments using isotopes (^{1}H, ^{13}C, ^{15}N) to obtain detailed information about structural and dynamic information of the biomolecules in solution. In order to determine the high-resolution 3D protein structure, the multidimensional NMR experiments have been designed. Typically, the structural analysis of the studied protein require a series of various experiments.

To explore molecular dynamic processes in the protein backbone, the ^{15}N relaxation experiments can be performed. Proteins acquired in ^{15}N-labeled form permit to obtain experimental data about R_1 and R_2 relaxations rates, and ^{1}H-^{15}N NOE. All relaxation experiments based on a 2D heteronuclear single quantum coherence experiment (^{1}H-^{15}N HSQC) showing a correlation between proton and nitrogen in the amide group for observed amino acid residues (not a proline). The relaxation measurements include the analysis of the longitudinal relaxation rate (R_1), transverse relaxation rate (R_2), and ^{1}H-^{15}N NOE. To describe molecular dynamics processes in protein backbone (Figure 34) the ModelFree approach (MFA) was developed[142]. This approach permits extracting information about dynamics processes in the proteins from NMR relaxation data without knowing the specific motion model[143].

For the isotropic rotation, the model-free approach takes mainly two parameters into account to describe the internal motions of backbone amide groups in the protein. The overall motion is described by the correlation time τ_R and internal motion(s) by a generalized order parameter S^2. The S^2 is measuring the degree of spatial restriction of the motion, and an effective correlation

time τ_{int} corresponding to the rate of this motion. The graphical visualization of dynamics protein processes explored by NMR relaxation is presented in Figure 34.

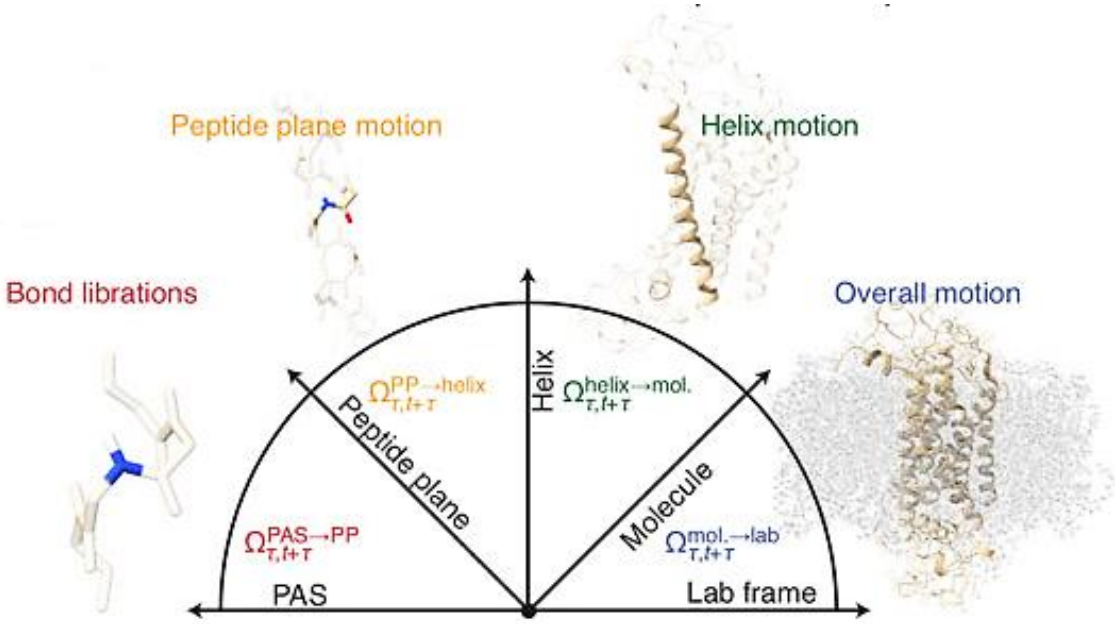

Figure 34. The figure shows the dynamics of protein which can be revealed by NMR experiments supported by MD (Adapted from: Zumpfe and Smith, 2021[143]).

4. Material and methods

4.1. Synthesis of Aβ peptides

Selected Aβ peptides

For this PhD project, three Aβ peptides were selected: 1-16, 3-28 and 1-42. The Aβ 1-16 was purchased from GenScript Biotech (Poland, purity >96 %). The Aβ 3-28 and Aβ 1-42 were synthesized and purified (~95 %) with microwave synthesis and chromatography during internship at Department of Biomedical Chemistry, University of Gdańsk under supervision of Aneta Szymańska (University of Gdańsk, Poland). The selected variants containing different sequences were used to study the wide spectrum of Aβ properties. However, Aβ 1-42 form is the most important aggregative peptide.

Solid-state synthesis

The selected Aβ peptides were produced in collaboration with Aneta Szymańska (University of Gdańsk, Poland). The peptides were synthetized by microwave synthesis on a solid sub-substrate using a Liberty Blue instrument (CEM Corp., Matthews, NC, USA), which uses microwave radiation for both coupling and deprotection of fluorenylmethoxycarbonyl (Fmoc) amino acids moiety (Figure 35). After synthesis and cleavage, the peptide from the resin, a series of HPLC purification steps were performed. The purity of the collected fractions were checked by analytical chromatography (Figure 36) and the final product was analyzed by mass spectrometry.

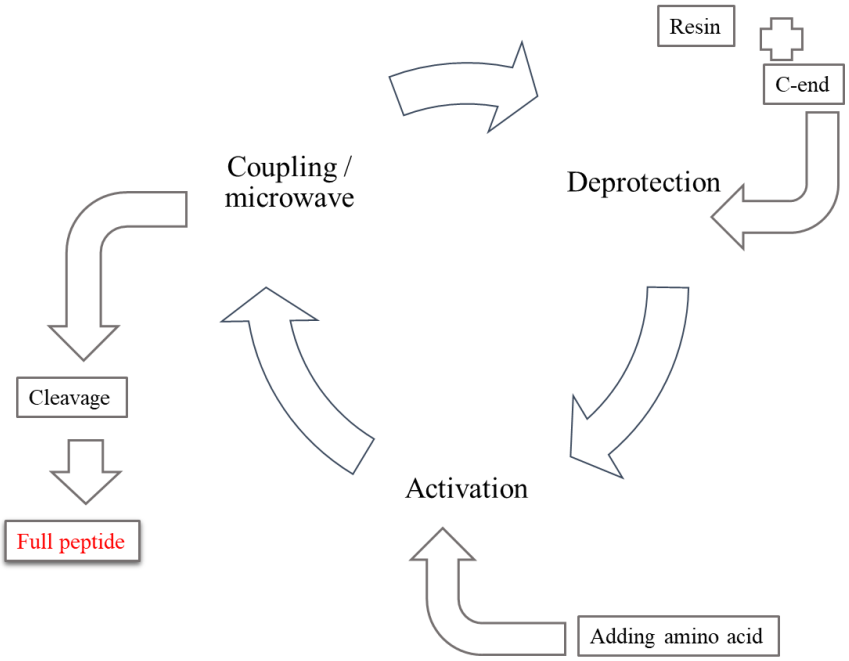

Figure 35. Synthesis of peptides on supports (resin). The Fmoc / tBu method consists of several steps: attachment of C-terminal end to the linker -resin; cyclically adding new amino acids; cleavage from resin and protective groups from side chains.

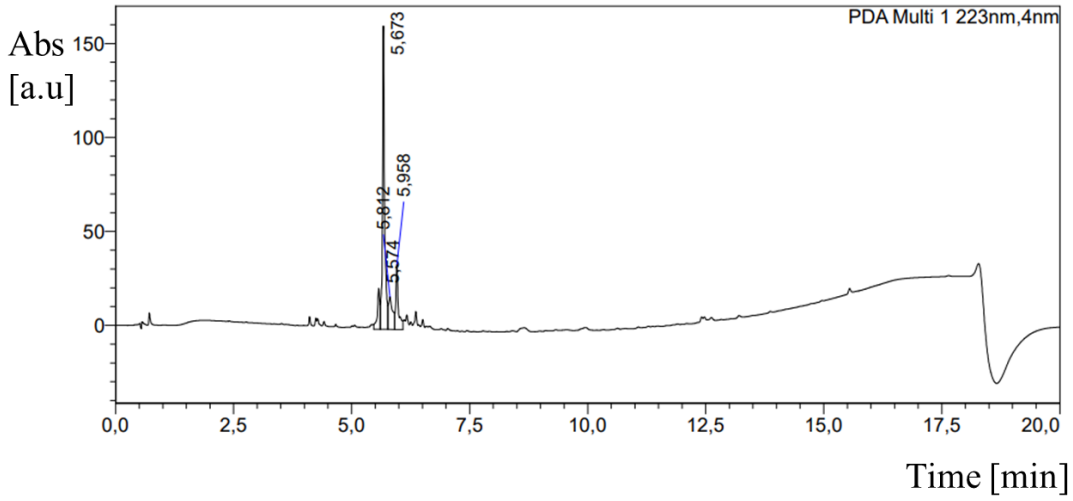

Figure 36. Exemplary analytical chromatography spectrum of crude 3-28 Aβ peptide after synthesis. Main peak is located at 5.6 min.

Purification by high-performance liquid chromatography (HPLC)

HPLC chromatography is a physicochemical method widely used to separate individual components of homogeneous mixtures because of their different partitioning between the mobile and stationary phases of a chromatographic system[144]. In HPLC separation of hydrophobic Aβ peptides, a combination of C4 or C8 silica-based stationary phases (Column Luna, 5 µm, 20 × 250 mm, Phenomenex, Torrance, CA, USA) and an acidic mobile phase were used.

After synthesis, the lyophilized peptides were diluted in 10 mL of buffer A (H_2O, 1% TFA (Trifluoroacetic acid)) in the highest possible concentration. Next, the solution was filtered and injected into the HPLC column. The few of different gradient method (buffer B, H2O, 1% TFA, Acetonitrile 80%) were tested and the most efficient was chosen to extract the purest peptide fractions. Then, the fractions were collected and in order to verify the purity checked with analytical chromatography. The main fraction have been put under the vacuum evaporator to get rid of TFA and acetonitrile. During the last step, the concentrated solution of peptide was lyophilized and evaluated with analytical HPLC (analytical RP-HPLC, Jupiter® C18 column, 5 µm, 300 Å, 4.6 × 250 mm, Phenomenex, Torrance, CA, USA) (Figures 37 and 38) and mass spectrometry (ESI LCMS IT TOF, Shimadzu, Jupiter C18 column, 5 µm, 300 Å, 4.6 × 250 mm, Phenomenex, Torrance, CA, USA).

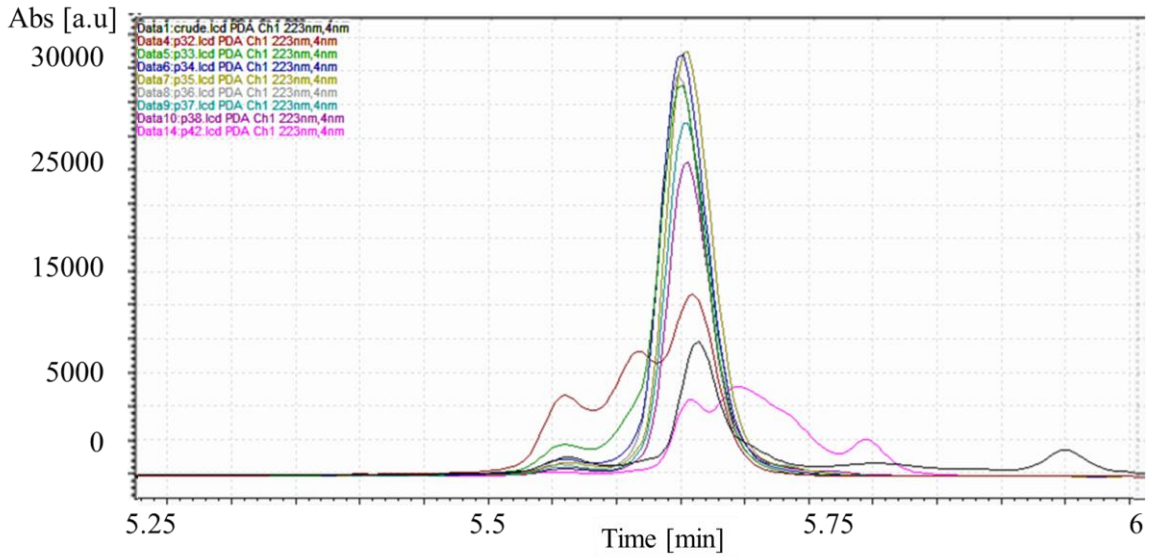

Figure 37. The absorbance spectrum in the vicinity of main peak peptide fractions after separation by HPLC.

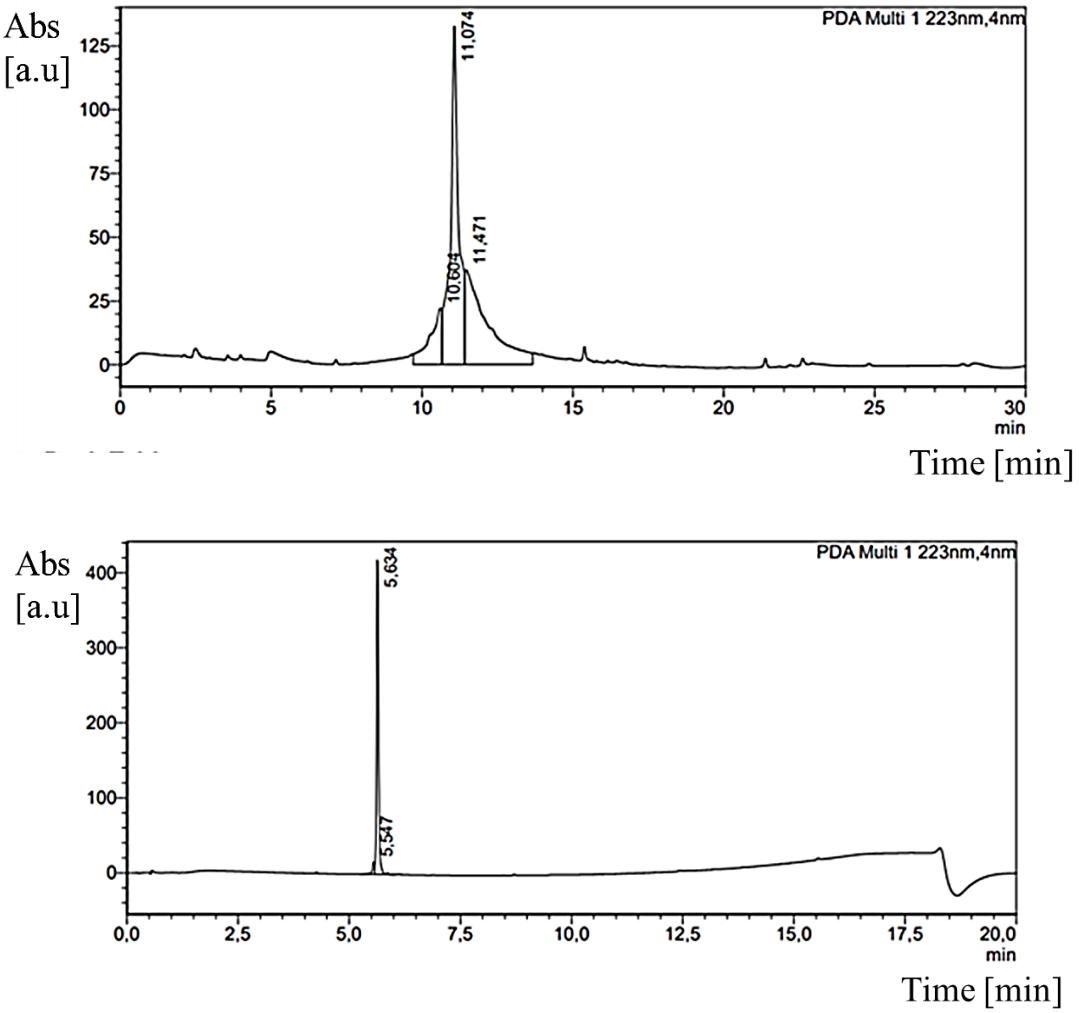

Figure 38. Absorbance spectrum for the purified of Aβ 1-42 (top) and Aβ 3-28 (bottom).

4.2. Disaggregation of Aβ peptide oligomers

Since Aβ peptides spontaneously aggregate into oligomers and ultimately fibrils the prior treatment of lyophilized peptides is required before to maximize their solubility in the solvent used for experiments. Several protocols were proposed for the monomerization of Aβ peptides[145] and few of them were tested in this work. Finally, the protocol with hexafluoroisopropanol (HFIP) which exhibits strong acidic pH was chosen. This compound breaks down the β-sheet secondary structure and allows for separation of Aβ peptides into a monomer.

Preparation of Aβ peptide solutions

The lyophilized Aβ peptides were placed in glass vials and dissolved in HFIP (1mg /1mL). Then, the solution was sonicated on ice in several time cycles (30 min of sonication followed by 30 min break). Then the solution was aliquoted into glass vials and left to dry in a fume cupboard under nitrogen stream. During the sample preparation, it was critical to dissolve peptide at a low temperature (4 ^{o}C) with very gentle mixing. For Aβ 1-42, the maximum dissolution reached without sudden aggregation and precipitation was around 1 mg/mL. The Aβ 1-16 and Aβ 3-28 were dissolved at concentration no higher than 2 mg/mL.

4.3. Overexpression of native HCC and deuterated HCC protein

The overexpression of HCC protein was performed using the protocol of Marley and co-workers[117]. The DNA plasmid with HCC sequence and the gene of antibiotic resistance ampicillin (AMP) were transformed into *E. coli* competent cells - BL21 (Novagen; Sigma Aldrich, USA). The bacteria were transferred to the Petri plate with lysogeny broth (LB) agar medium and AMP. For the overexpression step, bacteria were transferred into a small volume of LB media (one colony per flask) and left to grow overnight at 37°C. Next, 5 ml of overnight culture was passed to 500 ml of fresh LB medium containing antibiotics and to grow in a 2 L flask until OD_{600}=~0.6 was reached. Then, induction was started by increasing the temperature to 44°C for 20 min and the incubation was continued at 42°C for another 3 h. Next, the cells were harvested and lysed by sonication on ice (25% amplitude, 5 min in periodic 3 s pulse, 2 break). The lysate was centrifuged (7000 g at 4ºC, 30 min) and the collected supernatant was prepared for purification. The purification of the expressed HCC was performed with a two-step procedure involving the use of ion-exchange chromatography (HiTrap SP-Sepharose, GE, Healthcare Life Sciences, US) and size exclusion chromatography (Superdex 75 10/300 GL, GE, Healthcare Life Sciences, US). It was observed that the above protocol was not particularly efficient with D_2O-based media. The ampicillin resistance plasmids are not recommended in high density cell culture protocols with deuterated media. The deuterated conditions enhance the secretion of β-lactamase[146] which degrades antibiotics and causes the over-growth of plasmid-free cells.

High yield protocol for deuterium labelled HCC

The overexpression of protein in deuterated conditions is extremely challenging. The bacteria culture grown in the D_2O media exhibits high mortality, slow growth, a problem with induction of overexpression, and sometimes even an aggregation and precipitation of the desired protein. The process of optimization of the protocol was extremely time-consuming and required testing many different compositions of media, same as grown and induction conditions.

In order to increase efficiency of deuterium labeled HCC protein production, the high yield protocol was optimized (high OD_{600} value) in small culture volume. A new plasmid - pET-24(a) contains coded HCC gene, antibiotic resistance for kanamycin (KAN), and Isopropyl β-d-1-thiogalactopyranoside (IPTG)-controlled expression promoter. The transformation of the

plasmid was performed with competent *E. coli* cells (Shuffle T7B, New England Biolabs, USA). Different media with various Shuffle strains and KAN resistance were tested. The terrific broth (TB) medium was finally selected as optimal.

Transformed cells were passed into LB-agar-KAN plates at 18 ^{o}C for 48 hours. Next, bacteria were passed into 25 mL of LB medium (H_2O) containing KAN (50 mg/mL) for overnight growth at 30 ^{o}C. After incubation, the cells were transferred to sterile falcon tubes and centrifuged at low force (4500 g, 10 min). The supernatant was removed and the cell pellet was suspended in a fresh TB medium containing 80% of D_2O and KAN. The medium was incubated at 30 ^{o}C and slow agitation (220 rpm) until optical density reached OD_{600} = 5-6. In the next step, the induction of protein expression was initiated by adding 0.2 mM of IPTG. During the optimization, the sample was collected every two hours and analyzed on the SDS-PAGE (Bio-Rad, Mini-PROTEAN, USA) to track the protein expression level. Satisfying results were reached after 20 hours of overexpression at 18 ^{o}C. The cells were harvested by centrifugation (7500 g at 4 ^{o}C, 30 min) and lysed by sonication (25% amplitude, 5 min in periodic 3 s pulse, 2 break). Purification of the lysate was performed in two steps. First, ion exchange chromatography with HiTrap Q column (GE, Healthcare Life Sciences, US) was used (the flow-through fraction was collected). Collected fractions were then dialyzed in a 20 mM ammonium bicarbonate buffer (pH 7.8) and lyophilized. In the second purification step, the protein was diluted in ammonium bicarbonate buffer and purified by SEC chromatography with Superdex 75 10/300 GL column (3.2/30, Cyvita, Sigma Aldrich, USA). All steps were monitored with SDS-PAGE analysis using Mini-PROTEAN electrophoretic system.

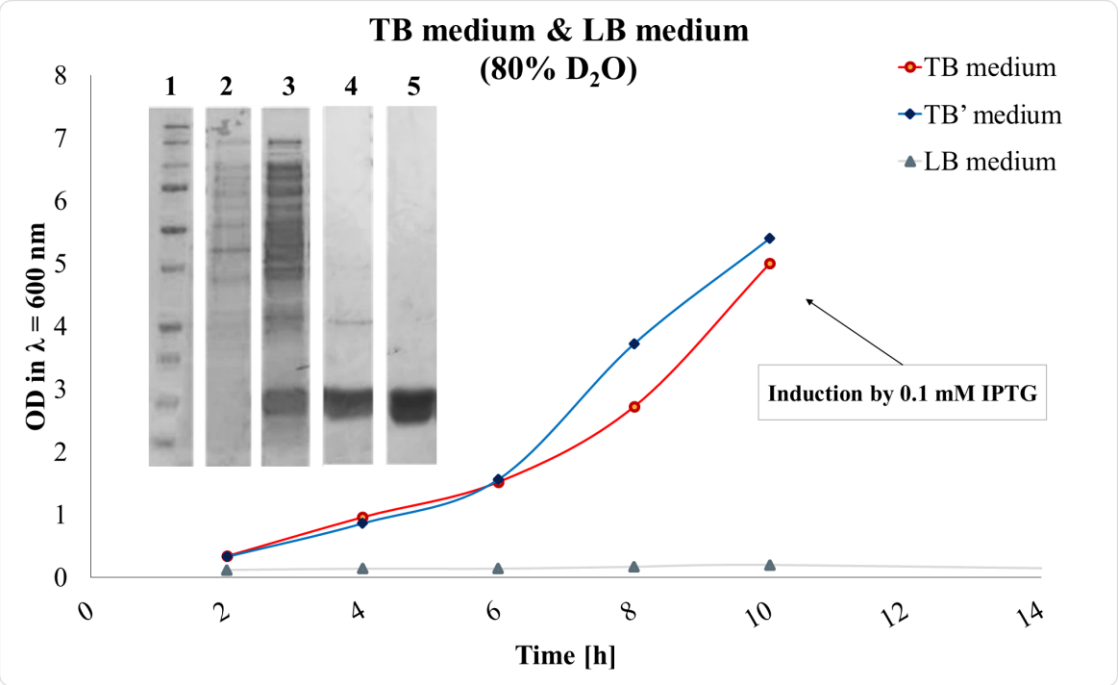

Figure 39. Summary of deuterated HCC protein expression procedure. OD of bacteria growth in LB and TB D_2O media. SDS-PAGE analysis legend: 1) Marker 2) Fraction before induction 3) Fraction after induction 4) Fraction after IEX chromatography 5) Pure protein after SEC chromatography.

4.4. Calculation of SAS parameters for proteins

To study protein complexes using the neutron scattering methods, it is recommended first to perform a calculation to estimate the optimal conditions for the contrast match SANS experiment. The biomolecular neutron scattering length density calculator (ISIS Biology group, www.psldc.isis.rl.ac.uk/Psldc) was used to determine the "match points" of HSA and HCC (D-HCC) in D_2O/H_2O buffer condition. This calculator uses information about the protein sequence, concentration, molecular weight (Mw), and estimated volume intensity (I_0) of the biomolecule. The contrast match point for 70% deuterated HCC is near 100 % of D_2O buffer solution. For HSA and Aβ peptides the contrast match was estimated around 42%. The calculated dependence of contrast matching buffer (H_2O/D_2O) for HSA and 70% deuterated HCC proteins is presented in Figure 40 (details in appendix).

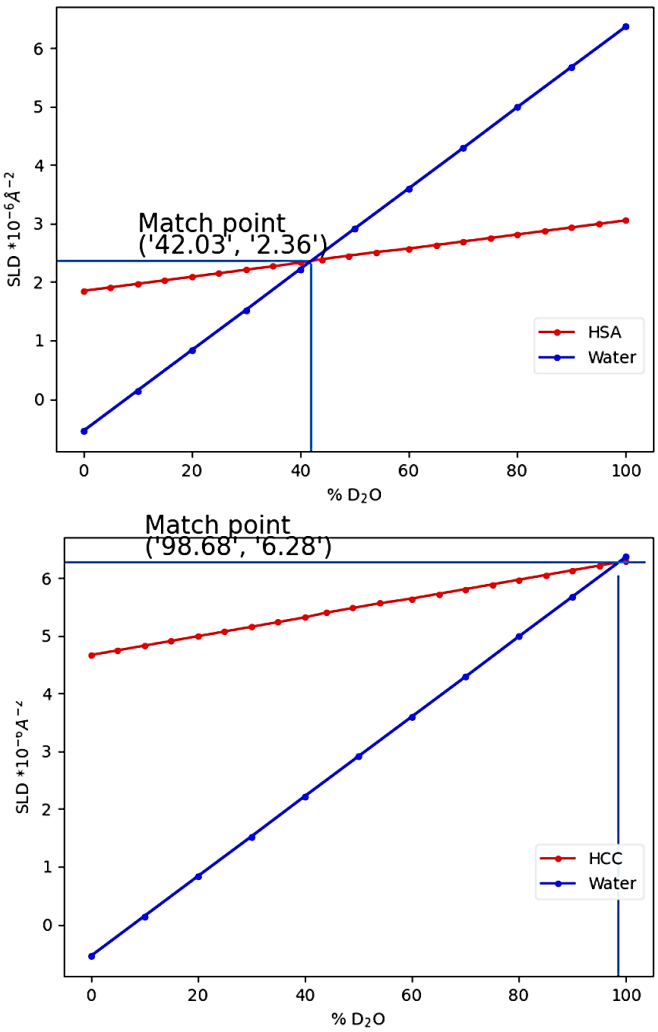

Figure 40. Plot showing a match points calculated for HSA (top) and HCC (bottom) in function of D_2O concentration.

4.5. SAXS data collection and processing

Small angle X-ray scattering measurements were performed using Xeuss 2.0 SAXS/WAXS system (Figure 41) available at the SAXS Laboratory (Department of Biomedical Physics, Faculty of Physics, Adam Mickiewicz University, Poznań, Poland). The low noise flow cell did not have a cooling system, so the experiments were performed at room temperature (20 °C). The volume of each sample was approximately 100 µL where the 50 µL is required to fill the flow cell. Depending on the concentration of the sample and the size of the studied molecule, measurement time could extend up to 20 cycles of 20 min (6 h). The buffer was measured before and after each sample measurement for later background subtraction.

In case of too high concentration the distance between the biomolecules decreases their intra-particle distances. These intra-particle interactions impact the scattering curve in the Guinier region and decrease the real R_G. However, the high concentrations lead to stronger signal with better statistical ratio to noise. To avoid artifacts in measured data the experiments were performed in several concentrations of a sample. All collected data were processed and merged with Primus (ATSAS[112]).

Figure 41. SAXS system (Xeuss 2.0) located at the Department of Biomedical Physics. 1) Vacuum tube 2), the experimental chamber with flow cell, 3) camera screen overlooking the measurement cell 4) control panel 5) Pilatus 1M detector (Dectris Ltd., Baden-Dättwil, Switzerland) 6) safety X-ray on/off signaling.

HSA characterization by SAXS

The HSA sample was purified by SEC (Superdex 200 Increase 10/300 GL, Cyvita, Sigma Aldrich, USA) to avoid dimers. Purified sample was checked on a dynamic light scattering (DLS) apparatus (Litesizer 500, Anton Paar GmbH, Austria). Then samples were measured in a series of concentrations of 1.9, 6.2, and 9.8 mg/mL in Tris 20mM NaCl 100mM buffer pH 7.5. The SAXS profiles obtained for 1.9 and 6.3 mg/mL concentrations were merged (at 160 data points) to avoid introducing intramolecular interaction artifacts to data (observed at the highest concentration – 9.8 mg/mL).

SAXS measurements of HSA-HCC V57G complex

HCC V57G protein was delivered by our collaborator Professor Aneta Szymańska (Gdańsk University, Gdańsk, Poland). Both proteins HSA and HCC V57G mutant were dissolved in Tris- HCl 50 µM buffer pH 7.5. SAXS data were collected for HSA at concentration 6 mg/mL and HCC at concentration 5.6 mg/mL. The samples of complexes were prepared in three molar concentrations: 200 µM, 100 µM and 50 µM in 1:1 ratio. All samples were measured in time of 3.5 h. Sample at concentration of 50 µM (HSA-HCC complex) was measured in time of 6 h. It was possible to merge SAXS profiles of measured HSA-HCC complex at 50 µM (up to $q < 0.2$) and 100 µM ($q > 0.2$).

SAXS measurements of HSA in complex with Aβ peptides 1-42, 1-26, 3-28

The SAXS samples were prepared at a concentration of 50 µM for the complex in a 1:1 ratio. HSA was dissolved in a Tris 50mM 50 NaCl pH 7 buffer at 4 °C. The Aβ peptides previously treated by HFIP (chapter 3.2), were portioned in glass vials. HSA solution was added to the glass vials containing peptides and dissolved by gentle stirring on ice. The samples were centrifuged in low-protein binding tubes at low speed for 5 min. Next samples were analyzed with the DLS apparatus (Litesizer 500, Anton Paar GmbH, Austria). Then, the prepared sample was injected into a SAXS instrument capillary. All SAXS measurements were made at room temperature (~20 ^{o}C) with a measuring time of 6 h.

SANS measurements of HCC, HSA, Aβ complexes

The initial characterization of samples and standardization of the experimental conditions was done by SANS method. Measurements have been performed on a small-angle neutron scattering (SANS) instrument YuMo located at the IBR-2 fast neutron pulse reactor in Join Institute for Nuclear Research (JINR, Dubna, Russian Federation)[147].The samples of selected Aβ peptides (Aβ 1-16, Aβ 3-28, Aβ 1-42), HSA, HCC and complexes were prepared at concentration in molar ratio 1:1 HSA-Aβ and 1:3 HSA-Aβ. Samples were suspended in 20 mM phosphate D_2O (99.9% D) pH 7.5 buffer. The standard sample exposition time was 2 h 30 minutes.

SANS measurement of D-HCC and Aβ fibrils

The SANS measurements were performed on the D22 beamline at the Institute Laue-Langevin (ILL, Grenoble, France) using granted "in-house" beam time. Two types of SANS experiments were conducted: the static measurements of Aβ peptides in presence of HCC and D-HCC, and the kinetics experiment. In the experiment's setup, the cuvettes containing samples were placed in a tumbling rack to avoid Aβ fibrils sedimentation through the measurement (Figure 42).

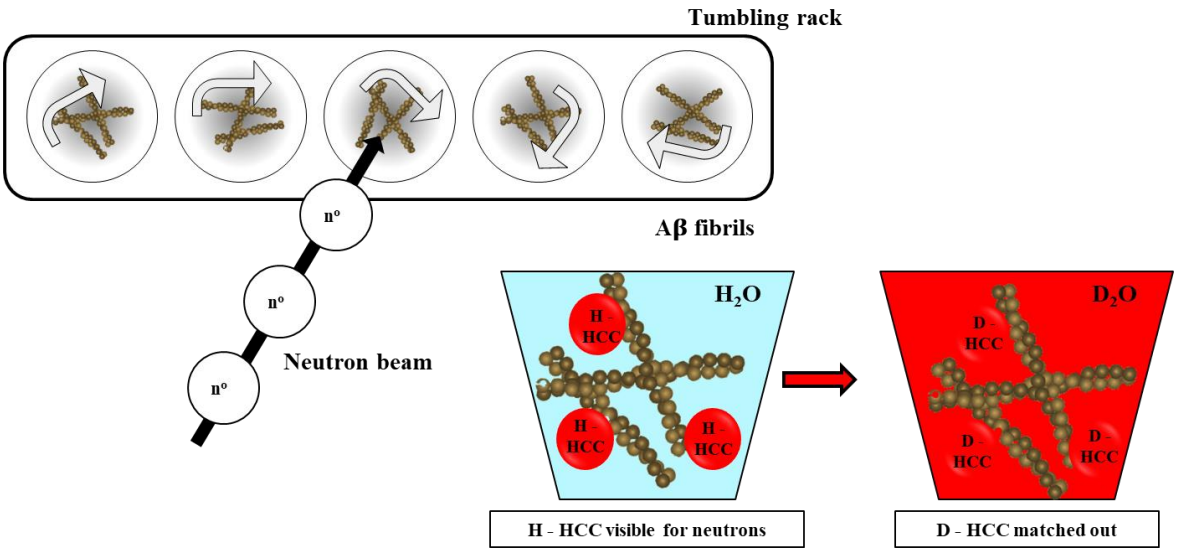

Figure 42. Schematic representation of the SANS experimental setup. The tumbling rack was used to prevent peptide sedimentation. Deuterated HCC was matched out which makes the possibility to observe only SANS profiles of Aβ fibrils.

During fibrils preparation, Aβ 3-28 and Aβ 1-42 were diluted in water at concentration 0.1 mg/mL, which was optimal for the controlled fibrillation process. The sample solutions were prepared in low protein binding sample tubes. The fibrillation process was performed by incubating the sample at 40 ^{o}C with agitation (up to 48 h). Then the fibril solutions were lyophilized. The lyophilized Aβ fibrils were suspended in the D_2O buffer up to an Aβ concentration around 1 mg/mL. SANS static experiment was performed for fibrils only and a mixture of fibrils and D-HCC or H-HCC in 100% D_2O (1.5 mg/mL). The samples were transferred to special cuvettes (300 µL each) and then placed in a tumbling rack and measured at room temperature (~20 ^{o}C). The kinetics measurements were conducted under elevated temperature (37 ^{o}C) to accelerate the possible reaction of Aβ peptide fibrils with HCC. The data were collected for Aβ fibrils only (Aβ 1-42 and Aβ 3-28) and fibrils in the presence of deuterated (invisible for neutrons) HCC at concentration 1mg/mL. The sample measurements were realized periodically: 1 sample every 20 min. The entire experiment lasted for over 9 hours. SANS profiles of samples were collected at a wavelength of 6 Å ± 10 % and two sample-detector distances: 17.6 m and 5.6 m, with a symmetric collimation of 40 mm by 55 mm cross section and a sample aperture of 13 mm diameter.

Modeling and visualization of Aβ fibrils

To compare the experimental SANS results with theoretical data, the experimentally solved (cryo-TEM) structure of Aβ 1-40 (PDB: 6SHS[36]) was chosen. To study the structure of the Aβ 3-28 fibril, homology modeling was performed by use of the Aβ 1-40 model as a template. The structure was optimized by molecular dynamics (MD) simulation with the UNRES web server (www.unres-server.chem.ug.edu.pl[129]).

Calculation of theoretical SAXS and SANS curves from full atom models

PEPSI-SAS

PEPSI-SANS (PEPSI stands for Polynomial Expansions of Protein Structures and Interactions) software[148] associated with the Pepsi-SAXS method for small-angle scattering allow to calculate theoretical curves based on the full atom models. For SANS, this fast and efficient approach allows to specify the deuteration level of the sample and the buffer and the exchange

rate of labile hydrogens. This program is also used for calculation of the scattering intensity in the absolute scale based on the protein concentration. The different set of neutron scattering curves, collected for HSA, HCC and models of possible HSA-HCC, complex were calculated.

SUBCOMP

SUPCOMB (ATSAS) program[149] enables the superposition of two spatial structures. This program was used to superimpose an experimentally solved model with the low-resolution model calculated from the scattering curve. The program analyzes the so-called normalized spatial distribution and performs the minimization that leads to specifying the best spatial alignment of the two models.

FoXSDock

FoXSDock[150] is a method using full atom structures and scattering SAXS profiles in order to predict the formation of biomolecular complexes. FoXSDock performs the docking using a PathDock[151] algorithm to generate many model structures. Those models are scored in reference to the SAXS data with the FoXS method (it is analogical to CRYSON method from ATSAS package). The FoXSDock output provides a set of possible models of the studied complex which are scored and ranked by an energy-based score and fitted to the SAXS profile.

Other programs used in the analysis of SAS data

To perform data processing and analysis a set of differed was used:

- To edit and process the data:
    - Primus (ATSAS[112]), Igor 8[152], and SASView[153]
- For low-resolution modeling of protein structure:
    - DAMMIN, DAMMINF[114], MONSA[113], and GASBOR[115] (ATSAS)
- For fitting functions to the scattering profiles:
    - Primus (ATSAS) and SASView
- To validate by χ^2 (value determines the discrepancy between the theoretical and experimental curve with the expected errors) the model against the SAS curves:
    - CRYSON[154] (ATSAS), and FoXS[150]
- Protein structures docking:
    - PatchDock[151]
- Protein structures docking supported by SAXS data:
    - FoXSDock web server (modbase.compbio.ucsf.edu/foxsdock)
- The visualization of the models:
    - PyMOL[155]

4.6. Transmission electron microscopy studies of HSA and Aβ fibrils

The samples after SANS measurements, were collected and imaged using a JEM-1400 transmission electron microscope (JEOL, Tokyo, Japan) operated at 120 kV (NanoBioMedical Centre, Adam Mickiewicz University, Poznań, Poland) with the assistance of dr Barbara Peplińska. The TEM imaging was performed after the SANS experiment to detect fibril content in samples (Aβ, Aβ+HSA). The samples were transferred to the mesh (Carbon type A, 300M CU PK/25m Ted Pella INC. Canada) and left to dry. Next, the 0.5% uranyl formate solution was applied for several seconds then rinsed three times with MiliQ water (10 µL). In the staining procedure, uranyl formate adhered to the edge of the adsorbed particles. In the results, the staining enhanced the contrast causing the electrons in the lens diaphragm to deflect and increase the sharpness of objects, i.e., the so-called negative staining.

4.7. Atomic force microscopy studies of selected Aβ peptides and HCC

The microstructure and topology of Aβ fibrils were also studied by AFM. All experiments were carried out with a Nanowizard IV atomic force microscope (JPK, Berlin, Germany) optimized for biological imaging. The prepared peptides were diluted in aqueous buffer (~0.2 mg/mL) and incubated overnight at 37 ^{o}C with agitation. Then, samples (1 µL) were diluted with MiliQ water (1:1000 ratio) and 10 µL of this solution was deposited on the prepared mica surface (mica V1 grade, Ted Pella INC. Canada) and left to dry.

To study the effect of HCC with Aβ fibrils of Aβ 1-42 or Aβ 3-28 peptides the mixtures of Aβ peptides with HCC in molar ratio 1:1 were prepared. Samples were incubated overnight at 37^{o}C. The solution was also diluted (1:1000) and deposited on the prepared mica surface and left until dry.

The samples were imaged by using the Tap150-G silicon soft tapping mode with an AFM probe (BudgetSensors Innovative Solutions Ltd. Bulgaria). The data analysis and visualization of the sample topology was carried out using Gwyddion 2.60.

4.8. Investigation of HSA-HCC complex with AUC

This work used the biophysics platform of the Grenoble Instruct-ERIC center (ISBG; UMS 3518 CNRS-CEA-UGA-EMBL) within the Grenoble Partnership for Structural Biology (PSB), supported by FRISBI (ANR-10-INBS-05-02) and GRAL, financed within the University Grenoble Alpes graduate school (Ecoles Universitaires de Recherche) CBH-EUR-GS (ANR-17-EURE-0003). The measurements were performed in collaboration with dr Aline Le Roy and dr Christine Ebel.

Sedimentation velocity experiments

Measurements were performed using an analytical ultracentrifuge XLA/XLI (Beckman Coulter Inc., USA) at 42000 rpm and at 20 °C, with a rotor Anti-50 (Beckman Coulter, Brea, USA), double-sector cells equipped with Sapphire windows (Nanolytics, Potsdam, Germany) and optical path lengths 12 and 1.5 mm. The sample was diluted in the PBS buffer and respectively the PBS buffer was used as reference in this experiment. The data collection was performed with measurement of absorbance at 280 nm wavelength and interference optics.

The data was processed with Redate software v1.0.1.[156] and analyzed with the SEDFIT[157], v16.36 and Gussi v1.4.2 software[158]. The buffer parameters (density, viscosity) were calculated with SEDNTERP software (http://www.jphilo.mailway.com/index.htm) and SEDFIT software, v16.3. The calculated density of the sample was 1.005 g/ml and viscosity 0.001018 Pa·s.

4.9. Investigation of HSA-Aβ complex with MS

Samples of HSA and Aβ 1-16, 3-28, 1-42 and mixtures of the complex were prepared in ammonium bicarbonate buffer at 4°C in 1:1 molar ratio and at the concentration of 50 µM. The 3 µL of sample was deposited on the measurement plate. Studies by electrospray ionization (ESI-MS) native mass spectrometry were performed with the assistance of Professor Paulina Czaplewska (Faculty of Biotechnology of UG, Gdańsk, Poland). Samples were measured in

three modes: reflectron positive, LINEAR – linear in small mass, LINEAR HM linear in a high mass. Data were collected using 2,5-dihydroxybenzoic acid (DHB) and sinapinic acid (SA, 3,5-dimethoxy-4-hydroxycinnamic acid) as a matrix for laser desorption.

4.10. NMR studies of HSA and ^{15}N HCC interactions

The sample was measured at the NanoBiomeical Centre (NCBM, UAM, Poznań, Poland) in collaboration with dr Igor Zhukov (NCBM, Poznań, Poland and IBB PAS, Warsaw, Poland) and dr Łukasz Popenda (NCBM, Poznań, Poland).

300 µM of the ^{15}N-labeled HCC V57G protein (derived by our collaborator Professor A. Szymańska, Faculty of Chemistry, UG, Gdańsk, Poland) were prepared by dissolving protein in 30 mM TRIS pH 7.0 buffer with 90%/10% H_2O/D_2O. The preparation NMR sample of the complex with HSA includes mixing the ^{15}N-labeled HCC V57G with HSA (99% purity, Sigma-Aldrich, USA) in a 1:1 molar ratio.

^{15}N relaxation data (R_1, R_2, and ^{1}H-^{15}N *NOE*) were conducted at 298.15 K (calibrated on methanol) in a magnetic field of 18.8 T utilizing sequences included in Biopack[159] (Agilent Inc., Palo Alto, USA) library and developed on previously published experiments[151]. The experimental R_1 data were obtained with 9 relaxation delays – 10, 90, 170, 290, 410, 550, 690, 850, and 1010 ms. Accordingly, the R_2 values were extracted from 8 experimental points – 10, 30, 50, 70, 90, 110, 130, and 170 ms. The steady-state ^{1}H-^{15}N NOE values were evaluated from two experiments – with and without ^{1}H saturation recorded with 6 s relaxation delay. All the collected relaxation NMR data were processed by NMRPipe[160] and analyzed with Sparky program[161]. The ^{15}N relaxation data (R_1, R_2, and ^{1}H-^{15}N *NOE*) were obtained for 97 residues (out of 111 signals expected), based on previously published NMR data.

4.11. Bioinformatics method used for modeling of 3D structures of studied biomolecules

To create a 3D model of Aβ 3-28 the cryo-TEM model (PDB: 6SHS[36]) of Aβ 1-40 was selected. The sequence was adjusted by the homology modeling approach. The initial structure of Aβ 3-28 was optimized with MD methods implemented by UNRES[129] MD method available under a web server. The distinct stages of the Aβ 3-28 structure modelling (pre- and post-optimization) are attached in the appendix.

In the study of the interaction of monomeric peptides with HCC (PDB: 6RPV[65]), the docking procedure was performed by Cabs Dock[162], a web server that allows to dock flexible peptides provided as a primary sequence input to the protein molecule. CabsDock generates a set of the most accurate models according to the energy function and clustering procedure.

To study HSA-Aβ complex, the rigid body molecular docking approach PathDock[151] was used. In the docking simulation (PDB: 6YG9[85]), monomeric structure of HSA was chosen and the different forms of Aβ were docked: monomer (PDB: 6SZF[163]), tetramer (PDB: 6RHY[164]), and the monomeric form with β-sheet conformation (PDB: 6RHY).

5. Results

Three Aβ peptides representing different, specific properties were selected for the study as model molecules. The Aβ 1-16 is the shortest peptide and less hydrophobic than longer variants. Even though the Aβ containing an aggregation core in the sequence do not exhibit a fibril formation, oligomers. The Aβ 3-28 peptide aggregates into fibrils but, slightly less aggregative than Aβ 1-4 and makes it possible to perform experiments at higher concentration. Aβ 3-28 is much more soluble than Aβ 1-42 peptide. Aβ 1-42 is the most pathological variant among the Aβ detected in the amyloid plaques.

5.1. Mass spectroscopy study of HSA with Aβ peptides

Native MS uses an alternative ionization (which has no negative influence on non-covalent quaternary structures) that allows the study of protein complexes and oligomers. The native MS, requires a higher concentration than denaturing MS. The aim of native MS experiments was to determine the quality of the sample as well as test the effectiveness of the protocol used for peptide disaggregation. By performing those measurements, it was possible to determine the degree of Aβ peptide oligomerization and interactions between HSA and Aβ peptides. The samples were prepared by dissolving the protein or peptide at the highest possible concentration. The concentration of Aβ peptides without precipitation was 1 mg/mL. The dissolving peptides were followed by centrifugation (at 4°C). A sample of the HSA-Aβ complex was prepared in 1:1 molar ratio at concentration of 100 μM. The prepared samples were immediately used for MS measurements.

Obtained mass spectra of Aβ peptide samples confirmed the method of disaggregation with HFIP effectively breaks the Aβ oligomers into monomers. However, analysis of the obtained MS spectra indicated that the oligomerization process of Aβ peptides started immediately and spontaneously. The MS data obtained for the initial state of the Aβ peptide samples show a mixture of oligomers (Figure 43). The MS analysis of Aβ peptides showed that peptides are prone for quick formation of oligomers, although it is not able to form fibrils. However, almost

99% of the signal for the Aβ 1-16 and Aβ 3-28 (main peak) in the MS spectrum comes from the monomer. Unfortunately, the sample of Aβ 1-42 could not be dissolved at the required concentration for the native MS method due to the precipitation.

Aβ 1-16

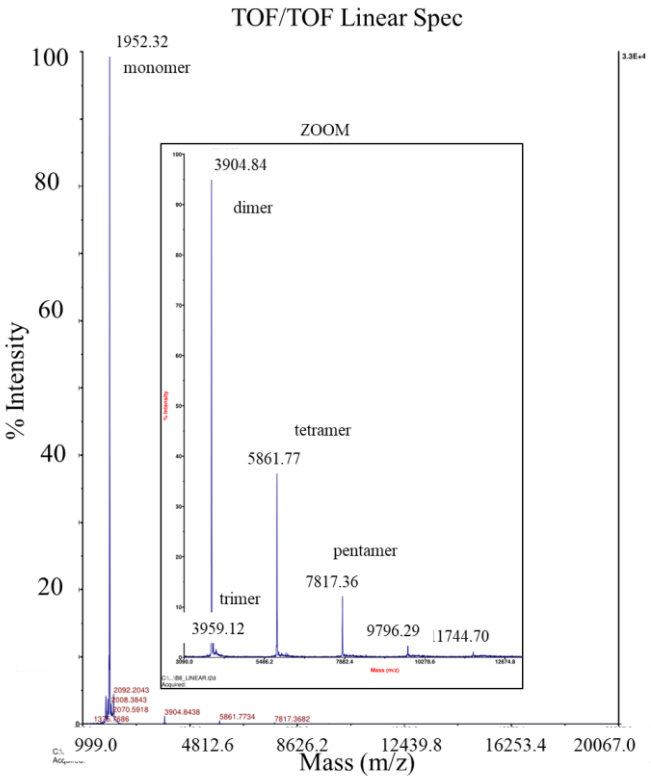

Aβ 3-28

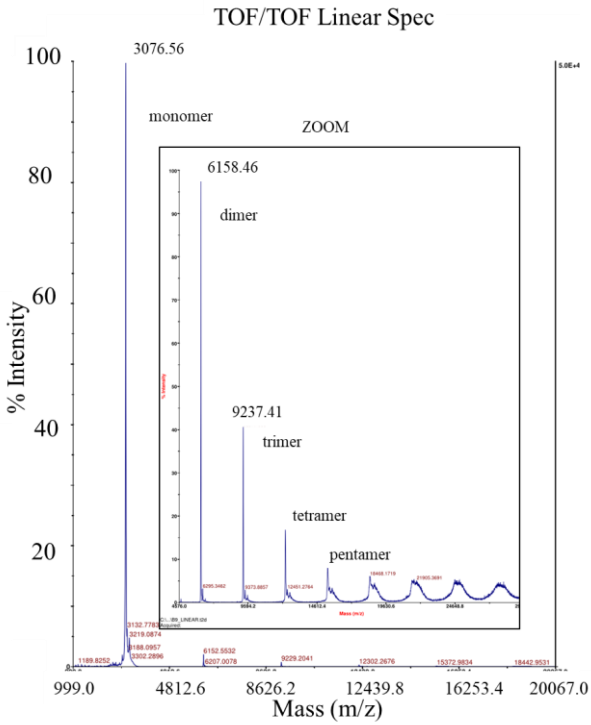

Figure 43. The MS spectra for Aβ peptides with the mass signals from the oligomers marked in the zoomed islets.

The native MS method allows also to test whether HSA can bind the monomer of the Aβ peptide. In the MS spectra obtained for samples of HSA-peptide mixtures (Table 3, Figure 44), the main peak is shifted by the mass of the Aβ peptide monomer. However, it should be noted that for the measurements of HSA itself the mass of the protein was slightly overestimated (Figure 44, Table 3). In HSA MS spectrum, the peaks of 1/2 and 3/2 HSA molecular weight are also present (ionization charge). It has been reported previously that HSA can bind monomers of Aβ 1-40 and Aβ 1-42[87]. HSA possesses the ability to bind and transport fatty acids[86]. These results combined with the general hydrophobic nature of Aβ peptides indicate similar mechanisms of interactions, meaning that the fatty acid binding sites may be responsible for the binding of peptides[86].

The MS analysis of samples containing a mixture of HSA and Aβ reveals a second higher mass peak (HSA Aβ 1-16: 71 337 Da, HSA Aβ 3-28: 69 886 Da). The shape of this peak shows a signal blur in the direction of higher masses due to the complexing HSA and Aβ peptides. This outcome could indicate a possibility that HSA can bind oligomers of Aβ (Figure 44). As HCC sample was not available, it was not possible to perform similar tests for HCC.

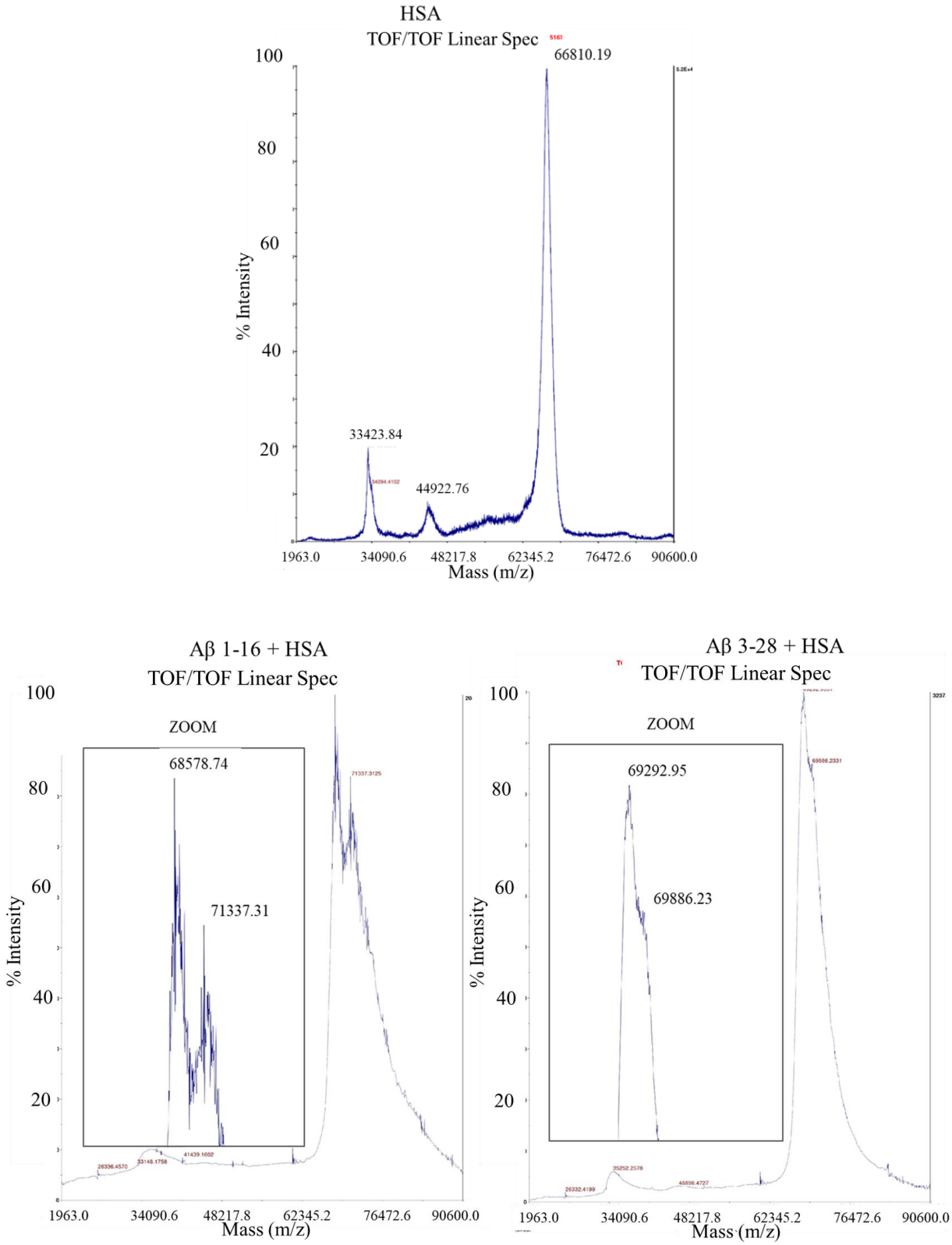

Figure 44. MS spectra show signals corresponding to mass of HSA (top) and its possible complex with Aβ peptides (bottom).

Table 3. Summary of MS measurements of the studied samples.

Sample	*Measured molecular weight [Da]*	*The molecular weight of the complex minus molecular weight of HSA [Da]*
HSA	66 810 / 66 348*	-
Aβ 1-16	1 952*	-
HSA-Aβ 1-16	68 455	2107
Aβ 3-28	3 076*	-
HSA-Aβ 3-28	69 292	2944

**theoretical mass computed from sequence*

5.2. TEM imaging of Aβ 1-42 peptide samples in presence of HSA after SANS experiments

TEM was used to characterize the morphology of possible Aβ1-42 fibrils with and without HSA protein after the SANS experiment (JINR, Dubna, Russian Federation). The goal of this short experiment was qualitative analysis of samples after SANS experiments. The samples recovered from SANS experiment were placed on the TEM carbon grid and stained to improve imaging contrast. Due to high precipitation, the sample was exceedingly difficult to study.

Nonetheless, TEM images of Aβ 1-42 fibrils were taken and the cross-section of the fibrils was estimated to be around 43 Å (Figure 45). The determined size of the fibril corresponds to the size of fibril cross-section registered with AFM imaging, as well as the size of cross-sections of the fibril structures deposited in the PDB database[36].

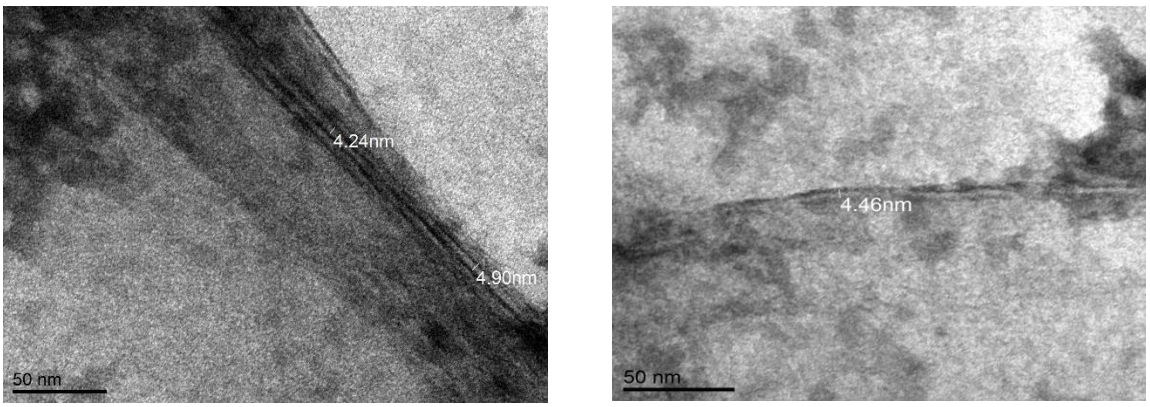

Figure 45. The TEM images of Aβ1-42 sample.

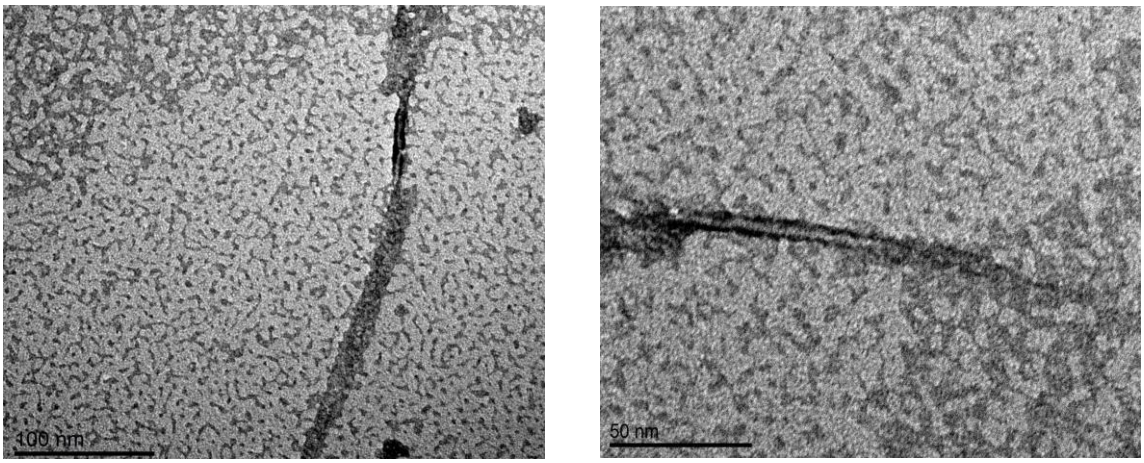

Figure 46. The TEM images of Aβ1-42 sample with HSA.

The images registered for a mixture of Aβ 1-42 and HSA showed shorter fibrils with disrupted ends (Figure 46). However, not many pictures of disrupted Aβ fibrils were collected. The image of disrupted fibrils can be artifacts caused by drying and staining procedure notwithstanding, the possibility of binding Aβ peptides by HSA was already confirmed by MS experiments (chapter: 4.1). The peptides in the sample with HSA fibrils were still present but they were much shorter. These studies indicate that HSA can slow down the aggregation of fibrils.

The inhibition of Aβ peptide aggregation by HSA protein appeared to be very difficult to follow by available experimental methods. Because of that, further studies of this work were more focused on the role of HCC in peptide aggregation inhibition.

5.3. Analytical ultracentrifugation measurements of possible HSA - HCC complex

To elucidate the formation of HSA-HCC complex, the analytical ultracentrifugation (AUC) method was used. The sedimentation velocity experiment by the sedimentation equilibrium method permits precise and selective observation of the sedimentation process in real time. AUC experiment determines the equilibrium concentration gradients at the sample at low centrifugal field. This method can characterize the molecular weight of studied macromolecules, sample monodispersity, or detect the presence of macromolecular complex.

The AUC instrument can measure several samples simultaneously. The samples of HSA and HCC were prepared at two concentrations (0.2 mM and 0.02 mM) and HSA-HCC mixture at three different molar ratios (1:2, 1:10, 1:20). The proportion of HSA and HCC protein in the sample was chosen based on the molecular weight difference of HSA and HCC (66.6 to 13.3 kDa). Analyzed data containing information about sample parameters have been presented in Table 4. The mass distribution of HSA and HCC is shown in Figure 47.

Table 4. AUC experimental data with maxima of detected peaks.

	Peak at 1.42 +/- 0.05 S			**Peak at 4 +/- 0.07 S**			**Peak at 6.2 +/- 0.2 S**		
	signal	M_w of NIS [kDa]	% of signal	signal	M_w of NIS [kDa]	% of signal	signal	M_w of NIS [kDa]	% of signal
HSA 0.2 mM Interference						92			7
				3.69	82.7		5.96	80.9	
HSA 0.2 mM Absorbance						92			7
				3.70	82.6		6.00	135.7	
HSA 0.02 mM Interference						83			10
				4.02	59.7		6.11	122.7	
HSA 0.02 mM Absorbance						88			10
				4.07	64.6		6.33	122.4	
HCC 0.2 mM Interference			98						1
	1.43	11.7					5.91		
HCC 0.2 mM Absorbance			99						
	1.43	11.8							
HCC 0.02 mM Interference			100						
	1.42	11.6							
HCC 0.02 mM Absorbance			97						
	1.43	13.6							
HSA 0.01mM : HCC 0.2 mM Interference			77			20			3
	1.41	12.6		3.94	58.8		6.24	139.3	
HSA 0.01mM : HCC 0.2 mM Absorbance			82			16			1
	1.44	12.5		3.98	62.9		6.28	144.0	
HSA 0.01mM : HCC 0.1 mM Interference			63			33			4
	1.39	13.2		3.96	66.8		6.21	131.4	
HSA 0.01mM : HCC 0.1 mM Absorbance			71			26			3
	1.43	11.4		4.03	57.7		6.36	129.3	
HSA 0.01mM : HCC 0.02 mM Interference			24			66			6
	1.40	12.3		4.00	60.1		5.91	127.0	
HSA 0.01mM : HCC 0.02 mM Absorbance			30			63			7
	1.42	13.9		4.06	60.2		6.27	125.9	

*NIS for non-interacting species

* S correspond to the sedimentation coefficient

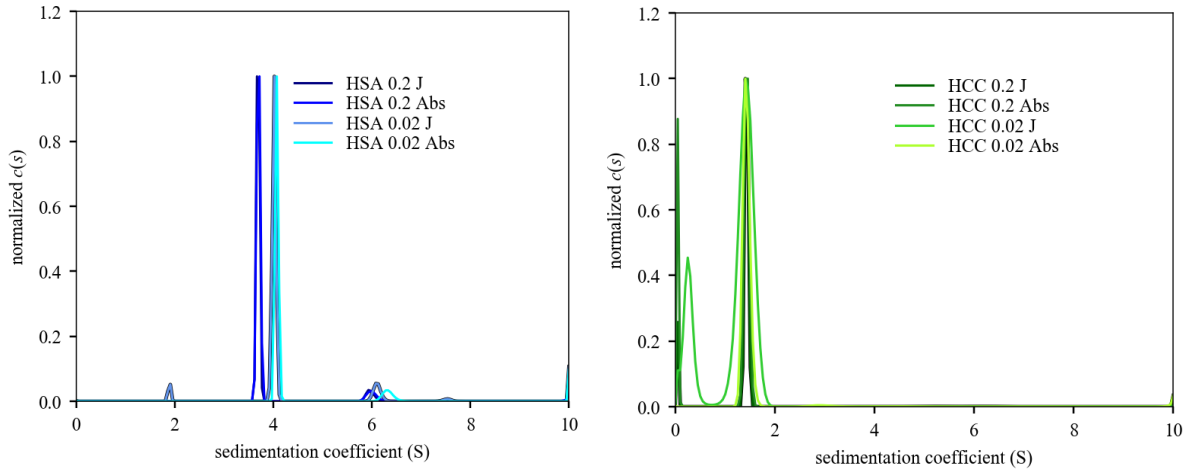

Figure 47. Comparison of sedimentation coefficient from interface and absorbance at two sample concentrations. On the left: HSA, on the right: HCC. (Abs – absorbance, J - interference)

HCC protein gives the main peak (98 % of all signal) at the maximum of 1.43 and 1.48 S, and the estimated from the experiment mass of HCC is 12.6 +/- 1 kDa, which corresponds to the real mass of HCC protein 13.5 kDa.

At higher concentration (0.2 mM) HSA protein signal locates the main peak (92% of signal) at 3.7 S. The lower concentration of HSA protein (0.02 mM) gives the main peak (85% of signal) at 4.05 +/- 0.03 S. Due to high sample concentration of 13.3 mg/mL, the main HSA peak shifted towards a smaller S coefficient. The analysis of the 0.02 mM HSA sample permits the calculation of molecular weight of HSA around 62 +/- 2.5 kDa (theoretical M_w=66.5 kDa). Besides the monomeric HSA signal, the signal of the dimeric form is observed at 6.15 +/- 0.15 S (7-10% of the signal), and it corresponds to the calculated molecular mass 122.5 kDa (theoretical molecular mass of a dimer of HSA is equal 133 kDa).

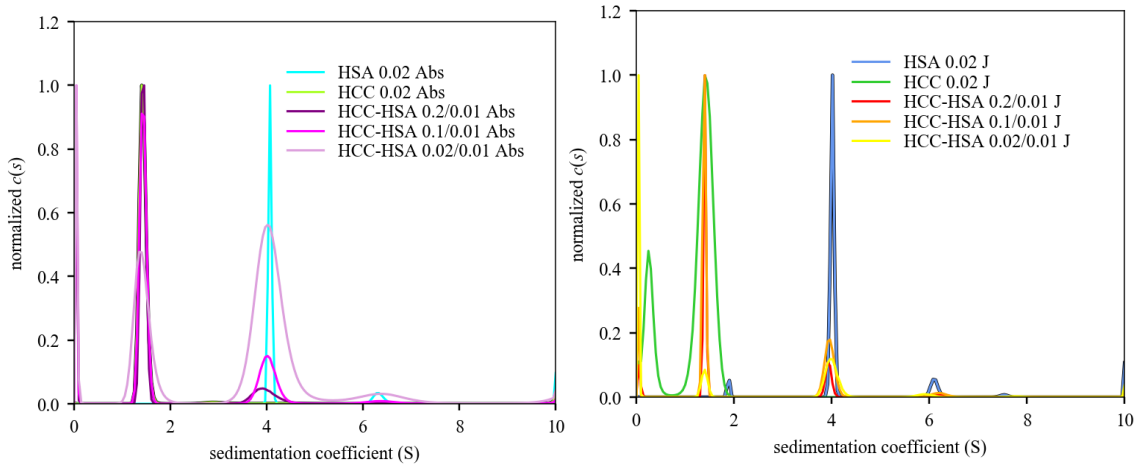

Figure 48. Comparison of the sedimentation coefficient from interface and absorbance in AUC experiment. Two different sample concentrations of HSA-HCC complexes were presented. On the left: absorbance, on the right: interference. (Abs – absorbance, J - interference).

For samples containing a mixture of HCC and HSA, three peaks of sedimentation coefficient distribution are detected. The maxima of each peak are at the same value of the sedimentation scale as in the separate measurements of both proteins (Figure 48).

Peak at 1.42 +/- 0.05 S corresponds to the molecular mass 12.7 +/- 1.3 kDa. The second peak located at 4 +/- 0.6S can be assigned to the molecular mass 62.3 +/- 4.5 kDa.

In addition, the peak from HSA dimer was observed at 6.15 +/- 0.3S and the molecular weight was calculated 135 +/- 9 kDa. In all samples, impurities were observed. There is no peak corresponding to the complex, and the peak maxima of each protein corresponds to the same place at the sedimentation scale.

5.4. Results of small angle X-ray and neutron scattering studies

Small angle X-ray and neutron scattering are the common and helpful techniques for the analysis of macromolecules in solution. The main principle of the small angle scattering experiment is the determination of the scattering intensity of a molecule as a function of the scattering vector, i.e., the so-called scattering profile. The data obtained using these methods allows for a wide study of the parameters of the particles as their size, shape or flexibility, but also constitutes an excellent reference for the modeling of high-resolution structures.

The SANS and SAXS experiment require a high concentration (typically 1-10 mg/mL) of biological samples thus increasing the amounts of needed substance. In the case of deuterated protein, the cost of the sample can rise significantly. It was possible to perform a series of SAXS and SANS experiments thanks to the sample availability. The protocols for peptide synthesis and overexpression of proteins were adapted or developed and applied in this work.

The SAXS and SANS methods were used to characterize studied biomolecules and particularly to investigate the interaction between them. The Aβ peptides with HSA and HCC proteins were measured by SANS and SAXS methods. Moreover, the possible structure of HSA-HCC complex was proposed from the SAXS experiment. The studies of possible interactions of HSA and HCC were motivated by the fact that both proteins are highly concentrated in CSF, and can provoke inhibition of Aβ peptide aggregation. Thanks to the collected scattering data the structural and dynamic properties of studied systems were analyzed. The SANS with contrast variation technique was used to follow the kinetics of Aβ fibrils disaggregation process.

5.4.1. Small angle X-ray scattering

5.4.1.1. Characteristics of reference system – human serum albumin

HSA is a protein with a flexible conformation which under different environmental conditions can form dimers and trimers. Currently, in the open database of collected scattering profiles of biomolecules (https://www.sasbdb.org) there are 11 records of different quality SAS data collected for HSA. The data are acquired at different resolutions and the low-resolution model indicates the conformational flexibility of HSA structure. In the PDB database, we can also find over 120 structures of HSA with ligands solved by X-ray crystallography.

The SAXS measurements were performed to characterize HSA behavior in the chosen buffer. These own data were used as reference in all described later results of other experiments. To remove all oligomeric forms of HSA the sample preparation was done with an application of centrifugation or SEC chromatography. It was important not to introduce an additional SAXS signal from a higher oligomeric state and perform measurements on a highly monodisperse sample. The measurements were performed in few concentrations to reduce inter-particle interactions (concentration effect).

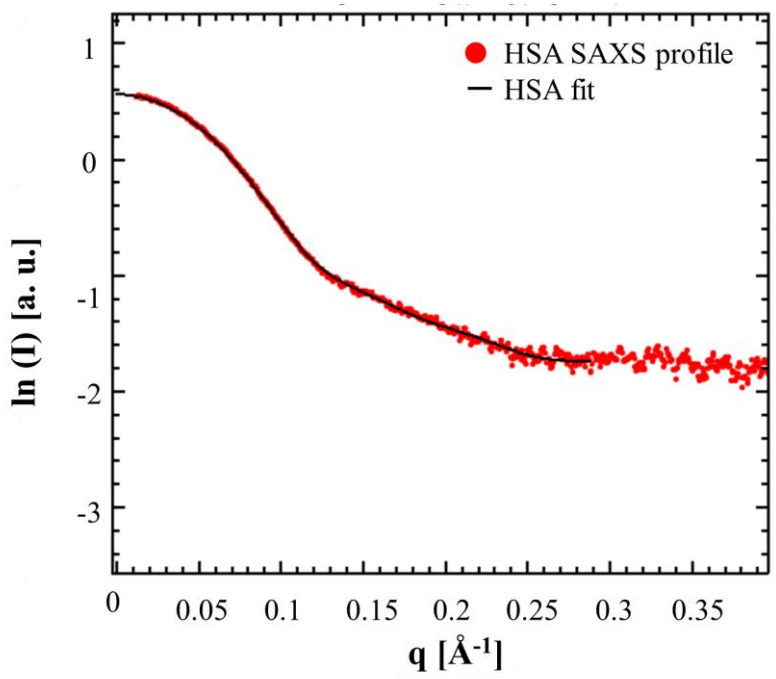

Figure 49. SAXS profile of HSA and function fit (GNOM - ATSAS package[112]).

The obtained SAXS data show a strong signal which was easy to analyze (Figure 49). The SAXS data obtained for HSA were processed and analyzed with the software included in the ATSAS package.

Guinier fit to HSA SAXS data resulted in the radius of gyration R_G=27.9 +/-0.3 Å. Similarly, calculation of the distance distribution function *P(r)* described HSA with R_G=27.7 +/- 1 Å (Figure 50, Table 5). The R_G from SASdb is about 28 Å for HSA. The same value can be calculated from structures of HSA solved with the X-ray diffraction technique. The scattering profile corresponds to the monomer HSA protein.

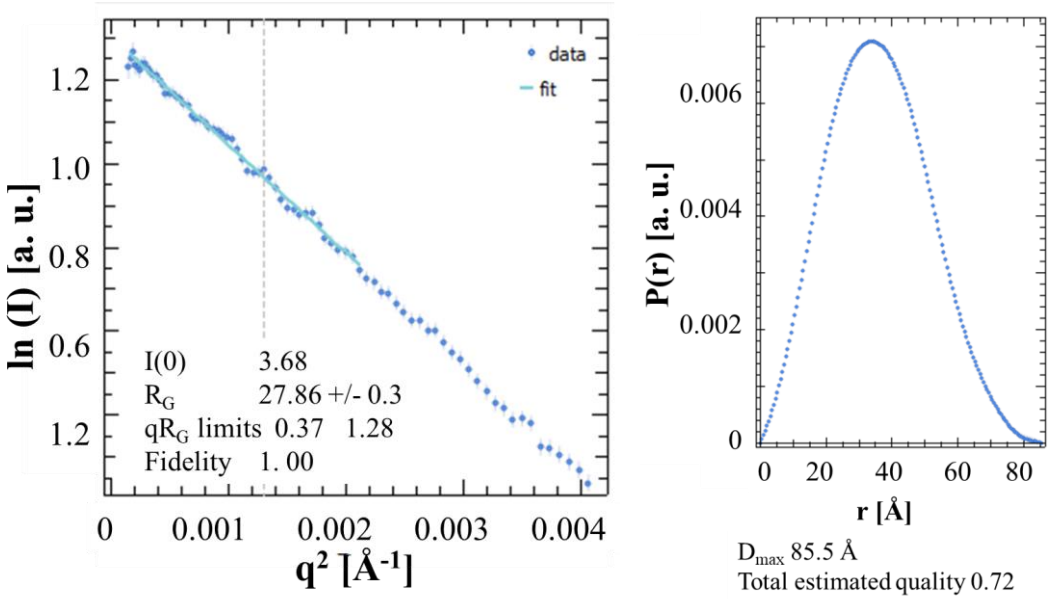

Figure 50. The Guinier function fit to HSA SAXS profile, on the right: P(r) plot.

P(r) function estimated by fitting to the SAXS data gave information about the shape of a molecule in the solution and D_{max}=85.5 Å. The SAXS data were used also for the determination of the low-resolution model of HSA by DAMMIN and GASRBOR programs. The GASBOR program calculates a low-resolution 3D model which also contains beads associated with the representation of buffer. In the presented model (Figure 51) the solution beads are colored

differently. In the model generated by GASBOR the little hollow with solution particles can be observed (Figure 51).

To validate the SAXS data collected for HSA protein the AMBIMETER method was used. The results of the AMBIMETER analysis showed that only one unique 3D shape exists for HSA SAXS profile.

The model structure of HSA (PDB: 2I30[165]) chosen as a reference was carefully checked and if necessary, the missing atoms and residues were reconstructed. The HSA crystal structure was used to score the experimental structure against SAXS data (χ^2 correlation test). Results from all calculations are set up in Table 5 and Figure 51. The 3D low-resolution models are also presented in Figure 51 as a comparison to the high-resolution structure.

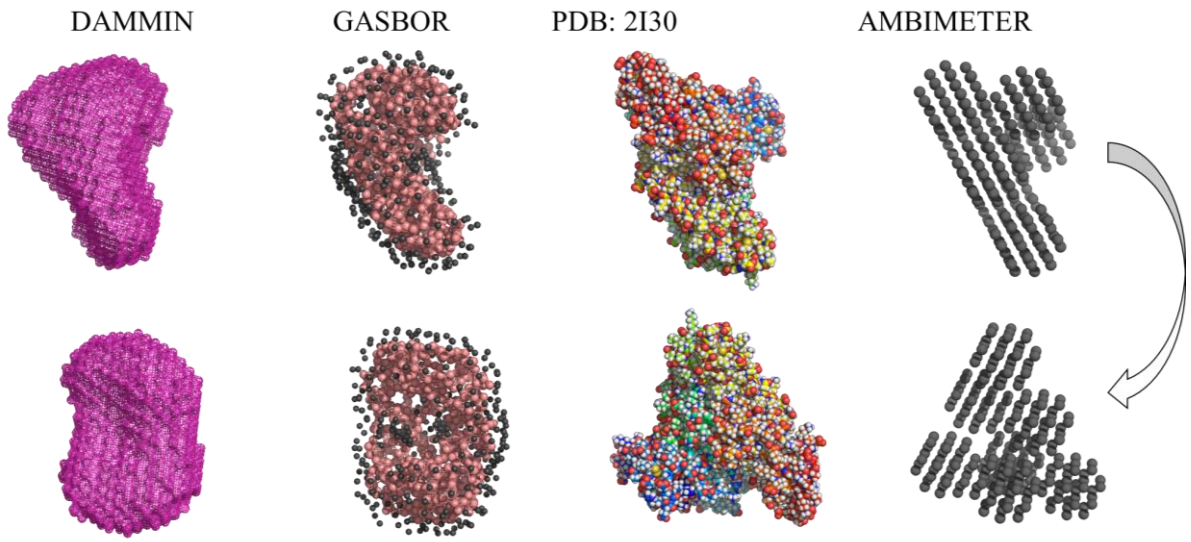

Figure 51. Presentation of atomic structure (PDB: 2I30) and low-resolution models calculated from SAXS data obtained for HSA using different programs.

Table 5. Structural parameters calculated for HSA models obtained using SAXS data.

SOFTWARE	R_G [Å]	χ^2	COMMENTS / INTERPRETATION
DAMMIN model (DAMMFIT - clustered)	28.2 +/- 0.5	0.74 (DAMMFIT)	SASRES computation: Ensemble Resolution = 30 +/- 2 Å
GASBOR model	28.4 +/- 0.5	0.71 (GASBOR) 0.96 (CRYSOL)	Number of waters molecules: 378 Total number of residues: 588
HSA PDB ID: 2I30	28.2 +/- 0.1	1.14	Fixed model of structure (SWISS-MODEL)
AMBIMETER „the best shape"	28.9 +/- 0.5	4.32	Number of compatible shape categories: 31 Ambiguity score: 1.491 3D reconstruction is potentially unique

HSA structure appears to be dynamic and displays high structural flexibility. Among all albumins, the dynamics of domains, DI and particularly DIII shows the most diversity due to the lowest sequence conservation and the highest dynamic flexibility[79]. On the contrary domain IIB shows the smallest flexibility. These interesting dynamics properties of HSA are possible to track by SAXS methods.

The alternative method used to calculate the structural parameters of studied molecules like proteins is DLS. Therefore, SAXS results were compared with the particle size distribution from DLS (Figure 52). The hydrodynamic radius R_H for HSA was 38.8 +/- 0.4 Å, which is 10 Å more than R_G. The R_H includes a hydration shell from the solution. The solvation layer around one protein to be distinct from bulk water out to ≈10 Å. The characteristic R_G/R_H value for a globular protein is ~0.775[166]. These values correspond very well to the actual structure of HSA in the solution.

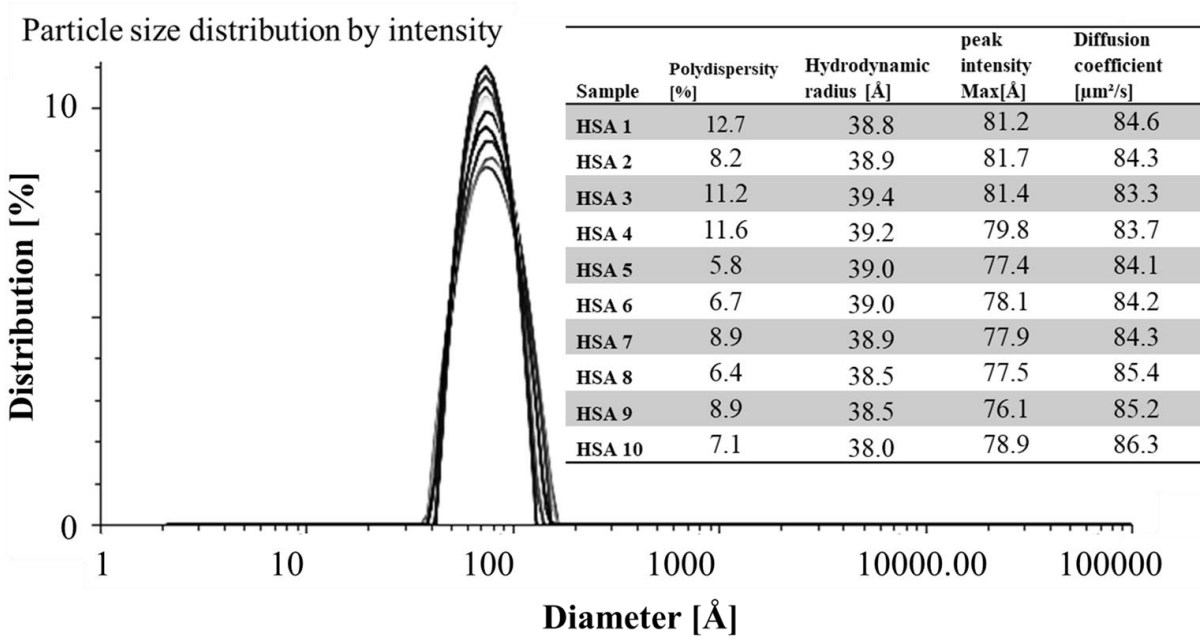

Sample	Polydispersity [%]	Hydrodynamic radius [Å]	peak intensity Max[Å]	Diffusion coefficient [µm²/s]
HSA 1	12.7	38.8	81.2	84.6
HSA 2	8.2	38.9	81.7	84.3
HSA 3	11.2	39.4	81.4	83.3
HSA 4	11.6	39.2	79.8	83.7
HSA 5	5.8	39.0	77.4	84.1
HSA 6	6.7	39.0	78.1	84.2
HSA 7	8.9	38.9	77.9	84.3
HSA 8	6.4	38.5	77.5	85.4
HSA 9	8.9	38.5	76.1	85.2
HSA 10	7.1	38.0	78.9	86.3

Figure 52. Particle size distribution for HSA sample calculated from DLS.

5.4.1.2. SAXS studies of HSA with selected Aβ peptides

The possible complex between HSA and selected Aβ peptides were studied by SAXS. After dissolving the lyophilized peptide with an ice-cold solution of HSA protein (to avoid aggregation), samples were centrifuged. However, the concentration after centrifugation slightly dropped due to precipitation of peptide aggregates into solution. The SAXS profiles were measured for HSA and its mixture with Aβ 1-16, Aβ 3-28, and Aβ 1-42 peptides. All measured scattering profiles are shown in Figure 53. The SAXS scattering profile obtained for the sample of HSA with Aβ 3-28 in Guinier region exhibits a high increase of scattering intensity indicating the presence of aggregates and sample polydispersity. However these data were presented for comparison with other complexes. For all collected data the R_G was calculated (Figure 54, Table 6). Analysis of data indicated that for the sample with aggregated HSA-Aβ 3-28 R_G value was overestimated.

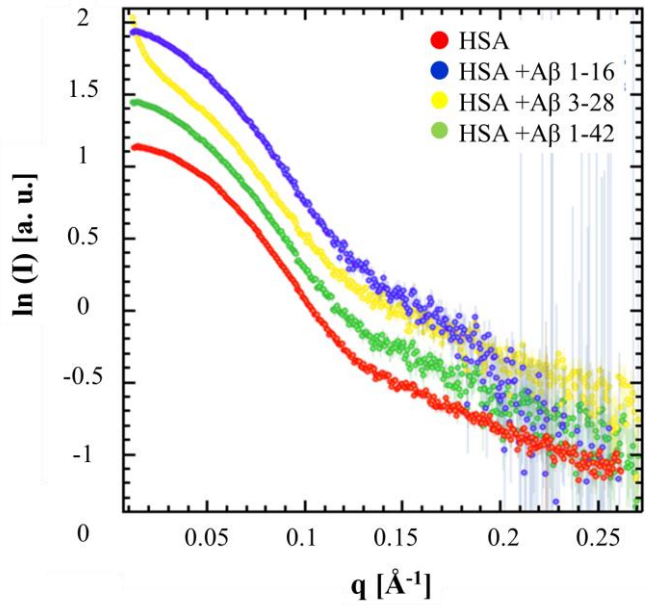

Figure 53. SAXS data collected for HSA and HSA with Aβ 1-16, Aβ 3-28 and Aβ 1-42 peptides.

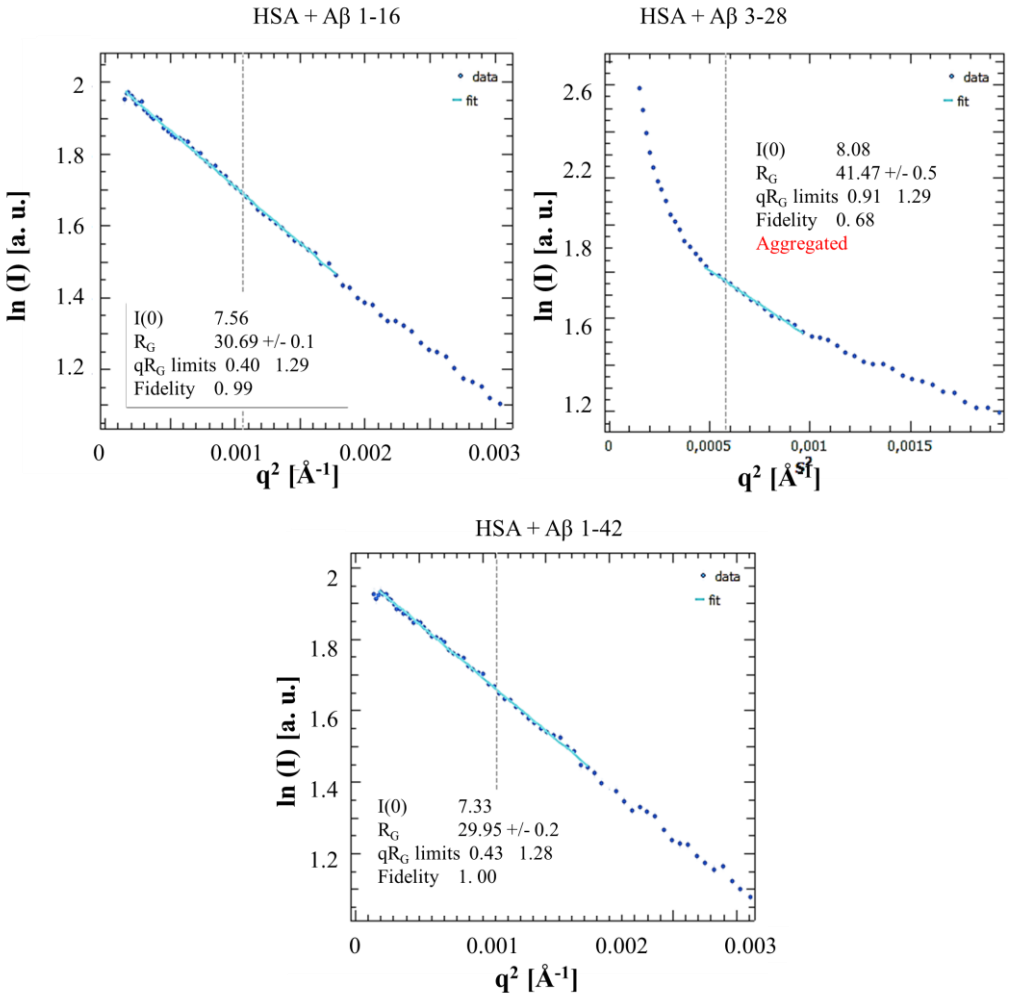

Figure 54. Guinier analysis of the SAXS data for HSA with Aβ peptides.

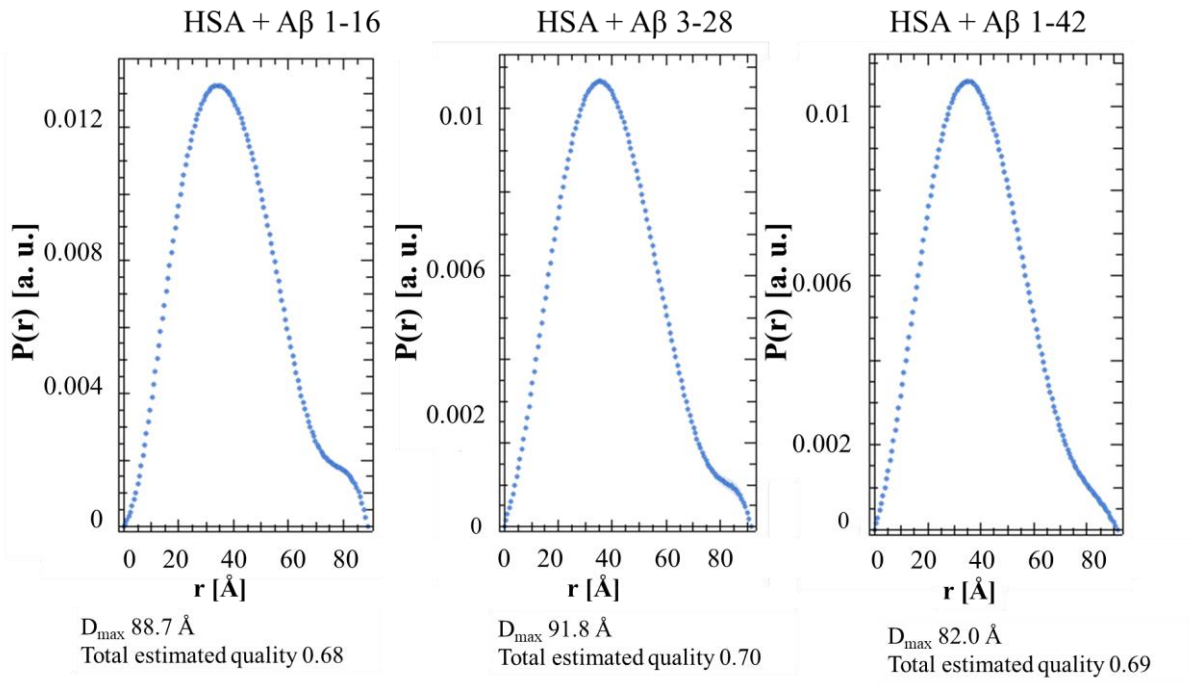

Figure 55. Fitting of P(r) function to SAXS data collected for HSA mixture with Aβ peptide.

The R_G for HSA mixture with Aβ 1-16 is 30.7 Å and around 1.9 Å bigger than R_G of HSA itself. This means that R_G can include some of the complex structures of HSA with Aβ peptides. However, the increase in the value of R_G is too big for introducing a peptide monomer to HSA structure only (M_w of HSA is more than 30 times bigger than M_w of monomeric peptide). This observation indicates that HSA may bind a few particles of Aβ peptides by hydrophobic interaction (like in the case of fatty acids) or it may bind a higher oligomeric form of Aβ (Figure 85). The size of the molecule in the sample with HSA and Aβ 1-42 mixture the R_G is 30.0 +/- 0.2 Å. This value is about 1.2 Å higher than for reference HSA (without peptide). Again, it could indicate that HSA can bind more than a single particle of Aβ peptide.

Table 6. Comparison of R_G calculated by Guinier function and P(r) using SAXS data collected for HSA and HSA with Aβ peptides.

SAMPLE	RADIUS OF GYRATION FROM GUINIER FIT [Å]	RADIUS OF GYRATION FROM P(R) [Å]
HSA	27.9 +/- 0.2	27.7 +/- 0.1
HSA-Aβ 1-16	30.7 +/- 0.1	30.1 +/- 0.1
HSA-Aβ 3-28	41.5 +/- 0.5	30.1 +/- 0.5
HSA-Aβ 1-42	30.0 +/- 0.2	28.4 +/- 0.2

The SAXS data collected for the systems of HSA with Aβ 1-16 and Aβ 1-42 peptides, were analyzed using *P(r)* function calculated in the *q* range from 0.0377 to 0.2575 $Å^{-1}$. For SAXS data of HSA-Aβ 3-28 the *P(r)* function was obtained in *q* range from 0.0298 to 0.25275 $Å^{-1}$ (to reduce aggregates impact in Guinier range). The *P(r)* function calculated for the SAXS data is presented in Figure 55. Due to the high polydispersity of the sample, the collected data does not represent the desired quality for reliable analysis and generation of low-resolution models.

5.4.1.3. SAXS studies of HSA-HCC (V57G) interactions

There is almost no available literature data about the details of the possible interaction between HSA and HCC, however those two proteins were detected in high concentration in CNS. In addition, they were independently described as Aβ peptides anti-aggregation factors. HCC is a protein whose structural core is held by hydrophobic interaction β-sheet (β1-5) and α-helix (α1). HCC exhibits conformational flexibility and sensitivity to external conditions like X-ray high flux which cause a conformational shift by domain swapping and dimerization to higher oligomers states and even fibrils[64]. Because of that phenomenon, the mutant of HCC V57G[65] was designed (exhibits a high monomeric conformational stability) and used for the SAXS experiment. The V57G mutant has a substitution of valine 57 by glycine in the hairpin loop L2

(responsible for domain swapping) between two β-sheets. This change of amino acid in V57G mutant stabilized a loop conformation.

The V57G HCC (Figure 56) was characterized by R_G=16.0 +/- 0.1 Å (Table 7) which corresponds to the crystal structure of HCC V57G monomer (PDB: 6RVP[65]).

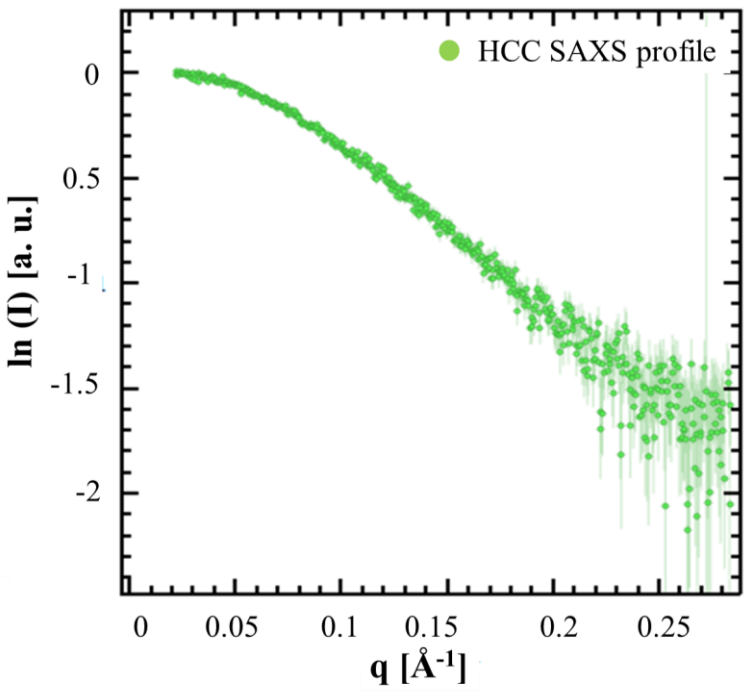

Figure 56. SAXS data collected for HCC V57G mutant (monomer).

To investigate the structure of possible complex structures between HSA and HCC proteins the scattering profile was measured. The samples containing a mixture of HSA-HCC were prepared at three different molar concentrations (50, 100, and 200 µM) in 1:1 molar ratio. The SAXS data collected for each sample are shown in Figure 57. The results of data analysis by Guinier and P(r) functions are presented in Figure 58 and Table 7. Comparison of experimental SAXS data for HSA alone and HSA-HCC complex are presented at a separate plot in Figure 57. These two measured profiles with a mixture of HCC-HSA and HSA are not overlapping indicating complex formation. For all collected data the 3D low-resolution models were generated by the DAMMIF method.

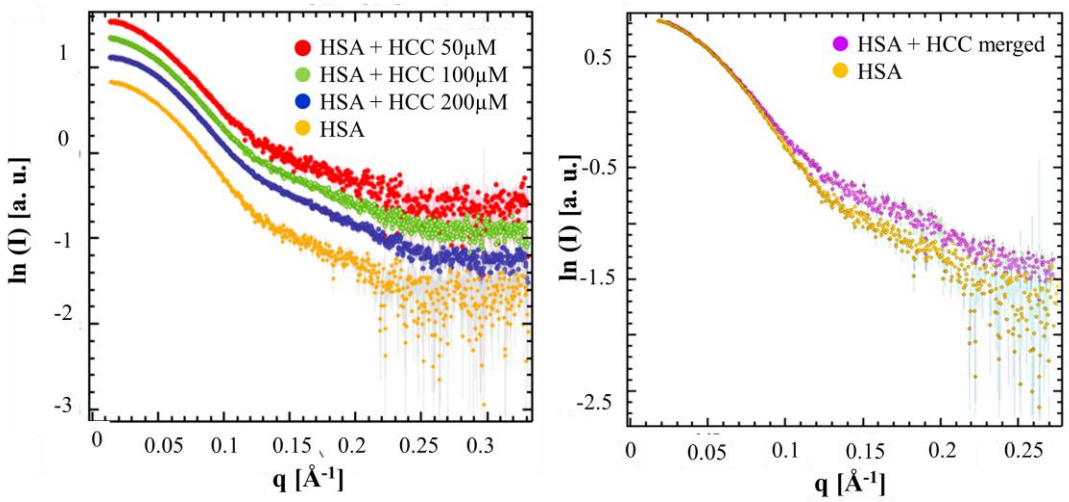

Figure 57. SAXS data collected for HSA-HCC samples. On the left: SAXS profile of HSA and HSA- HCC samples. On the right: comparison of SAXS data collected for HSA and HSA-HCC.

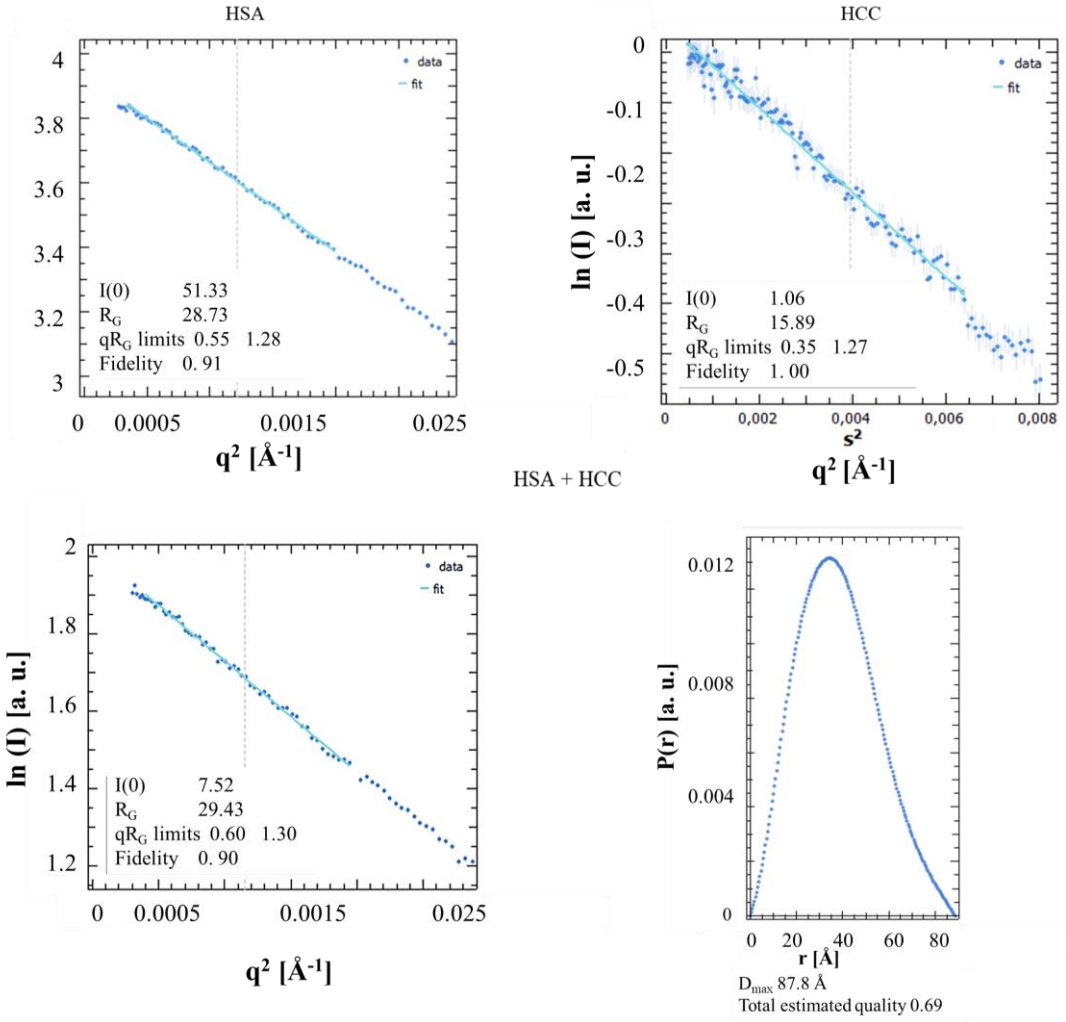

Figure 58. Guinier plots obtained for experimental SAXS profiles of HSA, HCC and HSA-HCC sample. P(r) function calculated for HSA-HCC sample.

The mixture of HSA and HCC (possible complex HSA-HCC) was characterized by a R_G 29.4+/- 0.1 Å. It is 0.7 Å more than in the case of the SAXS profile of HSA alone. Similar values were estimated by P(r) function (Table 7). Such small difference suggest, that possible complex is unstable and flexible or the HCC molecule can interact with HSA in several conformations.

Table 7. Guinier and P(r) analysis of SAXS data for HSA and HSA-HCC mixture.

SAMPLE	RADIUS OF GYRATION FROM GUINIER FIT [Å]	RADIUS OF GYRATION FROM P(R) [Å]
HSA	28.7 +/- 0.1	28.7 +/- 0.2
HCC	16.0 +/- 0.1	16.5 +/- 0.2
HSA-HCC 200 µm	25.7 +/- 0.1	-
HSA-HCC 100 µm	28.4 +/- 0.4	28.7 +/- 0.2
HSA-HCC 50 µm	29.4 +/- 0.1	29.5 +/- 0.2
HAS-HCC 100 & 50 µm	**29.4 +/- 0.1**	**29.5** +/- 0.2

The SAXS data can be used to model the interactions between macromolecules by combining the molecular docking. The usage of a scoring function allowing to validate full atom models against SAXS data. To obtain 3D structures (PDB: 2I30[165]) and HCC (PDB: 6RVP[65]), were used as an input. The results of the top six structures of the proposed complex set up with FoXS method scoring are shown in Figure 59.

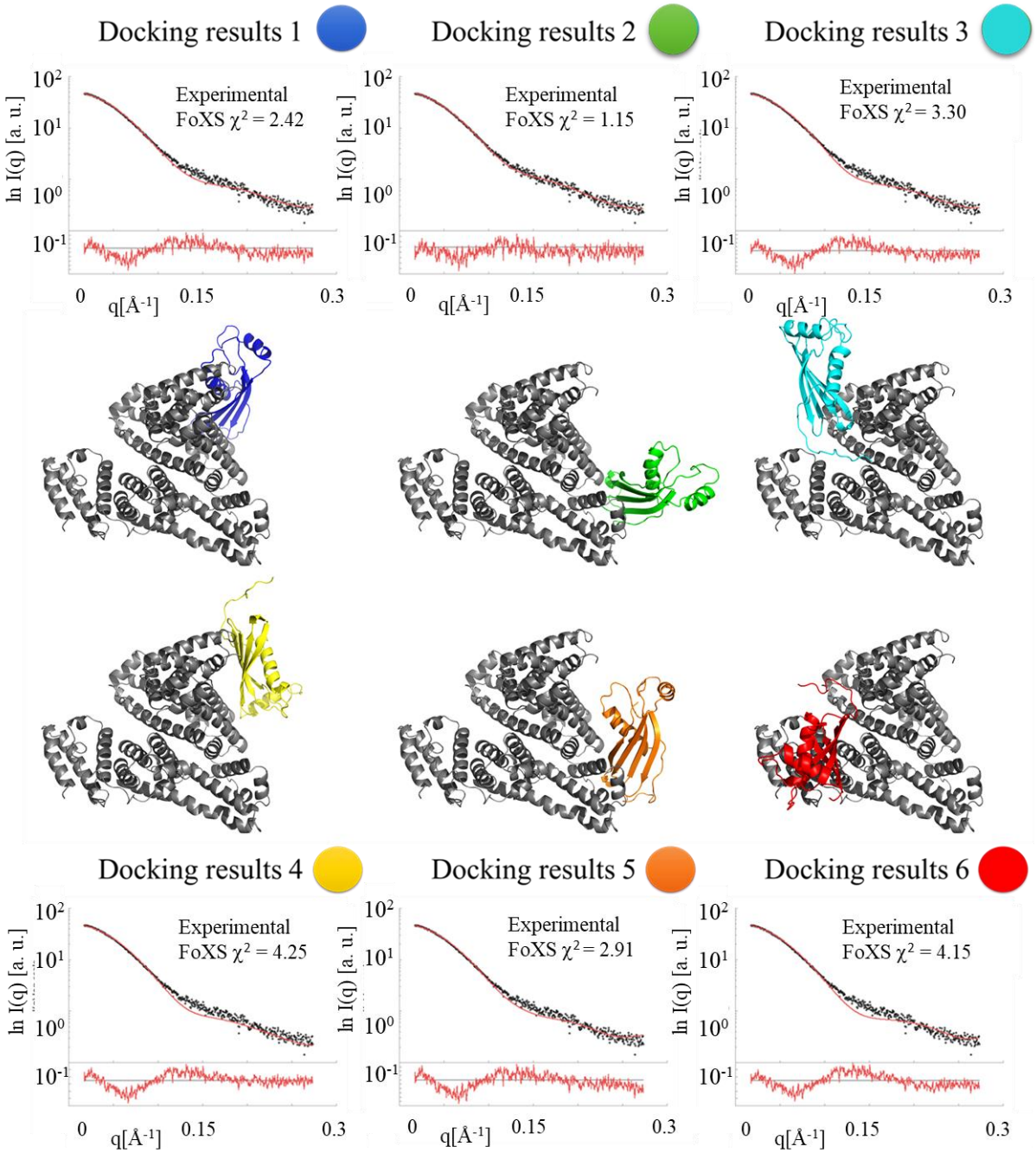

Figure 59. Visualization of HSA-HCC FoXSDock docking results. Each color represents a different model of binding between HCC and HSA. Plots present a comparison of the experimental and theoretical SAXS profile calculated from the model. The residuals of the fit are marked in red below each SAXS profile.

The FoXSDock models were scored according to the experimental data and allowed the selection of the best model of HSA-HCC complex. As is visible in the correlation scoring data, the surface of binding of HCC to HSA gives significant share to the scattering profile curve.

The model number two was characterized by the best fit to the experimental data (Figure 59, χ^2= 1.15, green model). This model was compared with the molecular envelope model generated by DAMMIF.

To compare the atomic structure with low-resolution models derived from SAXS data the SUBCOMP algorithm was used. This method gives the best superposition between these two representations (atomic structure and molecular envelope calculated from SAXS data). HSA structure was marked in red and HCC in blue (Figure 60-62). The high-resolution structures are well fitted into low-resolution molecular envelope. Some parts of HSA structure are placed outside the molecular envelope shape. This is most likely the consequence of the dynamic structure of HSA proteins in the solution. As it is known, HSA structure is very flexible in domain III. Similarly, HCC proteins have a very flexible unstructured N-end.

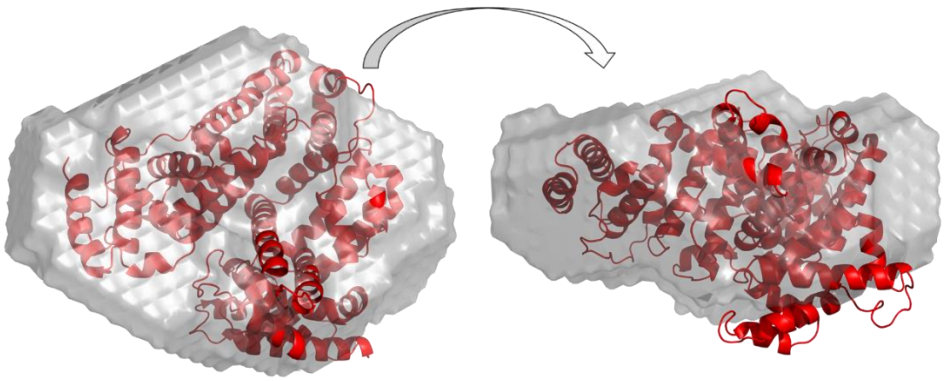

Figure 60. Superposition of HSA crystal structure (PDB: 2I30[165]) and molecular envelope calculated from SAXS data.

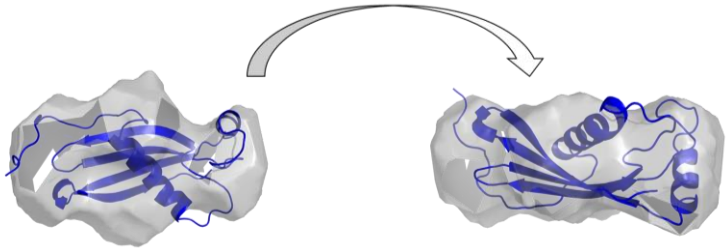

Figure 61. Superposition of crystal structure HCC monomer (PDB: 6RVP[65]) and molecular envelope calculated from SAXS data.

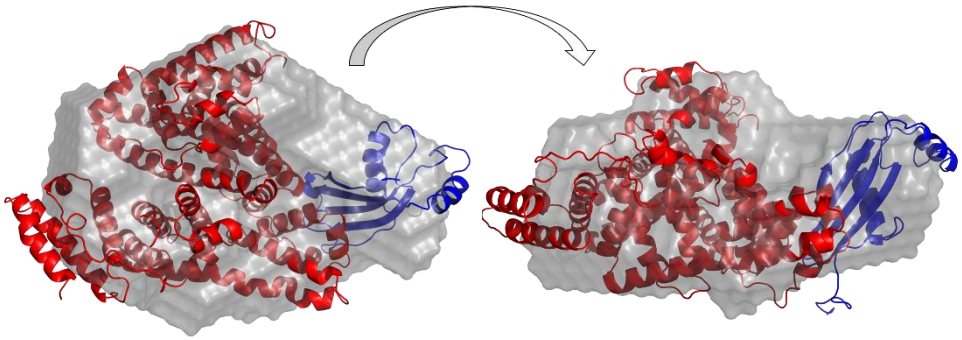

Figure 62. Superposition of HSA-HCC model from FoXSDock (Model 2) and molecular envelope calculated from SAXS data.

In the HSA-HCC complex model, HCC was attached to HSA between domain IIA and domain IIB (DIIA, DIIB) in close approximation to the to the Sudlow binding site (binding site II). Within 5 Å HSA and HCC interact within 62 amino acids, where the most occurring are aspartic acid D (polar, acidic) then glutamic acid E (polar, acidic), glycine G (nonpolar) and alanine A (nonpolar, aliphatic) (detailed information is in presented the appendix). HCC interacts with HSA with its β-sheet secondary structure. The visualization of the binding site of the complex is shown in Figure 63.

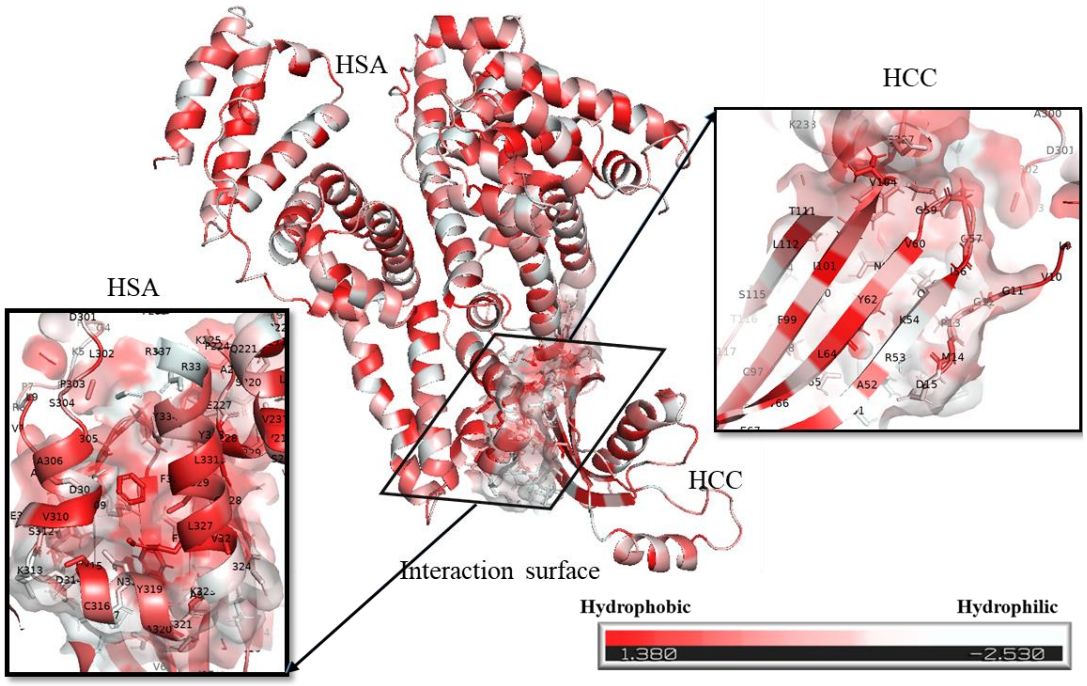

Figure 63. Graphical representation of interacting amino acids residues in the model of HSA-HCC complex (FoXSDock: model 2). The amino acid residues were colored by hydrophobicity.

The obtained data from the SAXS experiment indicates the binding of HCC by HSA in 1:1 molar ratio. Furthermore, thanks to the FoXSDock methods it was possible to predict a model of the complex corresponding to the molecular envelope calculated from the SAXS data of HSA-HCC complex. The R_G calculated from the SAXS scattering profile of the HSA-HCC complex corresponds to the presented model.

5.4.2. Small angle neutron scattering

5.4.2.1. SANS studies of HSA - Aβ complex

The SANS is a complementary method to SAXS except that the beam illuminating the sample is composed of neutrons produced in a specialized nuclear reactor. However, the measurements are performed much longer (depending on the neutron flux on a sample) for better measurement statistics. Notwithstanding, SANS does not cause radiation damages which defines the method as more suitable for studies of many sensitive biological samples. In addition, HCC is sensitive to X-rays and after the irradiation by high flux of X-ray photons the complex aggregates.

The initial SANS measurements of HSA and selected Aβ peptides (1-16, 3-28, 1-42) were performed at YUMO beamline at IBR-2 reactor of JINR (JINR, Dubna, Russian Federation). All samples were prepared with a concentration of 1 mg/mL. Nevertheless, because of the dissolution in the D_2O buffer, Aβ peptide aggregates began to precipitate. Due to the problematic sample preparation and relatively low flux of neutrons, the SANS measurements performed for HSA and Aβ peptides presented poor statistics. All data are presented in Figure 64. The data was analyzed by fitting to Guinier function. The Guinier plots and calculated macromolecule parameters are shown in Figure 65 and Table 8.

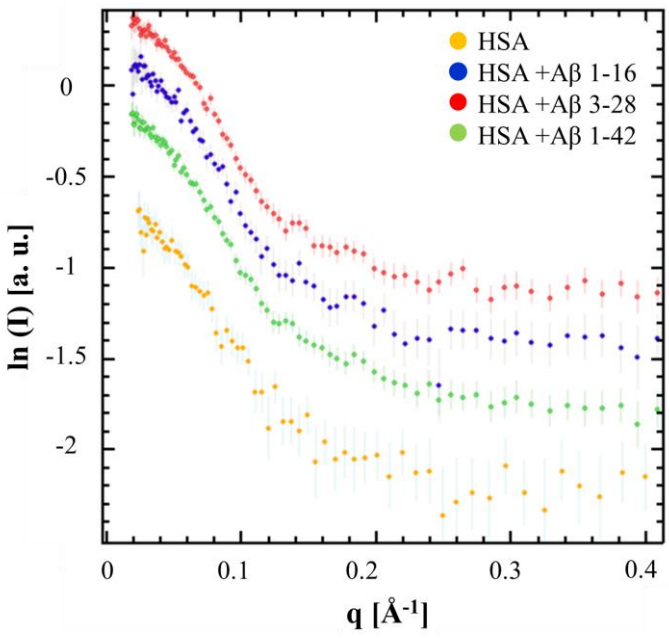

Figure 64. SANS data collected on YUMO beamline at BER-2 reactor (JINR, Dubna, Russian Federation) for HSA and HSA with Aβ 1-16, Aβ 3-28 and Aβ 1-42 peptides.

The neutron flux on YMMO beamline was not strong enough to study proteins in solution Therefore, the collected SANS data did not show a high signal to noise ratio however the R_G could be estimated. Unfortunately, the calculation of P(r) function was not possible. The R_G of HSA and its mixture with Aβ peptides was determined (Figure 65, Table 8). The R_G values were estimated within 27.6-28.4 Å, and corresponds to the reference value calculated for high-resolution HSA structure (PDB: 2I30[165]) and data from other SANS experiments[167].

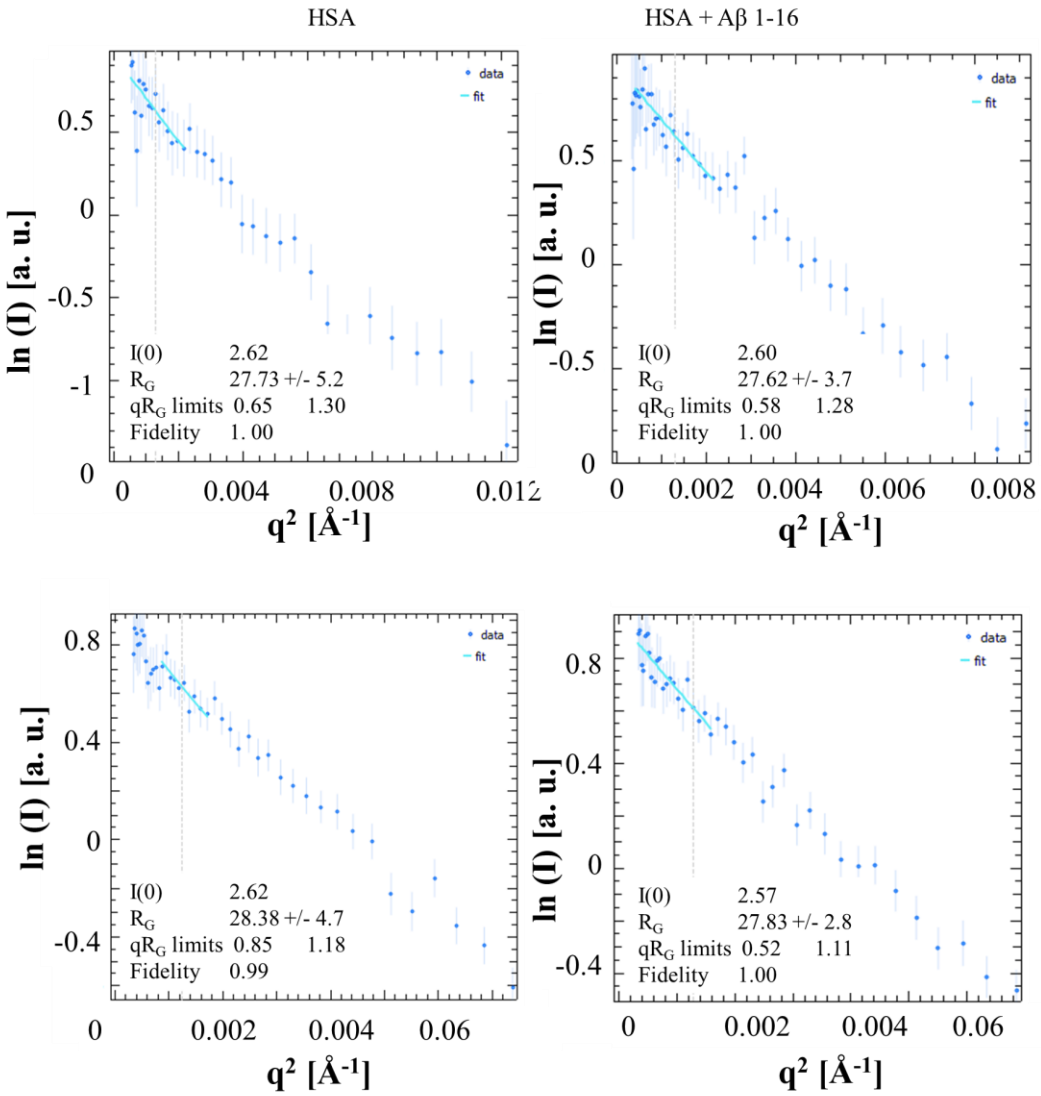

Figure 65. Guinier analysis of the SANS data for HSA mixture with Aβ peptides.

Table 8. Comparison of R_G calculated by Guinier function using SANS data collected for HSA and HSA with Aβ peptides.

SAMPLE	RADIUS OF GYRATION [Å]
HSA	27.7 +/- 5.2
HSA-Aβ 1-16	27.6 +/- 3.1
HSA-Aβ 3-28	28.4 +/- 4.7
HSA-Aβ 1-42	27.8 +/- 2.8

Unfortunately, the uncertainty of the calculated R_G was 3-5 Å (Table 8) which does not allow for unambiguous differentiation of samples based only on the calculated R_G value. However, the observed changes in R_G were useful information for modeling studies of HSA structure with Aβ peptides.

5.4.2.2. SANS studies of HCC and Aβ fibrils by the use of contrast variation

SANS profiles for Aβ fibrils 1-42, 3-28 in the presence of H-HCC, D-HCC

The contrast match SANS studies of Aβ 3-28, Aβ 1-42 peptide fibrils and deuterated (D-HCC) as well as non-deuterated (H-HCC) HCC were performed at the Institute Laue-Langevin (ILL, Grenoble, France) during the in-house beam time. Two types of experiments were performed.

The first experiment characterized the cross-section of Aβ 3-28 and Aβ 1-42 fibrils (Aβ 1-16 peptide did not create fibrils). The second experiment focused on monitoring the behavior of Aβ fibrils in the presence of HCC on a time-resolution scale. The SANS experiments were performed with the usage of contrast match for deuterated HCC meaning that HCC was invisible in the contrast match of the chosen buffer but still visible in the contrast match point for proteins about 45% of D_2O (Figure 66). The kinetics experiment was performed at an increased temperature (37 ^oC) to speed up the ratio of the possible reactions of HCC with Aβ. These experiments are described in detail in the next section.

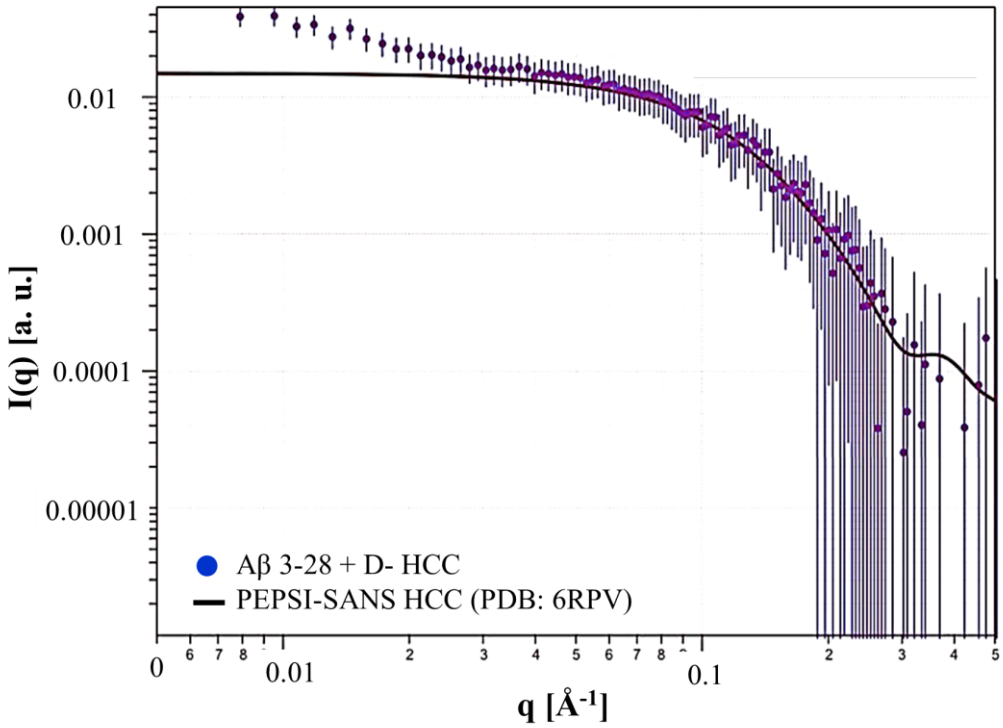

Figure 66. SANS profile of Aβ 3-28 fibrils (matched out) and D-HCC at 45% D_2O (in contrast point for non-deuterated proteins).

The SANS profile collected for D-HCC at 45% of D_2O are corresponding to SANS curves calculated from a model (PDB: 6RVP). In the acquired SANS profile for HCC and Aβ 3-28 peptides, there is no signal from fibrils. However, in small angles the intensity increased indicating the possible presence of larger aggregates. SANS profiles obtained from static experiments for Aβ fibrils could be characterized using power law ~ 4 as a result of the sharp interface of macromolecules in the sample (Figure 67). This scattering curve slope value is characteristic of sharp stiff fibrils (objects). The scattering curves for the mixture of D-HCC and Aβ 1-42 were described by values of 2-3, and this slope values describes the object with a less defined surface.

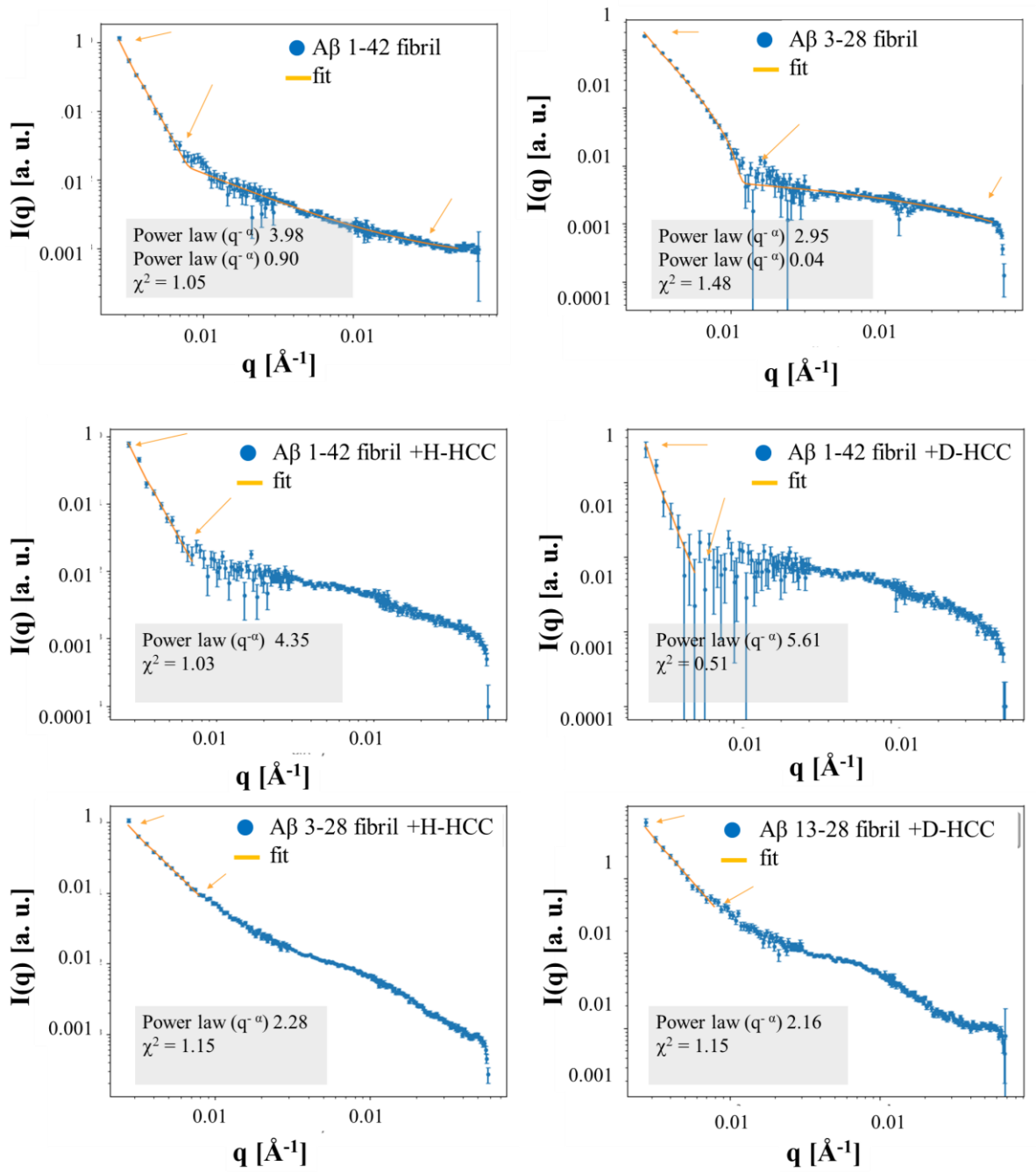

Figure 67. Fitting a slope with power-law functions to SANS scattering profiles of: Aβ 1-42 and Aβ 3-28 in presence of H-HCC and D-HCC (by SASView). Data (blue) with power-law fit (orange line).

For the sample containing D-HCC and Aβ 1-42, the signal loss was observed in small angles. This intensity decrease can be caused by the coverage of Aβ 1-42 fibrils by D-HCC. Consequently, the fibrils are matched out as well. In the SANS profiles of HCC samples, there

was also a "bulge" at about q ~ 0.1. The data from the scattering curve at q ~ 0.1 provides information on the cross section of the molecules in the solution. It is suspected that it could be the result of HCC coating protofibrils or fibrils and probably separating them from larger, denser aggregates. Thanks to this, the information about the fibril cross-section in the scattering profile became visible.

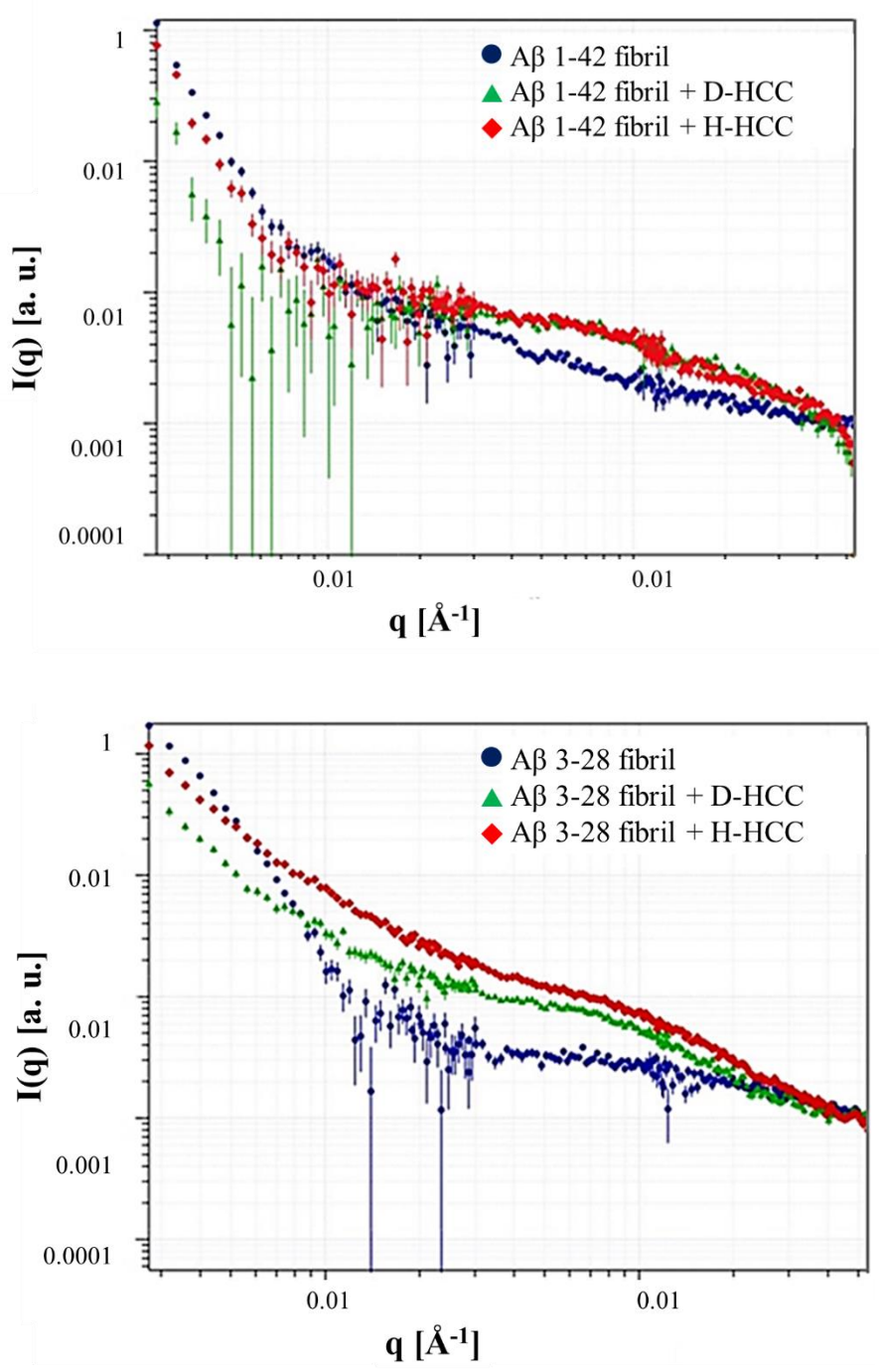

Figure 68. SANS profiles collected for Aβ fibrils in presence of H-HCC and D-HCC. Top: Aβ 1-42; bottom: Aβ 3-28 fibrils.

The parameters of cross-section fit were summarized in Tables 9, 10 and Figure 69. The ellipsoid-cylinder was chosen as geometrical model for the cross-section fitting. The calculated ellipsoid diameters were correlating with cross-section previously published fibrils cryo-TEM model (PDB: 6SHS[36]). For visualization of the shorter variant of peptide Aβ 3-28 which does not have a solved structure, homology modeling was used. As a homology template, the mentioned previously cryo-TEM structure (PDB code: 6SHS) was chosen. The homology model was optimized by MD using the UNRES force field. The optimized model of Aβ 3-28 fibril was characterized by a more collapsed structure. As a result, the semi-minor axis is larger (~10 Å instead of ~5 Å), and the semi-major axis is smaller (~34 Å instead of ~42 Å). The core of Aβ fibril is built by residues that are fully hydrophobic (Figure 69). The collapsed cross-section of the Aβ 3-28 fibril model does not have a groove like in the case of Aβ 1-40. Cross-section of fibril models, can be described as an ellipsoid.

Table 9. Parameters of ellipsoidal cylinder fitting cross-section to the SANS data for Aβ 1-42 fibrils.

Aβ 1- 42 parameters	**Fitted Aβ fibrils + D-HCC [Å]**	**Fitted Aβ fibrils + H-HCC [Å]**	**Cryo-TEM model [Å]**
Polar radius	38.6 +/- 4.3	38.1 +/- 3.9	41.6
Equatorial radius	4.8 +/- 0.3	4.7 +/- 0.3	5.5
χ^2	0.95	0.84	

Table 10. Parameters of ellipsoidal cylinder fitting cross-section to the SANS data for Aβ 3-28 fibrils.

Aβ 3-28 parameters	**Fitted Aβ fibrils + D-HCC [Å]**	**Fitted Aβ fibrils + H-HCC [Å]**	**Model**
Polar radius	37.2 +/- 2.1	36.3 +/- 1.5	33.8
Equatorial radius	10.4 +/- 0.2	9.3 +/- 0.2	9.9
χ^2	0.93	0.86	

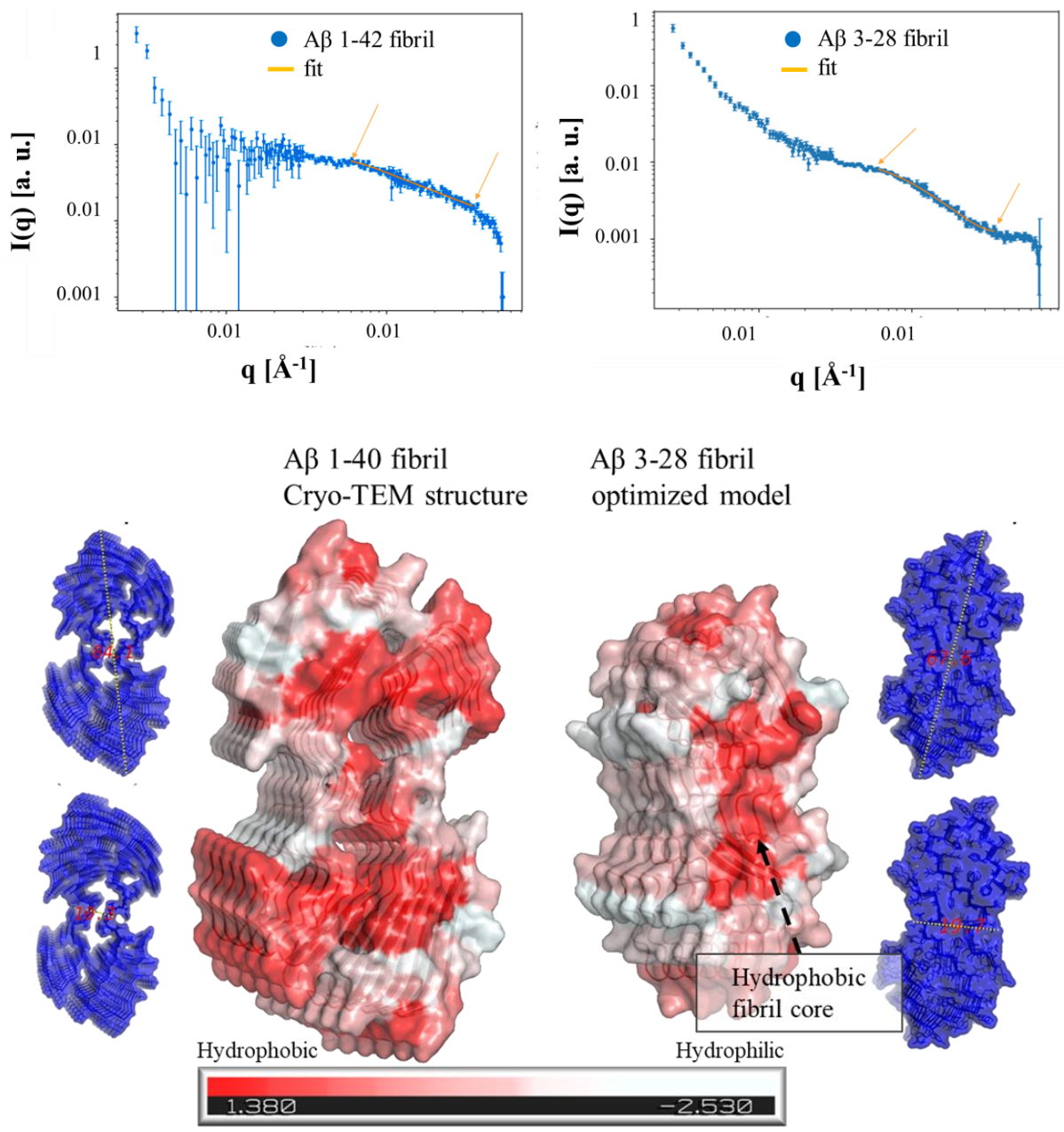

Figure 69. Cross section with the hydrophobic representation of Aβ fibrils. On the top fitting a cross-section to the SANS scattering profiles of Aβ 1-42 and Aβ 3-28 in presence D-HCC (by SASView). SANS data (blue) with envelope fit (orange line). On the bottom left: experimental model from the cryo-TEM[36], on the bottom right : structure obtained by homology modeling and MD structure optimization (this work).

The SANS method was therefore suitable to study the structure of fibrils. No significant effect of H-HCC on the cross-sectional signals of Aβ fibrils was observed.

5.4.2.3. Kinetic SANS experiment for Aβ 1-42, Aβ 3-28 fibrils incubated with and without HCC

A kinetic studies of the effect of HCC on the structure of fibrils Aβ 1-42 and Aβ 3-28 was carried out by a series of SANS experiments on the D22 beamline (ILL, Grenoble). The studies were conducted at an elevated temperature (~37 ^{o}C) in order to accelerate a potential reaction. The samples were placed in dedicated cuvettes, tightly closed, and then placed in the rotating adapter. Simultaneous mixing process during the measurement allowed to avoid sedimentation and dislocation of studied material from the neutron beam. Kinetic studies were carried out by a series of cyclic measurements (20 min exposition time) for each sample, and returned after traversing all samples placed in the trembling rack. Thanks to kinetic measurements, it was possible to track potential changes in Aβ fibril structure in time. Measurements were made for Aβ fibrils (as reference) and Aβ fibrils in the presence of D-HCC. The deuterated HCC at contrast match made it possible to observe the scattering signal only from the Aβ fibrils. The comparison of first and last kinetic measurements are presented in Figures 70 and 71. The scattering intensity was analyzed for a few data points at q> 0.1 for each kinetic step. The plot of the changes observed at the time scale is presented in Figures 70 and 71.

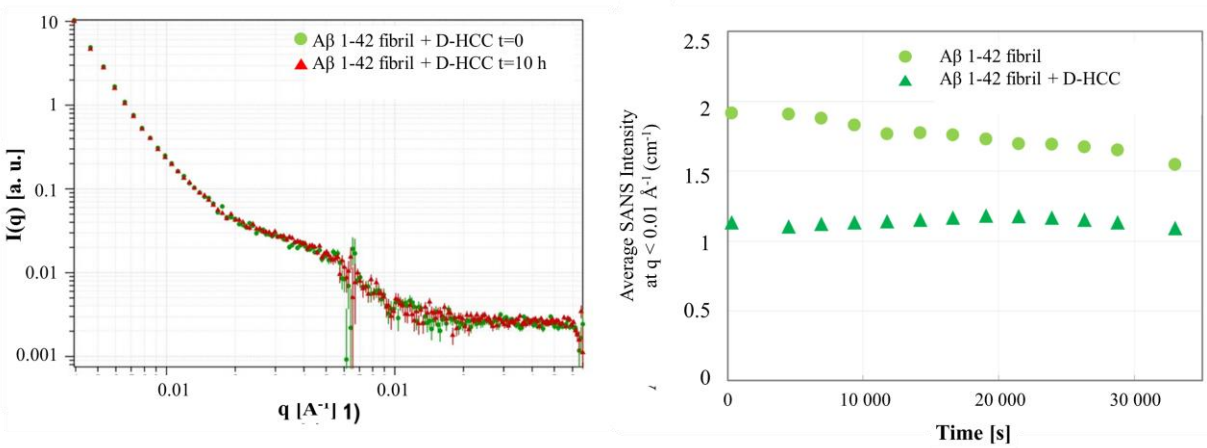

Figure 70. Plots showing SANS data from the kinetics experiments for Aβ 1-42 fibril with and without the presence of HCC. On the left: collected SANS profile at the beginning (green) and end (red) of the kinetics experiment; on the right: comparison of average intensity at q < 0.1 for each step of kinetics experiment.

For Aβ fibrils alone no change in the scattering profile after incubation at elevated temperature was observed. The shape and intensity of the last SANS profile cover the starting one (details in appendix). The samples containing the Aβ 1-42 peptides do not show any changes induced by HCC. In contrast to Aβ 1-42 peptide, Aβ 3-28 showed a significant intensity decrease in the presence of HCC. According to the small angle scattering theory, the larger object scatters the beam with higher intensity in smaller angles. In the sample with Aβ 3-28 and HCC, a significant decrease in the intensity was observed. It was caused by a decrease in the size of fibrils. Therefore, it can be concluded that HCC is able to break down the structure of fibrils and disaggregate them into smaller parts.

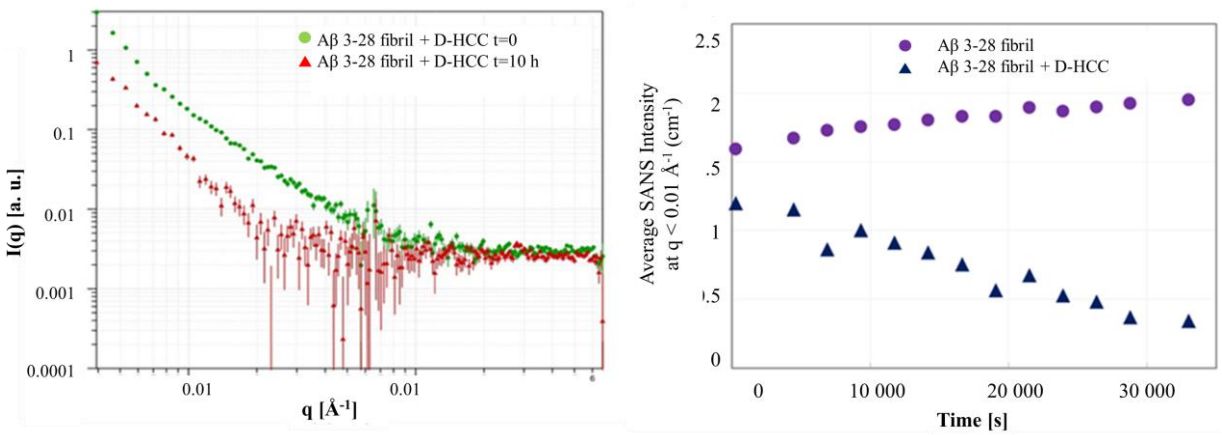

Figure 71. Plots showing SANS data from the kinetics experiments for Aβ 3-28 fibrils with and without the presence of HCC. On the left: collected SANS profile at the beginning (green) and end (red) of the kinetics experiment; on the right: comparison of average intensity at q < 0.1 for each step of kinetics experiment.

5.5. AFM characterization of Aβ fibrils in the presence of HCC

To characterize Aβ fibril formation and their topology, AFM imaging was used. Samples of HCC, Aβ 3-28 and Aβ 1-42 fibrils were characterized by analysis of their topology and measurements of their height profiles. The Aβ 1-16 was not analyzed because this peptide does not exhibit the ability of forming fibrils. However, the Aβ 1-16 was investigated by CD and appears to go through secondary structure conformational changes (appendix).

The samples of Aβ fibrils were diluted in MiliQ water and transferred into mica to dry. The lyophilized HCC protein was dissolved in MiliQ water and then diluted and transferred on mica to dry. To track possible disaggregating properties of HCC molecules, a procedure comparable to the one used in the SANS kinetics experiment was applied. The samples of Aβ fibrils (Aβ 3-28 and Aβ 1-42) alone and in mixture with HCC were prepared. Next, samples were incubated for 9 hours at 37 ^{o}C temperature. In the last step, samples were diluted in MiliQ water and deposited to mica to dry, and then imaged by AFM.

The AFM images obtained for Aβ 3-28, Aβ 1-42, and HCC are shown in Figure 72-74. The Aβ 3-28 fibrils appeared to have very unified unbranched thin and singular fibril forms. The determined height of the Aβ 3-28 is less than 20 Å and less than 40 Å if the fibrils overlap The Aβ peptide fibrils were several micrometers in length (Figure 72). The Aβ 1-42 are much thicker than Aβ 3-28 and slightly more disordered, they are assembled into irregular bundles. The profiles of fibrils were about 20 Å in height and 100 Å when overlapped. The Aβ 1-42 have a larger tendency to stick to each other and overlap (Figure 73). HCC at AFM image shows about 15 Å height (Figure 74).

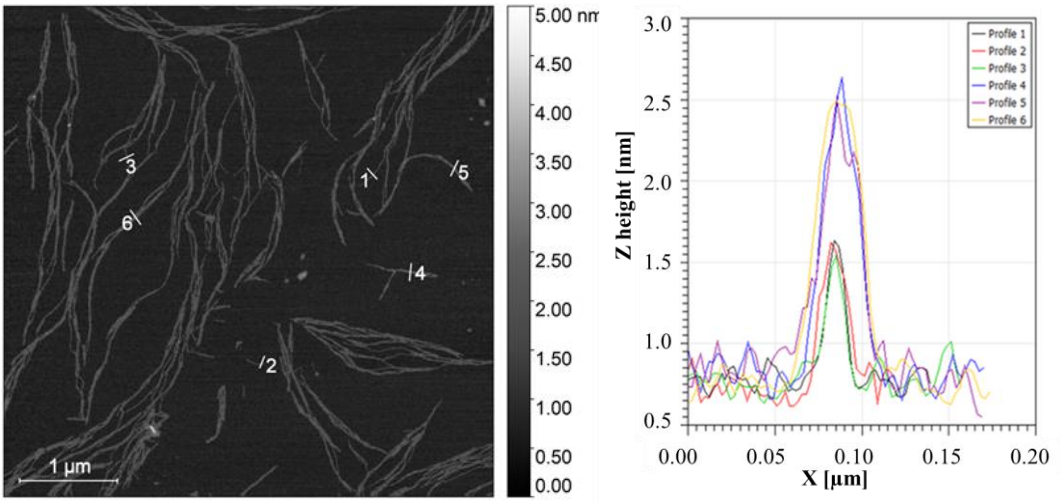

Figure 72. On the left: AFM image of Aβ 3-28 fibrils, on the right: height profiles of structures imagined on AFM picture.

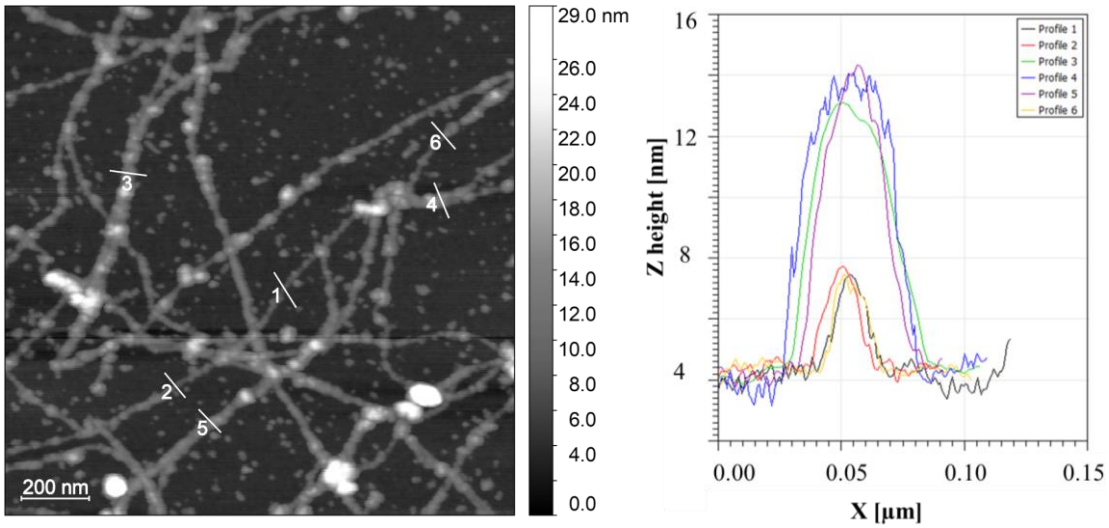

Figure 73. On the left: AFM image of Aβ 1-42 fibrils, on the right: height profiles of structures imagined on AFM picture.

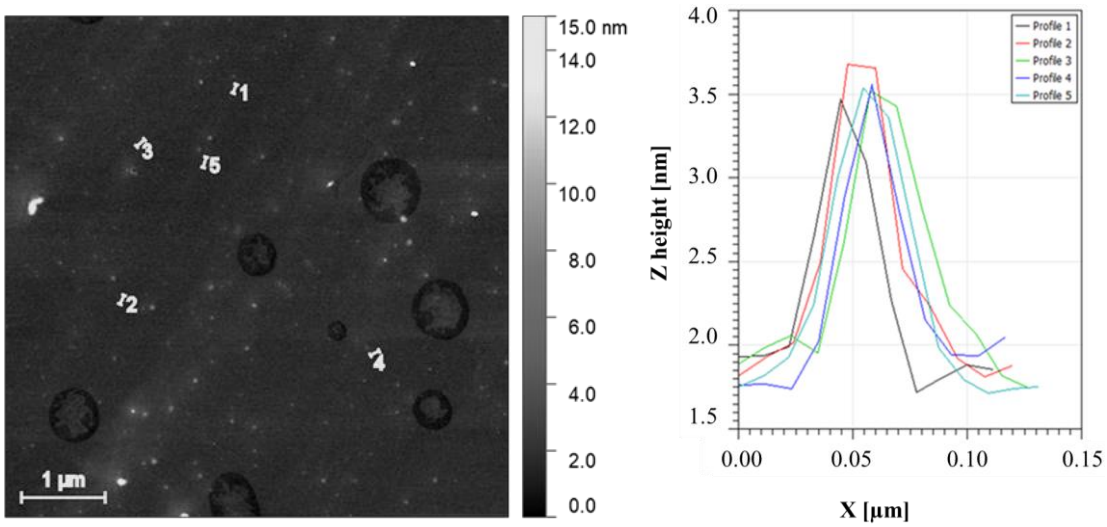

Figure 74. On the left: AFM image of HCC sample, on the right: height profiles of structures marked on AFM picture.

The data obtained by AFM topography for samples of Aβ fibrils after overnight incubation with HCC protein are shown in Figures 75 and 76. The sample containing Aβ 1-42 peptide fibrils and HCC presented only minor morphological changes. The fibrils in sample of HCC-Aβ 1-42 were preserved, however they seem more tangled, which can be the result of agitation process. The AFM micrographs showed that HCC probably adhered to the Aβ 1-42 peptide fibrils. The AFM imaging of Aβ 3-28 after incubation with HCC revealed that HCC disaggregated the fibrillary form almost completely. The uniform fibrils observed for Aβ 3-28 alone disappeared completely. Instead of fibrils, the AFM image of the sample showed spheroid-like aggregates of height up to 200 Å. This result perfectly correlates with the SANS kinetic studies.

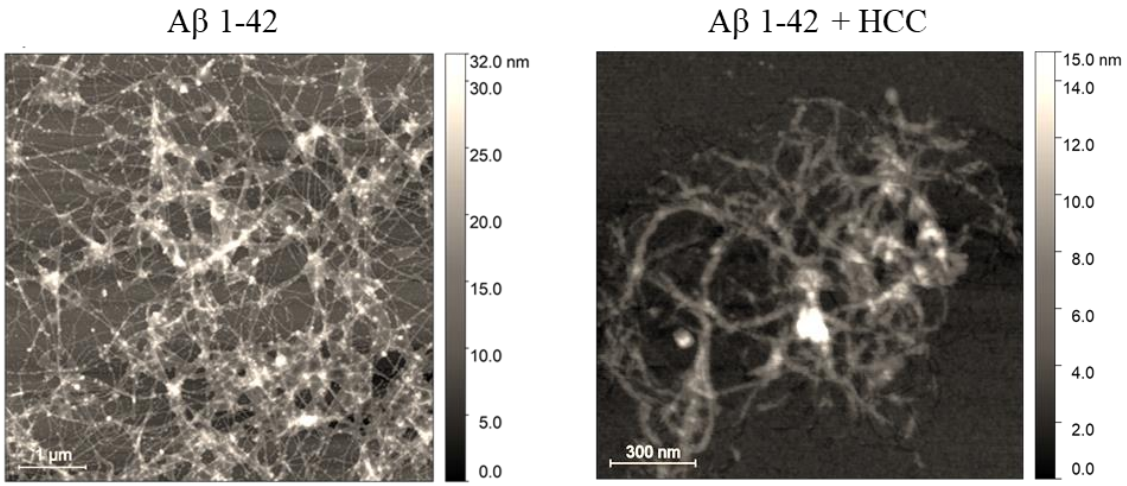

Figure 75. AFM images of studied samples. On the left: Aβ 1-42 fibrils; on the right: Aβ 1-42 after overnight incubation with HCC.

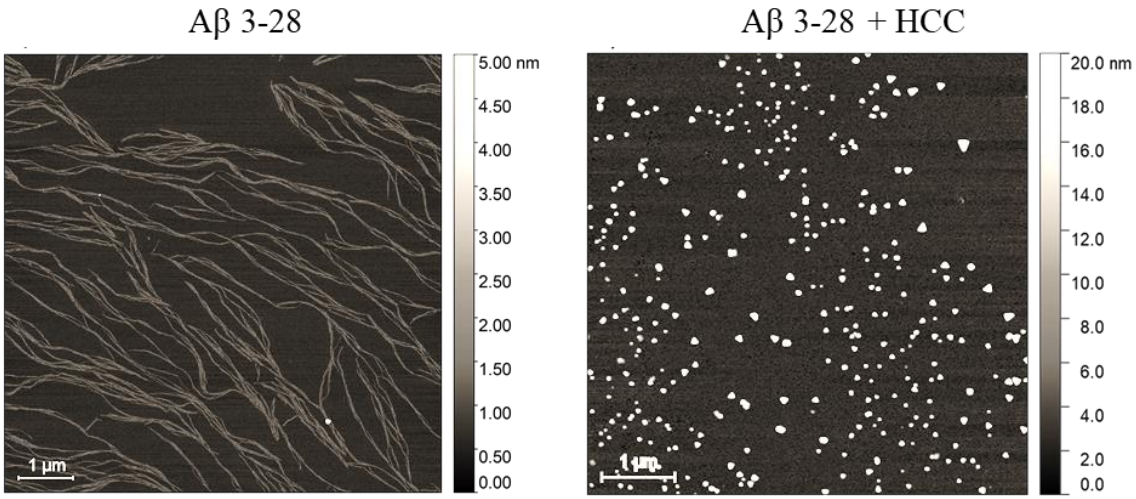

Figure 76. AFM images of studied samples. On the left: Aβ 3-28 fibrils; on the right: Aβ 3-28 after overnight incubation with HCC.

5.6. NMR measurements interactions between ^{15}N HCC and HSA

The sample of HCC V57G and HSA for NMR studies was prepared at concentration 300 µM, in 1:1 molar ratio. The overlay of the ^{1}H-^{15}N HSQC spectra of the ^{15}N HCC and ^{15}N HCC-HSA mixture is presented in Figure 77. Interestingly, signals from alanine A95 and phenylalanine F96 are not observed in the ^{1}H-^{15}N HSQC spectrum acquired for HCC V57G, but are present in the R_1 and R_2 relaxation spectra. Those signals appear after the addition of HSA to HCC solution.

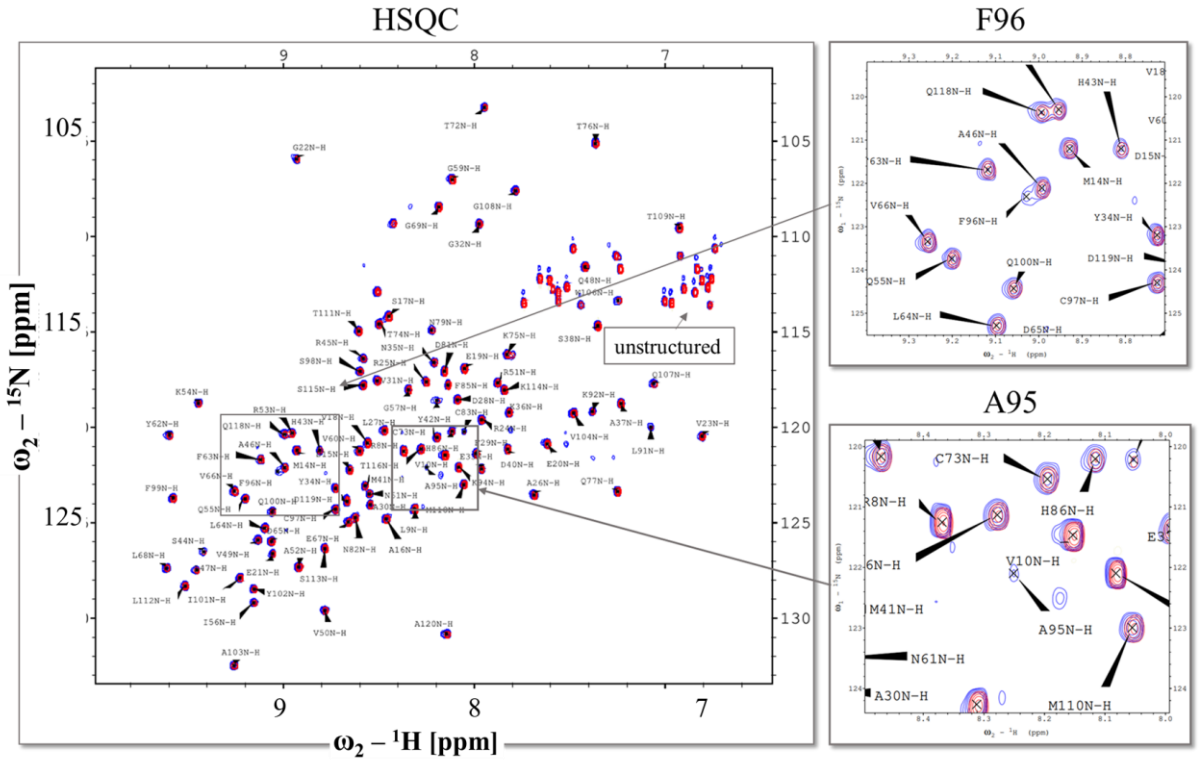

Figure 77. Overlapped ^{1}H-^{15}N HSQC 2D spectra of HCC, ^{15}N-labeled HCC (red) and HCC-HSA mixture (blue).

The analysis of all assigned peaks was done with the usage of the Sparky software with an estimation of decay for all peaks to their amplitudes. Those values were used to calculate the relaxation rate. The R_1 and R_2 for HCC and HCC - HSA samples are shown in Figure 78.

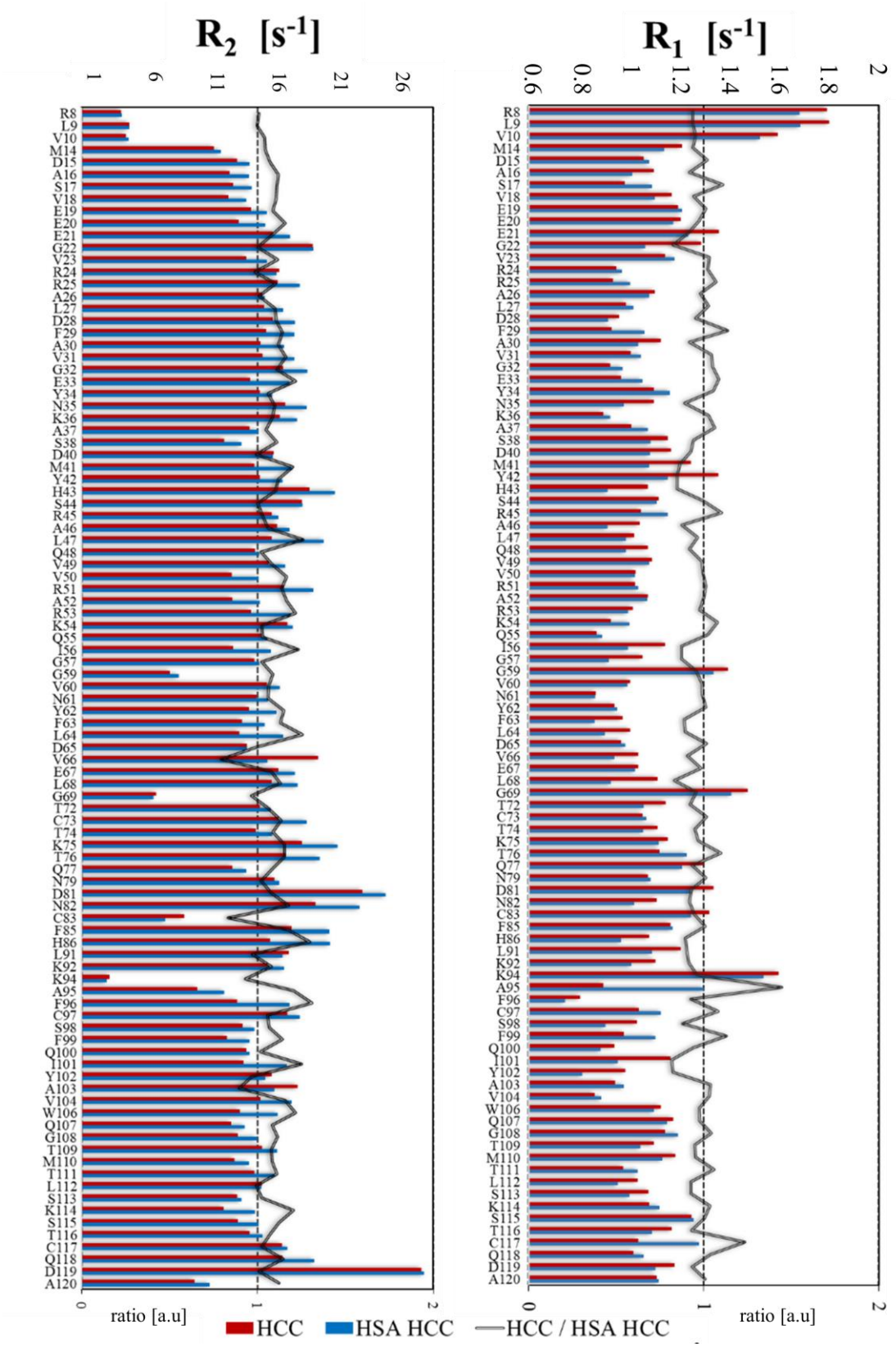

Figure 78. The ^{15}N relaxation data (R_1, R_2) measured for ^{15}N-labeled HCC (red) and HCC-HSA mixture (blue). Black line is representing relaxation rate amino acids of HCC to relaxation rate HCC-HSA ratio.

Comparison of the ^{15}N relaxation data R_1, and R_2 relaxation rates for HCC and HCC-HSA complex revealed a decrease in the R_1 and a slight increase in the R_2 rate for HCC molecules (an average change for R_1-1:0.98 and R_2 -1:1.09, Figure 78, grey lines). The most significant increase for R_1 was observed in order for alanine A95, cysteine C117, phenylalanine F29 and F98. The decrease of R_1 was detected for isoleucine I101, glycine G22, tyrosine Y102, leucine L68, and histidine H43. For R_2, the main changes were observed in the increase of R_2 for phenylalanine F96, histidine H86, leucine L47 and L64, and isoleucine I101. The most significant decrease in R_2 was observed for valine V66, cysteine C83, alanine A103, lysine K94 and glycine G69.

The relaxation rates of R_1 and R_2 reflect the different frequencies of molecular motion. R_1 is defined by the intensities of the high-frequency motions - about $10^8...10^{12}$ s^{-1}. R_2 describes the molecular movements occurring at different frequencies and the dynamics of a molecule at the microsecond and millisecond time scales. The lower R_1 value of the amide group in the polypeptide chain indicates reduced mobility of a structured part of the protein. Mobile amino acids may be a potential binding site with other molecules. Increased R_1 values indicate a reduction of a protein residues dynamics in nanosecond time scale (of these residuals), i.e., greater mobility in high-frequency range. In the collected R_1 rate experiment, we observe a decrease in the R_1 value of HCC-HSA mixture indicating the interaction of those proteins.

A significant increase in R_1 value and mobility for alanine A95 was observed. Alanine is a simple aliphatic amino acid with one methyl group (-CH_3) which is non-reactive, and there is no data on its direct and significant involvement in the protein function. The alanine A95 residue in HCC protein is located at one end of the β-sheet motive. Moreover, the following amino acids: cysteine C97, phenylalanine F99, and in the proximal distance the cysteine C117 (also with a higher R_1). C117 is placed in the β-sheet of HCC structure and forming the disulfide bridges with C97. This result indicates destabilization of the β-sheet secondary structure in HCC by interactions with HSA surface. The lateral relaxation rate R_2, is more sensitive to lower frequency movements (nanoseconds) and reflects contributions from the slower processes at the millisecond or microsecond scale.

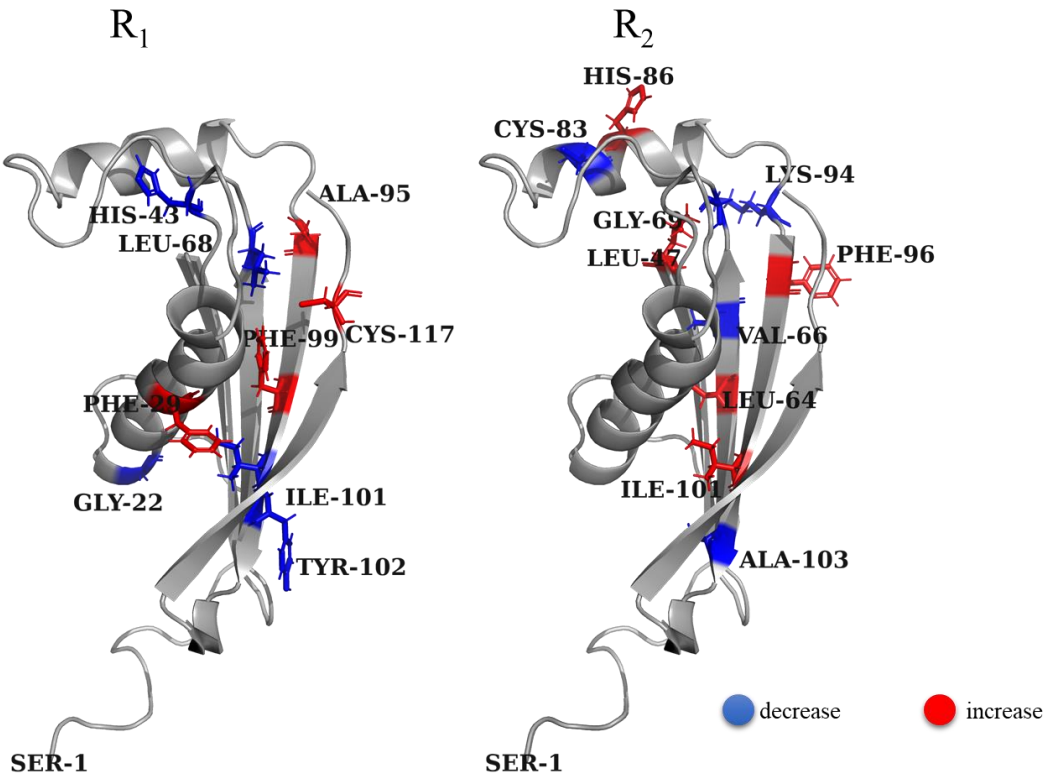

Figure 79. The 3D structure of HCC with marked amino acids residues involved in main changes in R_1 and R_2 rates.

The R_2 rate values at the N- and C- ends of HCC protein are much lower implying these amino acids are mobile and do not take part in the structuring HCC molecule (Figure 79). In contrast to the R_1 rate, the mean R_2 relaxation rate increases in the sample with HSA, which may also indicate interactions between the two proteins, despite no change in the chemical shift. Possibly, these proteins could interact in a non-direct way, driving hydrophobic interactions through the β-sheet motive.

6. Discussion

AD is a neurodegenerative disease associated with the occurrence of senile plaques in the CNS that leads to dementia and finally the death of patients. This disease most often affects people around the age of 65, so the symptoms of AD are often associated with age-related decreased mental performance. The disease has a remarkably high prevalence and impacts society, so it is important to study its mechanism in order to find an effective treatment and understand the molecular cause of its occurrence. The factors that influence the eradication of AD cases are primarily aging, but also comorbidities such as diabetes or genetics, e.g., having a family member affected with the same disease, or with a gene mutation causing the familial form of AD[11,69,91]. Even environmental pollution as well as lifestyle pose additional risk factors[4]. Moreover, it has been recently reported that SARS-Cov 2 virus causes oxidative stress in the brain and triggers changes similar to AD[168].

The Aβ produced through the degradation of the APP membrane protein forms senile plaques. Those senile plaques are an integral part of the AD symptoms and are considered the fingerprint of the disease. There are several pathways of APP degradation[20] which involve different sets of enzymes, and it remains unclear why the path of amyloidogenic degradation is favored in the disease state. Moreover, one theory states that the appearance of Aβ peptides causes AD[169]. The presence of these peptides in the CNS is extremely dangerous to health due to their ability to undergo/initiate rapid and drastic nucleation reactions to form oligomers, fibrils, and ultimately senile plaques[13]. The presence of Aβ deposits causes several different effects, ranging from the disruption of the cell membrane[96], ionic imbalance, etc., leading to apoptosis[33] and neuronal death, and ultimately dementia and patient death.

Aβ peptides were discovered in 1984, and since then their structural properties have been an object of interest in multiple studies. Thus, the development of possible treatments against this devastating disease has been underway. Although the vast majority of currently available therapies treat only symptoms of AD, in 2021 the US Food and Drug Administration (FDA) has approved Aducanumab (Aduhelm), a drug designed to slow down the progression of AD [23]. Aducanumab is the first drug for AD approved by the FDA since 2003. However, the FDA decision was considered controversial. In two Phase 3 clinical trials, researchers reported contradicting results. One trial showed that the drug slows down the progression of AD, while another showed that the drug was not effective. Despite that, the decision to introduce the drug

was positive, due to the lack of alternative and therapy, even for at least some AD individuals[170]. Aducanumab is a monoclonal IG1 antibody, designed to target oligomeric forms of Aβ, particularly the sequence of N-terminal amino acids (3-7: EFRH)[23]. The use of engineered proteins or monoclonal antibodies for therapeutic purposes is becoming increasingly promising. Therefore, designing biomolecules like antibodies interfering with Aβ based and involvement of the already existing proteins (like HSA and HCC) could bring innovative approaches and therapeutic strategies to address that issue.

The aim of the research presented in this doctoral dissertation was to characterize structure and interactions between Aβ peptides, HSA, and HCC proteins. The outcome of these studies can help to develop potential strategies for influencing this macromolecular system. This research was also conducted to demonstrate the role of HSA and HCC as preventive agents against Aβ aggregation. These two proteins, even though they perform various physiological functions, are relevant for understanding of possible disaggregation properties of Aβ fibrils, because of their individual properties and their presence in the CNS. HCC is an amyloidogenic protein with a flexible structure, which can undergo a domain-swapping process leading to fibrils formation[73] and is detected in the senile plaques deposit[171]. Moreover, Aβ peptides and other proteins, including serum amyloid A, interact with albumin and HCC, and may also be one of the potential partners of HSA. Therefore, the interplay between these proteins has been studied.

To carry out biophysical experiments designed in this work, effective methods have been used to produce Aβ peptides and assay them against selected proteins. In this work, a new protocol for overexpression and purification of deuterium labeled HCC was developed. The stable monomeric variant (V57G mutant) was further used for SAXS and NMR studies. Omitting that Aβ peptides are extremely difficult to work with, it was possible to carry out a series of biophysical experiments that allowed a description of the interaction of Aβ peptides with proteins associated with HSA and HCC. The conducted experiments allowed for the structural characterization of peptide variants and showed the ability of HCC to disaggregate Aβ 3-28, whereas the Aβ 1-42 variant was lacking this ability. Non-specific interactions between HSA and HCC have also been detected and described. The collected results shed more light on the phenomena of inhibition of Aβ aggregation occurring at the molecular level. The acquired knowledge can be used for scientific considerations to design new molecules like antibodies based on already known native proteins. For example, synthetic structural motives based on HCC sequence could interact with the amyloid deposit.

6.1. Model of interaction between Aβ peptides and HCC

Some studies support the theory that HCC has a meaningful protective role in CNS and especially in AD suffering individuals[70,71]. Results from this project about HCC and Aβ interactions (chapter 4.4.2.3.) exhibited disaggregation of Aβ 3-28 fibrils induced by HCC protein and possible inhibition of a fibril formation. It is worth underlining that HCC is a protein co-localized with Aβ peptides in CSF and senile plaques of AD brains[171]. The co-deposition of HCC and Aβ was confirmed by immunostaining of HCC-Aβ complexes in AD brains[171]. Moreover, the studies on transgenic mice with elevated expression of HCC protein also showed a decrease of Aβ aggregates in CNS[61]. HCC may be involved in the protection of neuronal cells and has a significant role in preventing neurodegeneration induced by Aβ oligomers[172]. However, there are not much data about the above-mentioned mechanism of the process. The research presented in this work shows that HCC can break down fibrils composed of Aβ 3-28 peptides. However, HCC does not have a significant impact on the Aβ 1-42 isoform. Even though the shorter variant can form fibrils, it is not resistant to HCC. On the other hand, the SANS studies performed by me at ILL, and AFM imaging experiments, demonstrated that HCC may cover the surface of Aβ 1-42 fibrils protecting them from future formation of larger aggregates. This conclusion also corresponds to the co-deposition of HCC in amyloid plaques[171].

The composition of plaques in AD brains includes Aβ 1-40, Aβ 1-38, and Aβ 1-42, and also several fewer-occurring species as Aβ 1-37 and Aβ 1-43[173]. The insoluble plaques do not include shorter peptides, which may be explained by the fact that they are soluble and possibly complexed with HCC.

The study of the degradation path of APP protein exhibited the complete set of Aβ species as a final products[43]. The occurrence of different isomers is caused by sequential cleavage by different enzymes and external conditions like oxidation of glycosylation level of APP[174]. Many shorter Aβ isoforms, for example Aβ 1–17, 1-18, 1-19, 1-20, can be produced by act of γ-secretase (schematic of APP cleavage is shown in Figure 10). The presence of other biomolecules like HCC may have a significant impact on the metabolism of Aβ peptides and protect the homeostasis of the neuronal cells.

Interactions between HCC and selected Aβ fibrils

The microstructure of fibrils Aβ peptides was already studied by several complementary methods including AFM[175], cryo-EM[36] or 2D solid state NMR[176]. The Aβ peptides form fibrils of approximately 45-100 Å diameter and can reach a length of several micrometers. The Aβ fibrils structure is remarkably dynamic and unpredictable due to the spontaneous molecular mechanism of peptide self-assembly reaction into oligomers and leading to fibrils formation. The nature of the intermolecular interactions that stabilize these fibril structures, as well as the arrangement of individual monomers in the fibrils, is driven by both hydrophobic forces and hydrogen bonds between the hierarchical β-sheet structures[36].

Interestingly, fibrils can be described as non-crystalline solid materials. The fibrils are not fully organized in comparison to the crystalline state, therefore, they pose an enormous challenge in 3D structure determination using standard methods of X-ray crystallography. Additionally, conducting the experiments using other methods, such as solution or solid state NMR, is also very difficult.

However, the fiber diffraction method can be used for the structural analysis of Aβ fibrils. Thanks to this method it was possible to obtain information, from the X-ray fiber diffraction pattern, about the secondary structure of elongated β-sheets. In this structure the β-sheet segments run approximately perpendicularly and the intermolecular hydrogen bonds are positioned in parallel to the long axis of the fibril[177].

Along with the advancements in electron microscopy technology, it was possible to unravel the structure of Aβ 1-40 by developing an electron density map from photos obtained using cryo-TEM. Reconstructed model revealed other structural features of Aβ fibrils at the molecular level, e.g., a polymorphism in creating fibrils same as ellipsoidal cross section and appearance of a groove in the cross-section (Figure 80).

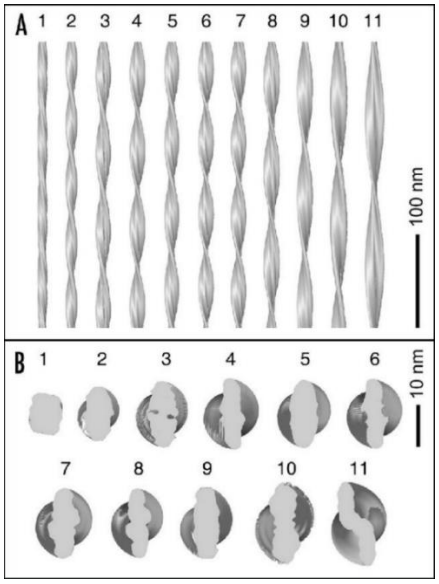

Figure 80. Representation of Aβ 1-40 fibril structures. Side (A) and cross-section (B) Cryo-TEM reconstructions of Aβ 1-40 fibrils from the same sample (Adapted from: Fändrich et al., 2005[100]).

The cryo-TEM model (PDB: 6SHS)[36] was further used as a template to build the Aβ fibril model of other sequences. The homology modeling approach used in this work was important to maintain the most essential interactions between peptide monomers.

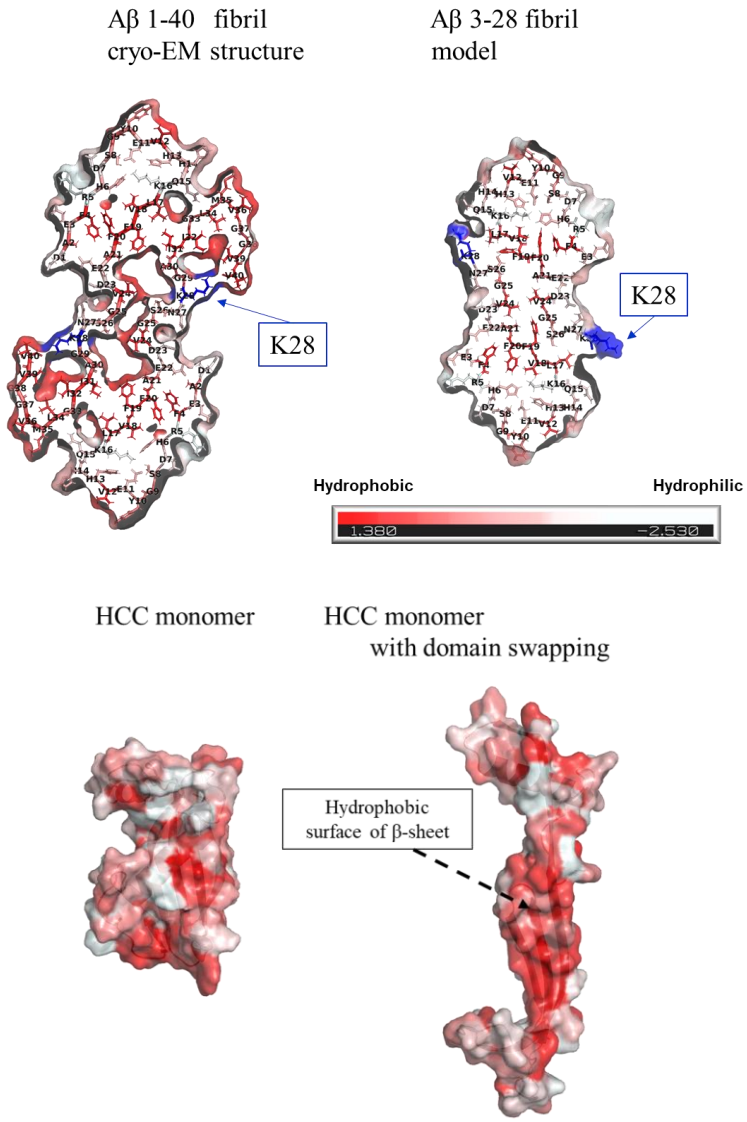

Figure 81. Representation of hydrophobic and hydrophilic surfaces on the studied macromolecules. On the top: the structures of 1 layer of fibrils with marked lysine K28 (blue). In the model of Aβ 3-28 K28 is exposed to solution and it is not stabilized by any interactions with other amino acids. On the bottom: the structure of monomer and dimer of HCC. All 3D structures are colored according to hydrophobicity (red) of amino acids.

Published studies characterizing structural parameters and interactions within Aβ fibrils pointing to the lysine K28[178] as crucial for Aβ fibril structure formation. The lysine K28 is supposedly involved in salt bridge formation with aspartic acid D23 or glutamic acid E22[179]. The formation of the fibril core is forced by a combination of hydrophobic and electrostatic interactions. In the model of Aβ 1-40 fibril, the K28 stabilizes the conformation loop together

with valine V40 by interaction of sidechains. In the model structure of fibril Aβ 3-28, the C-end is shorter and the lysine K28 is exposed to interaction with the external environment. Most likely HCC is able to disaggregate the Aβ 3-28 via its interaction with lysine K28. The N-end fragment of HCC is highly flexible and could be involved in the penetration and disruption of the Aβ fibril structure. The N-end of HCC sequence contains a triple glutamic acid E domain which can be involved in interactions with lysine K28.

In addition, as shown in Figure 69, the structure of the fibrils is dependent on a hydrophobic interaction, and the aggregation of Aβ peptide is accelerated in high salt aqueous environment[180]. In the model structure of Aβ 3-28 fibril, the core is mostly stabilized by hydrophobic amino acids. HCC in its native monomeric form is held by hydrophobic forces[181]. Also, HCC exposed to a certain condition (high-flux X-rays) can undergo conformational changes, such as domain swapping, and expose the hydrophobic β-sheet motife[63]. Furthermore, it was already known that the native HCC dimer structures show polymorphism (PDB: 1TIJ or PDB: 1G96) of an arrangement of β loop (βL), indicating high flexibility in HCC structure. The phenomenon of disaggregation of Aβ 3-28 fibrils by HCC, is directly connected with mentioned HCC flexibility and may be driven by the disruptions of hydrophobic forces and dynamic co-destabilization between those molecules.

Molecular docking of Aβ 3-28 monomer to HCC monomer and dimer

The progress in the computational methods used in the predictions of the 3D structure of biomolecular complexes is more accurate from year to year. The study of protein-protein interactions provides a deeper understanding of their properties and functions. The modeling of unfolded or disordered proteins (IDP) that gaining an organized structure during the complex formation remains the challenge. The Aβ peptide monomer exists mostly in unfolded coiled-coil conformation, but when it undergoes conformational changes to β-sheet secondary structure motives it starts forming co-complexes with other monomers and induces a rapid self-assembly process.

Because HCC can disaggregate the Aβ 3-28 fibrils and inhibit the aggregation process, it is highly probable that HCC molecules can form stable complexes with monomeric Aβ peptides. The published data[182] on experiments focusing on Aβ aggregation with and without HCC demonstrated that HCC protein can inhibit the oligomerization of monomeric Aβ to the fibrils.

The inhibition is the result of binding of monomer Aβ peptides by HCC. HCC may prevent Aβ peptide secondary structures shifting into β-sheet and thus prevent further aggregation.

To study the mechanism of interaction the molecular docking procedure was performed with the CabsDock method[162]. This method allows for predicting protein-peptide interaction with the use of course-grain approach, and more importantly, the docked peptide is flexible not a rigid body, similar to the receptor.

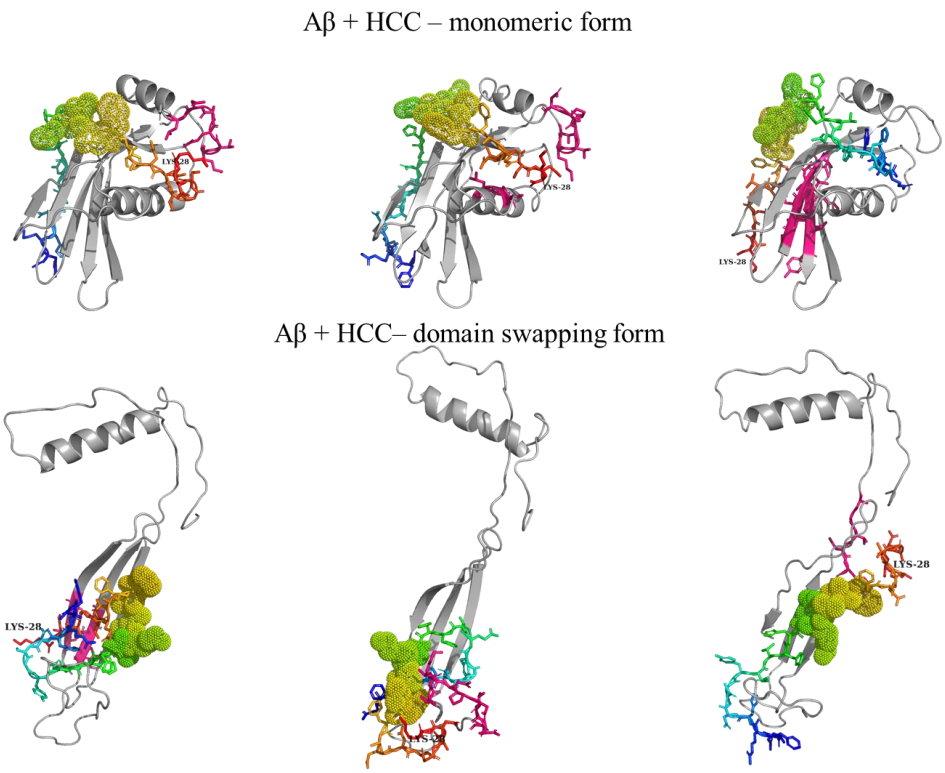

Figure 82. Graphical representation of top three models from docking of Aβ 3-28 peptide to HCC (grey) monomer (top) and HCC molecule in the domain swapped conformation (bottom). The residues interacting with lysine K28 are marked in pink and aggregation core of peptide (QKLVFF) is represented as "dots".

This method is limited to peptides of up to 30 amino acids in length of the length up to 30 amino acids, and it was suitable to perform the docking of Aβ 3-28 peptide to HCC molecule. The structure of HCC monomer (PDB code: 6RPV, V57G) and the structure of the domain swapped HCC dimer (PDB code: 1TIJ) were selected for this study. Peptide-ligand sequence was provided as an input. For each docking procedure 10 models were proposed. Figure 82 presents

the top three models that were obtained for both molecular systems. Results of Aβ 3-28 docking to HCC monomer showed that the Aβ 3-28 peptide is stuck to the β sheets motif (including a sequence of its aggregation core). The lysine K28 from Aβ 3-28 sequence is involved in the interaction with loop 75-81 or β sheet fragment. The predicted model of interaction of Aβ 3-28 with a domain swapped HCC molecule distinctly indicates interactions within the β sheet. It should be considered if HCC undergoes domain swapping due to interactions with Aβ.

It is worth to mention that, existing immunotherapy uses antibodies targeting the 1-7 fragment of the Aβ peptides sequence[183]. Published data and results presented in this work showed the C-terminus of Aβ peptide, in particular lysine LYS28[178], is crucial for the ability to form fibrils and resistance of their oligomeric structure. The research on specifying the Aβ-HCC complex structure will be fundamental in designing new antibodies focused more on the Aβ-LYS28.

6.2. Model of interactions of Aβ peptides with HSA

HSA is a protein transporting many particles[78] (mainly hydrophobic molecules: including fatty acids, metal ions and therapeutic drugs) in plasma. Moreover, the blood studies of AD patients showed that HSA binds 90% Aβ peptides occurring in the blood plasma[55,184]. The concentration of HSA in the CNS is significantly reduced from 640 μM (blood plasma) to only 3 μM, but it is one of the proteins that is still dominant in the brain[185]. Recent studies of Aβ aggregation process suggest that amyloid deposits are formed only in the brain due to a reduction of HSA level in CNS[186]. It has been confirmed that HSA can bind Aβ peptides and slow or nearly completely inhibit their aggregation[87]. There are many alternate results of HSA Aβ interaction studies. For example, some research published by Guo and Zhou revealed that fatty acids can

compete with Aβ peptides to bind with HSA[86]. However, the same group also demonstrated that the addition of copper ions or linoleic acid promotes HSA-Aβ interactions[187].

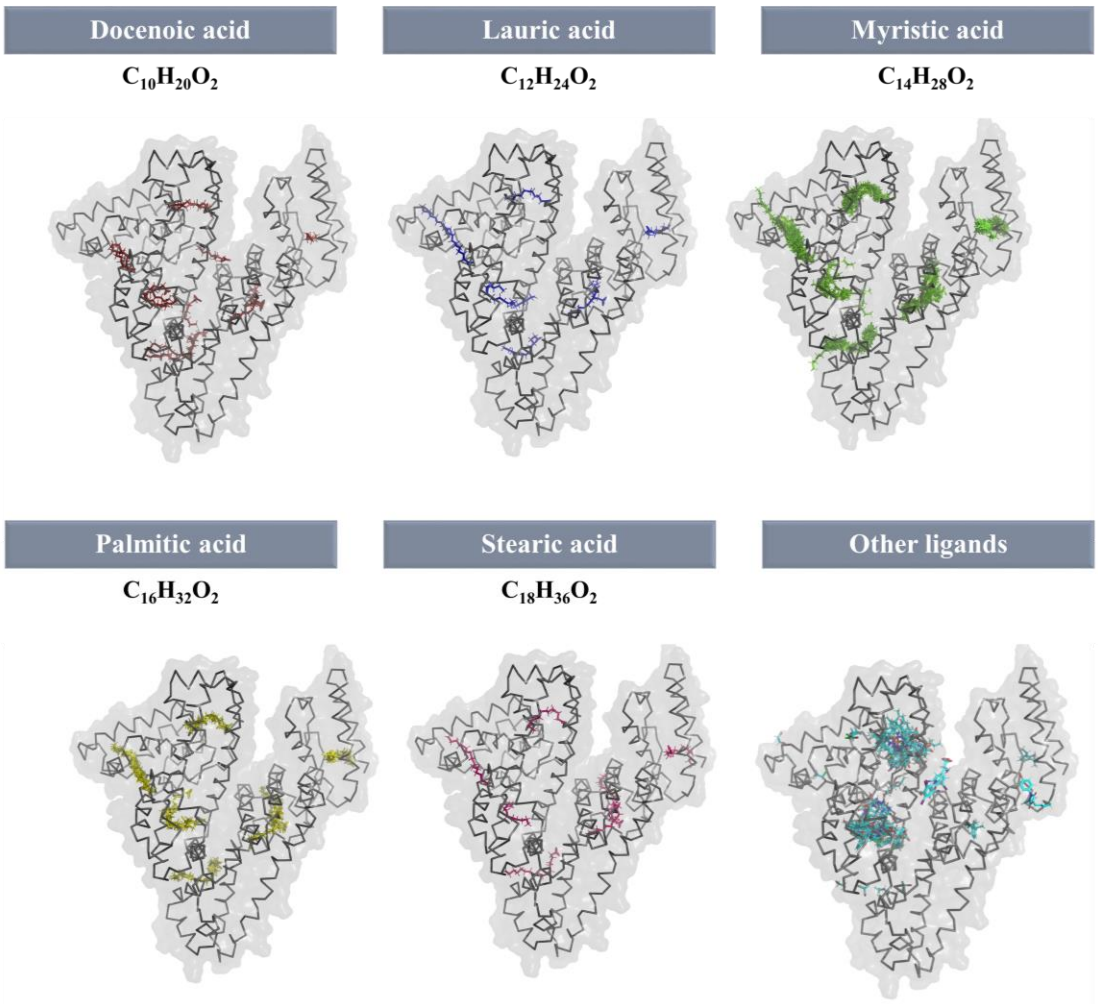

Figure 83. HSA structure with all overlapped of HSA-ligand complexes structures from PDB data base including fatty acid binding and other small molecule ligands.

Considering the potential HSA-Aβ complexes studied in this work, it is worth paying attention to the broad context of HSA interactions with various molecules. To illustrate all the binding sites the structures of HSA-ligand deposited in the PDB database were superposed and set up in Figure 83. HSA can bind a series of different fatty acids by hydrophobic interactions. Currently there are many structures solved by X-ray crystallography demonstrating HSA-fatty acids complexes. Besides the hydrophobic drug binding site, HSA (DI and DII, hydrophobic surface of HSA presented in Figure 84) have six fatty acid binding pockets (the most common

ligands are myristic and palmitic acid). The Aβ peptides are partly hydrophobic making the binding to HSA highly probable at the same locations as fatty acids.

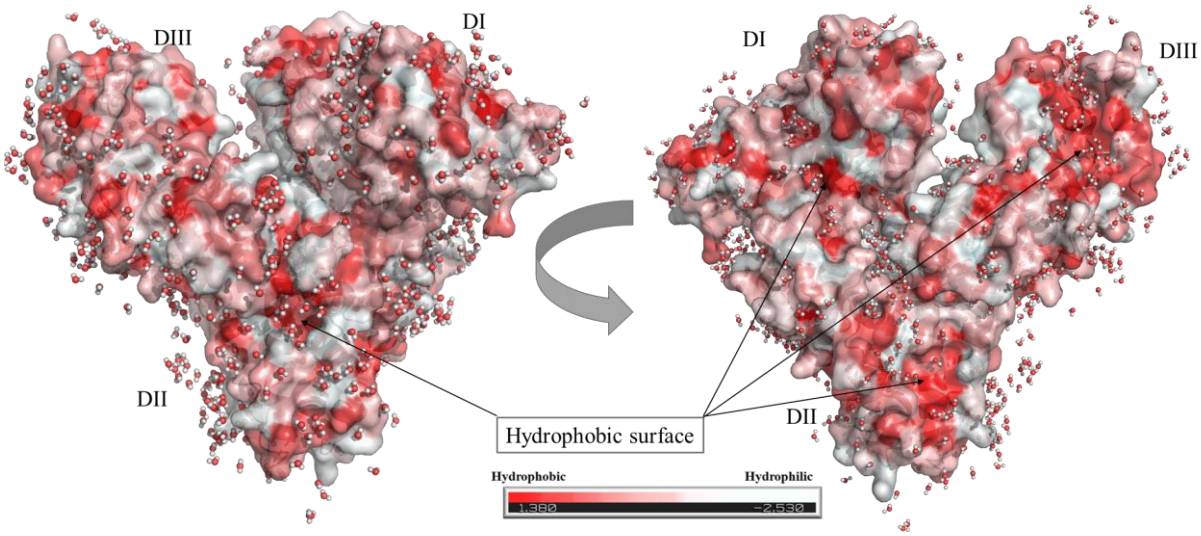

Figure 84. Representation of HSA hydrophobic (red) – hydrophilic (white) surface. The red area is expected to bind Aβ peptides which are characterized by mostly hydrophobic amino acids primary sequence.

Choi et al.[87] described interactions between HSA and Aβ 1-40 peptide and Aβ 1-42 peptide by different experimental methods. The authors confirmed the interaction of Aβ peptide with HSA by different methods such as mass spectrometry. Moreover, it has been reported that Aβ 1-42 has a stronger HSA affinity than Aβ 1-40[186]. The presents of ions itself can also stabilize the oligomeric form but completely prevent fibril formation[93].

These results correspond to the native MS studies that were successfully performed on HSA with Aβ 1-16 peptide and Aβ 3-28 peptide (chapter 4.1). The data demonstrate the ability of HSA to bind these variants of Aβ peptide as well. The sample containing Aβ 1-42 peptide was not measured due to high precipitation. The peak for Aβ-HSA observed in the mass spectrum is not symmetrical and shifted into higher masses and maxima of peaks corresponding to the mass of the HSA-Aβ peptide complexes. The presented results suggest the potential of binding more than one monomer of Aβ peptide.

The SAXS data by Choi et al.[87] presented no change in R_G in HSA-Aβ mixture. However, in this experiment HSA was described by R_G=30.4 Å. This value is almost 2 Å higher than in HSA

crystal structure solved by X-ray diffraction. In addition, in the manuscript there is no data about removing potential HSA dimers from the sample.

The SAXS data collected for HSA and Aβ 1-16, Aβ 3-28, and Aβ 1-42 indicate an increase in the R_G (chapter: 4.4.1.1). The fitting of Guinier function may include a signal from aggregates due to too low monodispersity of the sample. The data were not good enough to calculate the 3D low-resolution models for comparison with the atomic models. A similar problem was observed in the SANS measurements presented also in this work (data collected in JINR, Dubna, chapter 4.4.2.1). SANS method did not induce radiation damages contrary to synchrotron radiation and was better choice than SAXS. Unfortunately, the SANS data did not present good statistics to provide reliable conclusion about HSA and Aβ peptide interactions.

To propose a model HSA-Aβ interactions the rigid body molecular docking method was used (PathDock[151]). For docking simulation the monomeric structure of HSA was selected (PDB: 6YG9[85]). The few forms of Aβ 1-42 peptides were used: the unstructured monomer (PDB: 6SZF[163]), tetramer (PDB: 6RHY[164]) and monomeric form with β-sheet conformation (extracted from tetramer PDB: 6RHY[164]). The summary of the results is presented in Figure 85.

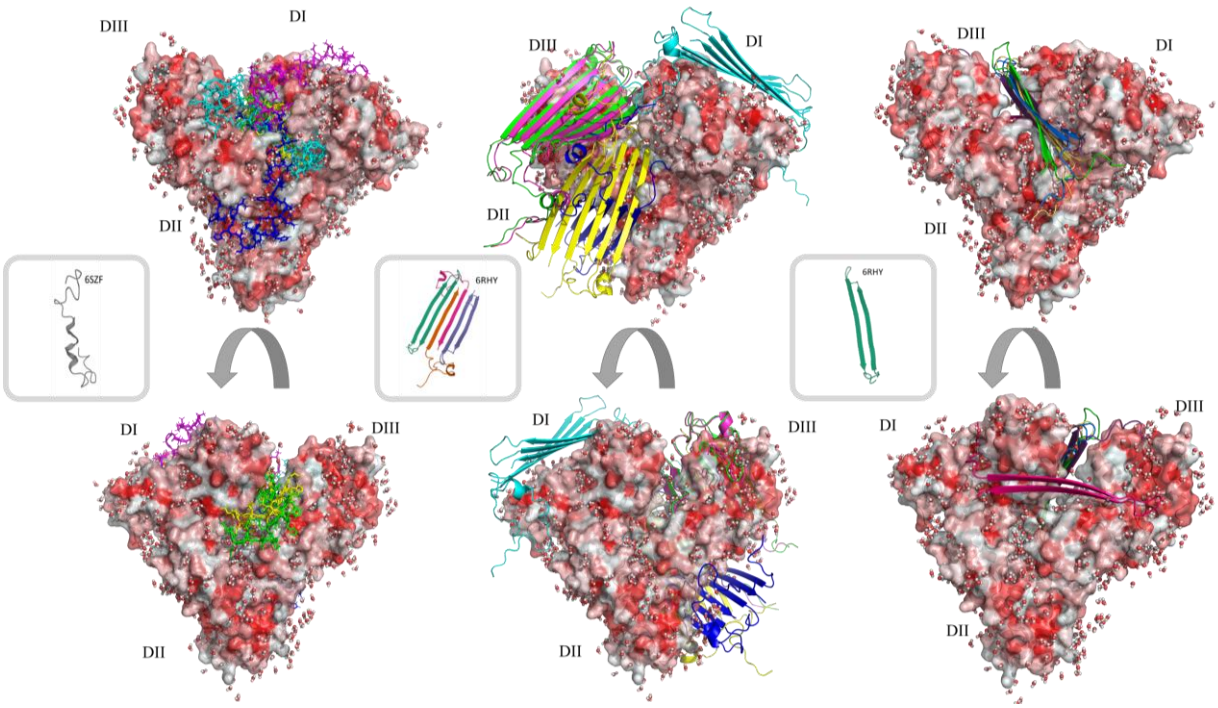

Figure 85. Docking models by PatchDock. Top 5 models of interactions proposed for three different Aβ peptide forms (gray square) overlapped on HSA crystal structure.

PatchDock method is performing a docking procedure by finding optimal fitting for the rigid molecular surfaces of docked molecules. The monomeric form of the Aβ peptide (unstructured), the same as the peptide with the transition into the β-sheet, was docked in the grove between DI and DIII. This result is extremely interesting, especially if taking into consideration the flexibility of HSA structure. The flexible structure of HSA may open and close in process of binding the monomeric Aβ peptide between DI and DIII (with proximity to Sudlow's site in DIB). It was reported that fusidic acid and bilirubin (both hydrophobic) bind specifically to sub-domain IB (by arginine R117) and data derived from the crystal structures of HSA indicate a high flexibility of DIB[188].

Similar interactions are reported for HSA and α-synuclein[189] which is a molecular cousin of APP's Aβ. Furthermore, it has to be pointed out that HSA is a large protein, and the bind of more than one of the Aβ peptide mer is admissible. The Aβ tetramer model is docked to DIII or DII domains and one model to DI. It is also observed that only one site of HSA surface is preferred which is probably connected with an accessible hydrophobic surface. The obtained models of HSA-Aβ interactions can fully illustrate mechanism of potential binding and transporting of Aβ peptides by HSA. The role of HSA as guardian of CNS and nonspecific binding of Aβ peptide is supported by experimental data from MS, SAXS and SANS (chapters: 4.1, 4.4.1.1., 4.4.2.1.).

Considering the fact that HSA can bind around 90% of Aβ in the blood plasma HSA is certain that HSA is involved in transporting the toxic Aβ peptides into blood plasma where they undergo further metabolizing. As a result, HSA prevents the creation of insoluble Aβ peptide deposits in peripheral tissue. Based on that phenomenon the approach of plasma exchange with HSA replacement is already well described and published as part of AD therapeutic strategy proposed by M Boada et al. (AMBAR Program)[190]. In this therapy, HSA bound with Aβ peptide is trapped and next is exchanged with a fresh therapeutic (Aβ free) HSA. The results of this approach gave a positive outcome in Phase 1, 2, and 2b/3 trials[191] according to Ace Alzheimer Center Barcelona and the Alzheimer's Disease Research Center in Pittsburgh, Pa., U.S.

6.3. Model of interactions between HSA and HCC

The complexation process between HCC and HSA proteins has not been characterized at an atomic resolution, however, both proteins are present in blood plasma and CNS in high concentrations. Moreover, both exhibited an interaction with Aβ, causing inhibition of Aβ aggregation. These interactions must therefore be of a similar nature. Moreover, it was reported that in the pathological state as kidney disease, which is also connected with occurrence of dimeric form of HCC[192], the homeostasis of body albumins is disrupted as well[80].

The AUC experiments studying the stoichiometry of the HSA-HCC complex did not give a positive result. The outcome of the experiment did not reveal a complex between these two proteins even though a different concentrations and molar ratio of HCC to HSA were tested. These results did not support the hypothesis suggesting the formation of the stable complex between HSA and HCC. However, the data collected from SAXS and NMR experiments suggest HSA-HCC interactions. Our data suggests that these two proteins can interact in a non-direct way, driven hydrophobic interactions.

The SAXS experiments showed an increase in the R_G of the HSA-HCC complex of 0.8 Å. A change in the scattering curve was also observed. Fitting the functions of potential models of the HSA-HCC complex gave a good correlation of χ^2=1.15 (chapter: 4.4.3.1.). The model shows the binding of HCC protein in HSA DII domain in the vicinity of binding site II via β-sheets. It is therefore quite possible that HSA can transport HCC in the blood plasma and can have a nonspecific involvement in the inhibition of aggregation of Aβ by HCC.

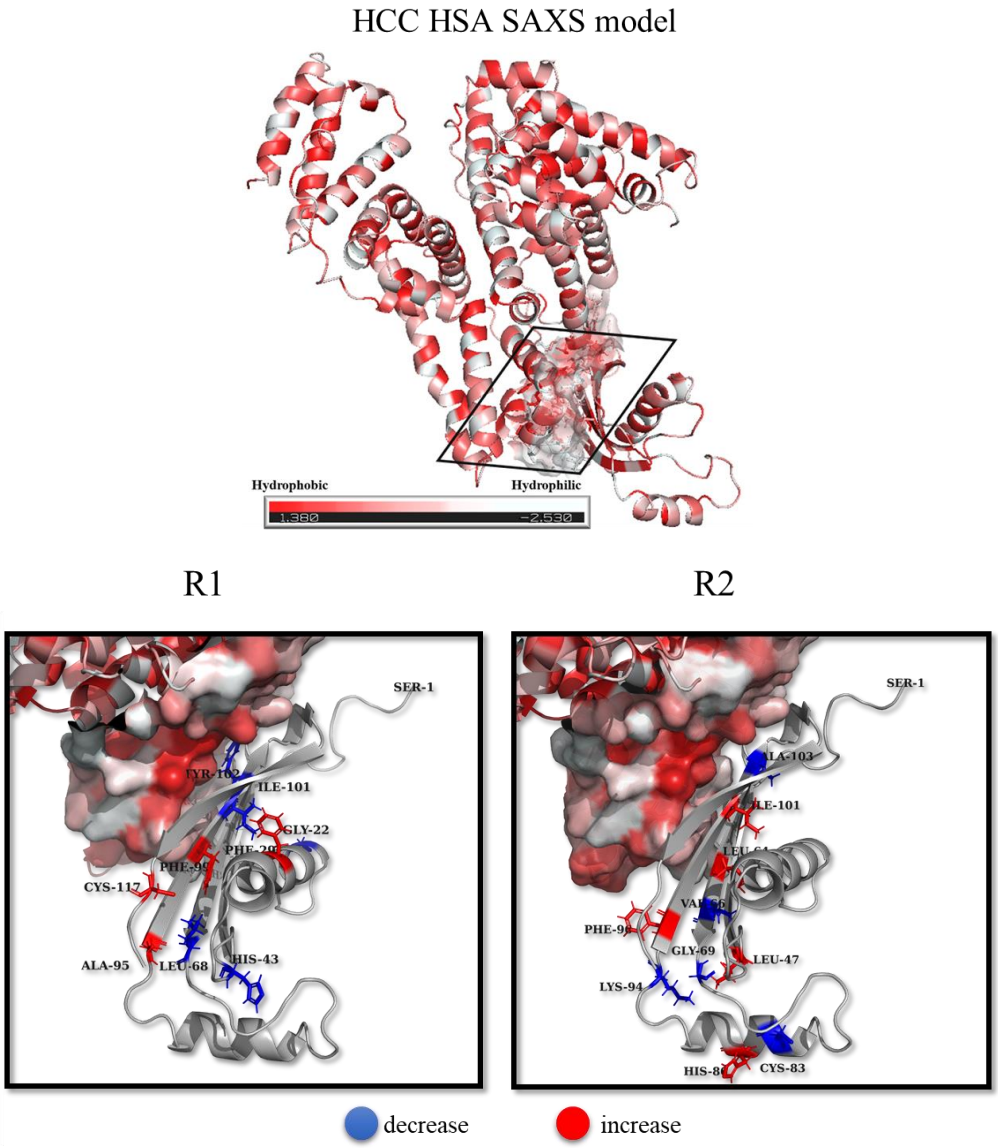

Figure 86. Analysis of relaxation data according to the SAXS data predicted model in comparison to NMR relaxation experiment. The interacting part of HSA was shown as the surface. HSA structure was presented according to the hydrophobicity of amino acids. HCC structure is colored in gray with amino acids marked according to R_1, and R_2 relaxation rates.

The results obtained by the NMR relaxation experiment correspond to the model predicted using SAXS data (Figures 59 and 86). In the proposed model HCC interacts with HSA by its few residues of unstructured N-end. HCC interacts with HSA mostly by β-sheet motive 102-116 fragment. The model correlates with relaxation NMR data (chapter: 4.6.). Direct interactions occurred within the amino acids in the 101-103 fragment of HCC, where the aromatic ring of tyrosine Y102 is exposed for hydrophobic interaction with HSA. The sticking

of HCC to the hydrophobic surface of HSA can destabilize HCC in β-sheet in 101-117 amino acids.

HSA protein can build complexes with many other body proteins (albumin-binding proteins: glycoprotein 60, gp18, apolipoprotein B-100, IgG receptor FcRn large subunit p51, fibronectin type III, SPARC, etc)[193]. For some of the above-described complexes, atomic structures can be found in the PDB database. Representative structures of HSA-protein complexes (e.g., immunoglobulin) were chosen to compare with obtained HSA-HCC model (PDB: 4HGM[194], 6ZL1[195], 2VDB[196], 6M58[197]; Figure 87).

The amino acids engaged in forming complexes have been found by inspecting interactions within 5 Å of HSA structure. Analysis of interaction within complex implicating that the model of HSA-HCC and other HSA-protein structures share the same surface of binding. In addition, three areas of interaction were overlapping in HSA sequence. HSA interacts with HCC and other analyzed proteins mostly within 220-235, 255-273, and 299-333 fragments (Figure 87).

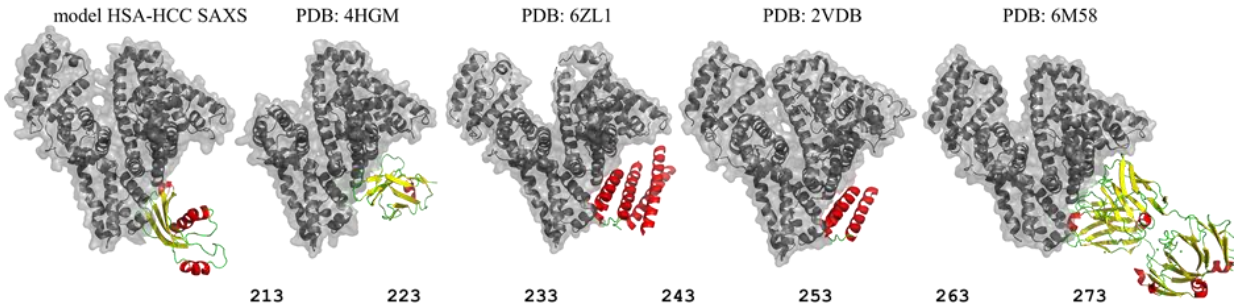

	213	223	233	243	253	263	273
model HSA-HCC SAXS	AWAVA RLSQR	FPKAE FAEVS	KLVTD LTKVH	TECCH GDLLE	CADDR ADLAK	YICEN QDSIS	SKLKE CCEKP
PDB: 4HGM	AWAVA RLSQR	FPKAE FAEVS	KLVTD LTKVH	TECCH GDLLE	CADDR ADLAK	YICEN QDSIS	SKLKE CCEKP
PDB: 6ZL1	AWAVA RLSQR	FPKAE FAEVS	KLVTD LTKVH	TECCH GDLLE	CADDR ADLAK	YICEN QDSIS	SKLKE CCEKP
PDB: 2VDB	AWAVA RLSQR	FPKAE FAEVS	KLVTD LTKVH	TECCH GDLLE	CADDR ADLAK	YICEN QDSIS	SKLKE CCEKP
PDB: 6M58	AWAVA RLSQR	FPKAE FAEVS	KLVTD LTKVH	TECCH GDLLE	CADDR ADLAK	YICEN QDSIS	SKLKE CCEKP

	283	293	303	313	323	333	343
model HSA-HCC SAXS	LLEKS HCIAE	VENDE MPADL	PSLAA DFVES	KDVCK NYAEA	KDVFL GMFLY	EYARR HPDYS	VVLLL RLAKT
PDB: 4HGM	LLEKS HCIAE	VENDE MPADL	PSLAA DFVES	KDVCK NYAEA	KDVFL GMFLY	EYARR HPDYS	VVLLL RLAKT
PDB: 6ZL1	LLEKS HCIAE	VENDE MPADL	PSLAA DFVES	KDVCK NYAEA	KDVFL GMFLY	EYARR HPDYS	VVLLL RLAKT
PDB: 2VDB	LLEKS HCIAE	VENDE MPADL	PSLAA DFVES	KDVCK NYAEA	KDVFL GMFLY	EYARR HPDYS	VVLLL RLAKT
PDB: 6M58	LLEKS HCIAE	VENDE MPADL	PSLAA DFVES	KDVCK NYAEA	KDVFL GMFLY	EYARR HPDYS	VVLLL RLAKT

Figure 87. Comparison of the model of the HSA-HCC complex obtained by docking supported by SAXS data with other HSA-protein complexes deposited in the PDB database. On the bottom: the HSA sequence with marked amino acids taking a part in complex interactions (within 5.0 Å of ligand, red).

6.4. Summary

In my dissertation, I presented the results of studies of the Aβ peptides, the hallmark of Alzheimer's disease, as well as their interactions with two proteins HSA and HCC. The relationship between Aβ peptide and potentially neuroprotective HSA and HCC proteins was explored. The result of studies conducted as a part of this doctoral dissertation allowed for a better understanding and characterizing interactions between Aβ and associated HSA and HCC proteins. Based on the combination of experimental and computational experiments a complex between HSA and HCC was likewise proposed.

To acquire a sample for research successful protocols for peptide synthesis and HCC protein production were developed and applied. The chosen methods allowed for the investigation of structures of selected biomacromolecules, characterization of disaggregation process of selected model Aβ fibrils by HCC protein, and also study of dynamics of the investigated molecular systems.

The main achievements reached during the conducted studies:

I. Many of the presented experiments could not be conducted without a successful synthesis and expression of different variants of Aβ peptides. Therefore, a protocol yielding a suitable quantity of high-grade sample was developed as part of this project.
II. This newly developed protocol for overexpression of deuterium labeled HCC allowed for the realization of a series of SANS experiments requiring large amounts of sample. In addition, cost of the D-HCC production was significantly reduced by applying a high-yield approach.
III. Thanks to the SAXS method supported by NMR relaxation it was possible to demonstrate HSA and HCC interactions despite the non-specific interactions holding the complex. As a result, low-resolution and atomic models were proposed.
IV. Experiments tracking the fibril formation of selected Aβ peptides led to the characterization of the Aβ 3-28 and Aβ 1-42 fibrils and demonstrated the inability of Aβ 1-16 to form fibrils.
V. The characterization of fibrils was performed by imaging methods such as TEM and AFM. The structural parameters of the fibrils were defined and confirmed with available experimental data.

VI. MS and SAXS experiments confirmed the binding of Aβ peptide by HSA protein and suggested that HSA may bind more than one molecule of the peptide in a higher oligomer state configuration. The atomic models of those interactions were also proposed in this project.

VII. Performed series of SANS experiments allowed determination of the cross-section of Aβ fibril in solution with and without the presence of D-HCC. The proposed atomic structure of Aβ 3-28 was derived by computational methods and correlated with obtained SANS data.

VIII. The most significant result of this work was to demonstrate that HCC can fragment Aβ fibrils of Aβ 3-28 variant but not Aβ 1-42 fibrils where HCC was covering the fibrils. This difference in fibril formation enabled the construction of a model of interactions of HCC and Aβ 3-28. The results were confirmed by the SANS and AFM experiments.

6.5. Study perspectives

Several decades of intense research on AD resulted in an unsuccessful development of effective pharmaceuticals for AD therapy. So far there is no effective treatment to reverse the terrible effects of this remarkable common disease. The discovery of the natural mechanisms the toxic Aβ oligomers utilization would allow the development of new therapies to heal disease states. Serum exchange therapy[190], including Aβ binding albumin, gives positive results in several trials. However, HCC protein provides a more significant protective function by directly interacting with Aβ peptide, and breaking them down or encapsulating Aβ peptide deposits which secure them through further aggregation. A closer look at these molecular mechanisms of HCC inhibition and neuronal protection could provide novel solutions in the fight against AD.

To better understand the molecular characteristics of the studied system the modern method of single particle cryo-EM reconstruction can be used. The newest microscopic equipment allows high precision (almost atomic level) to get information on the structure of molecules. This method seems to be the most relevant to study such a complicated system as Aβ fibril and its interaction with other proteins. Unpublished results from a group of a professor Kozak gives apo-HSA structure reconstruction from cryo-EM data at 3.8 Å resolution.

For a better understanding of the impact of the presence of HCC in CNS and its impact on the aggregation kinetics of the Aβ peptides, the next possible step is to investigate these systems with neuronal cell culture. The conceivable way to study phenomena is the vitality tests of cells in presence of amyloid oligomers and HCC. Extremely interesting is already confirmed by scientists fact that neurodegeneration diseases exclude the occurrence of cancer and the opposite. The study of these opposite cell systems in presence of Aβ and HCC can offer interesting outcomes.

7. List of figures and tables

List of figures:

List of tables:

8. Publications and conferences

The thesis convers partially the results described in the following scientific publications:

„Human cystatin c induces the disaggregation process of selected amyloid beta peptides – a structural and kinetic view."
A Zyla, A Martel, P Jurczak, A Moliński, A Szymańska, M Kozak, 2022
Submitted to: Nature - Scientific Reports.

„Model of interactions between Human serum albumin and human cystatin C."
A Zyla, I Zhukov, A Roy, C Ebel, M Kozak, 2022: Manuscript in preparations

Other publications:

„DNA: an almost indestructible data carrier with incomparable capacity"
A Zyla, Archeion, 2021, 122, p. 33-43, Dec. 2021. ISSN 2658-1264
doi:https://doi.org/10.4467/26581264ARC.21.014.14494

"RNA-Puzzles Round IV: 3D structure predictions of four ribozymes and two aptamers.", Miao Z, Adamiak RW, Antczak M, Boniecki MJ, Bujnicki JM, Chen SJ, Cheng CY, Cheng Y, Chou FC, Das R, Dokholyan NV, Ding F, Geniesse C, Jiang Y, Joshi A, Krokhotin A, Magnus M, Mailhot O, Major F, Mann TH, Piatkowski P, Pluta R, Popenda M, Sarzynska J, Sun L, Szachniuk M, Tian S, Wang J, Wang J, Watkins AM, Wiedemann J, Xiao Y, Xu X, Yesselman JD, Zhang D, Zhang Y, Zhang Z, Zhao C, Zhao P, Zhou Y, Zok T, **A Zyla,** Ren A, Batey RT, Golden BL, Huang L, Lilley DM, Liu Y, Patel DJ, Westhof E, RNA Journal 2020, doi: 10.1261/rna.075341.120

"RNArchitecture: a database and a classification system of RNA families, with a focus on structural information", Boccaletto, M Magnus, C Almeida, **A Zyla**, Astha, R Pluta, B Baginski, E Jankowska, S Dunin-Horkawicz, TK Wirecki, MJ Boniecki, F Stefaniak, JM Bujnicki, NAR 2017, gkx966, https://doi.org/10.1093/nar/gkx966

"SupeRNAlign: a new tool for flexible superposition of homologous RNA structures and inference of accurate structure-based sequence alignments", P Piątkowski*, J Jablonska*, **A Zyla,** D Niedziałek, D Matelska, E Jankowska, T Waleń,W Dawson, J Bujnicki, NAR-02758-Met-H- 2016.R1m, 2017, doi.: 10.1093/nar/gkx631

"Predicting the structure and vibrational frequencies of ethylene using harmonic and anharmonic approaches at the Kohn–Sham complete basis set limit"A. Buczek, T. Kupka, M. A. Broda, **A Zyla,** , J Mol Model. 2016; 22: 42. doi: 10.1007/s00894-015-2902-z

Conferences:

"Structural investigation of the amyloid aggregates in the presence of human serum albumin and human cystatin C", **A Zyla**, A Moliński , A Belczyk-Ciesielska, M Kozak, W Bal, Fourth Polish-Korean Conference on "Protein Folding: Theoretical and Experimental Approaches", Iława 9-13 Jul, 2018

"Structural insights into an amyloid β aggregation in the presence of human serum albumin and human cystatin C", **A. Zyla**, M Taube, M Kozak , K Szutkowski, W Bal, Poznań; NanoTech Poland 2019, 5-8 Jun 2019

"Theoretical and Biophysical Study of an amyloid β aggregation and complexation with human serum albumin and human cystatin C", **A Zyla**, M Taube, M Kozak , K Szutkowski, W Bal, AMPERE NMR School Poland, 23-29 Jun 2019

"Amyloids β aggregation in the presence of human serum albumin and human cystatin C – structural investigation", **A Zyla,** M Taube, M Kozak , K Szutkowski, W Bal, - Award for the best poster presentation, ISSRNS 2019 Poland: Synchrotron Radiation in Natural Science Vol. 18, No. 1-2 (2019)

"Structural investigation of beta amyloid aggregation in presence of human albumin and human cystatin C", **A Zyla**, P Jurczak, A Szymanska, M Taube, I Zhukov, M Kozak, EMBO: Small angle neutron and X-ray scattering from biomacromolecules in solution, France 23-27 Sep 2019

"Structural investigation interaction between amyloid-beta peptides and associated proteins the human serum albumin and human cystatin C", **A Zyla**, P Jurczak, A Szymanska, J Wolak, M Taube, I Zhukov, AI Kuklin, M Kozak CMR@IBR-2 Conference Online. 12-16 Oct 2020, Russia

"Interactions between amyloid-beta peptides, human serum albumin and human cystatin C studied by the use of X-ray and light scattering, NMR spectroscopy and bioinformatics", **A Zyla**, A Szymanska, J Wolak, M Taube, D Grobys, E Banachowicz, I Zhukov and M Kozak, Joint Meeting of Polish Synchrotron Radiation Society and SOLARIS Users, 9 - 11 Sep 2020 online,

"Structural studies and characteristics of interaction between amyloid-beta peptides and associated protein Human Cystatin C", **A Zyla**, A Martel, M Taube, P Jurczak, I Zhukov, M Kozak, A Szymanska NanoTech Poland 2021 - 11th International Conference, 9th-11th June 2021

"Characteristics of interaction between amyloid-beta oligomers with Human Cystatin C", **A Zyla**, A Martel, M Taube, P Jurczak, I Zhukov, M Kozak, A Szymanska, The Ampere NMR School Poland June 21-23, 2021

"Structural investigation interaction between amyloid-beta peptides and associated protein human cystatin C" **A Zyla**, International Seminar „Neutrons and Synchrotron Radiation in Investigations of Condensed Matter", Russia 12-13 Oct 2021 online

"Structural characterization of selected Aß peptides in the presents of protein human cystatin C", **A Zyla**, A Martel, P Jurczak, I Zhukov, A Szymanska, M Kozak, NanoTech Poland - 12th International Conference, 9th-11th June 2022

"ModeRNA 2.0: the use of multiple templates improves accuracy of RNA 3D structure models in automated homology modeling", **A Zyla**, P Piatkowski, M Rother, KM Rother, JM Bujnicki 22nd Annual Meeting of the RNA Society, Czech Republic 05.30 May – 06.3 Jun 2017

"ModeRNA 2.0: the use of multiple templates improves accuracy of RNA 3D structure models in automated homology modeling", **A Zyla**, P Piatkowski, M Rother, KM Rother, JM Bujnicki RNAtion, Poland 18-19 Sep 2017

"On the nature of pigments in red coral and African snail shell", T Kupka, P Tarnowski , **A Zyła,** M Stachow, A Buczek, R Szostak, HM Lin, L Stobinski, LW Fan, Polish-Taiwanese Conference From Molecular Modeling to Nano and Biotechnology, Poland 4-6 Oct 2014

9. References

1. Nichols, E. *et al.* Estimation of the global prevalence of dementia in 2019 and forecasted prevalence in 2050: an analysis for the Global Burden of Disease Study 2019. *Lancet Public Health* **7**, 105–125 (2022).
2. Biggs, S. *et al.* Dementia as a source of social disadvantage and exclusion. *Australas. J. Ageing* **38**, 26–33 (2019).
3. Livingston, G. *et al.* Dementia prevention, intervention, and care: 2020 report of the Lancet Commission. *The Lancet* **396**, 413–446 (2020).
4. Sharp, E. S. & Gatz, M. Relationship between education and dementia: an updated systematic review. *Alzheimer Dis. Assoc. Disord.* **25**, 289–304 (2011).
5. Lin, X. *et al.* Contributions of DNA damage to Alzheimer's Disease. *Int. J. Mol. Sci.* **21**, (2020).
6. Bakulski, K. M. *et al.* Heavy metals exposure and Alzheimer's Disease and related dementias. *J. Alzheimers Dis.* **76**, 1215–1242 (2020).
7. Nigam, D. Chapter: Free radicals and oxidative stress in neurodegenerative disorders. in *Book: Free Radicals in Human Health and Disease* 143–158 (Springer India, 2015).
8. Deuschl, G. *et al.* The burden of neurological diseases in Europe: an analysis for the Global Burden of Disease Study 2017. *Lancet Public Health* **5**, 551–567 (2020).
9. Baum, F. *et al.* New Perspective on Why Women Live Longer Than Men: An Exploration of Power, Gender, Social Determinants, and Capitals. *Int. J. Environ. Res. Public. Health* **18**, (2021).
10. Pike, C. J. Sex hormones aging and Alzheimer s disease. *Front. Biosci.* **E4**, 976–997 (2012).
11. Wimo, A. *et al.* The worldwide economic impact of dementia 2010. *Alzheimers Dement.* **9**, (2013).
12. Koffie, R. M. *et al.* Alzheimer's disease: synapses gone cold. *Mol. Neurodegener.* **6**, 63 (2011).
13. Pensalfini, A. *et al.* Intracellular amyloid and the neuronal origin of Alzheimer neuritic plaques. *Neurobiol. Dis.* **71**, 53–61 (2014).
14. Medeiros, R. *et al.* The role of tau in Alzheimer's Disease and related disorders: role of tau in AD and related disorders. *CNS Neurosci. Ther.* **17**, 514–524 (2011).
15. De Loof, A. & Schoofs, L. Alzheimer's Disease: is a dysfunctional mevalonate biosynthetic pathway the master-inducer of deleterious changes in cell physiology? *OBM Neurobiol.* **3**, (2019).
16. H. Ferreira-Vieira, T. *et al.* Alzheimer's disease: targeting the cholinergic system. *Curr. Neuropharmacol.* **14**, 101–115 (2016).
17. Ke, P. C. *et al.* Implications of peptide assemblies in amyloid diseases. *Chem. Soc. Rev.* **46**, 6492–6531 (2017).
18. Glenner, G. G. & Wong, C. W. Alzheimer's disease: Initial report of the purification and characterization of a novel cerebrovascular amyloid protein. *Biochem. Biophys. Res. Commun.* **120**, 885–890 (1984).

19. Kokjohn, T. A. & Roher, A. E. Amyloid precursor protein transgenic mouse models and Alzheimer's disease: Understanding the paradigms, limitations, and contributions. *Alzheimers Dement.* **5**, 340–347 (2009).
20. Chow, V. W. *et al.* An overview of APP processing enzymes and products. *NeuroMolecular Med.* **12**, (2010).
21. Mann, D. M. A. *et al.* The topography of plaques and tangles in Down's Syndrome patients of different ages. *Neuropathol. Appl. Neurobiol.* **12**, 447–457 (1986).
22. Schenk, D. *et al.* Treatment Strategies Targeting Amyloid -Protein. *Cold Spring Harb. Perspect. Med.* **2**, 6387–6387 (2012).
23. Silvestro, S. *et al.* Aducanumab and Its Effects on Tau Pathology: Is This the Turning Point of Amyloid Hypothesis? *Int. J. Mol. Sci.* **23**, 2011 (2022).
24. Kim, J. *et al.* The Role of Apolipoprotein E in Alzheimer's Disease. *Neuron* **63**, 287–303 (2009).
25. Liu, C.-C. *et al.* Apolipoprotein E and Alzheimer disease: risk, mechanisms and therapy. *Nat. Rev. Neurol.* **9**, 106–118 (2013).
26. Gratuze, M. *et al.* New insights into the role of TREM2 in Alzheimer's disease. *Mol. Neurodegener.* **13**, (2018).
27. Roussos, P. *et al.* The triggering receptor expressed on myeloid cells 2 (*TREM2*) is associated with enhanced inflammation, neuropathological lesions and increased risk for Alzheimer's dementia. *Alzheimers Dement.* **11**, 1163–1170 (2015).
28. Alzheimer's disease facts and figures. *Alzheimers Dement.* **17**, 327–406 (2021).
29. Bertram, S. *et al.* Exercise for the diabetic brain: how physical training may help prevent dementia and Alzheimer's disease in T2DM patients. *Endocrine* **53**, 350–363 (2016).
30. Szekely, C. A. & Zandi, P. P. Non-Steroidal Anti-Inflammatory Drugs and Alzheimers Disease: The Epidemiological Evidence. *CNS Neurol. Disord. - Drug Targets* **9**, 132–139 (2010).
31. Rapport: FDA-Approved Treatments for Alzheimer's, Alzheimer's association, https://www.alz.org/national/documents/topicsheet_treatments.pdf. (2021).
32. Chen, G. *et al.* Amyloid beta: structure, biology and structure-based therapeutic development. *Acta Pharmacol. Sin.* **38**, 1205–1235 (2017).
33. Picone, P. *et al.* Aβ oligomers and fibrillar aggregates induce different apoptotic pathways in LAN5 neuroblastoma cell cultures. *Biophys. J.* **96**, 4200–4211 (2009).
34. Bergström, P. *et al.* Amyloid precursor protein expression and processing are differentially regulated during cortical neuron differentiation. *Sci. Rep.* **6**, (2016).
35. Klajnert, B. *et al.* Dendrimers reduce toxicity of Aβ 1-28 peptide during aggregation and accelerate fibril formation. *Nanomedicine Nanotechnol. Biol. Med.* **8**, 1372–1378 (2012).
36. Kollmer, M. *et al.* Cryo-EM structure and polymorphism of Aβ amyloid fibrils purified from Alzheimer's brain tissue. *Nat. Commun.* **10**, (2019).
37. Di Scala, C. *et al.* Common molecular mechanism of amyloid pore formation by Alzheimer's β-amyloid peptide and α-synuclein. *Sci. Rep.* **6**, (2016).
38. Przygońska, K. *et al.* Side-chain moieties from the N-terminal region of Aβ are Involved in an oligomer-stabilizing network of interactions. *PLOS ONE* **13**, (2018).
39. Selkoe, D. J. Soluble oligomers of the amyloid β-protein impair synaptic plasticity and behavior. *Behav. Brain Res.* **192**, 106–113 (2008).

40. Spitzer, P. *et al.* Pharmacological Inhibition of Amyloidogenic APP Processing and Knock-Down of APP in Primary Human Macrophages Impairs the Secretion of Cytokines. *Front. Immunol.* **11**, (2020).
41. Duce, J. A. *et al.* Iron-Export Ferroxidase Activity of β-Amyloid Precursor Protein Is Inhibited by Zinc in Alzheimer's Disease. *Cell* **142**, 857–867 (2010).
42. Tyan, S.-H. *et al.* Amyloid precursor protein (APP) regulates synaptic structure and function. *Mol. Cell. Neurosci.* **51**, 43–52 (2012).
43. Coronel, R. *et al.* Role of Amyloid Precursor Protein (APP) and Its Derivatives in the Biology and Cell Fate Specification of Neural Stem Cells. *Mol. Neurobiol.* **55**, 7107–7117 (2018).
44. Zheng, H. & Koo, E. H. The amyloid precursor protein: beyond amyloid. *Mol. Neurodegener.* **1**, 5 (2006).
45. Coburger, I. *et al.* The structural biology of the amyloid precursor protein APP – a complex puzzle reveals its multi-domain architecture. *Biol. Chem.* **395**, 485–498 (2014).
46. Bhattacharyya, R. *et al.* Palmitoylation of Amyloid Precursor Protein Regulates Amyloidogenic Processing in Lipid Rafts. *J. Neurosci.* **33**, 11169–11183 (2013).
47. Tun, H. *et al.* Lipid Rafts Play an Important Role in A` Biogenesis by Regulating the `-Secretase Pathway. *J. Mol. Neurosci.* **19**, (2002).
48. Asuni, A. A. *et al.* Modulation of amyloid precursor protein expression reduces β-amyloid deposition in a mouse model: Targeting of APP Expression in AD Mice. *Ann. Neurol.* **75**, 684–699 (2014).
49. Jumper, J. *et al.* Highly accurate protein structure prediction with AlphaFold. *Nature* **596**, 583–589 (2021).
50. Bateman, A. *et al.* UniProt: the universal protein knowledgebase in 2021. *Nucleic Acids Res.* **49**, 480–489 (2021).
51. Porayette, P. *et al.* Amyloid-β precursor protein expression and modulation in human embryonic stem cells: A novel role for human chorionic gonadotropin. *Biochem. Biophys. Res. Commun.* **364**, 522–527 (2007).
52. Portelius, E. *et al.* The amyloid-β isoform pattern in cerebrospinal fluid in familial PSEN1 M139T- and L286P-associated Alzheimer's disease. *Mol. Med. Rep.* **5**, 1111–1115 (2012).
53. Nizynski, B. *et al.* Amyloidogenesis of Tau protein: Tau aggregation. *Protein Sci.* **26**, 2126–2150 (2017).
54. Brown, M. R. *et al.* Modulation of β-Amyloid Fibril Formation in Alzheimer's Disease by Microglia and Infection. *Front. Mol. Neurosci.* **13**, (2020).
55. Rijal Upadhaya, A. *et al.* The type of Aβ-related neuronal degeneration differs between amyloid precursor protein (APP23) and amyloid β-peptide (APP48) transgenic mice. *Acta Neuropathol. Commun.* **1**, (2013).
56. Lee, J. *et al.* Amyloid β ion channels in a membrane comprising brain total lipid extracts. *ACS Chem. Neurosci.* **8**, 1348–1357 (2017).
57. Kuo, Y.-M. *et al.* Amyloid-β Peptides Interact with Plasma Proteins and Erythrocytes: Implications for Their Quantitation in Plasma. *Biochem. Biophys. Res. Commun.* **268**, 750–756 (2000).
58. Östner, G. *et al.* Stabilization, characterization, and selective removal of cystatin c amyloid oligomers. *J. Biol. Chem.* **288**, 16438–16450 (2013).

59. Mussap, M. & Plebani, M. Biochemistry and clinical role of human cystatin c. *Crit. Rev. Clin. Lab. Sci.* **41**, 467–550 (2004).
60. Mi, W. *et al.* Complexes of amyloid-β and cystatin c in the human central nervous system. *J. Alzheimer's Dis.* **18**, 273–280 (2009).
61. Deng, A. *et al.* Elevation of Cystatin C in susceptible neurons in Alzheimer's Disease. *Am. J. Pathol.* **159**, 1061–1068 (2001).
62. Janowski, R. *et al.* Human cystatin C, an amyloidogenic protein, dimerizes through three-dimensional domain swapping. *Nat. Struct. Biol.* **8**, (2001).
63. Janowski, R. *et al.* 3D domain-swapped human cystatin C with amyloidlike intermolecular β-sheets. *Proteins Struct. Funct. Bioinforma.* **61**, 570–578 (2005).
64. Taube, M. *et al.* The domain swapping of human cystatin C induced by synchrotron radiation. *Sci. Rep.* **9**, (2019).
65. Maszota-Zieleniak, M. *et al.* NMR and crystallographic structural studies of the extremely stable monomeric variant of human cystatin C with single amino acid substitution. *FEBS J.* **287**, 361–376 (2020).
66. Chrabąszczewska, M. *et al.* Structural Characterization of Covalently Stabilized Human Cystatin C Oligomers. *Int. J. Mol. Sci.* **21**, (2020).
67. Xu, Y. *et al.* Developmental regulation of synthesis and dimerization of the amyloidogenic protease inhibitor cystatin c in the hematopoietic system. *J. Biol. Chem.* **289**, 9730–9740 (2014).
68. Lloyd, G. M. *et al.* Prominent amyloid plaque pathology and cerebral amyloid angiopathy in APP V717I (London) carrier – phenotypic variability in autosomal dominant Alzheimer's disease. *Acta Neuropathol. Commun.* **8**, (2020).
69. Finckh, U. Genetic association of a cystatin C gene polymorphism with Late-Onset Alzheimer Disease. *Arch. Neurol.* **57**, (2000).
70. Tizon, B. *et al.* Induction of autophagy by cystatin c: a mechanism that protects murine primary cortical neurons and neuronal cell lines. *PLoS ONE* **5**, (2010).
71. Sastre, M. *et al.* Binding of cystatin C to Alzheimer's amyloid β inhibits in vitro amyloid fibril formation. *Neurobiol. Aging* **25**, 1033–1043 (2004).
72. Kim, J.-T. *et al.* Cystatin SN neutralizes the inhibitory effect of cystatin C on cathepsin B activity. *Cell Death Dis.* **4**, 974–974 (2013).
73. Kaeser, S. A. *et al.* Cystatin C modulates cerebral β-amyloidosis. *Nat. Genet.* **39**, 1437–1439 (2007).
74. Dockal, M. *et al.* The three recombinant domains of human serum albumin. *J. Biol. Chem.* **274**, 29303–29310 (1999).
75. Karligiotou, E. *et al.* Expression of human serum albumin (HSA) mRNA in human granulosa cells: potential correlation of the 95 amino acid long carboxyl terminal of HSA to gonadotrophin surge-attenuating factor. *Hum. Reprod.* **21**, 645–650 (2006).
76. Raposo, A. C. *et al.* Comparative analysis of tear composition in humans, domestic mammals, reptiles, and birds. *Front. Vet. Sci.* **7**, (2020).
77. Levitt, D. & Levitt, M. Human serum albumin homeostasis: a new look at the roles of synthesis, catabolism, renal and gastrointestinal excretion, and the clinical value of serum albumin measurements. *Int. J. Gen. Med.* **9**, 229–255 (2016).

78. Hosseinpour Moghadam, N. *et al.* Preparation of a highly stable drug carrier by efficient immobilization of human serum albumin (HSA) on drug-loaded magnetic iron oxide nanoparticles. *Int. J. Biol. Macromol.* **125**, 931–940 (2019).
79. Belinskaia, D. A. *et al.* Serum Albumin. *Encyclopedia* **1**, 65–75 (2020).
80. Chubarov, A. *et al.* Reversible dimerization of human serum albumin. *Molecules* **26**, (2020).
81. Al-Harthi, S. *et al.* Towards the functional high-resolution coordination chemistry of blood plasma human serum albumin. *J. Inorg. Biochem.* **198**, (2019).
82. Handing, K. B. *et al.* Circulatory zinc transport is controlled by distinct interdomain sites on mammalian albumins. *Chem. Sci.* **7**, 6635–6648 (2016).
83. Lomis, N. *et al.* Human Serum Albumin nanoparticles for use in cancer drug delivery: process optimization and in vitro characterization. *Nanomaterials* **6**, (2016).
84. Sun, L. Human Serum Albumin (HSA) and its applications as a drug delivery vehicle. *Health Sci. J.* **14**, (2020).
85. Mishra, A. *et al.* Triantennary GalNAc Molecular Imaging Probes for Monitoring Hepatocyte Function in a Rat Model of Nonalcoholic Steatohepatitis. *Adv. Sci.* **7**, (2020).
86. Guo, C. & Zhou, H.-X. Fatty acids compete with Aβ in binding to serum albumin by quenching its conformational flexibility. *Biophys. J.* **116**, 248–257 (2019).
87. Choi, T. S. *et al.* Molecular Insights into Human Serum Albumin as a Receptor of Amyloid-β in the Extracellular Region. *J. Am. Chem. Soc.* **139**, 15437–15445 (2017).
88. Milojevic, J. & Melacini, G. Stoichiometry and affinity of the human serum albumin-Alzheimer's Aβ peptide interactions. *Biophys. J.* **100**, 183–192 (2011).
89. Litus, E. A. *et al.* The binding of monomeric amyloid β peptide to serum albumin is affected by major plasma unsaturated fatty acids. *Biochem. Biophys. Res. Commun.* **510**, 248–253 (2019).
90. Tang, T.-C. *et al.* Conformational changes induced by the A21G Flemish mutation in the amyloid precursor protein lead to increased Aβ production. *Structure* **22**, 387–396 (2014).
91. Wang, L. *et al.* Current understanding of metal ions in the pathogenesis of Alzheimer's disease. *Transl. Neurodegener.* **9**, (2020).
92. Strodel, B. & Coskuner-Weber, O. Transition metal ion Interactions with disordered amyloid-β Peptides in the pathogenesis of Alzheimer's Disease: Insights from computational chemistry studies. *J. Chem. Inf. Model.* **59**, 1782–1805 (2019).
93. Williams, T. L. *et al.* Stabilization of native amyloid β-protein oligomers by copper and hydrogen peroxide Induced cross-linking of unmodified proteins (CHICUP). *Biochim. Biophys. Acta BBA - Proteins Proteomics* **1864**, 249–259 (2016).
94. Trujano-Ortiz, L. G. *et al.* Redox cycling of copper–amyloid β 1–16 peptide complexes is highly dependent on the coordination mode. *Inorg. Chem.* **54**, 4–6 (2015).
95. Sun, J.-H. *et al.* The role of cholesterol metabolism in Alzheimer's Disease. *Mol. Neurobiol.* **51**, 947–965 (2015).
96. Dies, H. *et al.* The Interaction between Amyloid-β Peptides and Anionic Lipid Membranes Containing Cholesterol and Melatonin. *PLoS ONE* **9**, (2014).
97. Jurczak, P. Studies on the influence of protein-ligand and protein-cell membrane interactions on the amyloidogenic protein oligomerization process: the case of human cystatin. (Faculty of Chemistry, University of Gdańsk, 2019).

98. Sengupta, U. *et al.* The Role of Amyloid-β Oligomers in Toxicity, Propagation, and Immunotherapy. *EBioMedicine* **6**, 42–49 (2016).
99. Barrow-f, C. J. *et al.* Solution conformations and aggregational properties of synthetic amyloid peptides of Alzheimer's Disease. *J Mol Biol* **225**, 1075–1093 (1992).
100. Fändrich, M. *et al.* Structural polymorphism of Alzheimer Aβ and other amyloid fibrils. *Prion* **3**, 89–93 (2009).
101. Eisenberg, D. *et al.* Analysis of membrane and surface protein sequences with the hydrophobic moment plot. *J. Mol. Biol.* **179**, 125–142 (1984).
102. Ryan, T. M. *et al.* Ammonium hydroxide treatment of Aβ produces an aggregate free solution suitable for biophysical and cell culture characterization. *PeerJ* **1**, e73 (2013).
103. Gommes, C. J. *et al.* Small-angle scattering for beginners. *J. Appl. Crystallogr.* **54**, 1832–1843 (2021).
104. Petoukhov, M. V. & Svergun, D. I. Ambiguity assessment of small-angle scattering curves from monodisperse systems. *Acta Crystallogr. D Biol. Crystallogr.* **71**, 1051–1058 (2015).
105. Guinier, A. Small-angle scattering of X-rays. *N. Y. JOHN WILEY SONS Inc* (1955).
106. Feigin, L. A. & Svergun, D. I. *Structure Analysis by Small-Angle X-Ray and Neutron Scattering*. (Springer US, 1987)
107. Lombardo, D. *et al.* Structural characterization of biomaterials by means of Small Angle X-rays and Neutron Scattering (SAXS and SANS), and Light Scattering Experiments. *Molecules* **25**, (2020).
108. Bernado, P. & Svergun, D. I. Structural analysis of intrinsically disordered proteins by small-angle X-ray scattering. *Mol.BioSyst* **8**, 151–167 (2012).
109. Zhang, Y. *et al.* Novel X-Ray and Optical Diagnostics for Studying Energetic Materials: A Review. *Engineering* **6**, 992–1005 (2020).
110. Heller, W. T. Small-angle neutron scattering and contrast variation: a powerful combination for studying biological structures. *Acta Crystallogr. D Biol. Crystallogr.* **66**, 1213–1217 (2010).
111. Mahieu, E. *et al.* The power of SANS, combined with deuteration and contrast variation, for structural studies of functional and dynamic biomacromolecular systems in solution. *EPJ Web Conf.* **236**, (2020).
112. Manalastas-Cantos, K. *et al. ATSAS 3.0* : expanded functionality and new tools for small-angle scattering data analysis. *J. Appl. Crystallogr.* **54**, 343–355 (2021).
113. Svergun, D. I. Restoring low resolution structure of biological macromolecules from solution scattering using simulated annealing. *Biophys. J.* **76**, 2879–2886 (1999).
114. Franke, D. & Svergun, D. I. *DAMMIF* , a program for rapid *ab-initio* shape determination in small-angle scattering. *J. Appl. Crystallogr.* **42**, 342–346 (2009).
115. Svergun, D. I. *et al.* Determination of domain structure of proteins from X-Ray Solution Scattering. *Biophys. J.* **80**, 2946–2953 (2001).
116. Svergun, D. I. *et al.* Protein hydration in solution: Experimental observation by x-ray and neutron scattering. *Proc. Natl. Acad. Sci.* **95**, 2267–2272 (1998).
117. Marley, J. *et al.* A method for efficient isotopic labeling of recombinant proteins. *J. Biomol. NMR* **20**, 71–75 (2001).

118. Zhang, Q. *et al.* Expression, purification and identification of isotope-labeled recombinant cystatin C protein in Escheichia coli intended for absolute quantification using isotope dilution mass spectrometry. *Protein Expr. Purif.* **178**, (2021).
119. Cioni, P. & Strambini, G. B. Effect of heavy water on protein flexibility. *Biophys. J.* **82**, 3246–3253 (2002).
120. Opitz, C. *et al.* Deuterium induces a distinctive Escherichia coli proteome that correlates with the reduction in growth rate. *J. Biol. Chem.* **294**, 2279–2292 (2019).
121. Pakhrin, S. C. *et al.* Deep Learning-Based Advances in Protein Structure Prediction. *Int. J. Mol. Sci.* **22**, (2021).
122. Hollingsworth, S. A. & Dror, R. O. Molecular Dynamics Simulation for All. *Neuron* **99**, 1129–1143 (2018).
123. Friesner, R. A. *et al.* Glide: a new approach for rapid, accurate docking and scoring. *J. Med. Chem.* **47**, 1739–1749 (2004).
124. Bartuzi, D. *et al.* Recent Advances and Applications of Molecular Docking to G Protein-Coupled Receptors. *Molecules* **22**, (2017).
125. Vakser, I. A. Protein-Protein Docking: From Interaction to Interactome. *Biophys. J.* **107**, 1785–1793 (2014).
126. Ingólfsson, H. I. *et al.* The power of coarse graining in biomolecular simulations: The power of coarse graining in biomolecular simulations. *Wiley Interdiscip. Rev. Comput. Mol. Sci.* **4**, 225–248 (2014).
127. Levitt, M. & Warshel, A. Computer simulation of protein folding. *Nature* **253**, 694–698 (1975).
128. Kmiecik, S. *et al.* Coarse-Grained protein models and their applications. *Chem. Rev.* **116**, 7898–7936 (2016).
129. Czaplewski, C. *et al.* UNRES server for physics-based coarse-grained simulations and prediction of protein structure, dynamics and thermodynamics. *Nucleic Acids Res.* **46**, 304–309 (2018).
130. Varela, D. & Santos, J. Protein structure prediction in an atomic model with differential evolution integrated with the crowding niching method. *Nat. Comput.* (2020)
131. Vahabi, S. *et al.* Atomic Force Microscopy application in biological research: a review study. *J Med Sci* **38**, (2013).
132. Bayda, S. *et al.* The History of Nanoscience and Nanotechnology: From Chemical–Physical Applications to Nanomedicine. *Molecules* **25**, (2019).
133. Veerapandian, M. & Yun, K. Study of Atomic Force Microscopy in Pharmaceutical and Biopharmaceutical Interactions - A Mini Review. *Curr. Pharm. Anal.* **5**, 256–268 (2009).
134. Shen, P. S. The 2017 Nobel Prize in Chemistry: cryo-EM comes of age. *Anal. Bioanal. Chem.* **410**, 2053–2057 (2018).
135. Edwards, G. B. *et al.* Analytical Ultracentrifugation (AUC): an overview of the application of fluorescence and absorbance AUC to the study of biological macromolecules. *Curr. Protoc. Mol. Biol.* **133**, (2020).
136. Erickson, H. P. Size and and shape of protein molecules at the nanometer level determined by sedimentation, gel filtration, and electron microscopy. *Biol. Proced. Online* **11**, 32–51 (2009).

137. Schuck, P. Size-distribution analysis of macromolecules by sedimentation velocity ultracentrifugation and lamm equation modeling. *Biophys. J.* **78**, 1606–1619 (2000).
138. Olshina, M. A. & Sharon, M. Mass spectrometry: a technique of many faces. *Q. Rev. Biophys.* **49**, (2016).
139. Coon, J. J. *et al.* Tandem Mass Spectrometry for Peptide and Protein Sequence Analysis. *BioTechniques* **38**, 519–523 (2005).
140. Leney, A. C. & Heck, A. J. R. Native Mass Spectrometry: What is in the Name? *J. Am. Soc. Mass Spectrom.* **28**, 5–13 (2017).
141. Marion, D. An Introduction to biological NMR spectroscopy. *Mol. Cell. Proteomics* **12**, 3006–3025 (2013).
142. Lipari, G. & Szabo, A. Model-free approach to the interpretation of nuclear magnetic resonance relaxation in macromolecules. 1. Theory and range of validity. *J. Am. Chem. Soc.* **104**, 4546–4559 (1982).
143. Zumpfe, K. & Smith, A. A. Model-Free or Not? *Front. Mol. Biosci.* **8**, (2021).
144. Petrova, O. E. & Sauer, K. High-Performance Liquid Chromatography (HPLC)-Based Detection and Quantitation of Cellular c-di-GMP. in *c-di-GMP Signaling* (ed. Sauer, K.) vol. 1657 33–43 (Springer New York, 2017).
145. Stine, W. B. *et al.* Preparing Synthetic Aβ in Different Aggregation States. in *Alzheimer's Disease and Frontotemporal Dementia* (ed. Roberson, E. D.) vol. 670 13–32 (Humana Press, 2010).
146. Brinas, L. *et al.* -Lactamases in Ampicillin-Resistant Escherichia coli Isolates from Foods, Humans, and Healthy Animals. *ANTIMICROB AGENTS CHEMOTHER* **46**, 8 (2002).
147. Kuklin, A. I. *et al.* Scientific Reviews: Two-Detector System for Small-Angle Neutron Scattering Instrument. *Neutron News* **16**, 16–18 (2005).
148. Grudinin, S. *et al. Pepsi-SAXS* : an adaptive method for rapid and accurate computation of small-angle X-ray scattering profiles. *Acta Crystallogr. Sect. Struct. Biol.* **73**, 449–464 (2017).
149. Konarev, P. V. *et al.* Rapid automated superposition of shapes and macromolecular models using spherical harmonics. *J. Appl. Crystallogr.* **49**, 953–960 (2016).
150. Schneidman-Duhovny, D. *et al.* FoXS, FoXSDock and MultiFoXS: Single-state and multi-state structural modeling of proteins and their complexes based on SAXS profiles. *Nucleic Acids Res.* **44**, 424–429 (2016).
151. Schneidman-Duhovny, D. *et al.* PatchDock and SymmDock: servers for rigid and symmetric docking. *Nucleic Acids Res.* **33**, 363–367 (2005).
152. Kline, S. R. Reduction and analysis of SANS and USANS data using IGOR Pro. *J. Appl. Crystallogr.* **39**, 895–900 (2006).
153. SasView - open source, collaboratively developed software for the analysis of any small angle scattering data. *http://www.sasview.org/*.
154. Kozin, M. B. & Svergun, D. I. Automated matching of high- and low-resolution structural models. *J. Appl. Crystallogr.* **34**, 33–41 (2001).
155. Rigsby, R. E. & Parker, A. B. Using the PyMOL application to reinforce visual understanding of protein structure: PyMOL Application to Understand Protein Structure. *Biochem. Mol. Biol. Educ.* **44**, 433–437 (2016).

156. Zhao, H. *et al.* Quantitative Analysis of Protein Self-Association by Sedimentation Velocity. *Curr. Protoc. Protein Sci.* **101**, (2020).
157. Schuck, P. *et al.* SEDFIT–MSTAR: molecular weight and molecular weight distribution analysis of polymers by sedimentation equilibrium in the ultracentrifuge. *The Analyst* **139**, 79–92 (2014).
158. Brautigam, C. A. Calculations and publication-quality illustrations for analytical ultracentrifugation data. in *Methods in Enzymology* vol. 562 109–133 (Elsevier, 2015).
159. Varian. BioPack User Guide. 191 (2009).
160. Delaglio, F. *et al.* NMRPipe: A multidimensional spectral processing system based on UNIX pipes. *J. Biomol. NMR* **6**, (1995).
161. Lee, W. *et al.* NMRFAM-SPARKY: enhanced software for biomolecular NMR spectroscopy. *Bioinformatics* **31**, 1325–1327 (2015).
162. Kurcinski, M. *et al.* CABS-dock web server for the flexible docking of peptides to proteins without prior knowledge of the binding site. *Nucleic Acids Res.* **43**, W419–W424 (2015).
163. Santoro, A. *et al.* Exploring the early stages of the amyloid Aβ(1–42) peptide sggregation Process: An NMR study. *Pharmaceuticals* **14**, 732 (2021).
164. Ciudad, S. *et al.* Aβ(1-42) tetramer and octamer structures reveal edge conductivity pores as a mechanism for membrane damage. *Nat. Commun.* **11**, (2020).
165. Yang, F. *et al.* Effect of human serum albumin on drug metabolism: Structural evidence of esterase activity of human serum albumin. *J. Struct. Biol.* **157**, 348–355 (2007).
166. Kok, C. M. & Rudin, A. Relationship between the hydrodynamic radius and the radius of gyration of a polymer in solution. *Makromol. Chem. Rapid Commun.* **2**, 655–659 (1981).
167. Yu, S. *et al.* Stability of human serum albumin structure upon toxin uptake explored by small angle neutron scattering. *Polymer* **141**, 175–183 (2018).
168. Lingor, P. *et al.* SARS-CoV-2 and neurodegenerative diseases: what we know and what we don't. *J. Neural Transm.* (2022)
169. Kametani, F. & Hasegawa, M. Reconsideration of amyloid hypothesis and tau hypothesis in Alzheimer's disease. *Front. Neurosci.* **12**, (2018).
170. Cummings, J. & Salloway, S. Aducanumab: Appropriate use recommendations. *Alzheimers Dement.* **18**, 531–533 (2022).
171. Levy, E. *et al.* Codeposition of cystatin c with amyloid-β protein in the brain of Alzheimer disease patients. *J Neuropathol Exp Neurol* **60**, (2001).
172. Tizon, B. *et al.* Cystatin C protects neuronal cells from Amyloid-β-induced toxicity. *J. Alzheimers Dis.* **19**, 885–894 (2010).
173. Moore, B. D. *et al.* Overlapping profiles of Abeta peptides in the Alzheimer's disease and pathological aging brains. *Alzheimers Res. Ther.* **4**, (2012).
174. Singh, Y. *et al.* Mucin-Type O-Glycosylation Proximal to β-Secretase Cleavage Site Affects APP Processing and Aggregation Fate. *Front. Chem.* **10**, (2022).
175. Watanabe-Nakayama, T. *et al.* High-Speed Atomic Force Microscopy reveals the structural dynamics of the amyloid-β and amylin aggregation pathways. *Int. J. Mol. Sci.* **21**, (2020).
176. Tycko, R. Solid-State NMR studies of amyloid fibril structure. *Annu. Rev. Phys. Chem.* **62**, 279–299 (2011).

177. Selivanova, O. M. *et al.* X-ray diffraction and electron microscopy data for amyloid formation of Aβ40 and Aβ42. *Data Brief* **8**, 108–113 (2016).
178. Sinha, S. *et al.* A Key Role for Lysine Residues in Amyloid β-Protein Folding, Assembly, and Toxicity. *ACS Chem. Neurosci.* **3**, 473–481 (2012).
179. Mithu, V. S. *et al.* Zn++ Binding Disrupts the Asp23-Lys28 Salt Bridge without Altering the Hairpin-Shaped Cross-β Structure of Aβ42 Amyloid Aggregates. *Biophys. J.* **101**, 2825–2832 (2011).
180. Morel, B. *et al.* Environmental conditions affect the kinetics of nucleation of amyloid fibrils and determine their morphology. *Biophys. J.* **99**, 3801–3810 (2010).
181. Jurczak, P. *et al.* Human cystatin C monomer, dimer, oligomer, and amyloid structures are related to health and disease. *FEBS Lett.* **590**, 4192–4201 (2016).
182. Perlenfein, T. J. *et al.* Insights into the mechanism of cystatin C oligomer and amyloid formation and its interaction with β-amyloid. *J. Biol. Chem.* **292**, 11485–11498 (2017).
183. Basi, G. S. *et al.* Structural correlates of antibodies Associated with acute reversal of Amyloid β-related behavioral deficits in a mouse model of Alzheimer Disease. *J. Biol. Chem.* **285**, 3417–3427 (2010).
184. Biere, A. L. *et al.* Amyloid β- peptide is transported on lipoproteins and albumin in human plasma. *J. Biol. Chem.* **271**, 32916–32922 (1996).
185. Stevens, R. W. *et al.* Application of fluoroimmunoassay to cerebrospinal fluid immunoglobulin G and albumin. *J. Clin. Microbiol.* **10**, 346–350 (1979).
186. Stanyon, H. F. & Viles, J. H. Human Serum Albumin can regulate amyloid-β peptide fiber growth in the brain interstitium. *J. Biol. Chem.* **287**, 28163–28168 (2012).
187. Nemashkalova, E. L. *et al.* Effect of Cu2+ and Zn2+ ions on human serum albumin interaction with plasma unsaturated fatty acids. *Int. J. Biol. Macromol.* **131**, 505–509 (2019).
188. Zunszain, P. A. *et al.* Crystallographic analysis of human serum albumin complexed with 4Z,15E-Bilirubin-IXα. *J. Mol. Biol.* **381**, 394–406 (2008).
189. Bellomo, G. *et al.* Dissecting the Interactions between Human Serum Albumin and α-Synuclein: New Insights on the Factors Influencing α-Synuclein Aggregation in Biological Fluids. *J. Phys. Chem. B* **123**, 4380–4386 (2019).
190. Boada, M. *et al.* Plasma exchange for Alzheimer's disease management by albumin replacement (AMBAR) trial: study design and progress. *Alzheimers Dement. Transl. Res. Clin. Interv.* **5**, 61–69 (2019).
191. Loeffler, D. A. AMBAR, an encouraging Alzheimer's trial that raises questions. *Front. Neurol.* **11**, 459 (2020).
192. Xu, Y. *et al.* Cystatin C is a disease-associated protein subject to multiple regulation. *Immunol. Cell Biol.* **93**, 442–451 (2015).
193. Mishra, V. & Heath, R. J. Structural and biochemical features of human serum albumin essential for eukaryotic cell culture. *Int. J. Mol. Sci.* **22**, (2021).
194. Kovalenko, O. V. *et al.* Atypical Antigen Recognition Mode of a Shark Immunoglobulin New Antigen Receptor (IgNAR) Variable Domain Characterized by Humanization and Structural Analysis. *J. Biol. Chem.* **288**, 17408–17419 (2013).
195. Pannecoucke, E. *et al.* Cell-penetrating Alphabody protein scaffolds for intracellular drug targeting. *Sci. Adv.* **7**, eabe1682 (2021).

196. Lejon, S. *et al.* Structural basis for the binding of naproxen to human serum albumin in the presence of fatty acids and the GA module. *Acta Crystallograph. Sect. F Struct. Biol. Cryst. Commun.* **64**, 64–69 (2008).
197. Cho, S. Y. *et al.* Structural basis of serum albumin recognition by SL335, an antibody Fab extending the serum half-life of protein therapeutics. *Biochem. Biophys. Res. Commun.* **526**, 941–946 (2020).

10. Appendix

Appending contains supplementary and supporting information for better understanding of data processing or conclusion taken by certain procedures.

A. Aβ peptides

Sequences of Aβ peptides used for this study:

Aβ (1-42) Human

DAEFRHDSGYEVHHQKLVFFAEDVGSNKGAIIGLMVGGVVIA

Aβ (3-28) Human

EFRHDSGYEVHHQKLVFFAEDVGSNK

Aβ (1-16) Human

DAEFRHDSGYEVHHQK

B. Methods used to study Aβ and its interaction with HCC and HSA

Table S 1. Summary of the method used to study Aβ and its interaction with HCC and HSA.

Sample preparation		**Compound**	
Solid state synthesis	HPLC	**Aβ peptides**	
	FPLC	**HCC, D-HCC**	
overexpression in *E. Coli*			
Commercial source	Sigma Aldrich	**HSA**	
Study of interaction			**Data derived from experiment**
AFM		**Aβ, HCC + Aβ**	topology of the sample, aggregation tracking
AUC		**HSA + HCC**	complexing
MS		**HSA + A Aβ**	interaction
NMR		**HSA + HCC**	Complexing, model of the interactions
SANS		**HCC + Aβ**	Complexing, model of complex structure, kinetics of aggregation
SAXS		**HSA + Aβ, HSA +HCC**	Complexing, model of complex structure
TEM		**HSA + Aβ**	topology of the sample, aggregation tracking
computational modeling		**HSA + HCC, HSA Aβ, HCC + Aβ**	predicted model of interactions

C. Biomolecular neutron calculator

Table S 2. Biomolecular neutron calculator results of HSA and 70% deuterated HCC

	HSA			HCC		
%D_2O	0	42	100	0	42	100
The percentage of deuteration is	0			70		
The percentage of H/D exchange	90			90		
The concentration of the biomolecule in mg/mL is	1			1		
Total number of residues	585			120		
Chemical composition	C2936', 'N', 786, 'O', 877, 'S', 41, 'H', 4477.0, 'P', 0			C580', 'N', 170, 'O', 167, 'S', 7, 'H', 901.5, 'P', 0		
The molecular weight	67.314, kDa			13.771 kDa	13.861 kDa	13.984 kDa
The scattering length	1497.91 $x10^{-4}$Å	1909.16 $x10^{-4}$Å	2477.07 $x10^{-4}$Å	749.72 $x10^{-4}$Å	860.0 $x10^{-4}$Å	1012.28 $x10^{-4}$Å
The scattering length density (ρm) of the molecule	1.846 $x10^{-6}$Å^{-2}	2.353 $x10^{-6}$ Å^{-2}	3.053 $x10^{-6}$ Å^{-2}	4.666 $x10^{-6}$ Å^{-2}	5.352 x $x10^{-6}$6 Å^{-2}	6.3 x $x10^{-6}$Å^{-2}
The scattering length density (ρs) of the solvent	-0.554 $x10^{-6}$Å^{-2}	2.357 $x10^{-6}$ Å^{-2}	6.376 $x10^{-6}$Å^{-2}	-0.554 x $x10^{-6}$Å^{-2}	2.357 $x10^{-6}$ Å^{-2}	6.376 $x10^{-6}$Å^{-2}
The molecular volume	81123.7 Å^3			16067.4 Å^3		
The number of exchangeable hydrogens at pH 7.0	1048			224.5		
The density of the biomolecule	1.36 g/ml	1.37 g/ml	1.38 g/ml	1.42 g/ml	1.43 g/ml	1.45 g/ml
The estimate of intensity at zero scattering angle I(0) of the biomolecule	0.034 cm^{-1}	6.1e^{-08} cm^{-1}	0.065 cm^{-1}	0.031 cm^{-1}	0.01 cm^{-1}	6.4e^{-06} cm^{-1}
Match point	42%			100%		

D. PatchDock and MD of HSA and Aβ 1-42

Top model of docking was taken as input structure for MD simulation performed by Gromacs. The time of simulating was 10 ns and the 26 lowest energy frames was extracted. Docked Aβ 1-42 is well fitted into a HSA structure.

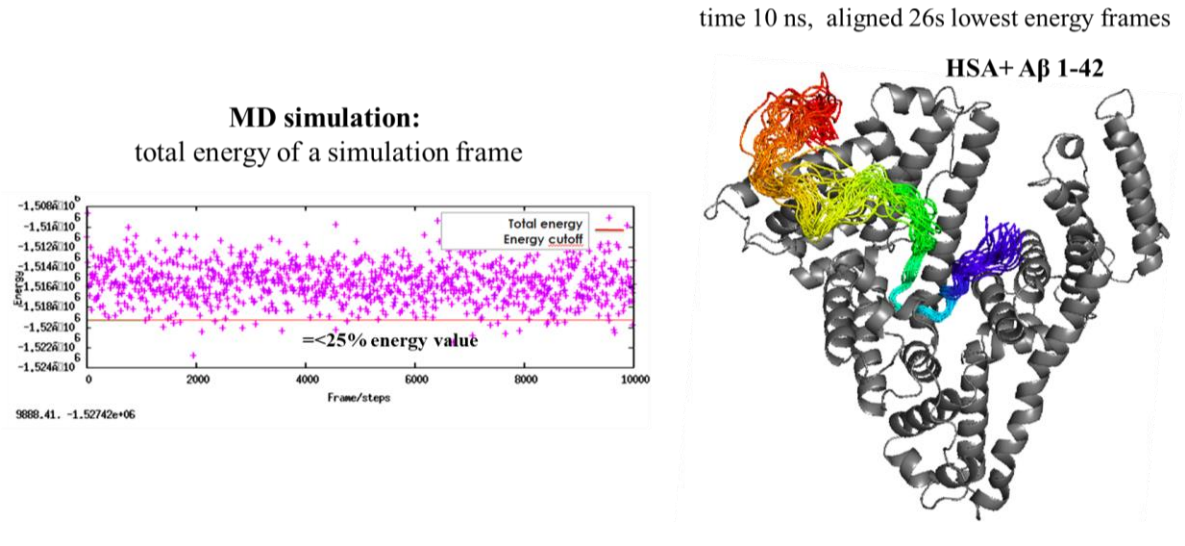

Figure S 1. MD simulation with energy minimization of HSA-Aβ 1-42 complex.

E. HSA + HCC complex AUC sedimentations profiles

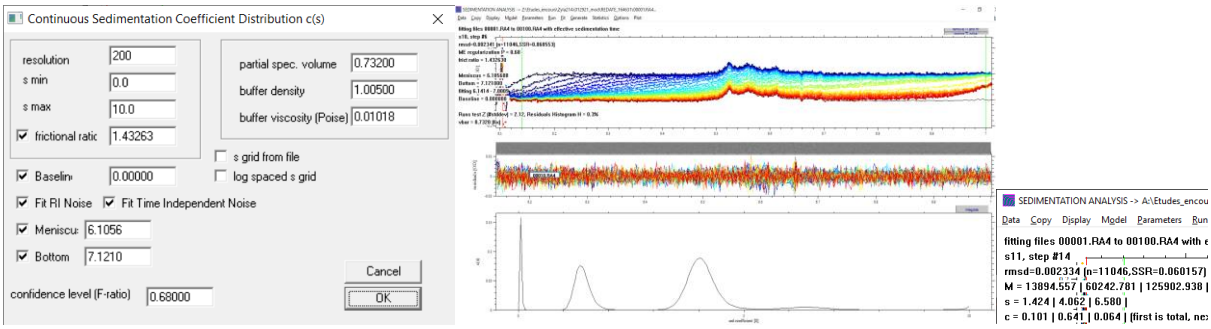

Figure S 2. AUC sedimentation profile of HCC:HSA 0.02:0.01 mM – absorbance.

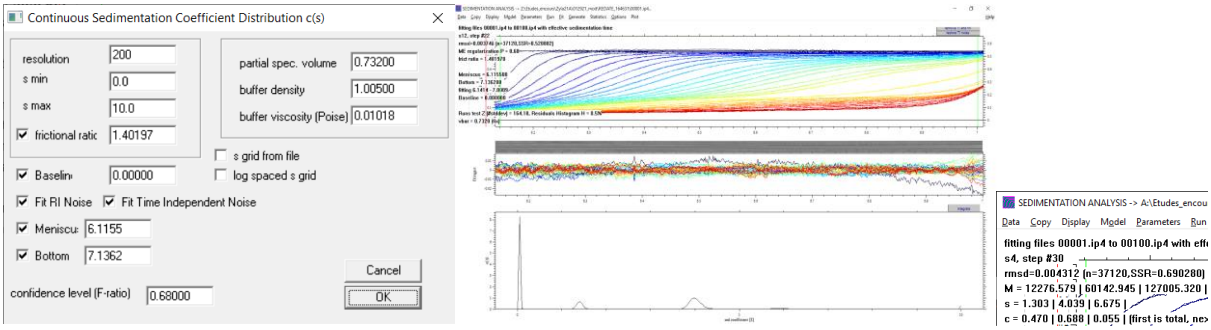

Figure S 3. AUC sedimentation profile of HCC:HSA 0.02:0.01 mM – interference.

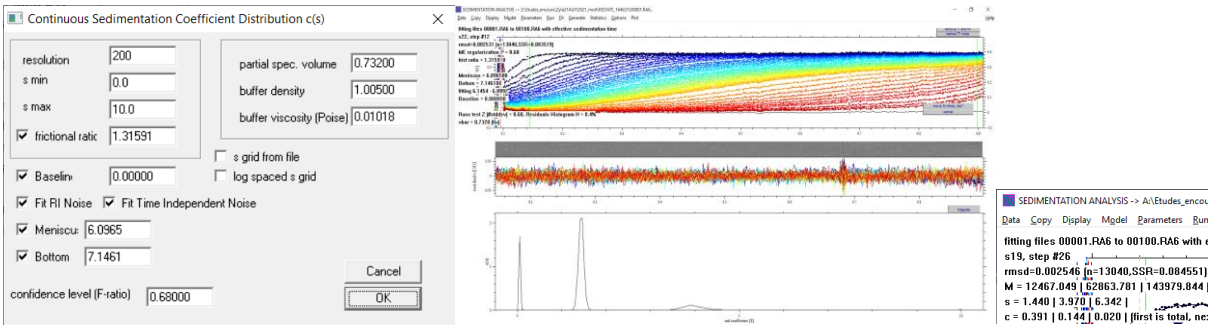

Figure S 4. AUC sedimentation profile of HCC:HSA 0.2:0.01 mM – absorbance.

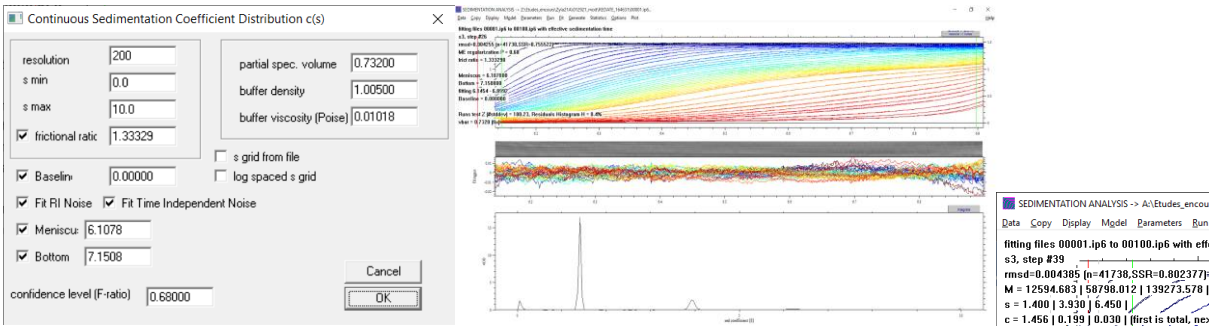

Figure S 5. AUC sedimentation profile of HCC:HSA 0.2:0.01 mM – interference.

F. Model of HSA-HCC complex – amino acids list

List of interacting residues within 5 Å proximity in Model 2 chosen as top one for structure representation of HSA-HCC complex derived by SAXS data.

HSA interacting residues

PRO303, ALA322, LYS317, TYR319, MET329, ALA229, GLU311, ALA320, ILE271, ARG336, LYS313, ALA307, VAL325, GLU230, ASP308, GLU333, ASP314, VAL315, ASP269, SER270, ASN318, LYS323, TYR332, ASP324, PHE326, GLU227, ARG337, LEU302, ASP301, GLU321, PHE228, SER312, PHE309

HCC interacting residues

GLN100, PRO13, GLY12, ASP15, GLN55, GLY59, ILE56, GLY108, GLY57, TRP106, ARG51, THR111, ASP65, GLY11, THR116, VAL104, ASN61, PHE63, SER98, LEU64, MET14, LEU9, ARG53, GLN107, TYR102, SER113, ALA58, PRO105, LYS114

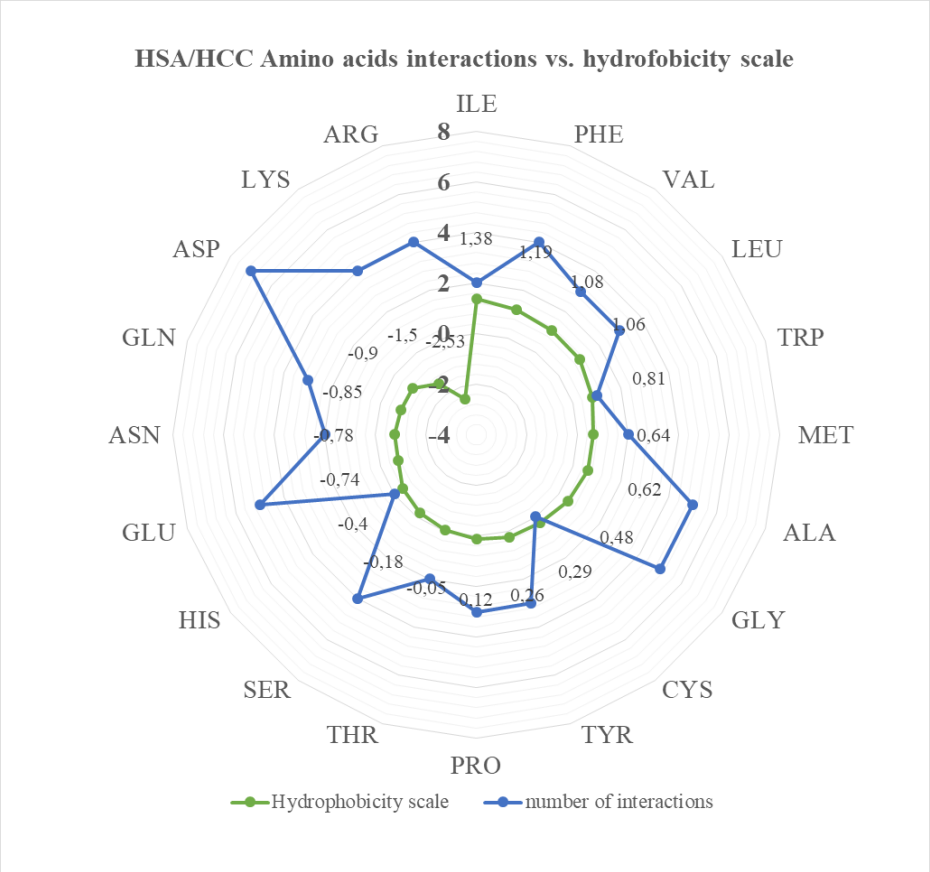

Figure S 6. Diagram of interacting amino acids in of HSA-HCC complex model with the hydrofobicy scale.

G. Amino acid scale: Normalized consensus hydrophobicity scale

Eisenberg D., Schwarz E., Komarony M., Wall R. Reference: J. Mol. Biol. 179:125-142 (1984)

Amino acid scale values:

Ala: 0.620	Leu: 1.060
Arg: -2.530	Lys: -1.500
Asn: -0.780	Met: 0.640
Asp: -0.900	Phe: 1.190
Cys: 0.290	Pro: 0.120
Gln: -0.850	Ser: -0.180
Glu: -0.740	Thr: -0.050
Gly: 0.480	Trp: 0.810
His: -0.400	Tyr: 0.260
Ile: 1.380	Val: 1.080

Source: http://us.expasy.org/tools/pscale/Hphob.Eisenberg.html

H. Kinetic measurements of secondary structure transition of Aβ 1-16 done by Circular Dichroism

The CD spectra showed the conformational change of Aβ 1-16 peptide from coiled coil toward β-sheet secondary structure. The peptide was incubated in 37 ºC with agitation and measured in the time lap.

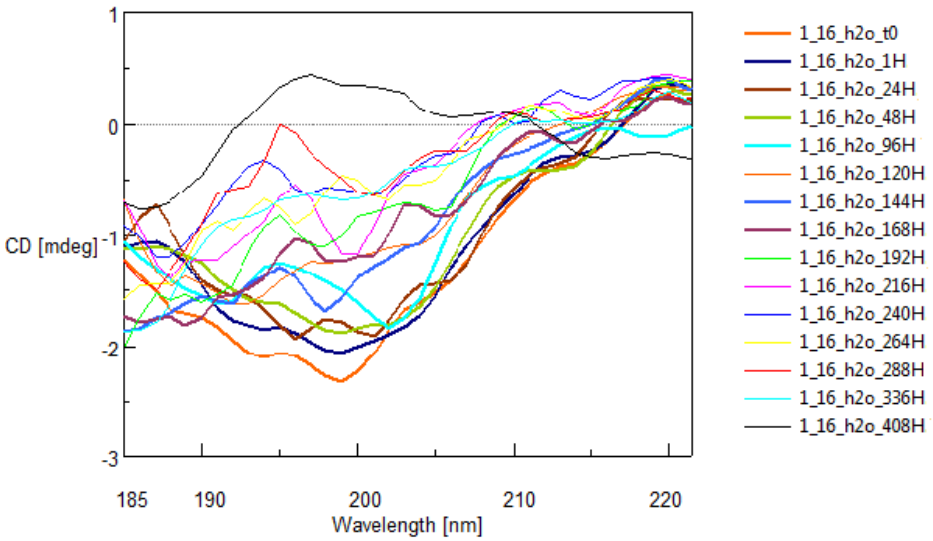

Figure S 7. Recorded time-scale CD spectra of Aβ 1-16 incubated in 37 ºC.

I. SANS kinetic for Aβ fibrils

There is no difference in SANS scattering profile between start (green) and the end of the kinetics experiments (red).

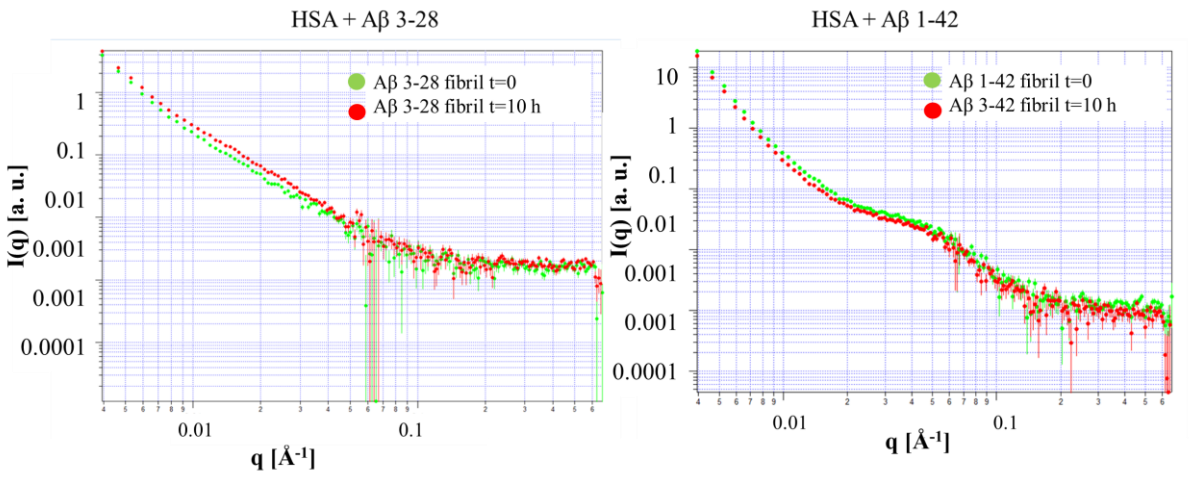

Figure S 8. SANS kinetics of Aβ peptide fibrils only. Start (green) and ending (red) SANS profile of Aβ fibrils.

J. Optimization 3-28 fibril model by Unres

Model of Aβ 3-28 fibril before and after MD optimization (one layer)

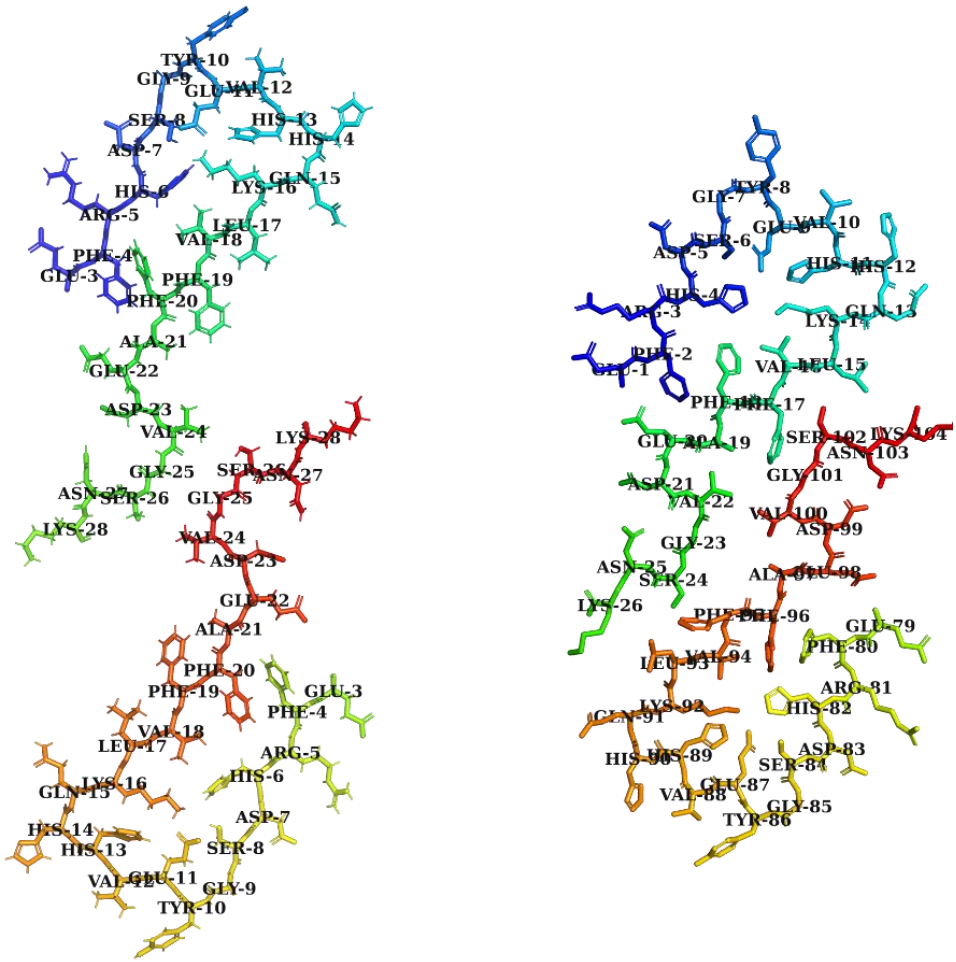

Figure S 9. One layer of the homology model of Aβ 3-28 peptides fibril before (left) and after optimization by MD (right).

K. NMR data processing

Example scripts for data processing

Data processing to NMRpipe format

```
##!/bin/csh

var2pipe -in /home/.../800MHz/hCC_15N_pH_7.0_R1_t24.7_800_101221.fid/fid \
 -noaswap  \
  -xN              2048  -yN                 9  -zN               192  \
  -xT              1024  -yT                 9  -zT                96  \
  -xMODE        Complex  -yMODE           Real  -zMODE        Complex  \
  -xSW        13020.833  -ySW            9.000  -zSW         2500.000  \
  -xOBS         799.708  -yOBS           1.000  -zOBS          81.043  \
  -xCAR           4.777  -yCAR           0.000  -zCAR         118.153  \
  -xLAB              HN  -yLAB              rd  -zLAB             N15  \
  -ndim               3  -aq2D          States                        \
| nmrPipe -fn TP \
| nmrPipe -fn ZTP \
| nmrPipe -fn TP -hyper \
| pipe2xyz -out /home/.../test%03d.fid -verb -ov
sleep 5
```

Data processing by NMRpipe with correcting a phase

```
#!/bin/csh -f

# 3D States-Mode HN-Detected Processing.
xyz2pipe -in test%03d.fid -x  -verb              \
| nmrPipe  -fn SOL                              \
| nmrPipe  -fn POLY -time                          \
| nmrPipe  -fn MAC -macro $NMRTXT/ranceY.M -noRd -noWr \
#| nmrPipe  -fn MAC -macro $NMRTXT/bruk_ranceY.M -noRd -noWr \
| nmrPipe  -fn SP -off 0.5 -end 0.95 -pow 2 -c 0.5  \
| nmrPipe  -fn ZF -auto                            \
| nmrPipe  -fn ZF -zf 2                         \
| nmrPipe  -fn FT                                  \
| nmrPipe  -fn PS -p0 28.0 -p1 0.0 -di -verb      \
| nmrPipe  -fn EXT -x1 5ppm -xn 11ppm -sw -verb    \
#| nmrPipe  -fn EXT -x1 0.0ppm -xn 6.0ppm -sw -verb    \
| nmrPipe  -fn TP                                   \
#| nmrPipe  -fn LP                                 \
#| nmrPipe  -fn LP -ps90-180                       \
| nmrPipe  -fn SP -off 0.5 -end 0.95 -pow 2 -c 0.5   \
| nmrPipe  -fn ZF -auto                           \
| nmrPipe  -fn ZF -zf 2                  \
#| nmrPipe  -fn ZF -size 512                \
| nmrPipe  -fn ZF -size 1024               \
#| nmrPipe  -fn ZF -size 2048                \
| nmrPipe  -fn FT                                    \
| nmrPipe  -fn PS -p0 3.0 -p1 0.0 -di -verb      \
#| nmrPipe  -fn POLY -auto -verb                 \
#| nmrPipe  -fn EXT -x1 0.0ppm -xn 0.0ppm -sw -verb    \
#| nmrPipe  -fn REV                              \
#| nmrPipe  -fn CS -rs 1                           \
#| nmrPipe  -fn POLY -auto -verb                 \
| nmrPipe  -fn TP                                 \
| nmrPipe  -fn EXT -y1 80.0ppm -yn 155.0ppm -sw -verb    \
#| nmrPipe  -fn POLY -auto -verb                  \
```

```
#| nmrPipe  -fn POLY -auto -xn 4.80ppm -verb                    \
#| nmrPipe  -fn POLY -auto -x1 4.40ppm -verb                    \
#| nmrPipe  -fn TP                                        \
| pipe2xyz -out test%03d_pha.ft2 -x
```

Fitting the T_1, T_2

The R_1 and R_2 was calculated though the fitting peaks decay with usage of Sparky software according to relation R=1/T.

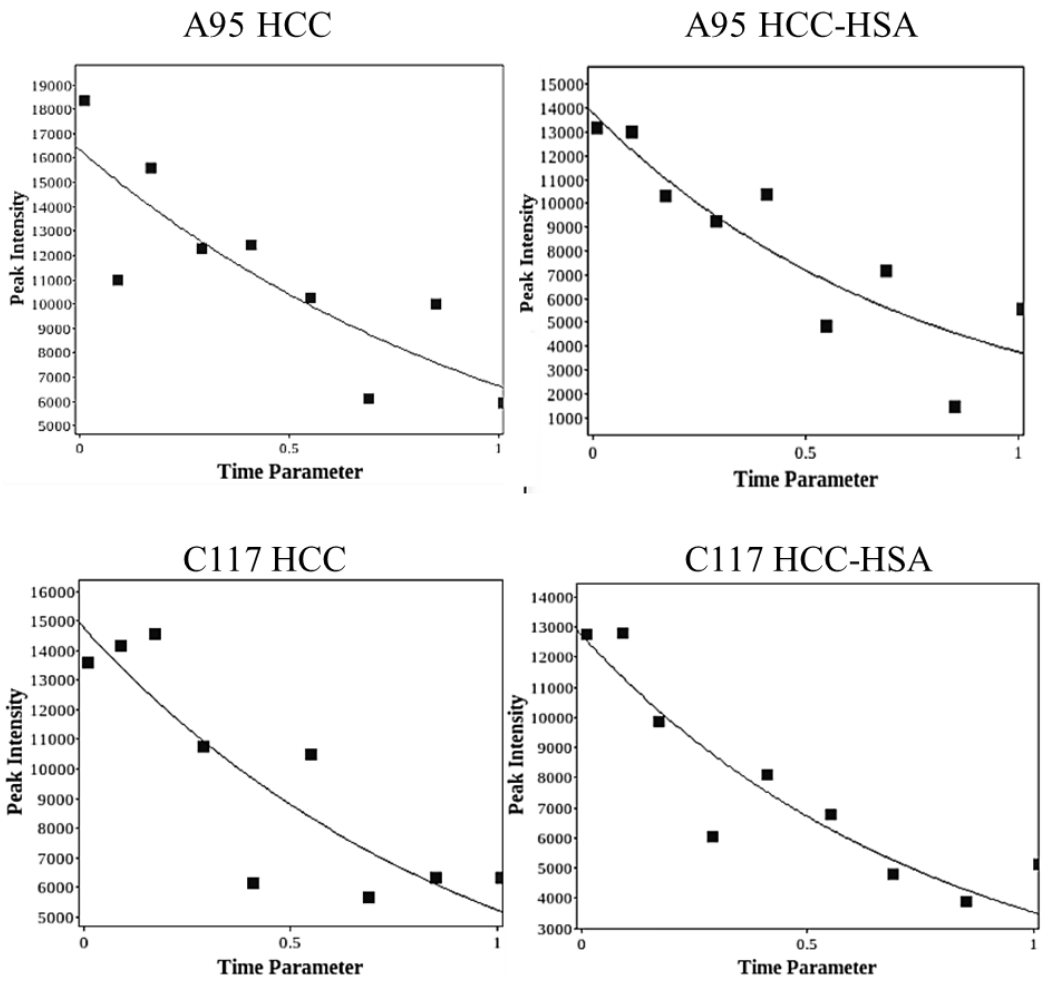

Figure S 10. Example of fitting correlation time (T_1) for chosen residues A95 and C117

Table S 3. The comparison of change R_1 and R_2 for HCC with and without HSA

Amin. Acid	R_1 HCC/HSA-HCC	Amin. Acid	R_2 HCC/HSA-HCC
I101	0.819	**V66**	0.794
G22	0.825	**C83**	0.834
Y102	0.826	**A103**	0.895
L68	0.833	**K94**	0.931
H43	0.850	**G69**	0.967
Y42	0.851	**L91**	0.970
M41	0.866	**Y102**	0.972
I56	0.871	**R24**	0.987
G57	0.873	**L112**	0.996
A46	0.875	**D40**	0.996
S98	0.879	**D65**	0.999
F63	0.887	**L9**	1.000
N35	0.890	**S44**	1.002
H86	0.896	**G22**	1.002
L64	0.898	**D119**	1.009
L91	0.905	**A26**	1.010
V66	0.906	**R8**	1.012
E21	0.910	**Q100**	1.019
K92	0.915	**Q48**	1.022
Q48	0.918	**N79**	1.022
N82	0.920	**K54**	1.024
A16	0.921	**S113**	1.025
A30	0.921	**C117**	1.026
T72	0.922	**G57**	1.026
L112	0.925	**Q55**	1.029
D40	0.926	**R45**	1.031
F96	0.927	**V10**	1.042
S113	0.929	**M14**	1.045
T116	0.932	**A37**	1.049
D81	0.932	**C97**	1.057
Q77	0.935	**T72**	1.059
D119	0.936	**N61**	1.061
L9	0.937	**A46**	1.061
R8	0.940	**Y34**	1.063
M14	0.941	**V60**	1.066
Q100	0.941	**S98**	1.069
S38	0.941	**D15**	1.071
V18	0.943	**T116**	1.073
C83	0.945	**T109**	1.079
T74	0.950	**E67**	1.080
T109	0.951	**D81**	1.080
D28	0.953	**K92**	1.082
V10	0.954	**K36**	1.083
M110	0.955	**Q107**	1.083
G69	0.957	**V49**	1.083
G59	0.959	**Q77**	1.084
K94	0.963	**E21**	1.085
L47	0.966	**M110**	1.086
K75	0.970	**E19**	1.087
E20	0.975	**T74**	1.089
W106	0.975	**G59**	1.089
Q107	0.979	**L27**	1.100
R53	0.980	**N35**	1.100
A26	0.982	**H43**	1.104
E67	0.987	**R25**	1.105
V60	0.990	**V18**	1.109
V49	0.990	**D28**	1.109
S44	0.992	**S38**	1.111
N61	0.995	**T111**	1.112
V50	0.997	**G32**	1.112
A52	0.999	**S17**	1.113
S115	1.005	**G108**	1.116
A120	1.008	**V23**	1.116
F85	1.008	**Y42**	1.119
Y62	1.011	**A30**	1.119
N79	1.012	**A16**	1.120
R51	1.014	**S115**	1.122
E19	1.014	**A120**	1.125
C73	1.016	**L68**	1.129
D65	1.018	**F63**	1.132
D15	1.020	**C73**	1.137
R24	1.023	**R51**	1.138
Q55	1.026	**F29**	1.144
L27	1.028	**F99**	1.144
K36	1.029	**Q118**	1.148
V23	1.032	**Y62**	1.151
V104	1.033	**T76**	1.155
K114	1.038	**K75**	1.156
A103	1.038	**V104**	1.158
Q118	1.041	**E20**	1.160
V31	1.043	**V31**	1.161
G108	1.046	**V50**	1.166
G32	1.053	**A52**	1.166
Y34	1.058	**F85**	1.171
T111	1.058	**N82**	1.178
A37	1.063	**M41**	1.203
R25	1.073	**A95**	1.205
K54	1.079	**K114**	1.205
C97	1.084	**R53**	1.218
E33	1.088	**W106**	1.218
T76	1.098	**E33**	1.218
R45	1.103	**I56**	1.231
S17	1.112	**I101**	1.251
F99	1.129	**L64**	1.257
F29	1.140	**L47**	1.260
C117	1.234	**H86**	1.300
A95	1.446	**F96**	1.310

L. Python scripts for Pymol

The script for Pymol software was written in Python 3 in order to extract information from HSA + ligands structures deposited in PDB database (Figure 83).

HSA structures in PDB DB (search by matching sequence):

4LB2,4L9Q,4LA0,4L9K,6WUW,1BM0,1AO6,4LB9,4L8U,1UOR,6EZQ,3B9L,5FUO,5UJB,1N5U,2BX8,2BXA,2BXB,2BXF,2BXG,2BXH,2VUE,6M58,4E99,2BXE,4BKE,1BJ5,3A73,2BXD,2BXL,2BXN,2BXO,2BXP,1E7E,6XV0,3SQJ,3TDL,1E7F,1E78,2BXC,4S1Y,6HSC,2YDF,5YB1,3LU8,3LU7,3LU6,1GNJ,2ESG,2VUF,1E7A,1E7B,2BXM,1E7I,3JRY,1E7C,2XVU,2XVQ,2XW1,2XW0,1GNI,1E7G,1E7H,2BXI,2VDB,5X52,2XVW,6M4R,1O9X,5YOQ,2BXQ,2BXK,1H9Z,1HA2,5Z0B,3CX9,6A7P,5ID7,6R7S,4G04,4G03,4IW1,5IJF,2XVV,2XSI,5IFO,4Z69,3UIV,5GIX,7D6J,4HGK,1BKE,4IW2,6YG9,4K2C,6M5E,4HGM,7JWN,6L4K,1TF0,4EMX,7AAE,7AAI,6M5D,1HK1,6QIP,1HK2,7DJN,1HK3,1HK4,3B9M,1HK5,5GIY,4N0F,7QFE,7OV6,7OV5,7OV1,2I2Z,2I30,7A9C,4K71,7VR9,6QIO,6ZL1,6JE7,4N0U,7EEK,3JQZ,5VNW,7DL4,6RQ7,6FAK,5OKL,1YSX,1J78,1J7E,1MA9,1KXP,1KW2,1LOT

Python scripts to process the files are upload into GitHub:

Create a list of structures, ligands and its interactions in 5 Å surroundings:

https://github.com/Aazyla/Pymols_scripts/blob/c4666430058e91820565c6b1f0fddcfc2a878cc8/show_me_your_ligand.py

To generate interactions maps:

https://github.com/Aazyla/Pymols_scripts/blob/c4666430058e91820565c6b1f0fddcfc2a878cc8/conv_file_intoarray.py